CORA Cork Open Research Archive
Cartlann Taighde Oscailte Chorcaí

Title	Nanostructured magnetic materials for integrated magnonic devices
Authors	Samanta, Arindam
Publication date	2024
Original Citation	Samanta, A. 2024. Nanostructured magnetic materials for integrated magnonic devices. PhD Thesis, University College Cork.
Type of publication	Doctoral thesis
Rights	© 2024, Arindam Samanta. - https://creativecommons.org/licenses/by-nc-nd/4.0/
Download date	2026-11-16 10:49:06
Item downloaded from	https://hdl.handle.net/10468/16982



UCC
University College Cork, Ireland
Coláiste na hOllscoile Corcaigh

Nanostructured Magnetic Materials for Integrated Magnonic Devices

Dissertation undertaken at the

Micropower Devices and Nanomagnetics Group

in

Tyndall National Institute

and

presented to the

School of Physics

at the

National University of Ireland, Cork – University College Cork

in partial fulfilment of the requirements for the degree of

Doctor of Philosophy (PhD)

in

Physics

by

Arindam Samanta

Supervisor: Professor Saibal Roy

November 2024

Declaration

This is to certify that the work I am submitting is my own and has not been submitted for another degree, either at University College Cork or elsewhere. All external references and sources are clearly acknowledged and identified within the contents. I have read and understood the regulations of University College Cork concerning plagiarism and intellectual property.

Signature: *Arindam Samanta*
Name: ARINDAM SAMANTA
Student ID: 118222210
Date: 29th November, 2024

© অরিন্দম সামন্ত, ২০২৪
সমস্ত অধিকার সংরক্ষিত অন্যথায় নির্দেশিত।
যেকোনো প্রয়োজনীয় অনুমতির জন্য লেখক বা মূল প্রকাশকের সাথে যোগাযোগ করুন।

© Arindam Samanta, 2024
All rights reserved unless otherwise indicated.
Contact the author or original publisher for any necessary permissions.

Acknowledgements

I would like to extend my sincere gratitude to the individuals who have played a crucial role in the successful completion of my PhD thesis, especially considering the unprecedented challenges posed by the global COVID-19 pandemic. Over the course of six years, their unwavering support, guidance, and collaboration have been invaluable; it has been an incredible journey of five years, filled with challenges, growth, and invaluable experiences.

First and foremost, I extend my deepest appreciation to my supervisor, Prof. Saibal Roy, for his continuous support, guidance, mentorship and constant encouragement throughout the course of my research. Despite the disruptions caused by the pandemic, his dedication to my research remained unwavering. I am truly grateful for your mentorship and the opportunities you provided. Thanks for steering me through the storm with wisdom, humor, and an unyielding belief in my caffeine-fueled endeavors.

I am indebted to my advisor, Dr. Andreas Amann, for his insightful suggestions, constructive feedback throughout the entire process. Your meticulous guidance turned my scribbles into a symphony. His expertise and attention to detail have significantly enhanced the quality of my work. I am sincerely thankful for his patience, encouragement, and the trust he has placed in me.

I would like to acknowledge Prof. Cian O'Mathuna, Head of the Micro & Nano Systems Centre; Eamon O'Riain, IT Manager; and Don Lynch, Senior PC Administrator at the Tyndall National Institute. Despite the limitations imposed by the pandemic, they went above and beyond to arrange and provide me with the necessary computational facilities for my research. I greatly appreciate their efforts to ensure that I had access to the required resources.

I would also like to extend my gratitude to Dr. Gianluca Gubbiotti from Istituto Officina dei Materiali - Consiglio Nazionale delle Ricerche (CNR-IOM), Perugia, Italy, Prof. Anjan Barman, Dr. Soma Dutta and Dr. Surya Narayan Panda from S. N. Bose National Centre for

Basic Sciences, Kolkata, India, who made the distance irrelevant from cooking up some brilliant collaborations. Despite the geographical distance and the limitations imposed by the pandemic, their willingness to engage in virtual discussions and their invaluable contributions have greatly enriched my research.

I extend my heartfelt appreciation to Sanjeev, Dinesh, Amit, Parnika, Rajvinder, and Risov for being exceptional companions throughout my doctoral journey—you turned the scholarly battlefield into a playground. Thanks to my newly joined junior groupmates, Subham, Karan, and Tilottoma for creating such wonderful memories in the last few months of Tyndall life. I am also deeply grateful to my IITKGP roommates, Priyabrata and Ashes, as well as friends Koushik, Pranesh, Sourabh, Avadh, Sudipta, Arabinda, Rohan, Isha, Deepali. The enduring bond formed between the rollercoaster mates is truly cherished; you've made this journey a crazy, beautiful ride. Additionally, my childhood friends Arundhati, Khepi (Arpita), Tathagata, Saikat, Gour Sebak and Dinesh with whom the stress-busting audio-video calls served as a breath of fresh air and lifeline in the doctoral roller-coaster.

A special mention of thanks goes to my extended family in Cork—Tanmay, Debapriya'da, Archishman, Rajannya'di, Samir'da, Seuli'di, Sambuddha'da, Ranu'di, Abhijnan, Somnath'da, Swastika'di, and the two adorable kids, tiny rockstars Shreyansh and Rayhansh.

Finally, I would like to express my deepest gratitude to my Maa, Santwana Samanta; Baba, Satrughna Samanta; Bhaai, Arijeet Samanta; sister-in-law, Moupriya Pal; and my family and friends for their unwavering support, understanding, and encouragement throughout this challenging journey. To the family and friends, your patience deserves a PhD too.

Last but not the least, special thanks to my wife, Dr. Susmita Changdar, my ride-or-die, for your supports and fights beyond the geographical distance. Your constant presence, encouragement, and belief in my abilities have been a source of strength for me and made the tough days bearable. Thanks for being my anchor in this doctoral storm.

To everyone who has played a part, whether a cameo or a lead role, you're the real MVPs in my academic pursuit — I offer my heartfelt thanks. Your contributions have been invaluable, and I am truly honored to have had the privilege of working with such remarkable individuals. This journey was wild, and you made it a blockbuster. Cheers to all the unsung heroes!

Arindam Samanta

Dedicated to my beloved Maa, Baba, Bhaai

Abstract

This PhD thesis explores the fabrication, characterization, and application of advanced exchange spring (ES)/exchange coupled (EC) nanoheterostructures and their magnetic properties. Current challenges in the field of magnetics include the development of materials that demonstrate tunable magnetic properties, particularly in terms of controlling anisotropy and spin dynamics at the nanoscale. This thesis addresses these challenges by utilizing an electrodeposition technique, we have been able to develop for the first time *in situ* amorphous/nanocrystalline cobalt-phosphorus (CoP) thin films at room temperature. These films exhibit a unique transverse exchange spring structure due to the interplay between in-plane (IP) and out-of-plane (OOP) anisotropies. The inherent IP anisotropy of the amorphous phase competes with the OOP anisotropy of the nanocrystalline structure, producing characteristic stripe domain structures that evolve into novel corrugated stripe domain shapes.

Systematic investigations reveal the evolution of hysteresis loops in these thin films, showing a transition from low coercivity non-ES loops to staircase-ES loops with multiple coercivities in thicker films. The First Order Reversal Curve (FORC) distributions demonstrate various reversal mechanisms within the samples, confirming the transition between non-ES and ES states based on the prevalent interfacial exchange coupling. Additionally, the field-dependent Brillouin Light Scattering (BLS) spectra unveil distinct spin wave modes, with ES films showing well-resolved bulk and Damon-Eshbach surface spin wave modes, while non-ES films exhibit mode doublets below a certain applied field threshold. These findings indicate a linear dependence of mode frequencies on magnetic field intensity and enhanced exchange coupling in thicker ES films.

On the other hand, ultrafast magnetization dynamics studies highlight the in-plane magnetic orientation (φ) dependent ultrafast demagnetization and precessional dynamics of electrodeposited non-exchange spring nanostructured CoP alloys. The precession frequency shows dominant two-

fold anisotropy superposed with moderate four-fold anisotropy, while the Gilbert damping coefficient exhibits four-fold anisotropy. The ultrafast demagnetization remains nearly isotropic with φ, suggesting a significant role of spin-orbit coupling (SOC) in anisotropic precessional dynamics and isotropic spin-flip scattering processes. These detailed studies of ultrafast spin dynamics reveal crucial dynamical properties for potential applications in high-frequency integrated magnetic passives for future monolithic on-chip power supplies.

Furthermore, this thesis introduces novel "Magnon Microwave Antennas" (MMAs) for generating tunable microwave frequencies without external bias magnetic fields. The MMAs, comprising patterned arrays of magnetostrictive nanomagnets embedded in piezoelectric heterostructures, generate multimode microwave frequencies through the phonon—magnon coupling. Static magnetic studies elucidate various magnetization reversal processes within the nanowire and nanodot arrays, unveiling the critical role of demagnetization energy distribution in tuning the domain configuration and power-phase distributions of these MMAs. Functional tuneability has been proposed to be achieved through amplitude-dependent training using different combinations of nanowire and nanodot dimensions, topologies, material properties, and array configurations. The non-volatile nature of the spin textures generated in MMAs under bias-free conditions holds promise for energy-efficient logic and low-power computing applications.

Thus, the comprehensive research presented in this thesis paves the way for the development and exploitation of next-generation nano-heterostructures for various cutting-edge magnetic vis-à-vis magnonic applications, including on-chip reservoir computing, leveraging the unique magnetic vis-à-vis magnonic properties and their tuneability in these advanced materials/devices.

রূপরেখা

এই পিএইচডি থিসিসটি উন্নত বিনিময় স্প্রিং (এক্সচেঞ্জ স্প্রিং, ES)/ বিনিময় সংযোজিত (এক্সচেঞ্জ কাপলড, EC) ন্যানোহেটেরোস্ট্রাকচার এবং তাদের চৌম্বকীয় বৈশিষ্ট্যগুলির বানোয়াট, চরিত্রায়ন এবং প্রয়োগের অনুসন্ধান করে। একটি ইলেক্ট্রোডিপজিশন কৌশল ব্যবহার করে, আমরা প্রথমবারের মতো ঘরের তাপমাত্রায় নিরাকার/ন্যানোক্রিস্টালাইন কোবাল্ট-ফসফরাস (CoP) পাতলা ফিল্ম তৈরি করতে সক্ষম হয়েছি। সমতল বা সমপৃষ্ঠ (ইন-প্লেন, আইপি,IP) এবং অসমতল বা অসমপৃষ্ঠ (আউট-অফ-প্লেন, ওওপি, OOP) অ্যানাইসোট্রপিগুলির মধ্যে আন্তঃপ্রক্রিয়ার কারণে এই চলচ্চিত্রগুলি একটি অনন্য ট্রান্সভার্স এক্সচেঞ্জ স্প্রিং কাঠামো প্রদর্শন করে। নিরাকার পর্যায়ের অন্তর্নিহিত আইপি অ্যানাইসোট্রপি ন্যানোক্রিস্টালাইন কাঠামোর OOP অ্যানাইসোট্রপির সাথে প্রতিযোগিতা করে, বৈশিষ্ট্যযুক্ত স্ট্রাইপ ডোমেন কাঠামো তৈরি করে যা অভিনব ঢেউতোলা (corrugated) ডোমেন আকারে বিকশিত হয়।

পদ্ধতিগত অনুসন্ধান এই পাতলা ফিল্মগুলিতে হিস্টেরেসিস লুপগুলির বিবর্তন প্রকাশ করে, যা কম কোএর্সিভিটি (Coercivity) যুক্ত নন-ইএস লুপ থেকে মোটা ফিল্মে একাধিক কোএর্সিভিটি সহ সিঁড়ির মতো-ইএস লুপগুলিতে একটি রূপান্তর দেখায়। প্রথম ক্রম প্রতিবর্তন বক্ররেখা (ফার্স্ট অর্ডার রিভার্সাল কার্ভ, First Order Reversal Curve , FORC) পরিমিতি (measurement) বিন্যাস/ডিস্ট্রিবিউশনগুলি নমুনার মধ্যে বিভিন্ন প্রতিবর্তন পদ্ধতি (রিভার্সাল মেকানিজম) প্রদর্শন করে, যা প্রচলিত আন্তঃসম্মুখস্থ বিনিময় যুগ্মীকরণ (ইন্টারফেসিয়াল এক্সচেঞ্জ কাপলিং) এর উপর ভিত্তি করে নন-ইএস এবং ইএস অবস্থার (স্টেটের) মধ্যে পরিবর্তন নিশ্চিত করে। অতিরিক্তভাবে, চৌম্বকক্ষেত্র-নির্ভর ব্রিলুয়াঁ আলোক বিচ্ছুরণ (Brillouin Light Scattering, BLS) বর্ণালী (Spectra) স্বতন্ত্র ঘূর্ণন/স্পিন তরঙ্গ (Spin wave) মোড উন্মোচন করে, যেখানে ES ফিল্মগুলি ভাল-সমাধানকৃত বাল্ক এবং ড্যামন-এশবাচ (Damon-Eshbach) পৃষ্ঠ ঘূর্ণন তরঙ্গ (সারফেস স্পিন ওয়েভ) মোডগুলি দেখায়, যখন নন-ইএস ফিল্মগুলি একটি নির্দিষ্ট প্রয়োগকৃত চৌম্বকক্ষেত্রের প্রান্তিক মানের (থ্রেশহোল্ডের) নীচে মোড প্রদর্শন করে। এই ফলাফলগুলি চৌম্বকক্ষেত্রের তীব্রতার উপর মোড তরঙ্গগুলির একটি রৈখিক নির্ভরতা এবং ঘন ES ফিল্মগুলিতে বর্ধিত বিনিময় সংযোগ নির্দেশ করে।

অন্যদিকে গবেষণায় আরও লক্ষ্য করা হয়েছে, অতিদ্রুত চৌম্বকীকরণ গতিবিদ্যা অধ্যয়ন (Ultrafast magnetization dynamics studies) ইলেক্ট্রোডিপোজিটেড অ-বিনিময় স্প্রিং ন্যানোস্ট্রাকচার্ড ফিল্মের সমতলীয় চৌম্বকীয় অভিযোজন (φ) নির্ভরশীল অতিদ্রুত তিরশ্চৌম্বকীকরণ (Ultrafsct demagnetization) এবং অগ্রগতিগত গতিবিদ্যা (Precessional dynamics) তুলে ধরে। অগ্রগতিগতসম্পন্ন তরঙ্গের মধ্যে (Precession frequency) মাঝারি ক্ষমতাসম্পন্ন চার ভাগে বিভক্ত অ্যানাইসোট্রপি প্রবল ক্ষমতাসম্পন্ন দুই ভাগে বিভক্ত অ্যানাইসোট্রপির ওপরে উপরিপন্ন হতে দেখা যায়, যখন গিলবার্ট ড্যাম্পিং গুণাঙ্ক (Gilbert damping coefficient) চার ভাগে বিভক্ত অ্যানাইসোট্রপি প্রদর্শন করে। φ এর সাথে অতিদ্রুত তিরশ্চৌম্বকীকরণ প্রায় আইসোট্রপিক থেকে যায়, যা অ্যানাইসোট্রপিক অগ্রগতিগত গতিবিদ্যা এবং আইসোট্রপিক স্পিন-ফ্লিপ বিচ্ছুরণ প্রক্রিয়াগুলিতে ঘূর্ণন—কক্ষপথ সংযোজন (স্পিন—অরবিট কাপলিং, এসওসি) এর একটি উল্লেখযোগ্য ভূমিকার পরামর্শ দেয়।

অতিদ্রুত চৌম্বকীকরণ গতিবিদ্যার এই বিস্তারিত অধ্যয়নগুলি ভবিষ্যতে মনোলিথিক অন-চিপ শক্তি সরবরাহের জন্য উচ্চ-তরঙ্গ সমন্বিত চৌম্বকীয় প্যাসিভগুলিতে সম্ভাব্য প্রয়োগগুলির জন্য গুরুত্বপূর্ণ গতিশীল বৈশিষ্ট্যগুলি প্রকাশ করে।

উপরন্তু, এই থিসিসটি বাহ্যিক চৌম্বকক্ষেত্র প্রভাব মুক্ত (external bias field free) প্যাটার্নসহ চৌম্বকীয় পীড়ন যুক্ত (ম্যাগনেটোস্ট্রিকটিভ) ন্যানোচুম্বক/ পিজোইলেকট্রিক হেটেরোস্ট্রাকচারে সীমাবদ্ধ পৃষ্ঠতলীয় ধ্বনিতাত্ত্বিক তরঙ্গ (সারফেস অ্যাকোস্টিক ওয়েভ, SAWs) দ্বারা সৃষ্ট স্পিন তরঙ্গের মাধ্যমে একটি ''ম্যাগনন মাইক্রোওয়েভ অ্যান্টেনা'' (MMA-এমএমএ) প্রবর্তন করে সমন্বয়যোগ্য মাইক্রোওয়েভ তৈরি করার জন্য। স্থৈতিক চৌম্বকীয় অধ্যয়নগুলি (Static magnetic studies) ন্যানোওয়ার এবং ন্যানোডট বিন্যাসগুলির মধ্যে বিভিন্ন চুম্বকীয়করণের প্রতিবর্তন প্রক্রিয়াগুলিকে (Reversal mechanisms) ব্যাখ্যা করে, এই এমএমএগুলির ডোমেন কনফিগারেশন এবং প্রভাব-পর্যায় বিতরণগুলিকে (পাওয়ার-ফেজ ডিস্ট্রিবিউশন) সমন্বয় করার ক্ষেত্রে তিরশ্চৌম্বকীকৃত শক্তি (demagnetization energy) বিতরণের গুরুত্বপূর্ণ ভূমিকা উন্মোচন করে। ন্যানোওয়ার এবং ন্যানোডটে ফোনন-ম্যাগনন-ফোটন কাপলিং উচ্চ সুরযোগ্যতার সাথে মাইক্রোওয়েভ ফ্রিকোয়েন্সি তৈরি করে, যা স্বল্প শক্তি সক্ষম যুক্তিবিদ্যা এবং ন্যূনতম শক্তি খরচ সম্পন্ন কম্পিউটিংয়ের সম্ভাব্য প্রয়োগ সরবরাহ করে।

এইভাবে, এই থিসিসে উপস্থাপিত বিস্তৃত গবেষণা অন-চিপ রিজার্ভার কম্পিউটিং সহ বিভিন্ন অত্যাধুনিক ম্যাগনেটিক এবং একই সঙ্গে ম্যাগনোনিক প্রয়োগগুলির জন্য পরবর্তী প্রজন্মের ন্যানো-হেটারোস্ট্রাকচারগুলির বিকাশ এবং অভিনিবেশের পথ প্রশস্ত করে, যা এই উন্নত এবং অত্যাধুনিক উপকরণ/ডিভাইসগুলিতে চৌম্বকীয় বৈশিষ্ট্য এবং তাদের সুরযোগ্যতা ব্যবহার করে।

List of Acronyms

nm	nanometre
μm	micron or micrometre
μ_0	permeability of free space
FM	Ferromagnetic
δ_H	Domain Wall Width of hard magnetic phase
l_{ex}	Exchange Length
H_C	Coercivity
M_{Sat}/M_S	Saturation Magnetization
M_R	Remanence Magnetization
ES	Exchange Spring
EC	Exchange Coupled
IP	In−plane
IC	Integrated Circuits
ID	Integrated Devices
IMD	Integrated Magnonic Devices
OOP	Out−of−plane
SFD	Switching Field Distribution
AFM	Atomic Force Microscopy
MFM	Magnetic Force Microscopy
SEM	Scanning Electron Microscopy
TEM	Transmission Electron Microscopy
BH_{max}	Energy Product

NHS	Nano-hetero-structure/Nanoheterostructure
NW/NWs	Nanowire/Nanowires
ND/NDs	Nanodot/Nanodots
λ_s	Linear magnetostriction constant
σ_p	Interfacial planar stress
S	Squareness ratio
MMA	Magnon Microwave Antenna
DE	Damon—Eshbach
BLS	Brillouin Light Scattering
TRMOKE	Time Resolved Magneto-Optic Kerr Effect
SW	Spin Wave
FFT	Fast Fourier Transform
LLG	Landau—Lifshitz—Gilbert
ME	Magnetoelectric
PE	Piezoelectric
RC	Reservoir Computing

List of Publications

• Journal Publication

5. Investigation of transverse exchange-springs in electrodeposited nano-heterostructured films through first-order reversal curve analysis, **A. Samanta**, S. Roy, *APL Materials*, **12**(9), 091118, 2024; DOI:10.1063/5.0223485
4. Tuneable power-phase distributions in phonon-magnon coupled Magnon Microwave Antenna for reservoir computing, **A. Samanta**, S. Roy, *Physical Review Applied*, **22**, 054076, 2024
3. Ultrafast Demagnetization and Gilbert Damping in Electrodeposited CoP Film, S. Dutta, **A. Samanta**, S. N. Panda, S. Roy and A. Barman, *Journal of Materials Science*, **58**, 14817, 2023; DOI:10.1007/s10853-023-08956-9
2. Spin Waves in Exchange Spring Nanoheterostructured Amorphous/ Nanocrystalline Films, **A. Samanta**, G. Gubbiotti, S. Roy, *Physical Review B*, **107**, 214449, 2023; DOI: 10.1103/PhysRevB.107.214449
1. Generation of Microwaves With Tuneable Frequencies in Ultracompact Magnon Microwave Antenna via Phonon-Magnon-Photon Coupling, **A. Samanta**, S. Roy, *IEEE Transaction on Electron Devices*, **70** (1), 335-342, 2023; DOI: 10.1109/TED.2022.3221026

• Conference/Symposium Publication

• International Conferences

7. Power−Phase Relation in Ultra-compact 'Magnon Microwave Antenna' for Generation of Microwaves with Tuneable Frequencies (Poster Presentation), **A. Samanta**, S. Roy, *"68th MMM Conference"*, Dallas, Oct. 30−Nov. 3, 2023

6. Power and Phase Profiles in Nano-constriction Based Synchronized Spin Hall Nano-oscillators near Threshold Current (Oral Presentation−Virtual), W. Ronayne*, **A. Samanta***, A. Amann, S. Roy, *Intermag 2023 Conference*, Sendal, Japan, May 15-19, 2023 [$*$ = equal contribution]
5. Stress-Engineered Microwave Generation induced by Phonon-Magnon-Photon Coupling in Patterned Arrays of Nanowires (Oral Presentation), **A. Samanta**, S. Roy, *' 67th MMM Conference'*, Minneapolis, MN, October 31-November 4, 2022.
4. Generation of High Amplitude Microwaves in Nanowires induced by Domain Wall Motion (Oral Presentation−Virtual), **A. Samanta**, S. Roy, *'2022 Joint MMM-Intermag Conference'*, New Orleans, LA, (Hybrid), January 10-14, 2022.
3. Structural and Magnetic Study of Single Nano-Hetero-Structured Co-Rich CoP Magnetic Thin Films (Oral Presentation−Virtual), **A. Samanta**, S. Roy, *'2022 Joint MMM-Intermag Conference'*, New Orleans, LA, (Hybrid), January 10-14, 2022.
2. Brillouin Light Scattering Study of Spin Waves in CoP Exchange Spring Thin Films (Oral Presentation), **A. Samanta**, G. Gubbiotti, S. Roy, *'Intermag 2021 Conference'*, (Virtual), April 26-30, 2021.
1. Exchange Spring Co-Rich CoP Nanomagnetic Thin Films (Oral Presentation), **A. Samanta**, S. Roy, *'Intermag 2021 Conference'*, (Virtual), April 26-30, 2021.

• National Conferences

4. Ultra-compact Magnon Microwave Antenna (MMA): Generation of Synchronized Microwaves with Tuneable Frequencies for IoT Application (Poster Presentation), **A. Samanta**, S. Roy, *CONNECT Plenary 2024*, Clonmel, Co. Tipperary, Ireland, May 14-15, 2024
3. Ultracompact "Magnon Microwave Antenna" (MMA) for Tuneable Microwaves Frequencies Generation, **A. Samanta**, S. Roy, *Tyndall Postgraduate Poster Competition*, Tyndall National Institute, Cork, Ireland, July 2023
2. Phonon−Magnon−Photon Coupling based Microwave Generation in Patterned Nanomagnetic Arrays for IoT Applications (Oral Presentation), **A. Samanta**, S. Roy, *CONNECT Plenary 2022*, Waterford, Ireland, September 7-8, 2022 [Category: ***Research Highlights***]
1. Exchange Spring Nanoheterostructure on a Co-Rich CoP Single Layer Amorphous Thin Film Using Conventional DC Electrodeposition (Oral Presentation), **A. Samanta**, S. Roy, *'ISE Satellite Student Regional Symposium on Electrochemistry'* at Trinity College Dublin; hosted by *'School of Chemistry, Trinity College Dublin'* on 14th November 2019.

Lists of Awards

1. Winner the *"BOC Gases Postgraduate Bursary 2024 Award"* for research excellence in PhD dissertation at Tyndall
2. Runner up at *"Tyndall Postgraduate Publication of the Year 2023"* (sponsored by Qualcomm)
3. Runner up at *"Tyndall Postgraduate Publication of the Year 2022"* (sponsored by Xceleprint)
4. Winner of *"Magnetic Sensors Challenge"* at the *MMM Conference 2022*
5. *"Sea Flower"* — Officially shortlisted in *"Magnetism at Art Showcase"* (*MMM Conference 2022*)
6. UCC *SEFS Travel Bursary Award* in 2022 for attending MMM Conference
7. Winner of Scientific Image Competition for *"Magnetic Maze"* at Tyndall National Institute in 2020
8. Winner of Scientific Image Competition for *"Magnetic Crown"* at Tyndall National Institute in 2020

Contents

Declaration iii

Acknowledgements vii

Abstract xi

Abstract (Bengali) xiii

List of Acronyms xv

List of Publications xvii

Lists of Awards xix

List of Figures xxv

List of Tables xxxvii

1 Introduction 1

1.1 Background 1

1.2 Ferromagnetism 3

1.3 Hysteresis Loop 4

1.4 First-order reversal curve (FORC) Measurement 6

1.5 Nanostructured Magnetic Materials 8

1.5.1 Nanostructured Soft Magnetic Materials 8

1.5.2 Nanostructured Hard Magnetic Materials . . . 9
1.5.3 Exchange Spring System . . . 9
1.5.4 Transverse Exchange Spring . . . 11
1.6 Energy Distribution in Ferromagnetic Material . . . 12
1.6.1 Exchange Energy . . . 12
1.6.2 Anisotropy Energy . . . 13
1.6.3 Demagnetizing energy . . . 13
1.6.4 Zeeman Energy . . . 14
1.6.5 Magnetoelastic Energy . . . 14
1.7 Fundamentals of Magnonics . . . 14
1.7.1 Spin Waves and Magnon . . . 14
1.7.2 Brillouin Light Spectroscopy (BLS) . . . 16
1.7.3 Time-resolved Magneto-Optical Kerr Effect (TRMOKE) . . . 17
1.8 Spin Dynamics . . . 18
1.9 Magnon Based Devices . . . 19
1.9.1 Miniaturized Conventional Antenna . . . 19
1.9.2 Magnon Microwave Antenna . . . 21
1.10 Motivation . . . 22
1.11 Thesis Outline . . . 23

2 Literature Review 25
2.1 Introduction . . . 25
2.2 Ferromagnetic Nanoheterostructured Materials for Integrated Devices . . . 26
2.3 Integratable Magnonic Devices . . . 29
2.4 Nanostructured Ferromagnetic Materials . . . 30
2.4.1 A Detailed Review of Electrodeposited Cobalt Phosphorous Alloys . . . 31
2.4.2 Exchange Spring Nanomagnets: Fundamentals and Applications . . . 36
2.4.3 Ultrafast Spin Dynamics . . . 42
2.5 Magnon Microwave Antenna . . . 44
2.6 Conclusion . . . 45

3 Theoretical and Experimental Techniques 47
3.1 Introduction . . . 47
3.2 Structural Design using COMSOL Multiphysics . . . 47
3.2.1 Utilization of AC/DC Module . . . 48
3.2.2 Integration of MEMS Module . . . 49

3.3 Micromagnetic Simulation with MuMax[3] . . . 50
3.4 Electrodeposition . . . 51
3.4.1 Cyclic Voltammetry (CV) . . . 53
3.5 Structural characterization . . . 55
3.5.1 Scanning Electron Microscopy (SEM) . . . 55
3.5.2 Stoichiometry Analysis . . . 56
3.5.3 X-ray diffraction (XRD) . . . 58
3.5.4 Atomic Force Microscopy (AFM) . . . 59
3.5.5 Transmission Electron Microscopy (TEM) . . . 60
3.6 Magnetic Property Characterization . . . 62
3.6.1 ShB Hysteresis Loop Tracer . . . 62
3.6.2 SQUID Magnetometer for High-resolution Magnetic Measurement . . . 62
3.6.3 First Order Reversal Curve . . . 67
3.6.4 Magnetic Force Microscopy (MFM) . . . 69
3.7 Dynamic Characterization . . . 70
3.7.1 Brillouin Light Scattering (BLS) Study . . . 70
3.7.2 Time-resolved Magneto-Optical Kerr Effect (TRMOKE) Study . . . 71

4 Fabrication of Nano-hetero-structured Magnetic Exchange Springs 73
4.1 Introduction . . . 73
4.2 Experimental Methods . . . 75
4.3 *"In situ"* NHS formation by hydrogen evolution . . . 77
4.4 Structural and Stoichiometry Analysis . . . 79
4.5 Static Magnetic Study . . . 83
4.6 First-Order Reversal Curve (FORC) Measurement . . . 84
4.7 Micomagnetic Simulations . . . 88
4.8 Conclusion . . . 91

5 Spin Waves in Exchange Spring Nanomagnets 93
5.1 Introduction . . . 93
5.2 Experimental Methods . . . 95
5.3 Structural Characterization and Elemental Analysis . . . 96
5.4 Static Magnetic Properties . . . 99
5.5 First—Order Reversal Curve (FORC) Distribution . . . 100
5.6 Analytical Formulation by Exchange Energy Calculation . . . 102
5.7 Brillouin Light Scattering Spectroscopy . . . 104

5.8 Conclusion . . . 109

6 Ultrafast demagnetization of nanostructured magnetic materials 111
6.1 Introduction . . . 111
6.2 Experimental Methods . . . 114
6.3 Static Characterization . . . 116
6.4 TRMOKE Measurement of Ultrafast Spin Dynamics . . . 118
6.5 Conclusion . . . 122

7 Magnon Microwave Antenna (MMA) 123
7.1 Introduction . . . 123
7.2 COMSOL Design of MMA . . . 124
7.3 Micromagnetic Simulations of MMA . . . 125
7.4 Simulated Magnetization Oscillations . . . 127
7.5 Simulated Power Spectra Analysis . . . 128
7.6 Frequency Tunability . . . 132
7.7 Conclusion . . . 134

8 Tunability of Magnon Power-Phase Distribution for Reservoir Computing 135
8.1 Introduction . . . 135
8.2 SAW Analysis: COMSOL Simulation . . . 138
8.3 Spin Wave Analysis: MuMax^3 Simulation . . . 139
8.4 Frequency Locking at Optimum Separation for effective synchronization . . . 152
8.5 Time-domain stability of MMA . . . 154
8.6 Static Magnetic Study . . . 155
8.7 Prospects of Reservoir Computing . . . 159
8.8 Stress Induced Frequency Tuning . . . 160
8.9 Conclusion . . . 162

9 Conclusions 163

10 Future Work 165

References 167

List of Figures

1.1 The variation of the inverse ferromagnetic susceptibility as a function of temperature, where T_C is the Curie Temperature of the material. 4

1.2 Simulated hysteresis loop of a typical ferromagnetic material. Here, H_C, $\pm M_S$, and M_R are the coercivity, positive/negative saturation magnetization, and remanence of the ferromagnetic material, respectively. The domains with the red and right arrows dictate $+x$ direction domians while that in blue and left arrows highlight the $-x$ direction domains. 5

1.3 (a) Simulated hysteresis loop of a magnetostrictive FeGa nanowire (NW) array. Here, 'I'—'VI' denote different values of magnetic field of the hysteresis loop. The dimension of each of the nanowires is $512\times120\times40$ nm^3 while the constituent NWs are separated at a distance of 160 nm. Each of the domain configurations of the position 'I'—'VI' is given in (b)-(g), respectively. 6

1.4 A typical example of a raw FORC distributions of a 0.68 μm cobalt based thin film alloy within the parent hysteresis curve revealing the series of minor/partial hysteresis loops. 7

1.5 A typical example of an unrotated FORC distributions of a 0.68 μm cobalt based thin film alloy in (H_R, H_F) plane. During the measurement, the sample was inclined at 15° out-of-plane angle with the applied magnetic field (H). Here, ρ is the required FORC parameter defined as a double derivative function of (H_R, H_F), which determines the reversibility or irreversibility of the magnetic phenomena. The terms, H_C and H_U represent the local coercivity and the present bias magnetic field of the sample. 7

1.6 Typically, (a) soft ferromagnetic materials show low coercivity (H_C) and high saturation magnetization (M_S), while (b) hard ferromagnetic material show high coercivity (H_C) and low saturation magnetization (M_S). 9

1.7 Schematic of hysteresis loops of nanostructured soft and hard magnets are in (a) and (b), respectively. Formation of magnetic nano-hetero-structures, namely (c) exchange spring and (d) exchange coupled nanomagnets depending upon the critical conditions. 10

1.8 Illustration of ferromagnetic (FM) energetics to graphically explain different energies, namely (a) exchange energy, (b) anisotropy energy, (c) magnetostatic energy (d) Zeeman energy, and (e) magnetoelastatic energy, respectively. 13

1.9 Top row illustrates the perspective view or the precessional dynamic behaviour of magnetization $\vec{M}$ vector denoted by violet arrow around the effective magnetic field vector, $\vec{H}$ denoted by red arrow, where the spins form an one dimensional (1D) chain with discrete translational symmetry. The bottom row displays the top view of the precessional dynamics, illustrated by an imaginary orange wave — like curve traced by one of the components of $\vec{M}$. 15

2.1 (a) Enough magnetic field applied to saturate the magnet (b) Demagnetization process starts when the magnetic field is applied in the reverse direction. (c)-(d) Demagnetization steps (e) Demagnetization complete. Here, the violet arrows denotes the magnetic moment for soft phase while that in the blue colour highlights the magnetic moments for hard phase. The rightward red arrow on top of the figure signifies that the magnetic field applied in the forward direction while that in the leftward direction indicates that the field is applied in the reverse direction. 38

3.1 IDTs made with Aluminium (Al) on Substrate in COMSOL Geometry design with Mesh for generating SAW to operate MMA. (a) Required 10 μm thick $LiNbO_3$ substrate with width 9 μm having IDT structure on it. (b) Magnified region of (a) illustrates the separation between two IDTs. Both the IDTs have similar structure having width 1 μm and thickness 5 nm as exhibited in (c) and (d), respectively. . 48

3.2 The S_{11} and S_{21} parameters estimate the SAW (surface acoustic wave) frequency as (a) $\sim$ 551 GHz (with $LiNbO_3$ substrate) and (b) $\sim$ 625 GHz generated in the MMA designed (with AlN substrate). 49

3.3 The software interface of CHI 660B potentiostat displaying different options: The right panel reveals all the possible available "Electrochemical Techniques" which could be performed with the CHI 660B potentiostat. Out of all those options, the "Chronopotentiometry" is highlighted as it was one of the selected techniques to utilize during one of the thin film fabrications. The left inset describes different "Chronopotentiometry Parameters" to perform the electrodeposition. The middle one is the confirmation panel after completing the electrodeposition. 52

3.4 Schematic representation of the CV excitation signal. 54

3.5 Schematic of SEM on analyser mode 56

3.6 (a) Schematic showing electron transitions to lower atomic levels, illustrating the generation of K, L, and M lines. (b) A typical experimental EDX spectrum, displaying characteristic X-ray lines from various elements in the sample. (c) Schematic detailing the components of a scanning electron microscope (SEM). (d) EDX system attached to the Zeiss FE-SEM utilized for sample characterization at Tyndall National Institute. 57

3.7 (a) Experimental setup of a PANalytical X'Pert Pro MPD X-ray diffractometer (XRD) in our lab at Tyndall National Institute. (b) Bragg's Law: Schematic illustration of the working principle of the XRD method. 59

3.8 Experimental setup of AFM (Bruker) in our laboratory at Tyndall National Institute. 60

3.9 An experimental setup of (a) Helios NanoLab 660i FIB SEM, (b) Jeol 2100 high resolution transmission electron microscope (HR-TEM) in our laboratory in Tyndall National Institute. (b) Schematic of the HR-TEM: The top row is the controller of the TEM while bottom two snippets are for high voltage control and valve status of the TEM. 61

3.10 (a) Experimental setup of Mesa 200HF hysteresis loop tracer (ShB Instruments Inc.) in our laboratory (b) Schematic of hysteresis loop tracer (MESA 200 HF) by SHB Instruments Inc. 63

3.11 Experimental setup of MPMS3 SQUID magnetometer in our laboratory at Tyndall National Institute. 64

3.12 Snippets of Quantum Design MPMS3 SQUID magnetometer compatible "MultiVu" software. 65

3.13 (a) Schematic of SQUID detection. (b) Sample offset value in mm to keep the sample holder in the center position. 66

3.14 (a) At room temperature, different hysteresis loops of a thin magnetic material grown on a diamagnetic substrate. (b) Magnified version (obtained after subtracting the substrate contribution) shows the real/actual magnetic behaviour of deposited magnetic material. 67

3.15 Schematic of working principle of MFM (magnetic force microscopy). Magnetic Forces cause the phase shift denoted by φ over different domains during the 'LiftMode Scan'. 69

3.16 Experimental setup of the Brillouin Light Scattering (BLS) setup in the GHOST laboratory at CNR-IOM, Perugia, Italy. 71

4.1 (a) Heterogeneous electron transfer: (i) oxidation of Co and (ii) reduction of P (b) The schematic of the electrochemically controlled NHS formation by hydrogen evolution. (c) A three electrode Cyclic Voltammogram curve recorded with standard Ag/AgCl electrode [1]. 78

4.2 (a) Typical EDX spectrum showing the presence of Co and P in the films. (b) Top: EDX linescan path on the surface (yellow line). Bottom: Red curve denotes linescan for Co, and green curve for P. (c) A cross-sectional HR-TEM image of the film showing the striations in nm range formed due to stress caused by $H-$evolution. (d) FFT of the TEM image (c) confirms crystalline phases ($Co-hcp$) present in the amorphous CoP matrix [1]. 80

4.3 Structural characterization. (a) XRD spectra of the 0.31 μm, 0.68 μm, 5.06 μm thick films having three dominant substrate peaks confirming the overall amorphousness of the samples. The magnified XRD spectra of the highlighted region in (a) is shown in (b) for 0.31 μm film and in (c) for 0.68 μm film, respectively. (d) Gaussian Fit to the 44^o $Co-hcp$ peak as marked in (c) [1]. 81

4.4 (a) Typical stripe domain structure in low current ($\sim 5.5\ mA/cm^2$) sample (thickness 0.31 μm). (b) Modified domains featuring corrugated stripes with domain branching in comparatively higher current $\sim 137\ mA/cm^2$ sample (thickness $\sim$ 5μm). Both the scale bars are 4 μm and right side is the image colour scale [1]. . 82

4.5 (a) Non-exchange-spring (ES) of 0.31 μm sample. (b) ES signature with 0.68 μm sample. (c) A small kink near $\sim$ 10 Oe observed when the thickness becomes 5.4 μm showing the OOP anisotropy starts dominating over the IP anisotropy. The ES state becomes a flat EC state, while the thickness is $\sim$ 11 μm in (d) due to the entire domination of the OOP anisotropy over the IP anisotropy. In (e), (f) the flat loops continue with the thicknesses 11.23 μm, 12.34 μm obtained, respectively. Here, for all the figures, $dir.\ Y = dir.\ X + 90^o$ [1]. 84

4.6 IP FORC measurement of (a) 0.31 μm and (b) 0.68 μm films in (H_C, H_U) plane [1]. 85

4.7 OOP Angle dependent raw FORC curves of 0.68 μm film. The inset shows the schematic of the sample and applied magnetic field orientation reveals that the OOP angle is varying along the z-direction while the applied magnetic field direction is fixed along the perpendicular direction [1]. 86

4.8 OOP angle dependent raw minor loops and its corresponding FORC distribution of 0.68μm film indicating transverse ES nature [1]. 87

4.9 (a) An average of dispersed 3.50 nm thick NHS utilized as an input image in simulation at YZ plane. (b) Simulated three slope hysteresis loop with the complex geometry. (c) Cross-sectional macro-spin behaviour of '*' marked position in the hysteresis loop. (c) thick NHS. (d) $\approx$ 6 times dense 21.41 nm thick NHS utilized as an input image in YZ plane. (e) The simulated large hysteresis loop considering the NHS in (c). (f) the macro-spin behaviour as marked in (e) [1]. 89

4.10 Variation of simulated (a) exchange energy (b) anisotropy energy (c) demagnetization energy and (d) total energy as a function of applied magnetic field for different widths of the NHS [1]. 90

5.1 Typical SEM top surface morphology of (a) stressed thin film, (b) stress free thin film. (c) EDX spectrum of one of the samples. (d) XRD-spectrum of the sample. (e) Cross-sectional TEM micrograph of the electrodeposited CoP thin films showing the individual striations (white lines in the NHS) in (thickness 2-5 nm) nm range, typical and (f) FFT of the selected region of TEM as highlighted in (e) [2]. 97

5.2 Hysteresis loop of the DC electrodeposited CoP thin films measured in ShB Hysteresis Loop tracer in XY plane; here, dir-2 = dir-1+ 90^o. The thickness of the films is (a) 1.4 μm, (b) 5.7 μm, for the electrodeposition time (a) 15 min, (b) 60 min, respectively. (c)-(d) Differential of magnetisation of the (a) 1.4 μm, (b) 5.7 μm thick thin films, respectively. Red dotted lines indicate different coercivities in the low field range. (e)-(f) The FORC distributions on (H_C, H_U) plane for non-ES and ES samples, respectively [2]. 101

5.3 Representations of reduced moments m_i and m_j at neighbouring sites i and j separated by a vector $\vec{r}_{ij}$. The angles between the reduced moments, m_i, and m_j, is θ_{ij} [2]. 103

5.4 BLS Spectra of (a) non-ES (1.4 μm) and (b) ES (5.7 μm) CoP thin film at different in-plane bias magnetic fields measured from 1.50 kOe to 0.25 kOe [in (a)] and 0.00 kOe [in (b)] with the backscattering geometry.(c) BLS Spectra of 5.7 μm in a bias magnetic field of $+1.0$ and -1.0 kOe revealing the effect of the reversal of the magnetisation on the frequency position of the Damon-Eshbach wave [2]. . . 105

5.5 Spin wave frequencies of (a) bulk mode (1.4 μm non-ES film), (b) bulk mode of ES and (c) Damon-Eshbach surface wave as a function of magnetic field of 5.7 μm ES CoP thin film [2]. 106

5.6 Lorentzian fittings of the anti-Stokes BLS peak as a function of magnetic field of (a) 1.4 μm non-ES and (b) 5.7 μm ES CoP thin film. (c) Lorentzian fitting to a typical elastic peak in the BLS spectra. BLS linewidth (Δf) as a function of (d) corresponding anti-Stokes magnon frequencies and. (e) applied bias magnetic field for 1.4 μm and 5.7 μm thick thin films. (f) The J_I^1/J_I^2 ratio as function of bias magnetic field. The symbols correspond to the experimental data while the lines joining the symbols are guide to eyes [2]. 108

6.1 (a) Typical EDX spectrum of the sample at room temperature showing the presence of Co and P. (b) AFM image showing the surface topography. (c) X-ray diffraction pattern showing the amorphous property with nanocrystalline Co-fcc phase. (d) Typically measured in-plane hysteresis loop of one of the samples at two different in-plane directions showing anisotropic nature of the sample, here, dir.-2 = dir.-1 + 90°. Inset: magnified hysteresis loop [3]. 116

6.2 The variation of the (a) coercive field (H_C), (b) saturation magnetization (M_{Sat}) and (c) anisotropy field (H_K) of the material as a function of angle (in degrees). The top row exhibits the polar plot of the corresponding parameters [3]. 117

6.3 (a) Schematic of experimental geometry, sample is in x-y plane and x-z is the plane of the laser beam and (b) typical TR-MOKE data from Si/Ti (20 nm)/Au (200 nm)/CoP (3.173 μm) sample at an external bias magnetic field of 1.35 kOe. The three important temporal regimes at pump fluence of 10 mJ/cm^2 are indicated in the graph [3]. 119

6.4 (a) Background subtracted time-resolved Kerr rotation data for external magnetic field of 1.35 kOe applied along three different in-plane angles (45°, 90° and 150°, respectively w.r.t. the x axis along x-y plane) at a fixed pump fluence of 10 mJ/cm^2. The solid lines are fitted curves using the damped sine function. (b) FFT spectra corresponding to three different angles showing the magnetic modes. (c) In-plane angle dependent precessional frequency at the same external magnetic field of 1.35 kOe. The solid line is fitted the Kittel mode. i.e., Eq. (6.2). (d) Bias field dependent Gilbert damping constant of the Kittel mode at $\varphi = 45°$, 90° and 150° reveals the suppression of extrinsic effects at higher field [3]. 120

6.5 The variation of α of Kittel modes (solid blue scattered points) and PSSW modes (open red scattered points) with different in-plane angles at an external bias magnetic field of 1.35 kOe with the pump fluence of 10 mJ/cm^2. Blue solid line is guide to eye [3]. 121

7.1 COMSOL design of the magnon microwave antenna with magnetostrictive nanowires: (a) 2D cross-sectional model in COMSOL to calculate the generated SAW frequency. Substrate width -9 μm, thickness -10 μm; Aluminium (Al) electrodes (the magnified version of the highlighted region) width -1 μm and thickness -5 nm. (b) S_{11} and S_{21} parameters confirm the surface acoustic wave (SAW) resonance frequency at 551.35 MHz. (c) Deformed shape plot of the resonance SAW mode confirms the maximum penetration depth of the SAW. (d) The magnetostriction effect in nanowires shows some mechanical displacement of NWs caused by the SAW [4]. 124

7.2 Micromagnetic modelling of NWs: (a) Initial random magnetization configuration. l, w are length, width of each of the NWs along the x, y directions, respectively, and s is the separation between the NWs along y direction of 40 nm thick NWs. (b) Multidomain state in presence of transverse stress along Y. (c) Single domain state upon launching of the SAW along X. (d) Final spin configuration after completion of 20 ns simulation confirms that the domain configurations are non-volatile in nature [4]. 127

7.3 Calculated magnetization oscillations as a function of spacing between the NWs in MMA along x, y, z directions in (a), (b), (c), respectively, while the exciting SAW frequency remain kept constant at 0.5 GHz throughout the simulations [4]. 129

7.4 Power distribution as a function of spacing between NWs along x, y, z directions in (a), (b), (c), respectively. Corresponding insets reveal magnified frequency spectra (0-2.5(5) GHz range) of M_X & $M_Y(M_Z)$ of the highlighted region at left side of the parent Power-Frequency spectra (0-50 GHz range) [4]. 130

7.5 (a)-(e) Final spin configuration of the NWs after completion of 20 ns of micromagnetic simulation showing the non-volatility nature of the domains for the separation values, 40 nm, 80 nm, 90 nm, 100 nm and 140 nm, respectively [4]. . . 131

7.6 (a) The phase and (b) power profiles of the spin waves at the dominant frequency, i.e., the 0.55 GHz mode showing the uniformity of the profile. The color bars are shown at the right side of each of the figures [4]. 131

7.7 Micromagnetic modeling of the patterned matrix of nanodots in the MMA (a) Initial random magnetization configuration of the arrays. (b) Obtained Multidomain configuration in each of the nanodots in presence of a transverse stress along Y direction. (c) The multidomain structures in (b) are diminished upon launching of the 0.5 GHz SAW along X direction. (d) Final spin configuration of the NWs after completion of 20 ns simulation showing the non-volatility nature of the domains [4]. 132

7.8 Calculated oscillations in the magnetization components, M_X, M_Y, M_Z, in a matrix of nanodots in the MMA along x-, y-, z- directions in (a), (b), (c), respectively, while the exciting SAW frequency remain kept constant at 0.5 GHz throughout the simulations [4]. 133

7.9 Power distribution of the patterned a matrix of nanodots in the MMA along $x-$, $y-$, $z-$ directions in (a), (b), (c), respectively. In each of the Graph, the corresponding insets reveal the magnified frequency spectra $(0-20$ GHz range) of M_X, M_Y, M_Z of the highlighted region at left side of the parent Power-Frequency spectra $(0-60$ GHz range) [4]. 133

8.1 (a) 3D schematic of the magnon microwave antenna (MMA) with magnetostrictive (FeGa) nanowires (NWs). $\vec{k}_{SAW}$ and $\vec{k}_{SW}$ are the wave vectors associated with the SAW and the SW, respectively. Here, the width and thickness of the piezoelectric substrate ($LiNbO_3$) are 9 µm and 10 µm and that of the interdigitated transducer electrodes [*IDT-1* and *IDT-2* in the schematic] of *Al* (stands for Aluminum) are 1 µm and thickness 100 nm, respectively. (b) S_{11} and S_{21} parameters confirm the resonance frequency of SAW at 550.75 MHz. (c) Deformed shape plot at the resonance SAW mode estimates the penetration depth of 45 nm [5]. . 138

8.2 For separation, 's' = 90 nm configuration, (a) $x-$, (b) $y-$ and (c) $z-$ components of the multidomain state in presence of the transverse stress along the y-direction and for nanodots that are in (d), (e) and (f), respectively. Length and width of the individual nanowires remain constant throughout the study at 512 nm and 120 nm, respectively. For the nanodots, while the separation along y-axis (vertical direction) is 90 nm that along the x-axis (horizontal direction) is 14 nm. Here, A_1 to A_5 denote the nanodot array while the E_{ij} denotes the individual nanodot elements for i^{th} row and j^{th} column, where $i, j = 5$ [5]. 140

8.3 Variation of the power distribution obtained from fast Fourier Transformation (FFT) of magnetization as a function of NW spacing [5]. 142

8.4 Variation of the exchange energy ratio to the demagnetizing energy as a function of spacing between the NWs for the single domain state and multidomain state, respectively. The same for the nanodot matrix is annotated on the graph [5]. . . . 143

8.5 Variation of the (a) Demagnetization Energy, (b) Exchange Energy, (c) Total Energy, as a function of simulation time of the MMA at 90 nm separation ensuring efficient coupling for the auto-oscillation and mutually synchronized state of the NWs [5]. 144

8.6 The (a) M_X, (b) M_Y and (c) M_Z components of each nanowire for 90 nm configuration, respectively while, the top row highlights the overall magnetization of the whole system [5]. 145

8.7 For the nanodot array, the (a) M_X, (b) M_Y and (c) M_Z components of each array, respectively while, the top row depicts the overall magnetization responses arising from the whole system [5]. 146

8.8 Magnon power profile and phase distribution for 's'=20 nm configuration showing out of synchronized state [5]. 147

8.9 Magnon power profile and phase distribution for 's'=40 nm configuration showing partially synchronized state [5]. 149

8.10 Magnon power profile and phase distribution for 's' = 90 nm showing the synchronized state with uniform distribution [5]. 150

8.11 Magnon power profiles and phase distribution for the array configuration showing complex synchronization state within the nanoelements of the matrix. 151

8.12 Magnetization dynamics along $x-$, $y-$, $z-$ directions as a function of SAW frequency altered from 1 GHz to 500 GHz with included with 0.5 GHz parent frequency. The inter-distance between the neighbouring five NWs remain constant at 90 nm to ensure sufficient exchange coupling and the dipolar interaction [5]. . 152

8.13 Power distribution of the frequency locked states as a function of frequency along $x-$, $y-$, $z-$ directions, respectively [5]. 153

8.14 Comparison between 20 ns and 50 ns long simulation to verify the time domain stability of MMA. The calculated oscillations of the components of the magnetizations along longitudinal, transverse, and out-of-plane direction in (a), (c), and (e), respectively. The corresponding FFT spectra yield the auto-oscillation resonance peaks of the mutually synchronized MMA in (b), (d), (f), respectively [5]. 154

8.15 Simulated hysteresis loops of 20 nm, 90 nm, 160 nm separated NWs (a)-(c) and the nanodots (d) before applying the SAW along transverse ($y-$) direction, while the same for the same configurations, (e)-(h) after the application of the SAW along longitudinal ($x-$) direction [5]. 156

8.16 Magnified (for field range ± 0.1 T) simulated hysteresis loop for the square nanodot matrices after applying the SAW along longitudinal ($x-$) direction, where 'A'-'H' signifying the different position of magnetic field which are shown in (b)-(i), respectively. *'Flower'* (parallel to the longitudinal axis), *'Leaf'* (domains parallel to the diagonal of the nanodots), *'Vortex'* (flux closure of the magnetization) are highlighted to signify different domain states originated in the square nanodot matrix [5]. 157

8.17 Illustration of reservoir computing to handle the amplitude variation (from A_1 to A_n) at the constant input frequency (f). I_{1-n} are the inputs to the magnon reservoir with the different sets of nanowires/nanodots array configurations (e.g., I to IX are such nine arrays). The reservoir yield the results into different outputs, O_{1-9} and subsequently, categorized into different classes, C_{1-n} depending upon the results [5]. 159

8.18 Variation of (a) magnetization oscillation and (b) its corresponding frequency as a function of applied stress [5]. 161

10.1 Several proposed design of nanostructured MMA to incorporate further nonlineaity in magnon power-phase distribution, which would eventually make the MMA compatible for reservouir computing. 166

List of Tables

4.1 Plating bath composition and conditions 75
4.2 Experimentally obtained values of different structural, stoichiometric and magnetic parameters for various electrodeposited CoP thin films. 77

8.1 The demagnetization energy, exchange energy, and total energy values of the different spatial configuration as a function of different magnetization configurations, namely, multidomain state and single domain state. 148

1 Introduction

This chapter provides a basic overview relevant to this dissertation work, starting with the fundamental aspects of ferromagnetism and the significance of nanostructured ferromagnetic materials in the integrated devices, including their static and dynamic characterizations. It then introduces a novel integrated magnonic device called the "Magnon Microwave Antenna" (MMA) [4] and briefly explains its advantages over conventional antenna devices, particularly for on-chip reservoir computing. Finally, the chapter concludes with the motivation behind this thesis and an outline of its structure.

1.1 Background

Historically, the study of magnetism can be traced back to ancient civilizations, where naturally occurring magnets, such as lodestones, were first discovered. The scientific exploration of nanostructured magnetic materials accelerated during the 19^{th} and 20^{th} centuries, leading to significant discoveries and the development of various magnetic devices. Therefore, magnetism [6–8], more particularly nanomagnetism [7, 8], a quantum phenomenon deeply rooted in the behaviour of atomic and molecular entities, has captivated the scientific community for centuries. A particularly intriguing element of nanomagnetism research is the close alignment between theoretical predictions and practical implementations, where nanostructured magnetic materials have been the cornerstone of the technological advancements for centuries [6–8]. These materials exhibit magnetic properties due to the alignment of magnetic moments, which can be manipulated by external magnetic fields. Understanding the behaviour of these materials is crucial for developing new technologies and improving existing ones. The exploration of the magnetic properties in nanostructured materials is not only a fundamental pursuit but also underpins the development of the cutting-edge technologies. The rapid advancement in nanotechnology has enabled significant

progress in the development and application of nanostructured magnetic materials [6–8].

Nanostructured magnetic materials can be classified based on their behaviour in magnetic fields, including categories such as diamagnetism, paramagnetism, ferromagnetism, ferrimagnetism, antiferromagnetism, and altermagnetism [9, 10]. This thesis entitled *"Nanostructured Magnetic Materials for Integrated Magnonic Devices"* will primarily focus on *ferromagnetism*, as the material under study is ferromagnetic thin films or confined nano-heterostructures. These materials, with their unique magnetic properties at the nanoscale, hold immense potential for a variety of applications, particularly in the field of integrated devices [11, 12] and integrated magnonic devices [13, 14].

Magnonics, a subfield of spintronics [15, 16], focuses on the manipulation of spin waves [6] (magnons, a quanta of magnetic excitations) for information processing and transmission. It is noted that the traditional conventional electronic devices mostly utilize the charge of an electron, while spintronics is the field built with a fusion of spin of the electron and electronics, which has emerged as a cutting-edge field with transformative implications for information processing and storage [6–8]. Incorporating spin degrees of freedom into traditional charge-based electronic devices, or relying solely on spin, offers several advantages over conventional semiconductor devices. These include nonvolatility, higher data processing speeds, reduced electrical power consumption, and increased integration densities. However, to integrate spins into current semiconductor technology, it is crucial to address several technical challenges. These include efficient spin injection, transport, control, manipulation, and detection of both spin polarization and spin-polarized currents. Integrated magnonic devices leverage the generated spin waves at relatively higher frequencies to achieve functionalities that are complementary to or surpass conventional electronic devices [17]. This PhD thesis attempts to explore the rich landscape of development, characterization, and application of nanostructured ferromagnetic materials in the context of integrated devices, integrated magnonic devices, addressing the fundamental science including both the static and dynamic studies, and the potential technological advancements.

Of late, Surface Acoustic Waves (SAWs) [18] have emerged as a revolutionary and versatile tool that promises to reshape the landscape of spintronics, information processing, and sustainable technology [19]. Within this realm of scientific exploration, SAWs offer a dynamic and highly controllable means of manipulating physical phenomena at the nanoscale [20]. Since the SAWs propagate along the material surface, inducing mechanical vibrations with a wide range of frequencies ranging from megahertz [4] to gigahertz [20] interact with electron spins within magnetic/magnetostrictive materials, the role of SAWs becomes pivotal in spintronics, which opens up a plethora of opportunities for manipulating spin configurations with precision and efficiency.

In order to understand spintronics, one needs to understand the dynamics of either the accumulation or phase of spins in a system or in short spin dynamics or commonly known as magnetization dynamics in ferromagnetic thin films and/or confined structures in detail, as spin dynamics play cruicial role in developing fundamental building block of spintronics [7, 8]. Most fascinating characteristics of spins are characterized by the spin degree of freedom. In spintronics devices, spin current, i.e., the flow of spins analogous to the movement of charge carrier, act as the required information carrier, which could be manipulated/tuned by applying a tiny external field. Furthermore, spins retain its curated state due to its long relaxation time while charge carriers could easily be perturbed by external impurities [7, 8]. Such spin dynamics or the magnetization dynamics is governed by Landau—Lifshitz—Gilbert equations 1.1 and 1.2 [4, 5].

$$\frac{\partial \vec{M}}{\partial t} = |\gamma|\vec{M} \times H_{\text{eff}} + \frac{\alpha}{M_S}\left[\vec{M} \times \frac{\partial \vec{M}}{\partial t}\right] \tag{1.1}$$

$$H_{\text{eff}} = -\frac{1}{\mu_0} \cdot \left[\frac{\partial E}{\partial \vec{M}}\right] \tag{1.2}$$

Therefore, elaborating the significance of spin dynamics or magnetization dynamics, in the context of emerging technologies becomes imperative for establishing a solid foundation in the field of nanomagnetism and magnonics in particular.

1.2 Ferromagnetism

Ferromagnetism is a fundamental magnetic property observed in certain materials where magnetic moments of atoms align parallel to each other within a region called a domain. This alignment results in a strong, permanent magnetization even in the absence of an external magnetic field. Ferromagnetic materials in nanostructured form are crucial for various technological applications due to their high magnetic permeability[1] (μ) and retention of magnetization. It is the strongest type of magnetism, marked by the spontaneous alignment of magnetic moments, i.e., net magnetization, $M \neq 0$. Understanding ferromagnetism at the nanoscale is vital for the development of advanced magnetic materials and devices, as it allows for the manipulation of magnetic properties through precise control of size, shape, and structure. Nanostructured ferromagnetic materials are of paramount importance for many industrial applications and modern technologies. They form the foundation for electrical and electromechanical devices such as electromagnets, electric

[1] The magnetic Permeability (μ) of a magnetic material is defined as the ratio of the magnetic flux density (B) in the material to the magnetic field strength (H) applied to it, given by the formula, $\mu = \frac{\partial B}{\partial H}$.

motors, generators, transformers, magnetic storage devices, and hard disk drives. These materials are typically metals like iron, cobalt, and nickel, or their alloys and compounds. However, only a few materials exhibit ferromagnetism, and they usually need to be in pure forms or specific alloys. However, the modern derivatives of many of the nanostructured ferromagnetic materials are pivotal in cutting-edge technological applications like heat assisted magnetic recording (HAMR) [21], magnetic data storage, magnetic random access memory (MRAM), and spintronics applications [22, 23]. So, understanding the intricacies of ferromagnetic behaviour is essential for advancements in device miniaturization and magnetic memory technologies. The variation of inverse of the magnetic susceptibility[2] (χ^{-1}) as a function of temperature (T) for ferromagnetic materials is depicted in Figure 1.1. The inset of Figure 1.1 illustrates the organized spin configuration of a ferromagnetic material, showing any spontaneous magnetization.

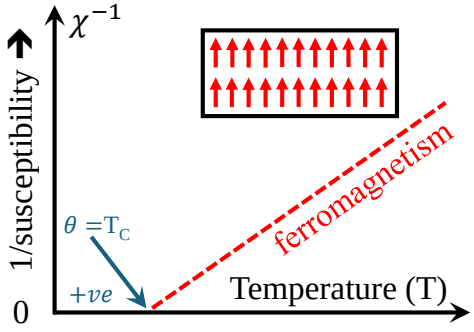


Figure 1.1: The variation of the inverse ferromagnetic susceptibility as a function of temperature, where T_C is the Curie Temperature of the material.

1.3 Hysteresis Loop

Hysteresis loop is a fundamental concept in materials science, in particular studying the nanostructured magnetic materials. The hysteresis loop characterizes the magnetic behaviour of ferromagnetic materials by depicting the relationship between the applied magnetic field (H or H_{ext}) and the resulting magnetization (M). Key parameters such as coercivity, remanence, and saturation magnetization are derived from the hysteresis loop, providing insights into the material's magnetic properties. In general, magnetism is a quantum and nonlinear phenomena. Due to such inherent nonlinearity present in the ferromagnetic material, we obtain such hysteresis loop from them. In nanostructured magnetic materials, the hysteresis behaviour can be significantly altered due to surface effects, quantum confinement, and interfacial interactions. Analysing the hysteresis loop is essential for optimizing the performance of magnetic materials in various applications, including data storage, magnetic sensors, and magnonic devices. An example of a simulated hysteresis loop of a ferromagnetic material utilizing a GPU accelerated micromagnetic simulation platform such as MuMax^3 [24] is schematically shown in Figure 1.2, which is obtained by following the three

[2]The magnetic Susceptibility (χ) of a magnetic material is defined as the ratio of the magnetization (M) of the material to the magnetic field strength (H) applied to it, given by the formula, $\chi = \frac{\partial M}{\partial H}$.

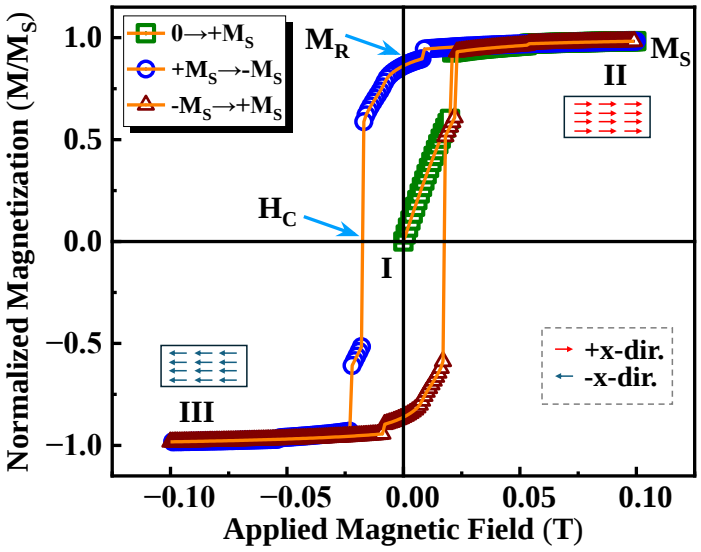


Figure 1.2: Simulated hysteresis loop of a typical ferromagnetic material. Here, H_C, $\pm M_S$, and M_R are the coercivity, positive/negative saturation magnetization, and remanence of the ferromagnetic material, respectively. The domains with the red and right arrows dictate $+x$ direction domians while that in blue and left arrows highlight the $-x$ direction domains.

steps: (i) First, the external magnetic field is applied (say along $+x$ direction) from 0 (zero) to a certain positive value, the virgin curve is obtained. Accordingly, the applied magnetic field starts eliminating the magnetic domains oriented in different directions. However, after a certain value of the magnetic field, the magnetic moment (and hence the magnetization) remain constant, even after increasing the value of the magnetic field, which is called as the saturation magnetic field ($+H_{Sat}$) and the magnetization is known as the saturation magnetization (M_S). After H_{Sat}, all the domains are aligned along the direction of the magnetic field, i.e., $+x$ direction as illustrated in Figure 1.2. (ii) Second, the magnetic field is reversed, i.e., applied along the opposite direction (i.e., $-x$ direction) and reduced from $+H_{Sat}$ to $-H_{Sat}$. Similarly, at $-H_{Sat}$ the magnetization along the opposite direction remain unchanged, i.e., the negative magnetization saturation ($-M_S$) achieved and now the domains are aligned along the $-x$ direction. In this process, it is observed that when the H_{ext} is restored at 0 (zero) field, the material shows a finite value of moment, which is denoted by M_R, known as Remanent magnetization of the material. On the other hand, at some finite negative value of H_{ext} the moment vanishes, i.e., the magnetization is reduced to zero, the field is called as coercive field of the Coercivity (H_C) of the material. (iii) Finally, the field is applied in reverse direction, i.e., from negative x to the positive x direction and all the negative domains further align along $+x$ direction with the direction of the magnetic field after reaching the $+H_{Sat}$ again. In this way, we obtain a full hysteresis loop of a material.

A more practical example is further discussed in this paragraph. The following Figure 1.3 reveals the different domain configurations of different positions for a magnetostrictive FeGa nanowire (NW) array. The simulation parameters, saturation magnetization M_{Sat} = 1.32 MA/m, exchange stiffness constant A_{ex} = 16 pJ/m, initial exchange anisotropy constant K_{u1} = 0 J/m^3 [4],

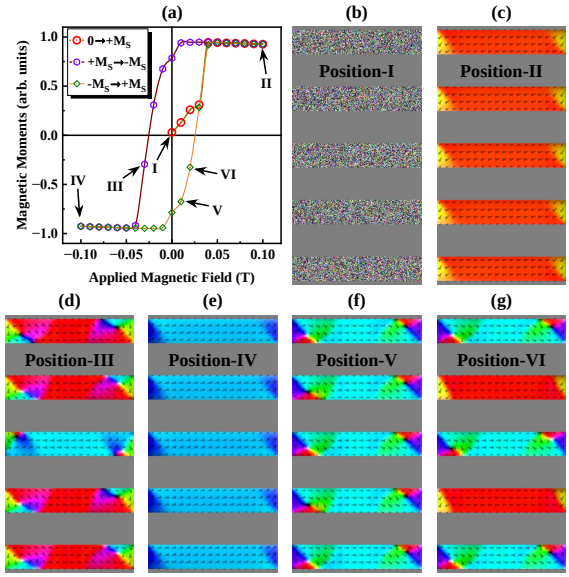


Figure 1.3: (a) Simulated hysteresis loop of a magnetostrictive FeGa nanowire (NW) array. Here, 'I'—'VI' denote different values of magnetic field of the hysteresis loop. The dimension of each of the nanowires is $512\times120\times40$ nm^3 while the constituent NWs are separated at a distance of 160 nm. Each of the domain configurations of the position 'I'—'VI' is given in (b)-(g), respectively.

are utilized to obtain the hysteresis loop as shown in Figure 1.3(a). The Figure 1.3(b) shows the initial domain configuration of random magnetization (Position-'I'), while Figure 1.3(c) exhibits the domain configuration at the positive saturation magnetization state (Position-'II') with field $+H_{\text{Sat}}$. The domain configuration of an intermediate state between $+H_{\text{Sat}}$ and $-H_{\text{Sat}}$, named Position-'III' is shown in Figure 1.3(d) while the domains of the negative saturated state at $-H_{\text{Sat}}$, i.e., Position-'IV' is shown in Figure 1.3(e). The domain configurations of the reverse intermediate state between $-H_{\text{Sat}}$ and $+H_{\text{Sat}}$, named Position-'V' is shown in Figure 1.3(f) and (g), respectively.

One can note that no domains are oriented in the Position-'I' as external field is zero while all of the domains in the Position-'II' is aligned with the direction of the applied magnetic field ($+H_{\text{Sat}}$). Similarly, domains of Position-'IV' are aligned with the reverse direction of the applied magnetic field ($-H_{\text{Sat}}$). However, the domains in the intermediate states, i.e., Position-'III', Position-'V' and Position-'VI' are oriented in a particular orientation such that the system stays in the overall minimized magnetic energy condition. A detailed explanation of such scenario is presented in Chapter 8.

1.4 First-order reversal curve (FORC) Measurement

While the hysteresis loop provides valuable insights into the macroscopic magnetic properties of a material, it often lacks the resolution to distinguish between different microscopic magnetic interactions and domain states. For instance, measurements like coercivity (H_{C}), saturation magnetization (M_{S}), and remanence magnetization (M_{R}) are certainly helpful, they only give us an

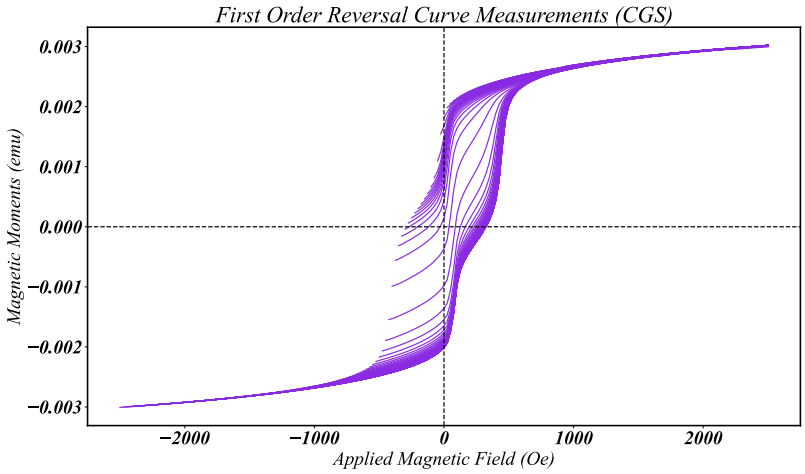


Figure 1.4: A typical example of a raw FORC distributions of a 0.68 μm cobalt based thin film alloy within the parent hysteresis curve revealing the series of minor/partial hysteresis loops.

average view of the whole sample. They do not tell us much about the variety of magnetic strengths and interaction fields present at the tiny, nanometre scale. That's where First-order reversal curve (FORC) diagrams come in.

The FORC measurement technique is an advanced method for characterizing the magnetic properties of materials, providing a more detailed and nuanced understanding than the traditional hysteresis loop. The FORC method involves measuring a series of minor/partial hysteresis loops, each starting from a different point on the major hysteresis loop and reversing to a saturation point, as shown in Figure 1.4. These diagrams offer a comprehensive view of the magnetic interactions and domain behaviour within the material. They gather data from the entire area within a major loop of a standard hysteresis loop, making them one of the best ways to measure

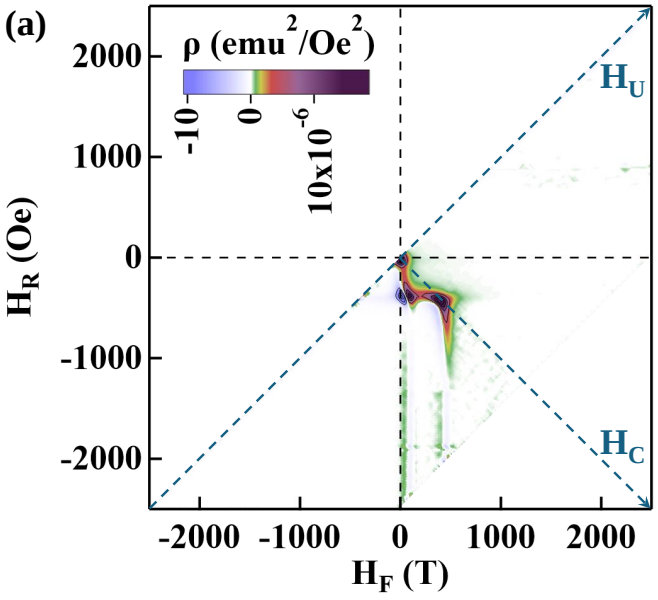


Figure 1.5: A typical example of an unrotated FORC distributions of a 0.68 μm cobalt based thin film alloy in (H_R, H_F) plane. During the measurement, the sample was inclined at 15° out-of-plane angle with the applied magnetic field (H). Here, ρ is the required FORC parameter defined as a double derivative function of (H_R, H_F), which determines the reversibility or irreversibility of the magnetic phenomena. The terms, H_C and H_U represent the local coercivity and the present bias magnetic field of the sample.

tiny-scale variations. The FORC technique addresses the limitation of normal hysteresis loop by capturing a richer dataset that reflects the complexity of magnetic behaviour such as domain wall dynamics, reversible and irreversible magnetization processes, and the spatial distribution of coercive fields within the material. This enhanced resolution is particularly important for nanostructured materials, where subtle interactions and variations in magnetic properties can significantly impact performance. FORC diagram can be presented in several ways, e.g., the raw minor curves, unrotated FORC diagram in (H_R, H_F), processed FORC diagram in (H_C, H_U) plane. A typical example of an unrotated FORC diagram is shown in Figure 1.5. The standard experimental procedure and the further explanations about the FORC measurements are described in Chapter 3.

1.5 Nanostructured Magnetic Materials

In the realm of advanced technology, researchers are constantly exploring new materials and methods to enhance the performance of the spintronics devices that involves high performance nanomagnetic systems, which hold great promise for revolutionizing the way we transmit and process information. However, the effective implementation of such high-performance nanomagnetic systems poses a significant challenge. These systems rely on intricate interactions between magnetic fields, microwaves in nanometre (one-billionth of a meter) level, making their design and optimization a complex task. To fully realize their potential, it is crucial to develop novel techniques and subsequently novel nanostructured magnetic material that can overcome the existing limitations and maximize the performance of these systems.

Since this PhD thesis explains some intriguing nanomagnetic phenomena generating out from a nanoheterostructured ferromagnetic material and paves the way to utilize such novel nanoheterostructures for novel potential applications, such as magnon microwave antenna etc. we consider now the ferromagnetic material only. Depending upon the energy dissipation as a function of heat within a system, nanostructured ferromagnetic materials are classified into two categories as discussed below. In a nanostructured ferromagnetic material, it is observed that the dissipated energy across a circuit of the hysteresis loop is proportional to the area of the loop.

1.5.1 Nanostructured Soft Magnetic Materials

Nanostructured ferromagnetic materials that are characterized by their low coercivity and high permeability are referred to as nanostructured soft magnetic materials, making them ideal for applications where easy magnetization and demagnetization are required, and energy loss per

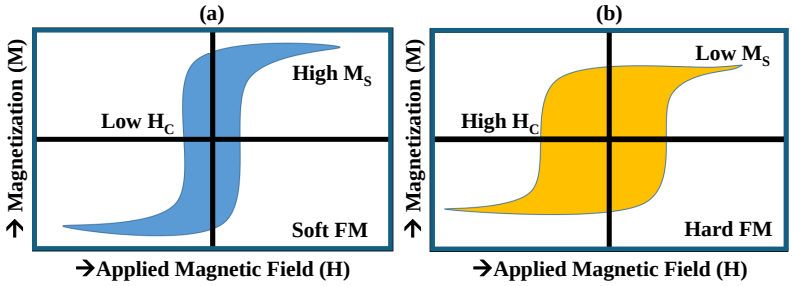


Figure 1.6: Typically, (a) soft ferromagnetic materials show low coercivity (H_C) and high saturation magnetization (M_S), while (b) hard ferromagnetic material show high coercivity (H_C) and low saturation magnetization (M_S).

cycle needs to be minimized, such as in transformers, inductors, and electromagnetic shielding. At the nanoscale, soft magnetic materials can exhibit enhanced magnetic softness and improved saturation magnetization due to reduced magnetic anisotropy and domain wall pinning effects. A low magnetostriction is often preferred to prevent the induction of a local anisotropy energy due to internal strains [6].

1.5.2 Nanostructured Hard Magnetic Materials

Nanostructured hard magnetic materials, on the other hand, possess high coercivity and remanence, enabling them to maintain strong magnetization in the presence of external magnetic fields. They are challenging to magnetize and demagnetize. These properties are essential for permanent magnets used in electric motors, generators, and microwave and heat-assisted magnetic recording media. Nanoscale engineering of hard magnetic materials can lead to superior magnetic performance, with applications in high-density data storage and advanced magnetic devices. In these applications, it is crucial to maintain the magnetization for an extended period. The energy dissipated in a hysteresis loop cycle is maximized to prevent spontaneous magnetization. Apart from large hysteresis, nanostructured hard magnets are characterized by narrow domain walls (large K), and ease of domain wall pinning. Large ion moments and substantial crystal fields contribute to hard magnetic properties, and suitable materials often include rare earths [6].

1.5.3 Exchange Spring System

Since the conventional nanostructured hard magnetic materials contain rare-earth material, researchers are looking for an alternative rare-earth free nanomagnet which has the potential to replace such conventional nanostructured hard magnetic materials for cutting edge applications. The exchange spring system [25] combines both the soft and hard magnetic materials in a heterostructure at the nanoscale to exploit their complementary properties. In comparison to the conventional single nanostructured ferromagnetic (FM) thin films, i.e., either nanostructured soft FM having high saturation magnetization (M_S), low coercivity (H_C), or nanostructured hard FM

having high H_C, low M_S, in the exchange spring systems, the sandwiched (bi/tri)-layered nano-hetero-structures (NHS) at the nanometre level aim to achieve simultaneously high M_S from the soft phase and high H_C from the hard phase, resulting in materials with superior magnetic performance. During the process of fabrication, the critical conditions [26] as highlighted in the insets of Figure 1.7(c)/(d) play an important role in defining the heterostructured system and subsequently the nature of the hysteresis loops. For instance, $L_s > 2d_h$ defines the system as Exchange Spring (ES) [Figure 1.7(c)] system while $L_s \leq 2d_h$ makes the system Exchange Coupled (EC) [Figure 1.7(d)] resulting into a staircase-like hysteresis loop and a rectangular hysteresis loop in the prior and later cases, respectively. Here, L_s is the thickness of nanostructured soft magnetic layer and d_h is the domain wall width of the nanostructured hard magnetic layer, which arises from the interplay between exchange interactions and magnetocrystalline anisotropy. This d_h is often defined as $\pi\sqrt{\frac{A_{ex,h}}{K_{u1,h}}}$. Here, $A_{ex,h}$ is the exchange stiffness constant and $K_{u1,h}$ is the anisotropy constant of the nanostructured hard magnetic layer.

In hard magnetic materials (such as SmCo or NdFeB), the anisotropy constant K_{u1} is large, which leads to a smaller domain wall width. The high anisotropy ensures that once a domain wall forms, it is energetically expensive to move or widen it, resulting in a very stable, narrow domain wall. The magnetostatic energy favors the formation of magnetic domains that minimize stray magnetic fields by favouring configurations with minimal external magnetic flux. When the soft magnetic layer thickness L_s exceeds $2d_h$, the soft layer can smoothly rotate its magnetization in response to the domain structure of the hard layer, which ensures the exchange spring effect. It is noted that the exchange energy ensures that the soft and hard layers remain coupled, but the soft layer can "unwind" more like a spring, gradually transitioning from the magnetization of the

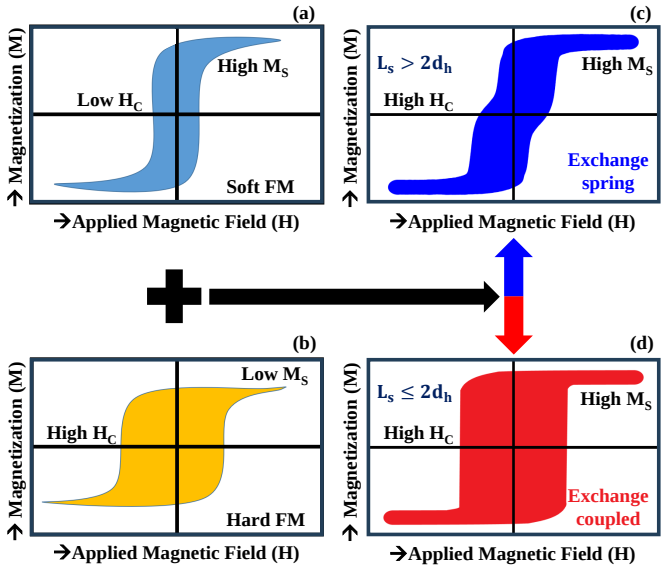


Figure 1.7: Schematic of hysteresis loops of nanostructured soft and hard magnets are in (a) and (b), respectively. Formation of magnetic nano-hetero-structures, namely (c) exchange spring and (d) exchange coupled nanomagnets depending upon the critical conditions.

soft layer to that of the hard layer. This is key to achieving the exchange spring effect, where the overall system exhibits high magnetization and high coercivity simultaneously. Therefore, the domain wall width d_h of the hard magnetic layer plays a crucial role in the exchange spring system by defining the scale over which the magnetization transition occurs. At that condition, the system can efficiently balance exchange, anisotropy, and magnetostatic energies. This allows the soft layer to rotate smoothly in response to an external field while maintaining strong coupling with the hard layer, resulting in the desired exchange spring behaviour with both high magnetization and coercivity.

The Energy Product, often denoted as BH_{max}, is a key figure of merit for magnetic materials, especially in the context of permanent magnets. The Energy Product is defined as the maximum value of the product of the magnetic flux density B and the magnetic field strength H within the second quadrant of the $B-H$ hysteresis loop of the material. This value represents the maximum magnetic energy density that the material can store in its magnetic field, which is a critical parameter for applications requiring strong and efficient permanent magnets. Mathematically, it is defined by the following equation 1.3:

$$BH_{max} = \max(B \cdot H) \tag{1.3}$$

Here, B is the magnetic flux density (measured in Teslas, T) and H is the magnetic field strength (measured in amperes per meter, A/m). Therefore, in order to determine the BH_{max}, one examines the $(B-H)$ hysteresis loop, which plots the relationship between B and H. The maximum energy product is found in the second quadrant of this loop, where the product $(B \cdot H)$ reaches its peak negative value. This is often referred to as the "demagnetization curve." The energy product BH_{max} is typically expressed in megaGauss-Oersteds (MGOe) in the CGS system or in kilojoules per cubic meter (kJ/m^3) in the SI system. 1 MGOe is equivalent to 7.958 kJ/m^3. Higher BH_{max} values signify materials that can produce stronger magnetic fields. Thus materials with high BH_{max} values are sought after for high-performance applications, e.g., application like electric motors, generators, magnetic storage devices, and other technologies requiring strong permanent magnets. Examples of materials with high energy products include neodymium-iron-boron (NdFeB) magnets and samarium-cobalt (SmCo) magnets.

1.5.4 Transverse Exchange Spring

The transverse exchange spring system [27] involves a history-dependent procedure and the lateral and orthogonal arrangement of soft and hard magnetic phases, offering unique magnetic behaviours and properties. This configuration can result in anisotropic magnetic properties and

enhanced magnetic performance, with potential applications in magnonic devices and advanced magnetic sensors. A transverse exchange spring is a magnetic system characterized by its response to external magnetic fields. In the context of a multilayer transverse ES system, one can conclude that a transverse ES shows the following key features: (i) **Zero Field**: In the absence of an external magnetic field, both the hard and soft magnetic moments exhibit no magnetic response in the measurement, indicating a neutral state. (ii) **Small Fields**: When a small magnetic field is applied, the hard moments show a reversible magnetic response due to their strong crystal-field anisotropy, which resists movement. Meanwhile, the softmoments in the soft layers can more freely align with the applied field, resulting in a larger reversible magnetic response. (iii) **Large Fields**: As the magnetic field strength increases, the hard moments are forced out of their initial plane to align with one of the easy axes, lie in-plane either [010] or [100]. This realignment leads to the loss of the transverse exchange spring property, and the magnetic response becomes irreversible. In essence, the transverse exchange spring behaviour is dependent on the strength of the applied magnetic field and the inherent properties of the materials involved.

1.6 Energy Distribution in Ferromagnetic Material

Ferromagnetism is rooted in the energetics of the system, which includes various contributions such as exchange energy (E_{ex}), anisotropy energy (E_{anis}), demagnetising energy (or stray field energy) (E_{demag}), Zeeman energy (E_{Zeeman}), and magnetoelastic energy (E_{ME}). In ferromagnetic materials, the total energy (E_{total}) is a combination of these various energy contributions as expressed by Equation 1.4. The interplay between these energies determines the magnetic behaviour of the nanostructured materials, such as domain formation, magnetic hysteresis, and response to external magnetic fields. Understanding and controlling these energy components is essential for analysing the behaviour of the nanostructured ferromagnetic materials and subsequently developing magnetic devices and applications.

$$E_{total} = E_{ex} + E_{anis} + E_{demag} + E_{Zeeman} + E_{ME} \tag{1.4}$$

1.6.1 Exchange Energy

Exchange energy arises from the quantum mechanical interactions between the spins of electrons in a ferromagnetic material. According to quantum mechanics, the Pauli exclusion principle and the Heisenberg exchange interaction lead to a lower energy state when neighboring electron spins are aligned parallel to each other. This energy can be expressed as given in equation 1.5:

$$E_{ex} = -\Sigma_{i,j} J_{ij}(S_i \cdot S_j) \tag{1.5}$$

where, J_{ij} is the exchange integral between spins S_i and S_j as illustrated in Figure 1.8(a). A positive J_{ij} favours parallel alignment, leading to ferromagnetism.

1.6.2 Anisotropy Energy

Anisotropy energy is the energy associated with directional dependence of material's magnetic properties, which arises because certain crystallographic directions in a ferromagnetic material are energetically more favourable for the alignment of magnetic moments. The simplest form of anisotropy energy, uniaxial anisotropy, can be written as in equation 1.6:

$$E_{anis} = K_{U1}[sin^2(\theta)] + K_{U2}[sin^4(\theta)] \tag{1.6}$$

where K_{U1} and K_{U2} are the anisotropy constants, being $K_{U1} >> K_{U2}$ and θ is the angle between the magnetization (M) and the easy axis (E_A, the direction of preferred magnetic alignment) as shown in Figure 1.8(b).

1.6.3 Demagnetizing energy

Demagnetizing energy, also known as stray field energy or magnetostatic energy, is the energy associated with the magnetic field produced by the magnetization of the material. This field, called the stray field, extends outside the material and interacts with the material itself. The magnetostatic energy can be expressed as given in equation 1.7:

$$E_{demag} = \frac{1}{2}\mu_0 \int (H_{demag} \cdot M) dV \tag{1.7}$$

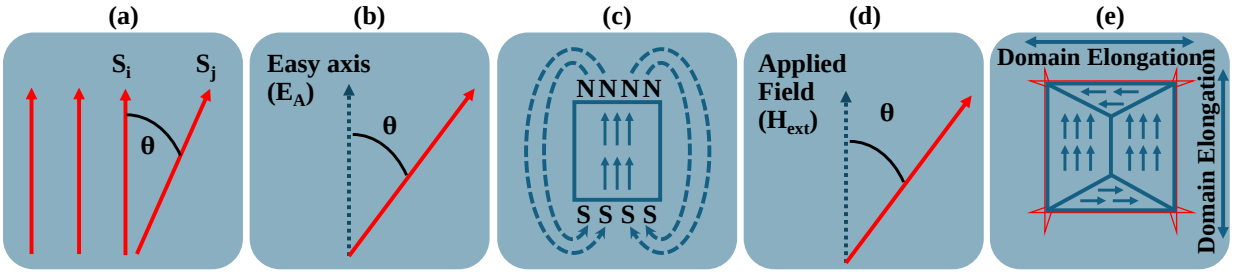


Figure 1.8: Illustration of ferromagnetic (FM) energetics to graphically explain different energies, namely (a) exchange energy, (b) anisotropy energy, (c) magnetostatic energy (d) Zeeman energy, and (e) magnetoelastatic energy, respectively.

where, H_{demag} is the demagnetizing field, M is the magnetization as illustrated in Figure 1.8(c), and μ_0 is the permeability of free space. Minimizing this energy often leads to the formation of magnetic domains. It usually depends on the shape of the material/sample.

1.6.4 Zeeman Energy

Zeeman energy is the energy due to the interaction between the magnetic moments in the material and an external magnetic field. This scenario is depicted schematically in Figure 1.8(d). This energy is given by [equation 1.8]:

$$E_{\text{Zeeman}} = -\mu_0 \int (M \cdot H_{\text{ext}}) dV \tag{1.8}$$

where, H_{ext} is the external magnetic field. The system lowers its energy by aligning the magnetization with the external field.

1.6.5 Magnetoelastic Energy

Magnetoelastic energy (as expressed by equation 1.9) arises from the coupling between the magnetic and elastic properties of a material. When a ferromagnetic material is magnetized, it undergoes a strain, leading to a change in its shape or dimensions (magnetostriction).

$$E_{\text{ME}} = \frac{3}{2} \lambda_S \cdot \sigma cos^2(\theta) \tag{1.9}$$

where, λ_S is the saturation magnetostriction constant, σ is the mechanical stress, and θ is the angle between the magnetization and the direction of applied stress. The closure domains try to extend horizontally, whereas the primary closure domain attempts to extend vertically. In this context, the elastic strain energy is directly proportional to the volume of the closure domains. This scenario is depicted schematically in Figure 1.8(e). While reducing the size of the domains can lower the magnetostrictive energy, it also increases the domain wall area, leading to a rise in exchange and magnetocrystalline energies.

1.7 Fundamentals of Magnonics

1.7.1 Spin Waves and Magnon

At absolute temperature (T = 0 K), a system lies in a perfectly ordered condition while a finite temperature weakens the ordered orientation by exciting the order parameter. This thermal ex-

citation disrupts the order parameter, e.g., the alignment of spins within the material, leading to various excitation phenomena within the system such as spin waves. Spin waves are one of the consequences of breaking the appearance of the spontaneous order or symmetry in the case of ferromagnetic material, analogous to the excitations in crystals known as lattice waves, quantized into phonons. [6]. The quanta of spin waves are collective excitations of the magnetic moments in a material. These spin waves, also known as magnons when quantised [6], play a crucial role in transferring and processing information, akin to the function of electromagnetic waves in electronic devices. The perspective view and the view from above is depicted in top and bottom rows of the Figure 1.9, respectively.

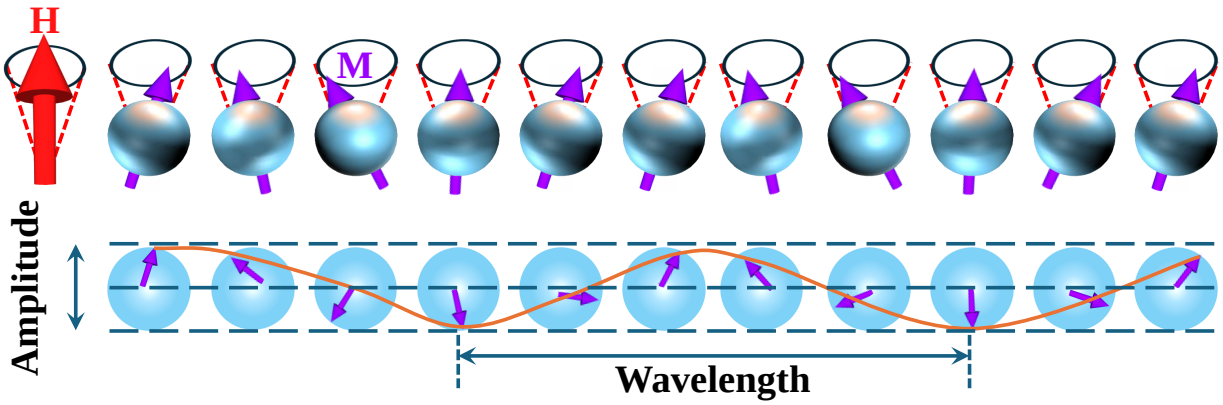


Figure 1.9: Top row illustrates the perspective view or the precessional dynamic behaviour of magnetization $\vec{M}$ vector denoted by violet arrow around the effective magnetic field vector, $\vec{H}$ denoted by red arrow, where the spins form an one dimensional (1D) chain with discrete translational symmetry. The bottom row displays the top view of the precessional dynamics, illustrated by an imaginary orange wave — like curve traced by one of the components of $\vec{M}$.

Spin waves exhibit a unique variety of dispersion characteristics, more so than electromagnetic or acoustic waves. These properties can be tuned through different parameters such as the type of magnetic material, sample shape, and the orientation and magnitude of the applied magnetic field. The combination of diverse linear spin-wave properties and pronounced nonlinear effects makes spin-wave systems a compelling subject for studying wave dynamics [28]. The power of a spin wave is determined by the number of spins involved in the excitation and their collective behaviour, while the phase refers to the relative timing or position of the spins within the wave. Since magnons obey the Bose—Einstein (BE) statistics [29], they are bosons with a spin of 1 and their energy states can be calculated by the following BE distribution 1.10:

$$\eta_{\mathrm{i,BE}} = \frac{1}{e^{\frac{\varepsilon_{\mathrm{i}}-\mu}{\kappa_{\mathrm{B}}T}}-1} \tag{1.10}$$

where, $\eta_{\mathrm{i,BE}}$ of the particles with energy ε_{i} with temperature T and the chemical potential μ. It is noted that the $\eta_{\mathrm{i,BE}}$ can be smaller than 1. The concept of spin waves was first introduced by Bloch and is described by Bloch's $T^{3/2}$ law (equation 1.11). This law is observed when an array of spins is locally disturbed by an external perturbation, causing the disturbance to propagate as a wave. In a nanostructured ferromagnetic medium, this wave is generated by the collective phase coherent precession of magnetization or spins.

$$n_{\mathrm{magnon}} \propto T^{3/2} \tag{1.11}$$

At low temperatures, spins are quantized, and small q (a wave vector) and small ω (angular frequency) become important, similar to lattice waves, which are termed as phonons. When the wave vector (κ) is large, implying a short wavelength (λ) of a spin wave, the wave is dominated by exchange interaction. These spin waves can be generated at room temperature without the need for external excitation like current or microwave and are measured by inelastic Brillouin Light scattering spectroscopy. In inelastic scattering, the magnitude of the incident wave vector κ differs from the magnitude of the scattered wave vector κ', leading to a change in energy from E $\left(\frac{\hbar^2\kappa^2}{2m}\right)$ to E' $\left(\frac{\hbar^2\kappa'^2}{2m}\right)$, as represented by equation 1.12.

$$E = E' + \hbar\omega \tag{1.12}$$

Understanding the power-phase relation of spin waves, often expressed as magnon power-phase distribution, which denotes the connection between intensity and phase, is integral to deciphering the intricate dynamic behaviour of spin waves. Generally, the magnon power-phase distribution is studied by post-processing the magnetization vector data [M $\rightarrow$f($\vec{r},t$)] that obtained through micromagnetic simulation [4]. This understanding is pivotal for guiding the design and optimization of their application in cutting-edge technologies.

1.7.2 Brillouin Light Spectroscopy (BLS)

Brillouin Light Spectroscopy (BLS) is a powerful and important technique for studying spin waves in nanostructured magnetic materials. BLS study provides detailed information on the dispersion and the dynamics of spin waves, enabling the investigation of magnonic properties and interactions in nanostructured magnetic materials. BLS study offers the advantage in measuring the frequency of the thermally excited spin waves in the absence of any external stimuli such as microwave driving magnetic field, electric field, electrical current, or optical pumping compared to available techniques for dynamic measurements, e.g., vector-network analyzer Ferromagnetic Resonance

(VNA-FMR) measurement, time-resolved magneto-optic Kerr (TRMOKE) effect. Momentum and energy conservation causes the annihilation of magnons (anti-Stokes process) and the creation of magnons (Stokes process) [2]. The linewidth of the inelastic peaks (i.e., the BLS spectra) relates to the magnetic inhomogeneity, while that of the elastic peak reveals the instrumental linewidth broadening. Typically, the BLS measurements are performed by saturating the sample by applying sufficient magnetic field, following the descending branch of the hysteresis loop of the sample [2], such that in that field range, the magnetization is always saturated and parallel to the applied magnetic field. In typical BLS measurements, usually, the outermost layer ($\sim 15-20$ nm) of the samples can be probed while the quasi-static magnetic measurements probe the entire sample volume, thus providing information on the overall sample magnetic parameters [30]. Therefore, BLS study may carry little misfits in the derived parameters, e.g., saturation magnetization (M_S) for a comparatively thicker samples, which are measured with bulk measurements [2]. Experimental methods involving spin waves were used to determine fundamental parameters of magnetic materials, such as saturation magnetization (M_{Sat}), exchange constant (A_{ex}), anisotropy constants (K_{U1}), parameters of magnetic dissipation, etc.

1.7.3 Time-resolved Magneto-Optical Kerr Effect (TRMOKE)

Time-Resolved Magneto-Optical Kerr Effect (TRMOKE) spectroscopy is an important technique used to study the ultrafast demagnetization processes in nanostructured magnetic materials. The TRMOKE spectroscopy offers insights into the fundamental mechanisms of spin dynamics and energy transfer at femtosecond timescales, crucial for understanding and optimizing magnonic devices. By understanding the ultrafast dynamics of magnetic materials, one can gain insights into the underlying mechanisms that affect their behaviour in high-frequency regimes, which can be leveraged to optimize the design and performance of state-of-the-art emerging technologies [3]. For example, studying the spin dynamics and relaxation processes at ultrafast timescales can provide information on the behaviour of nanostructured magnetic materials under rapid switching or dynamic conditions, which are prevalent in high-frequency operation. Such understanding can guide the selection of nanostructured magnetic materials with properties such as high saturation magnetization, low coercive field, and moderate anisotropy field and steer the engineering design for follow on highly miniaturized device topologies, which are desirable for minimizing losses at and achieving efficient performances at relatively higher operational frequencies.

It is noted that both BLS and TRMOKE spectroscopy are non-destructive characterization technique. However, the fundamental difference between them is the *TRMOKE spectroscopy* offers the magnetization precession in time domain which needs to be undergone through Fast

Fourier Transformation (FFT) to observe the response in the frequency domain while the *BLS Spectroscopy* provides the experimental dynamics data directly in frequency domain.

1.8 Spin Dynamics

In order to study the dynamic behaviour of magnetic materials/devices, one needs to understand the basic fundamentals of spin dynamics, which is a complex field encompassing a wide range of time scales. These time scales, determined by the interaction energies via the Heisenberg relation, categorize spin dynamics into different types. The fastest known process is the fundamental exchange interaction, occurring within 10 femtoseconds (fs). Spin—orbit coupling (SOC) and spin-transfer torque (SOT) occur over 10 fs to 1 picosecond (ps). Ultrafast spin dynamics can be studied by exciting ferromagnetic materials with ultrashort laser pulses [31]. Laser-induced demagnetization occurs in a few hundred fs, while remagnetization follows in 1—10 ps. These rapid processes are crucial for magnetic data storage, where writing via spin reversal occurs within nanoseconds (ns).

Optically induced ultrafast spin dynamics, first observed by Beaurepaire et al. in 1996 [32], showed nickel thin films demagnetizing in sub-ps times after sub-100 fs laser excitation. Subsequent studies confirmed these findings across various metals and alloys, sparking theoretical investigations into the rapid quenching of magnetic moments while conserving angular momentum. Despite progress, the full understanding of these mechanisms remains elusive. After demagnetization, electronic charges and spins relax within a few ps to ns, following a bi-exponential decay. The faster decay reveals the relaxation times of hot electrons and spins, mediated by electron-phonon interactions, occurring from a few to tens of ps. This relaxation leads to equilibrium temperatures for spins, charges, and the lattice, altering lattice temperature and magnetocrystalline anisotropy. This ultrafast change triggers magnetization precession. The longer relaxation time (sub-ns to a few ns) involves heat diffusion, damping magnetization precession and ending dynamic processes.

Energy dissipation in ferromagnets, though complex, can be approximated by a single damping parameter. Gilbert introduced a phenomenological term to describe the damping of magnetization precession, modelling it as ‘viscous’ damping through a dissipation term dependent on the time derivative of the magnetization [33]. This damping parameter includes contributions from various processes, leading to the coupling of uniform and non-uniform precession modes and other thermal baths in the magnetically ordered substance. Consequently, energy dissipates into non-magnetic degrees of freedom, typically transferring to the lattice and creating phonons, thus heating it.

To understand the different mechanisms contributing to damping, extensive experimental and theoretical research has been conducted on metallic and insulator ferromagnetic materials. Here, we focus on the mechanisms related to magnetic damping in metallic thin film ferromagnets. Instead of delving into the magnetization dynamics equation, we discuss the origin and mechanisms (e.g., local and non-local, intrinsic and extrinsic) of Gilbert damping [34]. Theoretical models such as the breathing Fermi surface model, s-d exchange model, and spin-flip scattering are covered, along with their limitations in explaining recent findings.

1.9 Magnon Based Devices

Magnon-based devices, which leverage spin waves for information processing, offer several significant advantages, including reduced power consumption, high-speed operation, and potential for miniaturization. These devices provide a promising alternative to traditional electronic devices, with potential applications spanning logic circuits, memory storage, and communication systems. The use of spin waves, or magnons, enables the propagation of information with minimal energy loss compared to electronic currents, making magnonics an energy-efficient technology. Additionally, the high-frequency operation of spin waves allows for faster data processing, which is crucial for advanced computing and communication technologies [35]. The inherent properties of magnons also facilitate the scaling down of device dimensions, paving the way for the development of highly compact and efficient components suitable for next-generation nanoelectronic systems.

Magnonic crystals [36] are periodic magnetic structures that can manipulate spin waves similarly to how photonic crystals control light. These materials exhibit bandgaps where spin wave propagation is forbidden, allowing for the creation of magnonic devices with tailored properties. The design and fabrication of magnonic crystals are fundamental to advancing the magnon based technology. The interactions between magnons play a pivotal role in the functionality of magnonic devices. These interactions include magnon scattering, magnon-phonon coupling [4], and nonlinear magnon dynamics [5]. Understanding these interactions enables the development of devices with enhanced performance and new functionalities.

1.9.1 Miniaturized Conventional Antenna

Antennas play a pivotal role in modern communication systems, serving as essential components that enable the transmission and reception of electromagnetic waves. Their design and functionality significantly impact the efficiency, range, and reliability of wireless communication. Various

types of antennas are employed in different applications, each with unique characteristics and advantages, e.g., Dipole Antennas, Monopole Antennas, Patch Antennas, Yagi-Uda Antennas, Parabolic Reflector Antennas, Phased Array Antennas. Among the various types of antennas listed, the Patch Antennas and the Phased Array Antennas can be considered as miniaturized (i.e., at the micro or nanometre level) conventional antennas. For instance, patch antennas, also known as microstrip antennas, hold the promise of miniaturization potential. Patch antennas are typically flat, low-profile antennas., can be fabricated using photolithographic processes, making them highly suitable for miniaturization. They are typically printed on a substrate with micro or nanoscale precision. They are commonly used in applications requiring compact and low-profile antennas, such as in mobile devices, wearable electronics, and medical implants. On the other hand, phased array antennas comprising multiple individual antenna elements similarly have miniaturization potential. Phased array antennas can electronically steer their beam without moving the physical structure. Generally, phased array antennas consist of multiple small radiating elements, which can be micro-fabricated and integrated on a single chip. The ability to electronically steer the beam without moving the antenna physically adds to their suitability for miniaturization. These antennas are used in advanced communication systems, radar, and satellite applications, where precise beam steering and high performance in a compact form are required.

The limitations imposed by the other types of the antennas, as described below, restricts themselves to miniaturize. For instances, dipole and monopole Antennas, Yagi-Uda antennas or parabolic reflector antennas belong to these categories. Among the simplest and most widely used types, dipole and monopole antennas consist of two conductive elements that transmit and receive electromagnetic waves. They are often used in television and radio broadcasting due to their simplicity and effective radiation pattern, providing omnidirectional coverage. While basic dipole and monopole antennas can be miniaturized to some extent, their performance typically degrades significantly at micro or nanoscale dimensions due to fundamental limitations related to wavelength and efficiency. Featuring multiple parallel elements, the Yagi-Uda antenna is directional and highly efficient. It is often employed in applications requiring targeted signal transmission, such as in radar and amateur radio. Since these antennas rely on multiple elements arranged in a specific configuration, face challenges in miniaturization due to the spacing and size requirements of each element. Known for their high gain and directivity, parabolic reflector antennas use a parabolic dish to focus signals onto a central feed. They are widely used in satellite communications, radio telescopes, and wireless networking. As they use a large reflective surface to focus signals, they are inherently challenging to miniaturize due to the necessity of a large aperture to achieve high gain.

Therefore, it can be summarized that the patch antennas and phased array antennas are the

most suitable candidates for miniaturization to the micro or nanometre level, maintaining functionality and performance in compact, integrated designs. The following section introduces a novel and ultracompact antenna, called as the "Magnon Microwave Antenna" (MMA) [4], which utilizes both the fundamental advantages of the patch antennas and the phase array antennas while working on different principle. Instead of the utilizing the conventional electrical/electromagnetic power-phase concepts, the MMA rely on the magnons (SW) and subsequently magnon based power-phase distribution, as described below.

1.9.2 Magnon Microwave Antenna

Miniaturization is a key trend in modern technology, driven by the demand for smaller, more efficient, and higher-performing devices. In this context, the concept of integrating magnonic devices with antennas offers exciting new possibilities. Magnonics, the study of spin waves in magnetic materials and nanoheterostructures, presents unique advantages such as miniaturization, high efficiency, and frequency tuneability. By leveraging these properties, the development of "Magnon Microwave Antennas" (MMAs) [4] represents a significant step forward in the quest for next-generation communication devices. This thesis focuses on the innovative integration of nanostructured magnetic materials into antenna design, specifically exploring the potential and applications of MMAs in integrated magnonic devices.

The Magnon Microwave Antenna (MMA) [4] represents a novel advancement in the field of integrated magnonic devices. Unlike conventional antennas that usually rely on the propagation of electromagnetic waves through free space, MMAs utilize spin waves or magnons—quanta of spin excitations—in nanostructured magnetic/magnetostrictive materials. Geometrically, the MMAs are comprised with nanostructured magnetostrictive materials on top of the piezoelectric (PE) substrates, where the PE substrate generates surface acoustic waves (SAW) upon launching an electrical potential and the SAW accordingly excites the magnetization within the patterned/nanostructured magnetostrictive materials. This approach offers several unique advantages: (i) **Miniaturization**: MMAs leverage the short wavelengths of spin waves, which are orders of magnitude smaller than those of electromagnetic waves at the same frequency. This property enables the design of highly compact antennas, making them ideal for integration into nanoscale devices and circuits. (ii) **Efficiency**: By harnessing the inherent properties of magnetic materials, MMAs can achieve high efficiency in converting electrical signals to spin waves and vice versa. This efficiency is crucial for applications where power consumption and signal loss need to be minimized. (iii) **Frequency Tuneability**: The frequency of magnons/spin waves in MMAs can be tuned by patterning the magnetostrictive materials into different shapes/geometry, allowing for

the dynamic frequency control and reconfigurability. This tuneability is a significant advantage for adaptive communication systems and frequency-agile applications. (iv) **Integration**: MMAs can be seamlessly integrated with other magnonic and electronic components, facilitating the development of complex, multifunctional devices. This integration capability is vital for advancing next-generation communication technologies, where compact and efficient system design is paramount. (v) **Low Interference**: Operating in the magnonic regime, MMAs can mitigate issues related to electromagnetic interference, enhancing the performance and reliability of communication systems in dense electromagnetic environments.

1.10 Motivation

Since its discovery in the ancient world, magnetism has profoundly impacted various applications, e.g., extending from loudspeakers and electromotors to microphones and windscreen wipers. Permanent magnets have been integral to these applications. Despite the longstanding nature of magnetism as a research field, nanomagnetism has emerged in recent decades as a vibrant area of scientific inquiry. This renewed interest is driven not only by fundamental scientific curiosity but also by the immense potential of nanomagnets in modern and future nanotechnologies.

In today's technology-driven world, devices like smartphones, laptops, and high-spec computers have become indispensable, highlighting the critical role of advanced technology in our daily lives. Researchers have made significant strides in developing and understanding high-performance magnetic systems and high-frequency antennas. Current research is focused on optimizing design parameters and materials to achieve higher data transfer rates and lower energy consumption. Both computational models and experimental approaches are employed to explore the high-performance behaviour and underlying physical phenomena of these systems.

What distinguishes our work from existing research is the integration of high-performance magnetic systems with high-frequency antennas, specifically *"in-situ"* electrodeposited nanostructured exchange spring systems and the Magnon Microwave Antennas (MMAs). By combining these cutting-edge technologies, we can leverage their strengths to create a novel platform for information processing, communication, and performing task. This integration offers new possibilities for high-speed data transfer, efficient energy utilization improved device performance, and, reservoir computing.

To validate our proposed solution, we utilize a combination of analytical formulations, experimental measurements, and micromagnetic simulations. This comprehensive approach aims to provide deeper insights into the underlying physics and develop design guidelines for practical implementation in telecommunications, data storage, and reservoir computing. The outcomes

of this work will contribute to the development of next-generation electronic devices that are faster, more reliable, and environmentally friendly, paving the way for a future driven by advanced technologies. In summary, the results of this thesis resulted into significant delineation of fundamental understanding of linear and non-linear magnon (quantized spin wave) dynamics and subsequent magnon power-phase distributions of a "Magnon Microwave Antenna" (MMA) working from MHz level to the GHz level, which could potentially be utilized as next generation reservoir computing/neuromorphic computing.

1.11 Thesis Outline

This thesis has presented a unique approach to address the challenges associated with such high-performance magnetic systems and high frequency antennas. The proposed solution involves the development of advanced fabrication techniques that enable precise control over the properties of the magnetic materials used in these systems. By tailoring the composition, structure, and interfacial properties of these materials, the aim is to achieve enhanced magnetic performance and transmission with lower energy consumption. The remainder of this thesis is organized as follows:

⇒ Chapter 2 provides the detailed overview of the state-of-the-art of the nano-hetero-structured systems, namely, exchange spring systems, relevant nanostructured magnetic materials, i.e., cobalt phosphorous in this case, and the miniaturized transmission devices, i.e., antenna comprises with suitably tailored nanostructures.

⇒ Chapter 3 elucidates the research methodologies, i.e., the experimental methods for fabrication of the *"in situ"* heterostructured thin films, the characterization techniques that have been utilized to characterize the developed samples and the micromagnetic modelling and simulation techniques employed for designing a novel transmission devices, featuring the magnon microwave antenna (MMA) and beyond.

⇒ Chapter 4 describes the electrochemical mechanism in detail, i.e., the required electrochemistry involving oxidation and reduction processes, behind the fabrication of the stress free, shiny, smooth, *"in situ"* nano-hetero-structured exchange spring amorphous and nanocrystalline thin films of Co-rich cobalt phosphorous (CoP) with conventional DC electrodeposition technique and its structural, compositional, quasi-static magnetic, and the micromagnetic studies.

⇒ Chapter 5 focuses on both the static and dynamic (Brillouin Light Scattering (BLS) spectroscopy study) magnetic studies. It explains the evolution from the low coercivity non-

ES loop to the staircase-ES loop, while the first-order reversal curve (FORC) distributions demonstrate the different reversal mechanisms. Finally, it calculates and compares the interfacial exchange of the *"in situ"* nano-hetero-structured exchange spring amorphous and nanocrystalline thin films.

⇒ Chapter 6 reports the investigation of the ultrafast magnetization dynamics of a non-exchange spring CoP film with partial demagnetization within few hundreds of femtoseconds (fs) followed by fast and slow relaxation in relatively longer timescale, and eventually elucidates that how such important dynamical properties will underpin the potential applications in high-frequency integrated magnetic passives for future monolithic power supply on-chip.

⇒ Chapter 7 introduces a novel transmission device called "Magnon Microwave Antennas" (MMAs), comprised of patterned arrays of magnetostrictive nanomagnets embedded in piezoelectric heterostructures, for the generation of microwaves with tuneable frequencies and explains its working principle, i.e., how the phonon-magnon coupling within the patterned array of nanowires and nanodots generates a multimode microwave frequencies with nonvolatile spin textures in both configurations, and finally paves the way to tune the frequency from the MHz level to the GHz level.

⇒ Chapter 8 presents the magnonic power-phase distributions and their tuneability of the surface acoustic wave (SAW) driven nano-patterned "Magnon Microwave Antennas" (MMAs) and additional functional tuneability through amplitude-dependent training using various combinations of nanowire and nanodot dimensions, topologies, material properties, and array configurations and finally introduces a novel alternative approach, paving the way to utilize these MMAs for on-chip reservoir computing, where amplitude varies at the operating frequency.

⇒ Chapter 9 finally concludes the novel research works presented in this doctoral thesis.

⇒ Chapter 10 briefly describes the way to carry forward the present research while summarising the future plan.

2 Literature Review

2.1 Introduction

Nanostructured magnetic materials [7, 8] have garnered significant attention due to their potential applications in integrated devices, particularly in integrated magnonic devices (IMD). The field of magnonics, which explores the manipulation and control of spin waves (SW) or magnons, offers promising pathways for developing next-generation communication technologies. This chapter focuses on the literature review, comprehensively examining the key concepts, material properties, fabrication techniques, and device applications pertinent to nanostructured ferromagnetic materials and their role in MMAs. The review synthesizes current research, highlighting advancements, challenges, and future directions.

The review begins by exploring nanostructured magnetic materials suitable for conventional integrated devices. These include micro-inductors [11, 12] and fluxgate sensors [37], which are critical for various applications in electronics and sensing technologies. Such nanostructured magnetic materials, which are suitable for integrated passives, mostly belong to nanostructured soft magnetic materials that means they have comparatively low coercivity (H_C) and high saturation magnetization (M_{Sat}). Following this, the focus shifts to IMDs (integrated magnonic devices) via high energy product (BH_{max}) nanostructured materials, which are essential for advanced communication systems and permanent magnetic applications, respectively. IMDs include possible devices for instance, Magnon Transistors, Magnonic Waveguides, and Magnonic Logic Gates [13, 14]. This thesis has introduced a key magnon based transmission device called as "Magnon Microwave Antenna" (MMA) while highlighting the importance of it. Additionally, the fundamentals of exchange spring (ES) nanostructured materials are examined in detail. This chapter also provides an overview of the miniaturization of integrated passives, ensuring an on-chip power supply [12] to achieve the ultimate level of device miniaturization. Such advancements

aim to enable the utilization of these devices for on-chip reservoir computing [38], thereby pushing the boundaries of current technology.

2.2 Ferromagnetic Nanoheterostructured Materials for Integrated Devices

High-frequency nanostructured magnetic films are essential for a range of advanced applications. These applications include enhancing the performance of high-frequency integrated micro-inductors, coupled inductors, and micro-transformers, all of which feature multi-nanomagnetic-layered cores. Such components are crucial for the development of on-chip power supplies, particularly for DC-DC switch mode power conversion, which is necessary for the efficient power delivery in next-generation microprocessors [11, 12]. Additionally, these materials are instrumental in enabling energy-efficient switching in magneto-resistive random access memory (MRAM) bits [39], as well as supporting the operation of future high-speed spin-based devices.

However, many high-frequency integrated magnetic devices face challenges related to eddy current losses. Eddy current losses are a prevalent dissipation mechanism in magnetic materials, resulting in the conversion of electromagnetic energy into heat. To address these losses, especially in thicker magnetic materials where reasonable power density is sought, materials with higher resistivity are needed. In addition, these materials must exhibit high saturation magnetisation, low coercivity, and a moderate anisotropy field (H_K) to minimise hysteresis losses and ferromagnetic resonance (FMR) losses in integrated inductors operating within the MHz-GHz range [40, 41].

Ferromagnetic resonance losses occur due to spin motion, which can be induced by a combination of direct relaxation to the lattice and indirect relaxation through the excitation of non-uniform magnetisation modes, such as spin waves [42]. Therefore, designing and modelling GHz-level integrated magnetic devices that operate efficiently near the FMR frequency regime requires a comprehensive study of spin dynamics and relaxation phenomena within this frequency range. Understanding these dynamics is crucial for optimising the performance of these devices and ensuring their efficiency [40–42]. Their ability to enhance component performance while mitigating energy losses through careful material selection and design underscores their potential in advancing microprocessor power supplies, memory technologies, and spintronic devices.

Integrated passive devices, such as inductors and transformers, span a broad range of applications and technologies. They are essential components in modern electronic circuits that often need to be miniaturized while maintaining high performance, which presents several challenges [12]. While most of the integrated circuits and systems focus on electrical and elec-

tronic integration, specific applications like magnetic sensors, MRAM [22], and certain MEMS devices rely on the nanostructured ferromagnetic materials for their functionality [23]. In order to maintain the performance and efficiency of the magnetic and spintronics devices, these nanostructured materials are crucial, more particularly nanostructured ferromagnetic materials, which hold specific magnetic properties that are essential [7, 8]. Therefore, we focus here on certain integrated devices that specifically require nanostructured magnetic materials for their operation. For instance, (i) magnetic sensors and magnetometers that often use materials like ferrites and rare-earth magnets which are used to detect magnetic fields and measure their strength and direction [43]; (ii) magnetic tunnel junctions (MTJs) [44] requiring layers of ferromagnetic materials separated by a thin insulating layer, which is a key component of spintronic devices and magnetic memory devices including magnetoresistive random access memory (MRAM) devices [23], that utilize magnetic storage elements and requires magnetic materials like ferromagnetic layers and spintronic components, hard disk drives (HDDs), that use magnetic disks to store data, requiring materials with strong magnetic properties for data recording; (iii) Inductors and Transformers which are used in power management ICs and RF circuits may require magnetic cores made from materials like ferrites; (iv) magnetic microelectromechanical systems (magnetic MEMS) which require nanostructured ferromagnetic materials for their operation.

Nanostructured soft ferromagnetic materials are particularly advantageous in various applications due to several inherent properties. They exhibit high permeability and inductance density, low magnetic losses, reduced eddy currents, and improved frequency response, while also offering thermal and mechanical stability. Conversely, nanostructured hard ferromagnetic materials are primarily utilised as sources of magnetic fields for position sensors, torque sensors, and for the biasing of magnetoresistors. These nanostructured magnetic materials often demonstrate higher magnetic permeability compared to their bulk counterparts [45].

Materials with high permeability can achieve higher inductance values within a smaller volume, which is critical for miniaturisation. The ability to achieve high inductance in a compact form factor is essential for integrated circuits where space is at a premium. Nanostructured materials facilitate the fabrication of components with higher inductance density. The small grain size in these materials restricts the path for eddy currents, thereby reducing eddy current losses. This reduction in eddy current losses is crucial for enhancing the efficiency of inductors and transformers, particularly at high frequencies [41].

Nanostructured ferromagnetic materials can operate efficiently at higher frequencies due to their reduced magnetic losses, making them suitable for RF and microwave applications. The ferromagnetic properties of nanostructured materials can be engineered by controlling the size, shape, and distribution of the nanoparticles. Such level of control enables for the optimization

of material properties to meet specific requirements of integrated passives. Some nanostructured materials exhibit higher saturation magnetization, which allows for higher energy storage capacity in magnetic components. Nanostructured materials often show better mechanical and thermal stability [46]. This is important for integrated passives that must operate reliably under varying environmental conditions. Nanostructured magnetic materials can be integrated with standard semiconductor fabrication processes, making it easier to incorporate passive components directly onto silicon chips. This compatibility is essential for producing highly integrated systems-on-chip (SoCs) [47].

Examples of nanostructured magnetic materials include ferrites: nanoscale ferrite materials are widely used in integrated inductors due to their high permeability and low losses at high frequencies [48]; metallic nanocomposites: these materials combine the high magnetic properties of metals with the reduced eddy current losses of nanostructured systems, providing a good balance of performance characteristics [49, 50]; magnetic nanoparticles: Embedded in a non-magnetic matrix, these particles can form materials with tailored magnetic properties suitable for specific applications [51, 52]. However, electrodeposited nanostructured ferromagnetic materials [46] offer several important advantages over ferrites, including higher magnetic saturation, superior mechanical properties, precise control of nanostructure, better integration with microelectronics, higher permeability at low frequencies, fabrication flexibility, higher electrical conductivity, and cost-effectiveness for thin films [53]. These advantages make electrodeposited ferromagnetic materials particularly valuable for a wide range of advanced technological applications, from magnetic storage and sensors to flexible electronics and high-performance inductive devices, which subsequently enable the creation of high-performance, compact passive components essential for modern electronic devices [41]. Nanostructured magnetic materials are vital for the development of integrated passives due to their superior magnetic properties, reduced losses, and compatibility with miniaturization and integration requirements.

Electroplated inductors with multi-nano-layered structures in CoP thin films have previously been developed, where phosphorus (P) is added to enhance resistivity and achieve amorphousness, making them suitable for integrated circuits [54]. Thicker nanostructured high-frequency magnetic materials, crucial for achieving high power densities, are essential for advanced technological applications. The electrodeposition technique is particularly advantageous for creating these films due to its cost-effectiveness, high yield, and adaptability to complex nanostructures [53]. While thin films of Cobalt Phosphorus alloys (CoP) have been extensively prepared and studied via electrodeposition by several research groups [46, 55–57], and their dynamic properties have been investigated [2, 46], the ultrafast dynamic properties of CoP thin films remain unexplored. To address these challenges and enhance the performance of high-frequency integrated inductors,

power delivery systems, energy-efficient MRAM bit switching, and future high-speed spin-based devices, it is essential to study the ultrafast dynamics of magnetic materials. This includes their response to external stimuli and the magnetization relaxation processes, providing significant insights into their high-frequency performance [3].

2.3 Integratable Magnonic Devices

From the discussion in Chapter 1, we already know that magnonic devices, on the other hand, are a class of spintronic devices [17] that utilize magnons [6] — the quasiparticles associated with the collective excitation of electron spins in a magnetic material [35]. Here, we shall discuss such magnonic devices, which have the potential to be utilized as IMDs (integrated magnonic devices). Those IMDs harness the properties of magnons for various applications, including data processing, communication, and sensing, where the distribution in magnon amplitudes and phases could be leveraged for information readout [58]. Spin waves, which typically occur in the microwave frequency range, can have their wavelengths reduced to the nanoscale [59]. This makes them a promising candidate for developing advanced microwave information processing devices [28]. Furthermore, introducing magnons into the integrated devices/circuits just not only enable the possibility to perform operations on-chip [38] at high frequency but also takes care about the Joule heating [60]. Note that, Joule heating is a fundamental issue in conventional data processors, limiting clock frequencies to just a few GHz. This thermal problem arises due to the resistive heating in electronic components as electric current passes through them, causing energy dissipation and temperature rise, which restricts the performance and efficiency of the processors. Moreover, such magnon based devices are potentially able to perform comparatively faster operations—thanks to the high spin density of the nanostructured magnetic materials compared with individual spins. Such faster operations in the sub-gigahertz to gigahertz regime can be easily achieved developing hybrid coupling between magnons and microwave photons [61].

Here are some of the integrated devices that could be utilized as integrated magnonic devices. For example, Magnetoresistive Random Access Memory (MRAM) utilizes magnetic tunnel junctions (MTJs), which can potentially be integrated with magnonic devices. Magnonic devices could be used for read/write operations, leveraging spin waves for data transfer and manipulation [39]. Spintronic sensors, such as those based on giant magnetoresistance (GMR) or tunnelling magnetoresistance (TMR), can be integrated with magnonic circuits [62]. Magnonic devices can enhance sensitivity and functionality by processing magnetic information via spin waves. Magnetic Logic Devices that use magnetic states to represent logical bits can be integrated with magnonic circuits. Magnonic logic gates and circuits can process information using spin waves,

offering low power consumption and high-speed operation [15]. While traditionally not associated with magnonic devices, inductors and transformers with magnetic cores can potentially be integrated with magnonic devices for energy-efficient signal processing and filtering using spin waves [3, 41]. Magnonic devices can be integrated with microwave and RF circuits to create tunable filters, oscillators, and signal processors. Spin waves can interact with microwave signals, providing new functionalities in communication systems [4, 20]. Yttrium iron garnet (YIG) and its derivatives took a crucial part in leading the "magnonics" field [28], due to its uniquely low magnetic damping. A flurry of research articles based on YIG and doped-YIG have been published in the few last decades [28, 63]. However, in this thesis we explore the possibility utilize phonon-magnon interaction for IMDs, where magnon will be excited in a top magnetostrictive material through the phonon, i.e., surface acoustic wave (SAW) generated on the bottom piezoelectric layer (Chapter 7 and Chapter 8). Therefore, we have chosen other magnetostrictive material (FeGa) which shows high magnetostriction property [64], which will ensure sufficient coupling between magnon and phonon [4, 5, 20]. In short, integrated magnonic devices represent a promising area of research and development, leveraging the properties of spin waves for advanced electronic and spintronic applications. Various integrated devices, particularly those involving magnetic materials and spintronics, can be adapted to utilize magnonic effects, opening new possibilities for data processing, communication, and sensing technologies [60].

2.4 Nanostructured Ferromagnetic Materials

Nanostructured ferromagnetic materials can be broadly classified into nanoparticles, nanowires, thin films, and nanocomposites. Each of these forms has distinct advantages and is synthesized using specific techniques. For example, typically nanoparticles are synthesized using chemical methods such as coprecipitation [65], sol-gel processes [66], chemical synthesis [67] and hydrothermal synthesis [68]. These methods allow precise control over particle size and distribution, which is crucial for achieving uniform magnetic properties [69]. Nanowires often are produced through template-assisted methods like electrodeposition [70] and chemical vapor deposition (CVD) [71]. Nanowires exhibit high aspect ratios, leading to anisotropic magnetic behaviour that can be exploited in various applications [71, 72]. On the other hand, thin Films are fabricated using techniques such as electrodeposition [2], sputtering [73, 74], molecular beam epitaxy (MBE) [75], and pulsed laser deposition (PLD) [76]. Thin films are essential for developing planar devices and offer a platform for studying two-dimensional magnetic phenomena. Nanocomposites are created by embedding magnetic nanoparticles in a non-magnetic or another magnetic matrix [77]. These composites can combine the desirable properties of different phases,

such as high saturation magnetization and low coercivity.

The following sections are organized as follows: first, we review nanostructured ferromagnetic materials featuring high saturation magnetization (M_S) and low coercivity (H_C) developed by conventional electrodeposition technique suitable for passive inductor applications. Next, we examine nanostructured ferromagnetic materials developed by sputerring, molecular beam epitaxy necessary for exchange spring structures with comparatively higher saturation magnetization (M_S) and higher coercivity (H_C). In this context, we review papers that include dynamic studies, particularly those using Brillouin Light Scattering (BLS) spectroscopy and Time-Resolved Magneto-Optic Kerr Effect (TRMOKE) spectroscopy, which align with the scope of this thesis.

2.4.1 A Detailed Review of Electrodeposited Cobalt Phosphorous Alloys

This section introduces the experimentally studied nanostructured soft ferromagnetic material in this thesis, i.e., cobalt phosphorus (CoP) alloy. It further covers its historical context and early research, advances in understanding and applications, technological innovations and magnetic properties, surface magnetic anisotropy and sensor applications, the effects of electrolyte pH and heat treatment, thermal stability and nanocrystalline alloys, optimal conditions and magnetic controllability, and addresses challenges with future directions.

The deposition of cobalt phosphorous (CoP) alloys began in 1946 when Brenner and Riddell produced cobalt deposits through a chemical reduction process [78]. This process involved the reduction of cobalt metal salts using hypophosphite at elevated temperatures, which resulted in deposits containing several percent of phosphorus. Although innovative, this electroless process was found to be uneconomical due to its slow deposition rate and the lack of control over the composition of the deposits. Consequently, research interest shifted towards the study of electrodeposition techniques for depositing metals with phosphorus.

In 1950, Brenner et al. [79] reported that alloys of cobalt containing up to 15% phosphorus could be obtained through electrodeposition from acid solutions containing phosphites. They achieved this composition at a temperature of approximately 75°C, marking a significant advancement in the control of phosphorus content in cobalt alloys through electrodeposition.

Further investigations into the properties of CoP alloys were carried out by Riveiro and Sanchez-Trujillo [80], who studied the anisotropy behaviour of DC electrodeposited amorphous CoP thin films. Their research revealed that films with a thickness below 400 nm exhibited in-plane anisotropy, while films with a thickness around 500 nm displayed out-of-plane anisotropy. This discovery highlighted the influence of film thickness on the magnetic anisotropy of CoP thin films.

In 1981, Riveiro and Rivero [81] reported the fabrication of multilayers consisting of alternate

phosphorus-deficient magnetic (M) and phosphorus-rich nonmagnetic (NM) layers of amorphous cobalt phosphorous. The magnetic layers, which were 30 nm thick, had a composition of $Co_{76}P_{24}$, while the nonmagnetic layers, which were 2-5 nm thick, had a composition of $Co_{67}P_{33}$. They proposed a method for producing electrolytically amorphous CoP samples with planar magnetic anisotropy using a rectangular alternating density current that was variable in amplitude and width. The samples consisted of alternate layers of two different CoP concentrations, and compositional analysis was carried out using Auger spectroscopy. Structural analysis was performed using X-ray diffraction, and saturation magnetization was measured using the extraction method. They found that the behaviour of H_C varied with the thickness of the layers with the highest Co concentration, and different types of domain walls were observed using the Bitter technique.

In another study, Riveiro et al. [82] described a method for obtaining electrodeposited amorphous CoP alloys with differing anisotropies by employing an alternating current density of very low frequency. This method allowed for the production of samples with high permeability. For samples without perpendicular anisotropy, a distribution of the magnetization in the plane with 180° domains was observed.

Riveiro et al. [83] conducted an extensive study of the magnetic structure of electrodeposited multilayered amorphous CoP alloys using an unconventional electrolytic process with a rectangular alternating current. Their findings suggested the presence of "exchange interaction" between the layers. They also observed that the period and amplitude of the zig-zag pattern of the 'charged walls' were strongly affected by small energy variations. The origin of the in-plane magnetic anisotropy in the samples was investigated, and it was found to be susceptible to magnetic annealing, with results indicating anisotropy induced by directional order.

In 1982, Riveiro [84] explored the changes in perpendicular magnetic anisotropy in electrodeposited amorphous CoP alloys during heat treatment in the presence or absence of a magnetic field. Their results showed that, apart from columnar shape anisotropy, other mechanisms of anisotropy were present in the samples. These included stress anisotropy, which could reach values comparable to shape anisotropy, and directional-order anisotropy, which occurred only when the sample was heated to over 140°C.

In early 2000s, Sinnecker et al. [85] made significant advancements by electrodepositing $Co_{90}P_{10}$ amorphous microtubes onto Cu wire substrates. These samples exhibited radial magnetic anisotropy, as deduced from hysteresis loops and magnetic force microscopy imaging. The microtubes also showed a notable giant magnetoimpedance (GMI) effect, with the amplitude depending on the layer thickness and frequency. The small hysteresis observed in the GMI curves was attributed to the radial anisotropy, which is important for technological applications.

Further research by Garcia et al. [86] involved the electrodeposition of magnetic microtubes of

amorphous $Co_{90}P_{10}$ over cylindrical Cu substrates. These samples also exhibited radial anisotropy, and the evolution of the domain structure and GMI behaviour in the MHz frequency range was analysed. Perez et al. [55] reported obtaining multilayer films of Co_xP_{1-x} with different compositions by modulating the current densities during the deposition process. These films exhibited planar anisotropy, high permeability, and very low coercive force.

In 2001, Garcia et al. [87] presented the magnetic properties, magnetoimpedance, and magnetic force microscopy analysis of electrodeposited CoP magnetic microtubes. They found that the electrodeposited CoP was a heterogeneous material consisting of non-magnetic wires coated with magnetic layers of amorphous CoP. These microtubes exhibited a GMI effect up to high magnetic fields, with only small hysteresis at low fields. They enhanced the GMI sensitivity of the microtubes through proper annealing, achieving a 270% increase in GMI after annealing at 473K for 1 hour. This improvement was explained by the change in anisotropy of the magnetic layer after annealing.

Garcia et al. [88] studied the domain structure of electrodeposited $Co_{90}P_{10}$ microtubes, which exhibited radial magnetic anisotropy and GMI effect. They characterized the domain structure using magnetic force microscopy and impedance measurements, finding that the size of the closure domains increased with the CoP layer thickness. They also determined the depth of the closure domains from the high-frequency behaviour.

In 2002, Favieres et al. [89] obtained amorphous soft magnetic CoP multilayers with controlled surface magnetic anisotropy. They demonstrated that the surface magnetization easy direction could be continuously altered from an initial perpendicular position to a final arrangement within the longitudinal plane during sample production. This continuous change in magnetization direction eliminated the need for subsequent treatments such as thermal, stress, or magnetic field annealing. The magnetic domain configurations, observed using the Bitter technique, revealed a continuous variation from an initial stripe domain structure to a final configuration with planar longitudinal magnetization and visible domain walls. The control of magneto-optic behaviour in these multilayers was highlighted as being of interest for technical applications.

Perez et al. [37] combined printed circuit board (PCB) technology with electrodeposition to produce a new 2D fluxgate sensor using amorphous ferromagnetic CoP alloys. This fabrication procedure avoided the use of glue to integrate the core into the device, improving performance and making the production process more reproducible. By properly choosing the frequency and amplitude of the driving current, they achieved high sensitivity (160 V/T) or a large linear range (0-250 μT). The use of electrodeposited amorphous CoP opened new perspectives for improving the performance of inductive microdevices such as fluxgates, inductors, and transformers.

Lucas et al. [56] studied the effects of different pH values in the electrolytes used for electrode-

positing CoP alloys at room temperature. They found that high internal stresses due to hydrogen evolution during the electrodeposition process caused cracks and fractures in samples using stiff substrates. However, samples electrodeposited onto flexible substrates did not show surface cracks. They also reported an increase in coercivity when the pH of the electrolyte decreased, corresponding to increased hydrogen evolution and internal stresses.

In their 2007 study, Ciudad et al. [90] reported a method to optimize coercivity while maintaining a constant magnetostriction value in electrodeposited CoP multilayers for use in magnetoelastic magnetic sensors. They deposited multilayers of two different compositions of CoP ($Co_{0.74}P_{0.26}$ and $Co_{0.83}P_{0.17}$) and studied the influence of layer thickness while keeping the total thickness constant. Their results showed that saturation magnetostriction was independent of layer thickness, but reducing layer thickness led to a significant reduction in the coercive field to values as low as 0.5 Oe and a large increase in permeability. They also found that hydrogen flow during deposition influenced the direction of anisotropy, allowing for customization of the material for magnetic sensor applications.

Lucas et al. [91] investigated the pinning field and coercivity of electrodeposited soft magnetic $(Co_{76}P_{24}/Co_{85}P_{15})_N$ multilayered films. They observed a linear dependence of the pinning field on the number of layers (N) for frequencies below 1 kHz, attributed to the pinning of domain walls at the interfaces between the layers. For frequencies above 1 kHz, the magnetic behaviour was controlled by eddy currents, with the coercivity's frequency dependence being independent of N.

McCloskey et al. [57] prepared cobalt phosphorous thin films on silicon wafers, using a top conducting seed layer of 20 nm titanium (Ti) and 200 nm copper (Cu). They used the same bath chemistry as Riveiro and Rivero [81] and Perez et al. [55], employing a square-like current waveform with optimized forward and reverse current densities and intermediate off times. They showed the effect of pH on the composition and magnetic properties, achieving a saturation magnetization of around 1.6 T, and discussed the reasons behind material removal during the reverse duty cycle.

The interest in electrodeposited CoP thin films has grown due to their high-frequency performance, large magnetic susceptibility, relatively high resistivity, and growth rate. Yanqiu Li et al. [92] synthesized both amorphous and nanocrystalline CoP films on copper foil using multi-pulse electrodeposition. They investigated the effects of negative average current density on the film composition, crystalline structure, and surface morphology. Their results showed that the phosphorus content could be greatly varied by changing the negative pulse current density, providing a flexible tuning knob for CoP films. The surface morphology varied with phosphorus content, and the film growth pattern was nodular. Additionally, applying an external magnetic

field during electroplating resulted in CoP films on copper-coated silicon wafers with good soft magnetic properties (H_C of $1 \sim 2$ Oe) and high permeability (~ 700).

In 2010, McCloskey et al. [46] discussed the thermal stability of cobalt phosphorus alloys. Due to its high resistivity and good magnetic properties, electrodeposited amorphous CoP (a-CoP) is an attractive material for integrating on-chip inductors into silicon process technology. However, the properties of a-CoP change dramatically upon crystallization. They reported a novel electrodeposited magnetic alloy, a-CoPRe, with significantly improved thermal performance compared to a-CoP, retaining a coercivity (H_C) of less than 92 A/m after thermal annealing at 571 K. These results were obtained for alloys with compositions of $Co_{100\text{-}x\text{-}y}P_xRe_y$, where $9.7 < x < 17.5$ and $0.4 < y < 7.6$. Other important properties, such as saturation magnetization (M_S) and resistivity (ρ), were largely unaffected by the addition of Re.

Kosta et al. [93] prepared magnetic nanocrystalline CoP alloys using a Watts-type cobalt bath containing additives. They obtained coatings several microns thick using galvanostatic pulse plating (PP) and direct current (DC) electrodeposition. Both methods produced compact deposits with slightly different grain sizes. The CoP deposits were magnetically softer than both amorphous P-richer CoP electrodeposits and crystalline Co and Co-alloys prepared by previous electrodeposition methods.

Tung et al. [94] conducted a systematic study on the influences of phosphorus content and CoP layer thickness on the magnetic properties and giant magneto-impedance (GMI) effect in electrodeposited CoP/Cu composite wires. Their results showed a correlation between the structure, soft magnetic properties, and GMI effect. Among the compositions investigated, the optimized magnetic properties (i.e., the lowest coercivity) and the largest GMI ratio were achieved in $Co_{85}P_{15}$/Cu wires derived from an electrolyte containing 30 g/L of H_3PO_3 with a plating duration of 3 minutes and a current density of 750 mA/cm^2.

Recently, Lucas et al. [95] discussed the magnetic properties of CoP electrodeposited alloys, which can be easily controlled by layering the alloys and modulating the phosphorus content of the different layers using pulse plating in the electrodeposition process. However, the study of interface quality, crucial for optimizing the soft magnetic properties of these alloys, is complex due to the amorphous nature of the material. Using Rutherford backscattering spectroscopy (RBS), they determined that electrodeposited $Co_{0.74}P_{0.26}/Co_{0.83}P_{0.17}$ amorphous multilayers with layers down to 20 nm-thick had well-defined layers with interfacial roughness below 3 nm. Magnetostriction measurements indicated that 4 nm was the lower limit for layer thickness, below which the layers mixed, resulting in magnetic behaviour similar to single layers, transitioning from in-plane to out-of-plane magnetic anisotropy. These findings established the range within which the magnetic properties of these alloys could be controlled by layering.

There are limited studies on the X-ray diffraction (XRD) analysis of nanocrystalline cobalt phosphorous prepared by pulse plating or direct current plating, or Dicobalt Phosphide Heterostructure. Sharp XRD peaks, such as (020), (040), (060), and (080), indicate the crystallinity in Dicobalt Phosphide Heterostructure [96]. These findings underscore the need for further optimization of the electrodeposition process to enhance the stability and properties of CoP films. Despite these advances, all the studies discussed required comparatively high temperatures ($\sim$ 75°C to 85°C) for the reported forms of CoP, leading to wastage of raw materials due to vaporisation. In some cases, an external magnetic field was also used during electroplating. Issues with bath chemistry stability were also noted, necessitating optimization to achieve smooth, shiny deposits.

2.4.2 Exchange Spring Nanomagnets: Fundamentals and Applications

Exchange spring magnets hold significant promise for advanced applications due to their unique properties of high energy products, coercivity, and magnetic anisotropy. Ongoing research and development in nanostructuring, fabrication techniques, and material design continue to push the boundaries of what is possible with these magnets. Future directions include further optimization of material interfaces, exploration of new magnetic coupling mechanisms, and integration into practical devices for various technological applications. The subsequent section reveals the journey of exchange spring through their development and theoretical studies, experimental studies and fabrication techniques and advanced applications and future directions.

In 1991, the concept of the Exchange Spring (ES) magnet was first introduced by Kneller and Hawig [25]. This idea postulates that the permanent magnets could be created from composite materials composed of two mutually exchange-coupled ferromagnetic phases. One of these materials is the nanostructured soft ferromagnetic, providing a high saturation (M_S), while the other one is the nanostructured hard ferromagnetic, offering a high coercive field (H_C). The soft phase should surround the hard phase regions in order to prevent their corrosion. Theoretically, such systems can achieve a high energy product (BH_{max}) compared to conventional nanostructured hard ferromagnetic material, featuring a reversible demagnetization curve (exchange spring). Along with these, in certain cases, an unusually high isotropic remanence ratio (or squareness ration, M_R/M_S). To be coherently magnetically exchange coupled and consequently crystallographic, all phases involved in such exchange spring magnetic materials must emerge from a common metastable matrix phase in order.

Skomski and Coey further investigated exchange hardening of nanostructured two-phase systems composed of an aligned hard phase and a soft phase with high saturation magnetization. Analytic nucleation fields were derived from the micromagnetic vector equation, accounting for

interactions between the nanostructured soft regions [97]. In suitable structures, the nucleation field is proportional to the volume-averaged anisotropy constant. For instance, a multilayer composed of alternating 2.4 nm hard-magnetic $Sm_2Fe_{17}N_3$ layers and 9 nm $Fe_{65}Co_{35}$ layers can have an energy product as high as 1 MJ/m^3 (120 MGOe), with a rare-earth content of only 5 wt%. Giant energy products may also be achieved in suitable cellular and disordered structures.

Numerical calculations by Schrefl et al. explored the coercive field of a magnetically soft prismatic grain of irregular cross-section embedded in a hard magnetic matrix [98]. A finite element technique was utilized in solving the corresponding two-dimensional micromagnetic problem. Despite significant deviation of the spontaneous magnetic polarization in the soft magnetic phase at low external fields, the calculations reveal remarkably high values of the coercive field when the size of the soft magnetic grains is sufficiently small.

The concept of "megajoule" magnets was posed by Skomski [99]. Micromagnetic calculations investigated coercivity and energy products of these magnets. Compared to the theoretical limit of 516 kJ/m^3 for single-phase $Nd_2Fe_{14}B$, the energy product in suitable nanostructured $Sm_2Fe_{17}N_3/Fe_{65}Co_{35}$ composites was predicted to be as high as 1090 kJ/m^3. The study explored the influence of the texture and shape, and comparison between the aligned nanocrystalline two-phase magnets and remanence-enhanced isotropic magnets. Notably, the nucleation-based analytical approach breaks down in the isotropic limit. Finally, study outlined conceivable processing methods and discussed the potential applications of "megajoule" magnets.

In their work, Fullerton et al. investigated magnetic reversal process in magnetron sputtered epitaxial SmCo($1\bar{1}00$)/ TM (TM = Fe,Co) bilayer films [73]. The SmCo films have an uniaxial anisotropy of 20T and coercivities >3T at room temperature. Interestingly, the coercivities double upon cooling. For an exchange spring system, it is expected that, the TM layers are exchange coupled to the Sm-Co layer, resulting in reversible demagnetization curves. They further presented numerical solutions from one-dimensional model, revealing the spin configuration for each atomic layer. By comparing the experimental results with the model simulations, they gained insights into the exchange spring behaviour based on the intrinsic parameters of the hard and soft layers. Furthermore, they extended their simulations to estimate the potential energy product enhancement achievable through the exchange hardening principle [100].

In another study, Fullerton et al. provided an overview of exchange spring coupled magnetic films and multilayers. These structured, created through the magnetron sputtering deposition process fabrication methods, allow precise control of thicknesses and magnetic anisotropy at the nanometre scale [26]. Similar to their previous work [73], they investigated epitaxial SmCo/Fe and SmCo/Co bilayers and superlattices, exhibiting characteristic features of exchange spring magnets. They predicted that the formation of the ES systems is generally favoured by the critical

conditions, i.e., the thickness (L_s) of the soft ferromagnetic phase being larger than twice the domain wall width (δ_h) of the hard phase $L_s > 2\delta_h$ [26], where the soft and hard phases reverse at the distinguishable field at the same time and act like different units in the same system. Here, δ_h is defined as $\pi\sqrt{\frac{A_{ex,h}}{K_{u1,h}}}$, where, $A_{ex,h}$ is the exchange stiffness constant and $K_{u1,h}$ is the anisotropy constant of the nanostructured hard ferromagnetic layer. On the other hand, if $L_s \leq 2\delta_h$, soft and hard phase both reverse at indistinguishable fields, resulting in a rigidly coupled soft-hard exchange-coupled structure. Ultimately, this approach allows us to maximize the energy product of the system [25].

Figure 2.1 schematically illustrates the behaviour of spins in soft and hard layers within an exchange spring system. For simplicity, in Figures 2.1(a)-(e), the top blue layer represents the soft ferromagnetic layer, and the bottom yellow layer represents the hard ferromagnetic layer. The thicknesses of these layers are denoted by L_s and L_h, respectively. Soft ferromagnetic spins are depicted by violet arrows, while hard layer spins are shown in blue. Initially, both layers are saturated by applied magnetic field, as shown in Figure 2.1(a) with a rightward red arrow ($\Rightarrow$).

When the magnetic field reverses ($\Leftarrow$), weaker soft ferromagnetic spins begin to align with the field, while strong hard spins remain unchanged as seen in Figure 2.1(b). This behaviour persists as the field strength increases, as illustrated in Figure 2.1(c). Near the interface, soft spins remain in an intermediate state due to strong coupling with hard spins. As the field further increases (Figure 2.1(d)), most soft spins align with the field, and hard spins also adjust their orientation. Finally, when sufficient reverse field is applied (Figure 2.1(e)), both soft and hard spins align with the field.

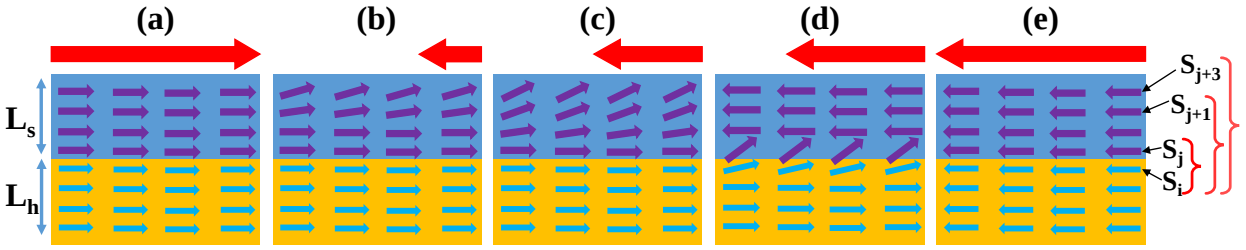


Figure 2.1: (a) Enough magnetic field applied to saturate the magnet (b) Demagnetization process starts when the magnetic field is applied in the reverse direction. (c)-(d) Demagnetization steps (e) Demagnetization complete. Here, the violet arrows denotes the magnetic moment for soft phase while that in the blue colour highlights the magnetic moments for hard phase. The rightward red arrow on top of the figure signifies that the magnetic field applied in the forward direction while that in the leftward direction indicates that the field is applied in the reverse direction.

Recalling the exchange interaction equation 1.5, where, $E_{ex} = -\Sigma_{i,j} J_{ij}(S_i \cdot S_j)$, and J_{ij} is the exchange integral between spins S_i and S_j. As illustrated in Figure 2.1, we note that S_i corresponds to the hard ferromagnetic spins, while $S_j/S_{j+1}/S_{j+3}$ belong to the soft ferromagnetic spins. The

interaction between S_i and S_j is much stronger than that between S_i and S_{j+1}, S_{j+2}, and so on, i.e., $J_{ij} > J_{ij+1} > J_{ij+2}$ and therefore, $E_{ex,ij} > E_{ex,ij+1} > E_{ex,ij+2}$. This means that the exchange interaction varies with the applied external magnetic field and depends on the relative positions of the spins in the respective layers. In such nano-heterostructured systems, the interface acts as a magnetic spring connecting the soft and hard layers through exchange interactions. Hence, these complex nano-heterostructured systems are called Exchange Spring systems by analogy with the elastic motion of a mechanical spring [26].

Zeng et al. explored exchange spring magnets in their work with nanocomposites fabricated using nanoparticle self-assembly, composed of magnetically hard and soft phases, exhibiting strong magnetic exchange coupling [77]. FePt-Fe_3O_4 (a magnetically hard phase) and Fe_3Pt (a soft phase) served as nanometre-scale building blocks in binary assemblies. Subsequent annealing transformed into $FePt - Fe_3Pt$ nanocomposites. By precisely manipulating the size and composition of the individual building blocks, they achieved an optimum exchange coupling, resulting an energy product of 20.1 MGOe, which exceeds the theoretical limit of 13 MGOe for non-exchange-coupled isotropic FePt by over 50%. Therefore, such systems are promising for advanced permanent magnetic applications. Low-dimensional magnetic heterostructures, fundamental in spintronics, were defined by the magnetic interactions between different materials, which induced magnetic order through proximity effects [101]. This resulted in exchange spring magnet behaviour and exchange bias, with long-range interactions playing a crucial role [102]. Direct exchange coupling via proximity-induced magnetization through non-magnetic layers had often been overlooked due to the presumed short range of these effects. However, it was found that magnetic order could be induced throughout a 40 nm thick amorphous paramagnetic layer via proximity to ferromagnets, mediating both exchange spring magnet behaviour and exchange bias. Long-range interactions were necessary to account for the induced magnetization. Monte Carlo simulations demonstrated that nearest-neighbour magnetic interactions were inadequate to explain the observed effects, emphasizing the significance of considering interaction range in low-dimensional heterostructures and the potential new functionalities offered by magnetic proximity effects.

Brillouin light scattering was used to observe the evolution of spin waves in exchange-coupled [Co/Pd]-NiFe films exhibiting out-of-plane/in-plane magnetic anisotropy [103]. The ability to tune the magnetization tilt had significant impacts on the spin wave frequency gap: a notable increase occurred with a reduction in the soft NiFe layer thickness, whereas even minor tilting angles resulted in a substantial reduction compared to films containing only the hard [Co/Pd] component. The spin wave frequency was also replicated in samples with thicker upper Pd layers, where the weakening of interlayer exchange caused a sudden change in tilting at the hard/soft

interface.

Exchange spring magnets, composed of a [Co(0.5 nm)/Pd(1 nm)]5 multilayer with perpendicular magnetic anisotropy and a $Co_{20}Fe_{60}B_{20}$ film with easy-plane anisotropy of varying thickness t_{CFB}, were investigated using Brillouin light scattering [104]. When t_{CFB} was reduced in the range of $0.8-2.3$ nm, the spin-wave frequency gap significantly increased from nearly 448 GHz, reflecting the rapid increase in the tilting angle of the magnetization relative to the film normal. These results were explained using a one-dimensional model where each atomic layer was assumed to be uniformly magnetized, subjected to an effective out-of-plane or easy-plane anisotropy based on its position in the stack, and exchange-coupled to its two nearest neighbour atomic layers. Compared to previously studied [Co/Pd]-NiFe hybrid magnets, a greater frequency tuneability was observed, albeit restricted to a narrower range of soft layer thicknesses.

Spin waves in Permalloy ($Ni_{80}Fe_{20}$)/Cobalt (Co) exchange spring bilayer thin films were also studied using Brillouin light scattering (BLS) experiments [105]. Magnetic hysteresis loops measured by the magneto-optical Kerr effect showed a monotonic decrease in coercivity with increasing Py thickness. The BLS study revealed two distinct modes, modelled as Damon-Eshbach and perpendicular standing wave modes. The linewidths of the frequency peaks increased significantly with decreasing Py layer thickness. Interfacial roughness caused fluctuations in exchange coupling at the nanoscale, with a more pronounced effect in thinner Py films. Quantitative analysis of the magnon linewidths indicated the presence of a strong local exchange coupling field, much larger than the macroscopic exchange field.

In their study, McNulty et al. investigated twisted magnetization phases, which they identify as exchange springs, in NdN/GdN superlattices and compared them to SmN/GdN interfaces [106]. NdN exhibits complex magnetic behaviour due to orbital dominant ferromagnetism, resulting in a large net magnetic moment. They further explored how temperatures and magnetic fields affect the twisted magnetization those semiconductor structures. Notably, the findings suggest that tunable twisted magnetization in ferromagnetic semiconductors could impact spintronics devices, potentially advancing tunneling magnetoresistance and other applications.

To date, the ES system has not been reported in an in-situ single nano-heterostructured (NHS) thin film prepared through the electrodeposition technique and characterized through dynamic measurements. It is worth noting that *ex situ* refers to bi/tri-layer structures prepared with multiple sources of materials (such as multiple targets in sputtering techniques), while *in situ* signifies that a single source of materials (in an electroplating bath) is sufficient to prepare bi/tri-layer nano-heterostructures. For instance, SmCo/Fe or NiFe/[Co/Pt] ES structures have been prepared using two different sputtering targets. However, in this reported work, the NHSs were prepared from a single bath, without requiring a second bath in the electrodeposition process to generate the

bi-layer structures. The electroplating technique was chosen to fabricate ES NHS due to its low cost and high yield, accommodating complex nano-topologies [11, 53]. Additionally, as discussed in the previous section 2.4.1, although thin films of cobalt phosphorous alloys (CoP) have been prepared by electrodeposition and extensively studied by several groups [46, 55–57, 80, 81, 84, 107, 108], the emergence of ES magnetic structures in in-situ amorphous and nanocrystalline CoP films as a result of self-organized processes from a single bath electrochemical deposition technique has not been identified, studied, or reported yet [2].

Furthermore, the exchange spring nano-heterostructures discussed here were mainly based on in-plane magnetic anisotropy. Over the past three decades, exchange spring magnets have been studied through static magnetic measurements, with very few attempts to study them dynamically [73, 105]. The out-of-plane exchange springs remain relatively unexplored [27, 109]. Microwave and heat-assisted magnetic recordings have greatly increased the capacity of hard disk drives. By employing non-collinear spin structures, which combine perpendicular and in-plane magnetic anisotropy, the efficiency of the magnetic recording process can be further improved. Recently, in [Co/Pt]/NiFe out-of-plane exchange spring samples, Dąbrowski et al. investigated both microwave and optically excited magnetization dynamics [110]. For an extended magnetic field and frequency range, the resulting canted magnetization within the nanoscale [Co/Pt]/NiFe interfacial region allowed for optically stimulated magnetization precession to be observed. The results can be explained by the formation of an imprinted domain structure, which locks the magnetization orientation and makes the structures more robust against external perturbations. Tuning the canted interfacial domain structure may provide greater control of optically excited magnetization reversal and optically generated spin currents, which are crucial for future ultrafast magnetic recording and spintronic applications.

Though the pulse reverse (PR) electroplating process is not new, in 2019, Mallick et al. explored a new technique to develop permanent magnets for magnetic MEMS applications [111]. They used a combination of forward and reverse pulses with optimized duty cycles during deposition and suitable bath chemistry, significantly reducing film stress, resulting in smooth, crack-free films up to 26 μm thick. The $\sim 3\mu$m thick deposited film showed a coercivity of 268 kA/m, a remanence of 0.4 T, and a maximum energy product (BH_{max}) of 35 kJ/m^3 in the out-of-plane direction. They proposed that a block of permanent magnet could be replaced by a micro-patterned array of magnets, maintaining the same total volume, which diminishes the demagnetizing field and enhances the magnetic stray fields.

Previously, electroplated inductors have been developed with multi-nano-layered structures in CoP thin film, where phosphorous (P) was added to increase the resistivity and simultaneously achieve the amorphousness in the material for integrated circuits [54]. Relatively, thicker nano-

structured high-frequency magnetic materials to achieve high power densities are of paramount importance for use in cutting-edge applications. Additionally, utilizing the electrodeposition technique to develop such films is of great importance as it is a low-cost, high-yield process and lends itself to patterned complex nano-topologies [53]. Though thin films of Cobalt Phosphorus alloys (CoP) have been prepared by electrodeposition technique, and have been extensively studied by several groups [2, 46, 55–57, 80, 81, 84, 107, 108], and their dynamic properties have been reported [2, 46, 57, 107]; however, the ultrafast dynamic properties of CoP thin film have never been reported so far. Addressing those aforementioned challenges and enhancing the performance of high-frequency integrated inductors, power delivery systems, energy-efficient switching of MRAM bits, and future high-speed spin-based devices, it is essential to study the ultrafast dynamics of magnetic materials, including their response to external stimuli and the relaxation processes of the magnetization, which provide significant insight about their performance at high frequencies.

2.4.3 Ultrafast Spin Dynamics

In 1998, Hübner and Zhang dived deeper into the fascinating world of ultrafast spin dynamics in nickel following these steps spin relaxation, exchange interaction, spin-orbit coupling, and theoretical modelling [112]. When nickel absorbs light, its electrons get excited to higher energy states. The subsequent relaxation involves the electrons releasing energy and returning to their original states. In nickel, this process occurs at an astonishingly fast timescale—within femtoseconds (10^{-15} seconds). Understanding this rapid spin relaxation is crucial for applications like magneto-optical recording. In ferromagnetic materials, neighbouring electrons interact through exchange interactions [113]. These interactions influence the alignment of electron spins, affecting the overall magnetic behaviour. In nickel, the exchange interaction plays a pivotal role in determining how quickly the spins relax after excitation. Spin-orbit coupling couples the electron's spin with its orbital motion due to relativistic effects. In nickel, this coupling affects the spin dynamics, leading to intricate interactions between the spin and the lattice. These interactions can be probed experimentally using techniques like time-resolved magneto-optical spectroscopy. Researchers used theoretical models to describe these processes. The exact diagonalization method, which avoids perturbation theory, provides a more accurate representation of strong electron correlations. By considering both intrinsic factors (like Coulomb interaction and band structure) and extrinsic factors (such as laser pulse duration), scientists gain insights into the ultrafast spin behaviour. In short, nickel's ultrafast spin dynamics hold promise for next-generation information storage technologies. By unravelling the mysteries of these rapid processes, they provided insights for

innovative applications in magneto-optics and beyond [32]. The femtosecond laser pulse can induce a transient temperature rise in the magnetic material. TRMOKE measurements can be used to investigate the impact of these thermal effects on magnon behaviour. For instance, thermal effects can lead to changes in magnon frequency and damping due to thermally excited spin fluctuations. Understanding these thermal effects is crucial for developing MMAs that operate reliably under varying temperature conditions, especially when considering potential integration with other heat-generating electronic components.

Malinowski et al. explored the rapid reduction of magnetization in nickel thin films following femtosecond-laser excitation [114], a phenomenon first discovered in 1996 [32]. This study has significant implications for spintronics and the understanding of magnetization dynamics in non-equilibrium states. The research elucidated how the direct transfer of spin angular momentum influences the speed and efficiency of ultrafast demagnetization in ferromagnetic materials. By employing specially engineered Co/Pt multilayers, the researchers aimed to facilitate this transfer and accelerate the demagnetization process. Utilizing the time-resolved magneto-optical Kerr effect (TRMOKE), they observed the demagnetization dynamics and analyzed the TRMOKE hysteresis loops to determine the contributions from different multilayers. Key findings from the study include a reduction in demagnetization time by up to 25% due to interlayer transfer of spin angular momentum in [Co/Pt] multilayers, effectively bypassing angular momentum conservation constraints in single ferromagnetic layers. Additionally, the total demagnetization increased by almost the same amount, indicating a more efficient process. These results suggest new pathways for enhancing ultrafast demagnetization speed and efficiency, which could be leveraged in designing advanced spintronic devices. Controlling these dynamics at sub-picosecond timescales holds promise for significant advancements in data storage and magnetic switching technologies.

As in the relatively lower frequency (sub-MHz—MHz level), the operational frequency is not only limited by the eddy current losses or losses due to the domain wall (DW) movement/rotation but also by spin losses and a decrease of the permeability, as we reach higher frequencies, such as GHz level. Additionally, any inhomogeneities of the magnetic ordering present in the material can result in the coexistence of the different dynamical processes, such as DW assisted dynamical responses and ferromagnetic resonance (FMR) assisted dynamical responses, independent of the orientation of the driving field. Moreover, from practical device applications point of view, study of the lifetime of the spin wave modes is also crucial because the presence of the eddy currents not only restrict the lifetime of the wave but also significantly alter its effective dispersion relation. Hence, to identify the exact nature of the dynamical processes for such highly miniaturized devices operating at ultra-high frequencies, one needs to understand comprehensively the high-frequency dynamics for accurate evaluation of the spin losses of the system as well.

Therefore, by understanding the ultrafast dynamics of magnetic materials, one can gain insights into the underlying mechanisms that affect their behaviour in high-frequency regimes, which can be leveraged to optimize the design and performance of emerging technologies. For example, studying the spin dynamics and relaxation processes at ultrafast timescales can provide information on the behaviour of magnetic materials under rapid switching or dynamic conditions, which are prevalent in high-frequency operation. Such understanding can guide the selection of magnetic materials with properties such as high saturation magnetization, low coercive field, and moderate anisotropy field and steer the engineering design for follow on highly miniaturized device topologies, which are desirable for minimizing losses at and achieving efficient performances at relatively higher operational frequencies [3].

2.5 Magnon Microwave Antenna

The emergence of the Internet of Things (IoT) devices develops a great interest in microwave-based technologies [115], particularly in applications such as autonomous driverless/autopilot cars, efficient radars/antennae, and various other advanced communication systems. These applications rely heavily on the generation of microwave frequencies with relatively lower power consumption, strong signal amplitude, and good frequency stability. These high-end features become the prerequisites for these advanced systems to perform necessary operations smoothly and reliably. However, conventional voltage-controlled oscillators (VCOs) typically consume a large amount of power to perform the required operations [116].

Previously, spin torque oscillators (STOs) have been investigated as a source of microwaves. STOs are, in general, highly tunable and offer a small chip size compared to existing VCOs [117]. Despite these advantages, STOs suffer from weak output signals, which significantly hinder their practical application in IoT devices. To circumvent this issue, researchers have studied arrays of synchronized phase-locking STOs, which aim to amplify the overall output signal strength. Additionally, the synchronization time of such phase-locking STOs is extremely short, which is beneficial for quick response times. However, in practical applications, the synchronization of the STOs itself becomes one of the biggest challenges. Achieving and maintaining precise synchronization among multiple STOs is complex and often unreliable, thereby limiting their utilization for cutting-edge IoT applications. Moreover, the operation of STOs typically requires some form of external bias, such as an electric or magnetic field, to control their functionality [15]. This requirement adds another layer of complexity and potential power consumption, further complicating their integration into low-power IoT systems.

Conventionally, electromagnetic antennas typically operated by driving an alternating current

or electromagnetic wave through a metallic or non-metallic element, causing it to emit electromagnetic waves of the same frequency. However, a significant limitation arose when the antenna's physical dimensions were much smaller than the emitted wavelength, leading to poor radiation efficiency and gain. When the antenna impedance did not surpass that of free space (377 Ω), the radiation efficiency was approximately limited to $\approx A/\lambda^2$ (with A being the antenna's emitting area and λ the emitted wavelength), and the gain was similarly restricted. This challenge made miniaturizing antennas without compromising performance quite difficult.

Recently, advancements were made with a novel magneto-elastic antenna, which transcended these traditional efficiency limits. This antenna design comprised elliptical magnetostrictive nanomagnets attached to a piezoelectric substrate. A low-frequency acoustic wave (144 MHz) in the substrate periodically strained the nanomagnets, causing their magnetizations to oscillate due to the inverse magnetostriction (Villari) effect. Consequently, these time-varying magnetizations emitted electromagnetic waves at the excitation frequency of 144 MHz (λ = 2 m) with efficiency surpassing the A/λ^2 limit by more than five orders of magnitude. However, this high efficiency was limited to low frequencies (below 1 GHz) as the Villari effect could not produce magnetization oscillations with sub-nanosecond periods.

In their work, Fabiha et al. used tripartite coupling between phonon-magnon-photon to demonstrate spin-wave an electromagnetic antenna based nano-antenna [20], capable of efficiently radiating at higher frequencies (5−35 GHz). This antenna operated by using a surface acoustic wave (SAW) in the GHz range to generate confined spin waves in nanomagnets via phonon-magnon coupling. The induced spin waves then interacted with electromagnetic radiative modes through magnon-photon coupling, resulting in the emission of electromagnetic waves. The study indicated that those ultra-miniaturized antennas exhibited high radiation efficiency and gain, exceeding traditional theoretical limits by more than two orders of magnitude at specific frequencies (5 and 14 GHz). This high performance was attributed to effective energy transfer from a microwave source to the SAW, due to good impedance matching, and the efficient excitation of high amplitude spin waves in the nanomagnets through phonon-magnon coupling. Micromagnetic simulations corroborated that high amplitude spin waves were indeed generated by SAWs at these frequencies, providing detailed power and phase profiles that revealed complex spatial variations.

2.6 Conclusion

This chapter has reviewed the existing literature on nanostructured magnetic materials, spin waves (magnons), and their application in magnon-based microwave antennas (MMAs). The crucial role of nanostructured materials in tailoring magnetic properties for efficient magnon generation

and propagation has been highlighted. Characterization techniques like BLS and TR-MOKE have been discussed, emphasizing their importance in understanding magnon dynamics. Finally, the potential advantages and challenges associated with MMAs have been explored. As research progresses in overcoming these challenges, MMAs hold great promise for miniaturized and integrated spintronic devices, paving the way for advancements in information processing and communication technologies. MMAs represent a promising avenue for future spintronics research, with the potential to revolutionize miniaturized wireless communication and on-chip signal transmission.

3 Theoretical and Experimental Techniques

3.1 Introduction

As already discussed, we fabricated the cobalt phosphorous (CoP) thin film [1, 2] alloys using conventional electrodeposition techniques and studied its structural, static [1, 2] and dynamic [2, 3] magnetic properties, while the magnonic device introduced in this PhD thesis is a magnon microwave antenna (MMA) [4, 5] consisting with patterned magnetostrictive material on the piezoelectric (PE) substrate and subsequently it proposed how such MMA could be utilized for magnon based on-chip reservoir computing [5]. This chapter first provides an overview of the required theoretical techniques and then of the experimental procedures and the involved characterization methods regarding the associated works of the PhD thesis.

3.2 Structural Design using COMSOL Multiphysics

In this section, the technique associated with the surface acoustic wave (SAW) based simulations of MMA using COMSOL Multiphysics [118] is discussed. COMSOL Multiphysics, a finite element method (FEM) based tool, stands as a cornerstone in this doctoral thesis. It facilitates in exploration the intricate physical phenomena governing various engineering systems by designing and subsequently simulating the initial device structure, aiming to unravel fundamental insights. A typical design of interdigitated transducer (IDT) electrodes on the piezoelectric substrate with COMSOL to generate the required SAW is shown in Figure 3.1. There are several modules available in COMSOL which helps to understand complex phenomena, e.g., electrical, magnetic, radio frequency (RF), mechanical, thermal, acoustic and chemical properties etc. However, in this

PhD thesis, we have utilized the AC/DC and MEMS modules. Therefore, the following sections discuss their requirement and the importance of them.

3.2.1 Utilization of AC/DC Module

In this PhD thesis, the AC/DC module within COMSOL Multiphysics played a pivotal role in analysing electromagnetic fields and their interactions with surrounding media. This module delves into the intricate dynamics governing the magnon microwave antenna (MMA) design, particularly focusing on the phonon-magnon coupling phenomenon. By employing the AC/DC module, the electromagnetic behaviour of the MMA could be simulated and analysed, considering factors such as electrode configurations and substrate materials. This enabled to predict and optimize crucial parameters like the surface acoustic wave (SAW) resonance frequency, a fundamental aspect of the functionality of the MMA. Additionally, the AC/DC module facilitated the estimation of reflection coefficients, providing insights into the power coupled to the SAW and the subsequent

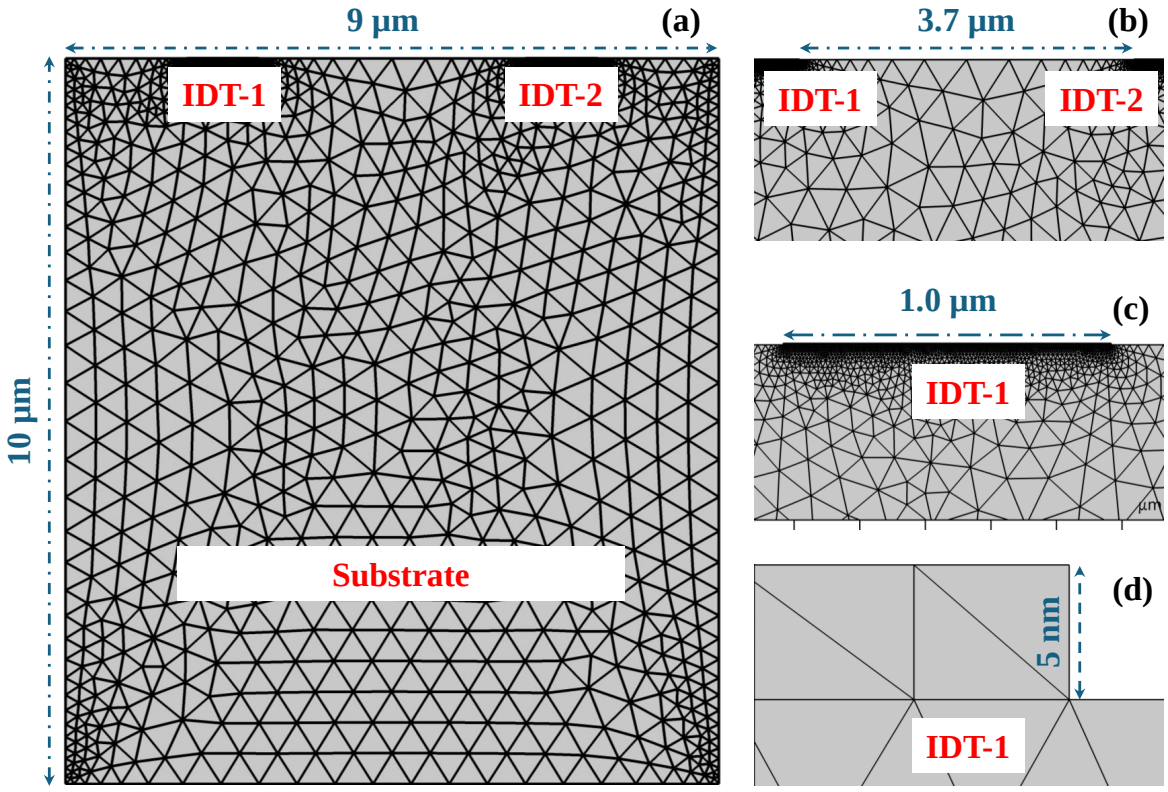


Figure 3.1: IDTs made with Aluminium (Al) on Substrate in COMSOL Geometry design with Mesh for generating SAW to operate MMA. (a) Required 10 μm thick $LiNbO_3$ substrate with width 9 μm having IDT structure on it. (b) Magnified region of (a) illustrates the separation between two IDTs. Both the IDTs have similar structure having width 1 μm and thickness 5 nm as exhibited in (c) and (d), respectively.

stress generated on the substrate. These analyses underscored the significance of electromagnetic considerations in the design and operation of the device, highlighting the indispensable role of the AC/DC module within COMSOL Multiphysics.

3.2.2 Integration of MEMS Module

In conjunction with the AC/DC module, the MEMS module within COMSOL Multiphysics offered to explore the intricate dynamics of the MMA, focusing on its mechanical response to surface acoustic waves (SAWs). By integrating the MEMS module, the stress profile induced by the SAW on the substrate could be simulated, providing crucial insights into the mechanical behaviour of the device. This analysis informed the design of the MMA, ensuring that nanowire dimensions were optimized to effectively transfer strain from the SAW to the magnetostrictive nanowires. Furthermore, the seamless integration of the MEMS module with other functionalities of COMSOL Multiphysics facilitated a holistic approach to the dissertation, enabling us to explore the interdisciplinary phenomena governing the operation of the MMA. This interdisciplinary perspective underscored the importance of MEMS considerations in the design and optimization of our device, highlighting the indispensable role of the MEMS module within COMSOL Multiphysics. A typical COMSOL simulation shows that we can generate a frequency range of ∼550 MHz with $LiNbO_3$ substrate to ∼625 MHz with AlN substrate, as shown in Figure 3.2(a) and (b), respectively.

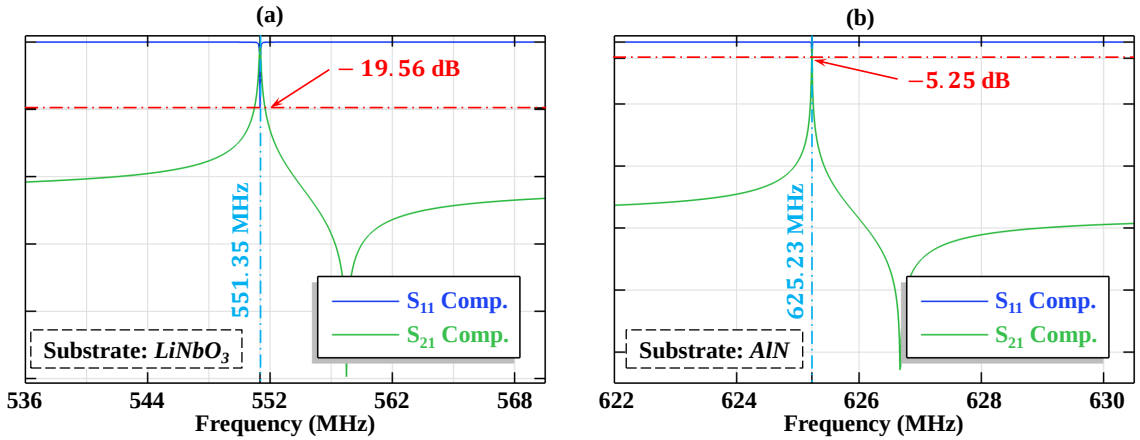


Figure 3.2: The S_{11} and S_{21} parameters estimate the SAW (surface acoustic wave) frequency as (a) ∼ 551 GHz (with $LiNbO_3$ substrate) and (b) ∼ 625 GHz generated in the MMA designed (with AlN substrate).

Thus, the utilization of COMSOL Multiphysics, particularly the AC/DC and MEMS modules, served as a cornerstone in modelling, simulating, and analysing the MMA. Apart from these, COMSOL Multiphysics could be leveraged for a comprehensive platform for modelling and

simulating the mechanical, thermal, and electrical behaviour of microelectromechanical systems (MEMS). These computational tools not only facilitated a deeper understanding of underlying physical phenomena but also paved the way for innovative solutions and methodologies. However, COMSOL Multiphysics alone cannot perform the required dynamic magnonic response of the MMA. Therefore, micromagnetic simulations are required to be performed, which generates the necessary magnetization response and associated modulation of the magnetic domain structures.

3.3 Micromagnetic Simulation with MuMax^3

In this section, the micromagnetic simulations technique using MuMax^3 [24] software has been discussed. MuMax^3 is an open-source GPU accelerated Finite difference Method (FDM) based software and has been developed at Ghent University, Belgium. Considering the magnetization as uniform throughout the sample, the micromagnetic simulations have been performed to simulate/reproduce the experimental results such as the static curves (hysteresis loops, i.e., magnetization vs. applied magnetic field curve), the dynamic curves (magnetization oscillation vs. simulation time curve) and the magnetic domain structures etc. The time range in the dynamic simulations are generally in nanosecond (ns) order. In the process of obtaining the magnetization dynamics, MuMax^3 solves the well known Landau-Lifshitz-Gilbert (LLG) equations as already mentioned in equation 1.1 and 1.2 in Chapter 1. Let us recall the equations here again for the continuation, as given in equation 3.1 and 3.2:

$$\frac{\partial \vec{M}}{\partial t} = |\gamma| \vec{M} \times H_{\text{eff}} + \frac{\alpha}{M_S} \left[\vec{M} \times \frac{\partial \vec{M}}{\partial t} \right] \tag{3.1}$$

$$H_{\text{eff}} = -\frac{1}{\mu_0} \cdot \left[\frac{\partial E}{\partial \vec{M}} \right] \tag{3.2}$$

where, $\vec{m}$ is the unit vector of local magnetization, $\gamma_0 = \mu_0 |\gamma|$, γ - gyromagnetic ratio (GHz/T), $\vec{H}_{\text{eff}}$ is the effective magnetic field originates from demagnetization energy, exchange energy, magnetic and shape anisotropy, α is the Gilbert damping factor, μ_0 is the free space permeability, M_S is the saturation magnetization (A/m).

To reproduce the experimental results by performing micromagnetic simulation, the following typical material parameters for the ferromagnetic material: Saturation Magnetization (M_S) [in A/m units], Exchange Stiffness constant (A_{ex}) (in J/m unit), Anisotropy Constant (K_{u1}) (in J/m^3 unit) are assumed. Depending upon the nature of the anisotropy (in-plane or out-of-plane to the axis), K_{u1} is often illustrated as $anisU$ in the simulation, e.g., $anisU$ is defined as $< 100 >$ direction for

IP anisotropy or $< 001 >$ direction for OOP anisotropy. In each of the micromagnetic simulations, the cell size for the simulation is $c_x \times c_y \times c_z$ considered in such way that $c_x/c_y/c_z$ is smaller than the exchange length $\left(l_{ex} = \sqrt{\frac{2A_{ex}}{\mu_0 {M_S}^2}}\right)$ of the material [119], which confirms the inclusion of all the magnetic exchange interaction properly. Here, c_x, c_y, c_z represent the length, width and thickness of the material, respectively. It is noted that the cell geometries are in rectangular/cubic in nature.

The magnetic behaviour of a double-layer/nanoheterostructured exchange spring structure composed of two different magnetic materials could be simulated utilizing MuMax^3. In order to obtain the staircase like hysteresis loop, the simulation typically performs static simulations over a field range from $+B_{ext}$ to $-B_{ext}$ (e.g., $B_{ext} = \pm 50000$ Oe). In the script, we can define two different regions within the shell: Region 1 for Material A and Region 2 for Material B along the z-direction. Individual magnetic material parameters for each region are required to assign. For instance, for Material A, these parameters include saturation magnetization (`M_SA`), uniaxial anisotropy constant (`K_U1A`), anisotropy direction (`vec_A`), and exchange stiffness (`A_exA`). For Material B, it sets similar parameters: `M_SB`, `K_U1B`, `vec_B`, and `A_exB`. The script specifies an interlayer exchange interaction between the two regions using the `ext_InterExchange` function and initializes the magnetization state randomly. It then relaxes the system to minimize high-energy states. The external magnetic field (`B_ext`) is varied from 0 to `B_sat` Oe in steps of `Bstep` (e.g., 50 Oe), first increasing and then decreasing to `-B_ext` and back to `+B_ext`. Note that, in MuMax^3, '+' symbol is not required to denote any positive number. In each step, the script sets the external magnetic field vector, minimizes the system's energy, and saves the resulting state to a table. This looping process captures the hysteresis behaviour of the double-layer exchange spring system under varying magnetic fields.

3.4 Electrodeposition

Electrochemistry involves the transfer of electrons in an electrochemical reduction, leading to a chemical change such as the oxidation or reduction of a metal complex. In this context, the anode [e.g., cobalt (Co)] usually undergoes oxidation to form ions (Co^{3+}) through heterogeneous electron transfer as shown in 4.1(a). This process is driven by applying a voltage to the counter electrode (anode) using an external power source, specifically the CHI 660B potentiostat in this case. The applied voltage creates an energy difference for the electrons. During oxidation, Co loses electrons as the electrons in its lowest unoccupied molecular orbital (LUMO) are at a higher energy level compared to the surrounding solution, referred to as the bath. Consequently, electrons from Co are transferred to the bath, leading to oxidation in the bath, as illustrated in top row (i) of Figure 4.1 (a). The driving force for this electrochemical reaction is the energy difference between

the LUMO of Co^{2+} and the bath. Conversely, a similar principle applies to the reduction process of reduced phosphorus (P), where electrons are gained instead of lost, also depicted in bottom row (ii) of the Figure 4.1(a). The detailed procedure for generating metallic phosphorus through this electrochemical reaction is elaborated in the Chapter 4. Thermodynamics of an electrochemical cell is determined by the following equations: $\Delta G = -nFE_{\text{Cell}}$ and $\Delta G = -RT\ln K$. Combining these two equations and using the concentrations rather than activities for the reversible reaction, $O^{n+} + ne^- \rightleftharpoons R$ gives,

$$E_e = E_e^\theta + \frac{RT}{nF}\ln\left(\frac{C_O^\infty}{C_R^\infty}\right) \tag{3.3}$$

This equation 3.3 is known as Nernst Equation, which controls the thermodynamics of electrochemical reactions. Cyclic voltammetry (CV) is an electrochemical technique that measures the current developed in an electrochemical cell when the voltage is cycled and exceeds that predicted by the Nernst equation. CV is performed by cycling the potential of a working electrode and measuring the resultant current, as described in the following Section 3.4.1. To study the electrochemistry, one needs a potentiostat. The following Figure 3.3 exhibits the detailed software interface with different option available with the CHI 660B Potentiostat. For instance,

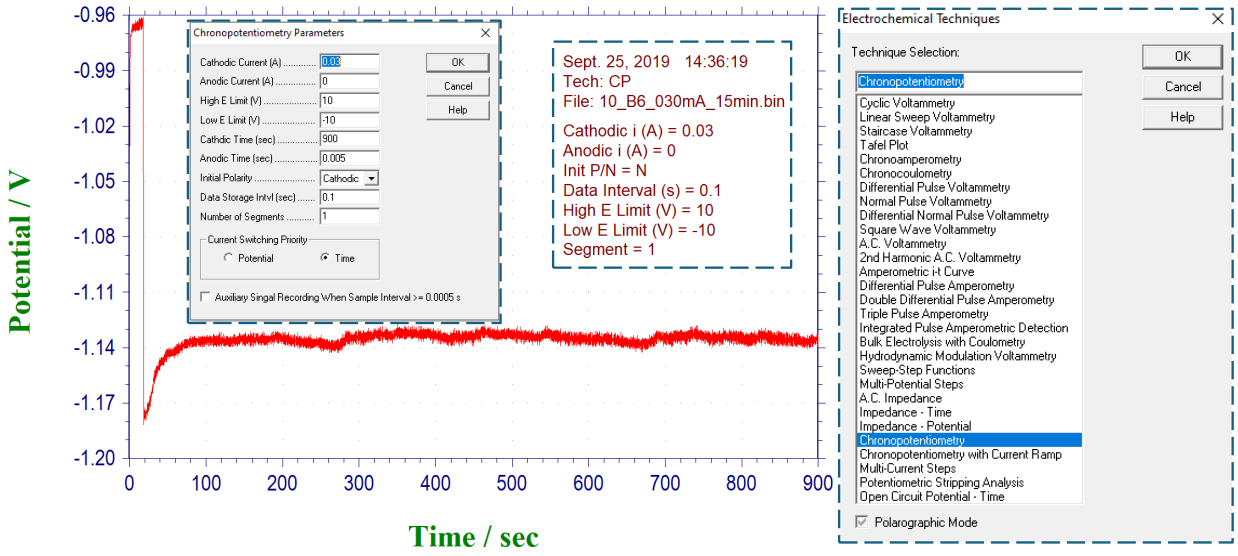


Figure 3.3: The software interface of CHI 660B potentiostat displaying different options: The right panel reveals all the possible available "Electrochemical Techniques" which could be performed with the CHI 660B potentiostat. Out of all those options, the "Chronopotentiometry" is highlighted as it was one of the selected techniques to utilize during one of the thin film fabrications. The left inset describes different "Chronopotentiometry Parameters" to perform the electrodeposition. The middle one is the confirmation panel after completing the electrodeposition.

the chosen "Electrochemical Technique" is "Chronopotentiometry" which helps in depositions required alloys on the conducting surface, while we could perform CV by selecting the option "Cyclic Voltammetry" (on the top).

The kinetics of electrochemical reactions can be controlled through several mechanisms. One primary method is electron transfer control, which directly influences the rate at which electrons are exchanged in the reaction. Another significant factor is mass transport control, which includes several sub-mechanisms such as diffusion and convection. Diffusion is driven by concentration gradients, while convection involves external mechanical forces. Convection can further be influenced by factors such as density gradients, gas bubbling, and temperature effects. These convection-related challenges can be mitigated through methods like forced convection, cathode movement (e.g., rotation), solution flow, and mechanical solution agitation. Additionally, the migration of charged particles in a potential gradient also plays a role in controlling electrochemical reaction kinetics. This migration issue can be mitigated by using a supporting electrolyte with a high ionic concentration, which helps stabilize the system and maintain consistent reaction kinetics. By understanding and manipulating these factors, one can effectively control the kinetics of electrochemical reactions.

3.4.1 Cyclic Voltammetry (CV)

Cyclic Voltammetry (CV) [120] is a fundamental electrochemical technique with extensive applications and significant importance across various scientific and industrial fields. One of its primary roles is in electrochemical characterization, where it is used to study the redox properties of compounds, identifying redox potentials and elucidating electron transfer processes. This technique provides critical insights into reaction mechanisms, including the number of electrons involved and the sequence of electron transfer steps. In material science, CV is essential for characterizing electrode materials, assessing their electrochemical stability, conductivity, and catalytic activity. It is particularly crucial in evaluating the electrochemical properties of nanomaterials, which have potential applications in sensors, batteries, and fuel cells. In sensor development, CV plays a key role in designing and optimizing both biosensors, which detect biological molecules like glucose and DNA, and chemical sensors, which detect environmental contaminants such as heavy metals and pollutants. CV is also vital in the fields of energy storage and conversion. It is extensively used to study the electrochemical performance of battery materials, understand charge-discharge mechanisms, and improve battery efficiency.

In fuel cell research, CV helps evaluate catalysts and understand the kinetics of fuel oxidation and oxygen reduction reactions. Additionally, CV is employed in corrosion studies to investigate

the behaviour of metals and alloys, aiding in the development of corrosion-resistant materials and coatings. In the pharmaceutical and biochemical industries, CV is used to analyse the electrochemical behaviour of pharmaceuticals, assisting in drug design and quality control. It also helps in understanding the electrochemical aspects of biochemical processes and the behaviour of biomolecules. In synthetic chemistry, CV is utilized to develop new synthetic pathways for organic and inorganic compounds and to study catalytic cycles, contributing to the development of efficient catalysts. Analytical chemistry benefits from capabilities of CV in quantitative analysis, providing sensitivity and specificity in detecting various substances. It is also effective in trace analysis, detecting minute amounts of analytes in complex matrices. In environmental science, CV is used for detecting and quantifying pollutants, contributing to environmental monitoring and protection. It is particularly valuable in assessing water quality by detecting contaminants like heavy metals and organic pollutants. In summary, Cyclic Voltammetry is a versatile and powerful tool in electrochemistry, offering valuable insights into a wide range of chemical, biological, and material systems. Its ability to elucidate fundamental electrochemical properties and mechanisms makes it indispensable in research, development, and quality control across multiple disciplines. Therefore, we have also performed the CV following the basic of the electrodeposition, as shown in the following Figure 4.1(b).

The schematic of a CV excitation signal is shown in the Figure 3.4. In cyclic voltammetry (CV), the potential is scanned in both negative and positive polarities between two extreme voltage points, labelled as (a) and (g). At point (a), the voltage is typically set higher than at point (g), which serves as the lower extreme. The transition point (d) between these two extremes is crucial as it marks the switching potential where either oxidation or reduction processes can occur,

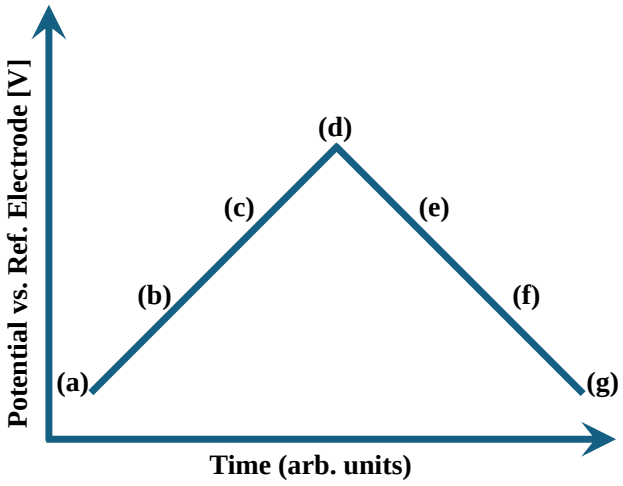


Figure 3.4: Schematic representation of the CV excitation signal.

depending on whether the potential is sufficiently high or low. During the scan from (a) to (d), reduction reactions generally occur, where substances gain electrons. Conversely, from (d) to (g), oxidation processes dominate, involving the loss of electrons. The scan rate used in CV determines the slope of the resulting voltammogram, influencing the speed at which potential changes occur and thereby affecting the observed electrochemical behaviour. Understanding these principles allows researchers to analyse and interpret the redox behaviour and kinetics of substances under study using cyclic voltammetry techniques.

During the potential scan by measuring the current at the working electrode, a cyclic voltammogram is obtained. The experimentally measured voltammogram in the electroplating laboratory is shown in the Figure 4.1(c), and explained in detail in Chapter 4.

3.5 Structural characterization

The structural characterization of developed materials are performed with Scanning Electron Microscopy (SEM), X-ray diffraction (XRD), Transmission Electron Microscopy (TEM), Atomic Force Microscopy (AFM), respectively, and Stoichiometry Analysis by Energy dispersive X-ray spectroscopy (EDS or EDX). The working principle of the instruments are described briefly below.

3.5.1 Scanning Electron Microscopy (SEM)

An image of three-dimensional objects can be interpreted by scanning a very narrow electron beam across the sample surface using a scanning electron microscopy (SEM). Electron column, vacuum system, scanning system, detector, and electronics controls are the main components of a typical SEM. Typically, an SEM includes electron optical column, Specimen chamber, EDS/EDX detector Gemini, Monitors, Personal computer (PC), etc.

The schematic of SEM in "analyser" is shown in the Figure 3.5. Most of the SEMs can generate an electron beam with spot size less than 10 nm with probe diameter in the range of 1 nm to 1 μm and probe current pA to μA. In order to obtain high resolution images, the probe diameter needs to be adjusted to the imaging scale of interest, in contrast to situations where only probe current and scan rate settings are modified. Being operated the SEM under high vacuum, the specimens should be compatible with high vacuum ($\sim 10^{-5}$ mbar). The SEM instrument cannot deal with the materials containing any liquids and other volatile components directly. Also for the powder samples, they need to be converted to hard pallet form. It is always very difficult to image those materials which are non-conductive in nature, do not allow electrons to flow freely, so when the electron beam hits the surface, the excess electrons cannot dissipate. This leads to a buildup

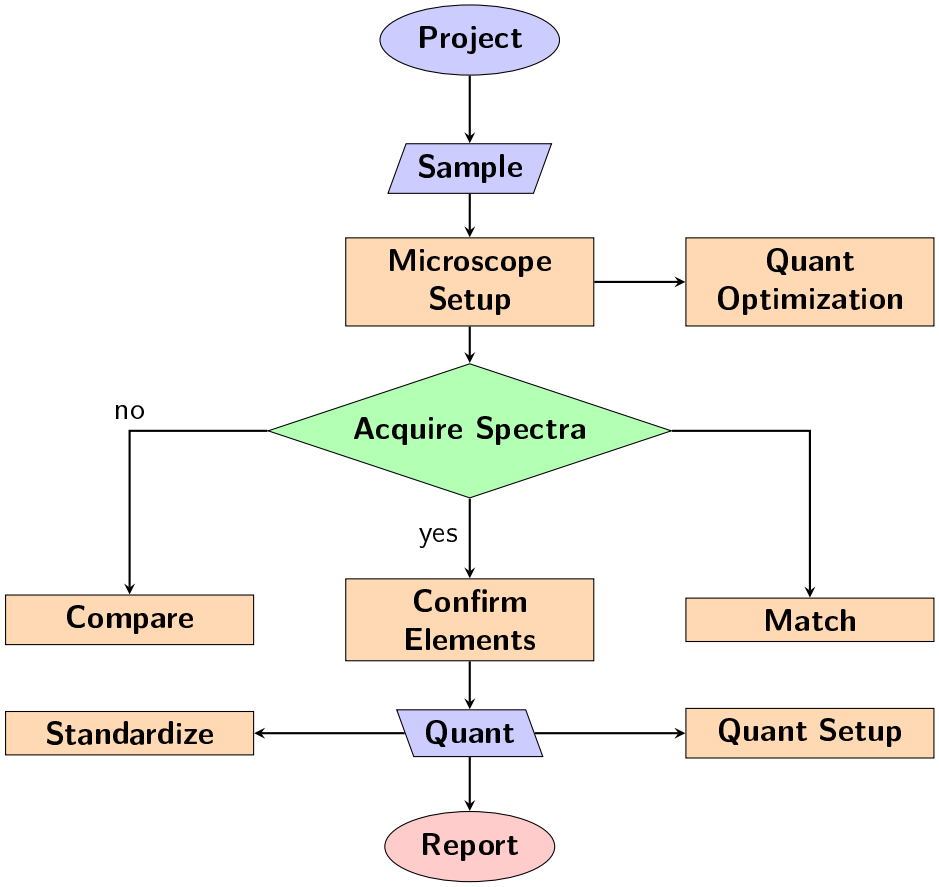


Figure 3.5: Schematic of SEM on analyser mode

of negative charge on the surface, causing image distortions, blurring, and bright spots.. Those non-conductive materials need to be attached to a conductive specimen holder (carbon substrate/ copper tape) or coated with a very thin conductive film by sputtering or evaporating metal (Au, Pt, Pd, their alloys) or carbon.

3.5.2 Stoichiometry Analysis

Energy dispersive X-ray spectroscopy (EDS or EDX) is commonly employed to determine the stoichiometry or elemental composition of materials. This method involves stimulating the sample to emit characteristic X-rays by directing an electron beam at it. The emitted X-rays indicate the elements present and their respective weight percentages. When a high-energy electron beam strikes the sample, it ejects inner shell electrons, creating vacancies. Outer shell electrons then transition to these lower energy levels, emitting X-rays with energy corresponding to the difference between the energy levels, denoted by principal quantum numbers (n=1, 2, 3, 4) as K, L,

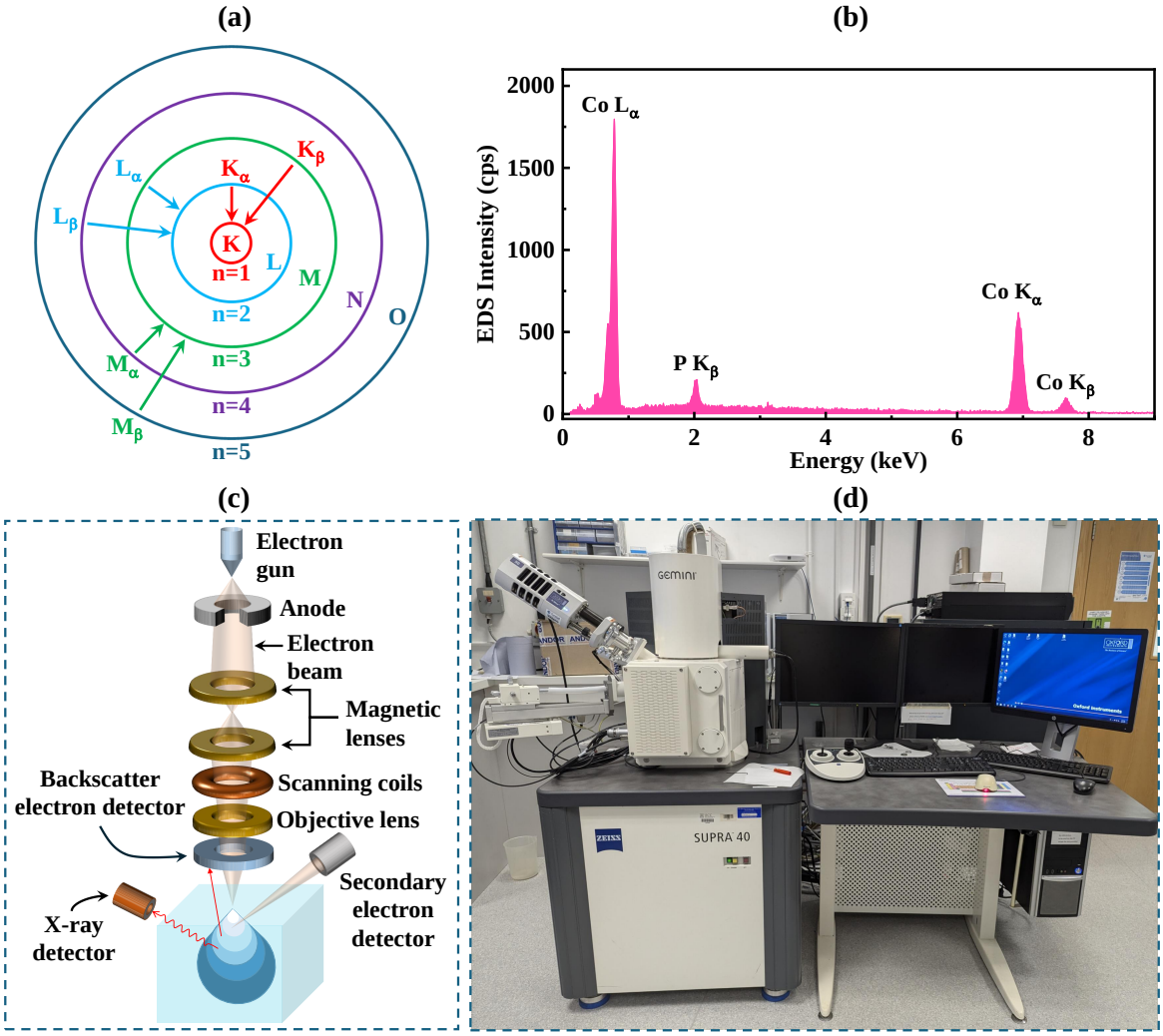


Figure 3.6: (a) Schematic showing electron transitions to lower atomic levels, illustrating the generation of K, L, and M lines. (b) A typical experimental EDX spectrum, displaying characteristic X-ray lines from various elements in the sample. (c) Schematic detailing the components of a scanning electron microscope (SEM). (d) EDX system attached to the Zeiss FE-SEM utilized for sample characterization at Tyndall National Institute.

M, and N, respectively. Figure 3.6(a) illustrates the generation of these characteristic X-rays. For instance, a transition from the L to K shell produces a K_α X-ray, while a transition from the M to K shell produces a K_β X-ray. Similarly, transitions from the M and N shells to the L shell generate L_α and L_β X-rays. Each element's unique atomic structure allows for identification by detecting these characteristic X-rays.

Figure 3.6(b) presents a typical EDS spectrum showing K_α, K_β, L_α and L_β peaks for elements like Co and P. The intensity of each peak depends on the likelihood of the specific electron transition, with L to K transitions being more probable than M to K transitions, resulting

in higher intensity K_α peaks compared to K_β peaks. The relative peak intensities provide the weight percentages of the elements, and atomic percentages are calculated based on the atomic weights. The setup for EDS measurements, shown in Figure 3.6(d), includes a Field Emission Scanning Electron Microscope (FESEM). This type of SEM uses a field emission gun, rather than thermionic excitation, to generate a finely focused electron beam, achieving a resolution better than 1.5 nm, suitable for observing surface morphology at the nanometre scale. Figure 3.6(c) shows a schematic of an SEM, with EDS being one component. To collect an EDS spectrum, a 20-25 kV electron beam is focused on the sample in a $\sim 10^{-5}$ mbar vacuum. A Silicon drift detector then captures the emitted characteristic X-rays from the sample, allowing for the calculation of the elemental composition based on the counts of each X-ray line.

3.5.3 X-ray diffraction (XRD)

X-ray diffraction (XRD) is a crucial non-destructive technique for analysing the crystalline structure of various materials. The Debye-Scherrer method is fundamental to the XRD technique. In this method, X-rays are directed at powdered or crystalline samples, which are positioned on the axis of a spectrometer. Scherrer equation is denoted as follows: $\tau = \frac{\kappa \cdot \Lambda}{\beta \cdot cos\,\theta}$, where τ is the mean grain size, κ is a numerical dimensionless factor frequently referred to as the crystallite-shape factor with a value close to unity (κ = 0.9 is a good approximation), Λ is the X-ray wavelength (1.54 Å), β is the line broadening at half the maximum intensity (FWHM) of the crystalline peak, and θ is the Bragg angle (in degrees). As the X-rays interact with the sample, they are diffracted by the crystal lattice planes in all possible orientations. The intensity of the diffracted X-rays is measured and recorded in three-dimensional reciprocal space. These intensities are then plotted against the rotation angles of the sample to produce a one-dimensional X-ray diffraction pattern. This pattern is characteristic of the material's crystal structure and can be used to identify and analyse the phases present within the sample.

The operation of an XRD instrument involves several key components and steps: 1. X-ray Source: X-rays are generated, typically using a cathode ray tube, and directed towards the sample. 2. Sample Holder: The sample, either in powder or crystalline form, is placed on a holder that can be rotated to various angles. 3. Goniometer: This device precisely controls the angle between the incident X-rays and the sample, allowing for accurate measurement of diffraction angles. 4. Detector: Positioned to detect the diffracted X-rays, the detector moves around the sample to capture diffraction data at various angles. As X-rays penetrate the sample, they are scattered by the electrons in the crystal lattice. Constructive interference occurs at specific angles, where the path difference between the scattered waves corresponds to integer multiples of the X-ray

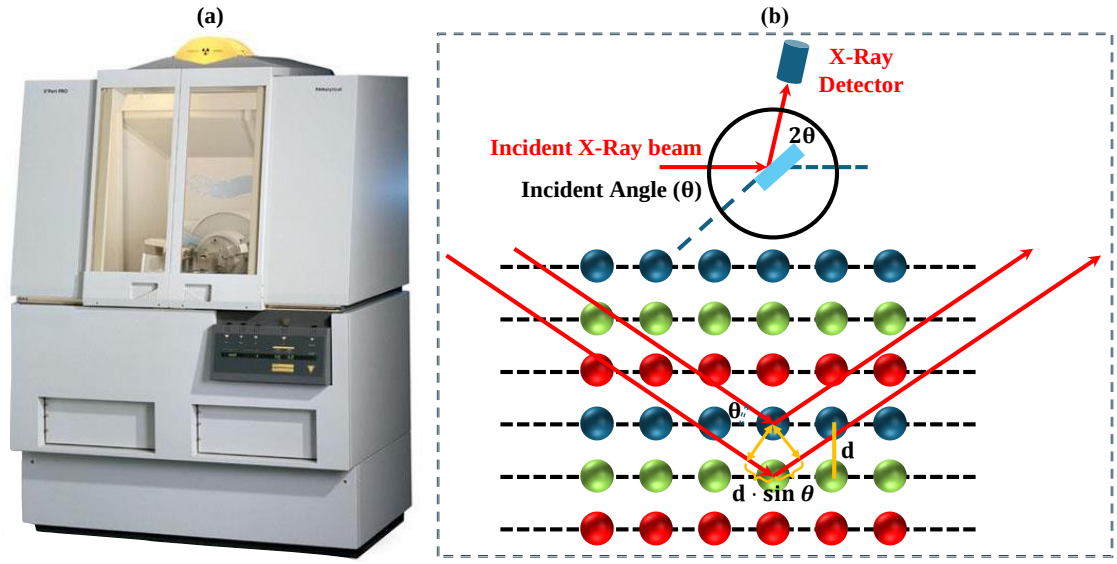


Figure 3.7: (a) Experimental setup of a PANalytical X'Pert Pro MPD X-ray diffractometer (XRD) in our lab at Tyndall National Institute. (b) Bragg's Law: Schematic illustration of the working principle of the XRD method.

wavelength, according to Bragg's Law [$n\lambda = 2d \cdot \sin\theta$]. This results in peaks of intensity at these angles, which are recorded by the detector.

The data collected by the detector are processed to generate the X-ray diffraction pattern. This pattern consists of a series of peaks corresponding to the different crystal planes in the sample. Each peak's position and intensity provide information about the crystal structure, including lattice parameters, phase identification, crystallite size, and the presence of any defects or strains in the material. The experimental setup of an XRD instrument is illustrated in Figure 3.7(a), showing the arrangement of the X-ray source, sample holder, goniometer, and detector. Figure 3.7(b) provides a schematic of the working principle, detailing how X-rays are diffracted by the crystal planes and detected to form the diffraction pattern. In summary, XRD is a powerful technique for elucidating the crystalline structure of materials, providing detailed information about their phase composition and structural properties through the analysis of their diffraction patterns.

3.5.4 Atomic Force Microscopy (AFM)

Surface characterization was performed using an Atomic Force Microscope (AFM), specifically the Bruker Dimension Icon model, as illustrated in Figure 3.8. The AFM provides detailed surface topography information, including film thickness and surface roughness. The AFM operates by scanning a probe over the sample surface to create a precise map of its topology. The AFM probe (Model no: RTESPA-300) is typically made from n-type antimony (Sb) doped silicon. This

specific probe features a cantilever with dimensions of 125 µm in length, 40 µm in width, and 3.4 µm in thickness. It oscillates at a frequency of 300 kHz and has a spring constant of 40 N/m. The RTESPA-300 probe is designed with a reflective aluminium coating on its backside to enhance the laser signal used in detecting cantilever deflections, while the front side remains uncoated. This precise construction allows for highly sensitive and accurate measurements of the sample surface characteristics, contributing significantly to the reliability of AFM analyses.

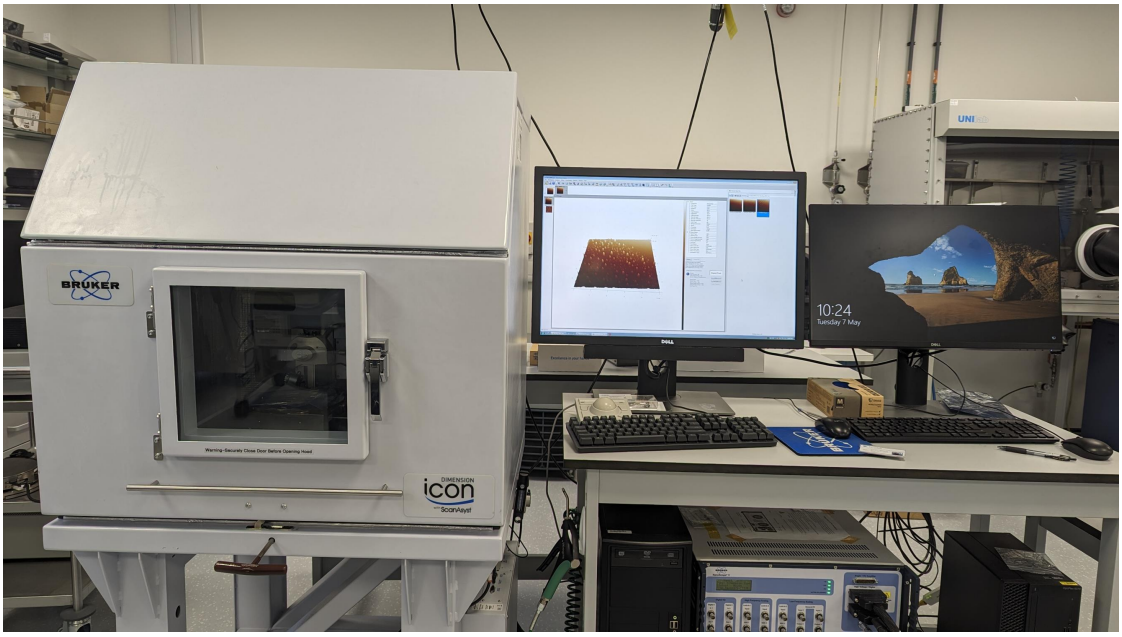


Figure 3.8: Experimental setup of AFM (Bruker) in our laboratory at Tyndall National Institute.

3.5.5 Transmission Electron Microscopy (TEM)

Transmission Electron Microscopy (TEM) is a powerful technique used to observe the fine details of the microstructure of a specimen at very high resolution. The operation of TEM involves several critical steps and components to achieve detailed imaging and analysis. Before a sample can be examined using TEM, it needs to be carefully prepared into a very thin lamella, typically less than 100 nanometres thick. The preparation process described involves the use of a DualBeam focused ion beam (FIB) system, specifically the FEI Helios NanoLab 600i [Figure 3.9(a)]. The steps are as follows: (1) Deposition of Protective Layers: A 50 nm carbon (C) layer and a 300 nm platinum (Pt) layer are deposited within the FIB chamber by electron beam induced deposition. This is followed a thicker 2 µm Pt layer is then deposited using ion beam induced deposition. These layers protect the sample from damage during the milling process. (2) Milling Process: The FIB system is used to precisely mill and shape the sample into a thin lamella suitable for

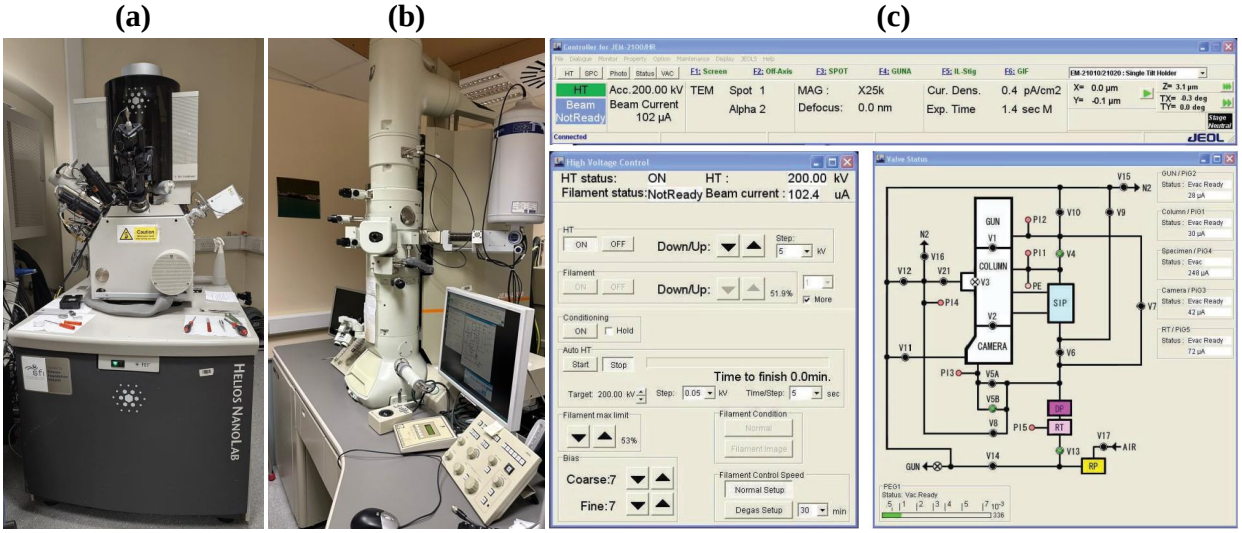


Figure 3.9: An experimental setup of (a) Helios NanoLab 660i FIB SEM, (b) Jeol 2100 high resolution transmission electron microscope (HR-TEM) in our laboratory in Tyndall National Institute. (b) Schematic of the HR-TEM: The top row is the controller of the TEM while bottom two snippets are for high voltage control and valve status of the TEM.

TEM analysis. Then, initial thinning is performed at 30 kV to achieve the desired thickness. Final polishing at 5 kV (with a current of 47 pA) is conducted to minimize ion-beam induced damage, reducing it to a layer less than 2 nm thick on both sides of the lamella.

Once the lamella is prepared, it is analysed using a High-Resolution Transmission Electron Microscope (HR-TEM), such as the Jeol 2100 [Figure 3.9(b)] operating at 200 kV with a double tilt sample holder. The TEM operation can be broken down into the following steps: Electrons are generated by an electron gun, typically a tungsten filament or a field emission gun, and accelerated to high energies. The high-energy electron beam is focused and directed towards the thin sample using a series of electromagnetic lenses. As the electron beam passes through the sample, electrons interact with the atoms in the material. Depending on the thickness and density of the sample, some electrons are transmitted, while others are scattered or absorbed. Transmitted electrons are collected and focused by additional electromagnetic lenses to form an image on a fluorescent screen, a CCD camera (Gatan Inc.), or a similar detector. The resulting image represents the electron density and provides detailed information about the sample's internal structure at the atomic or molecular scale. High-resolution images reveal the samples microstructure, including defects, grain boundaries, dislocations, and other features. Techniques like electron diffraction can be used to obtain crystallographic information, providing insight into the crystal structure and orientation.

The schematic of the TEM, shown in Figure 3.9, illustrates the main components and the path

of the electron beam through the microscope. This includes the electron gun, electromagnetic lenses, sample holder, and the imaging system. TEM is an invaluable tool in materials science, biology, and nanotechnology, which enables researchers to (a) visualize structures at the atomic level, (b) analyse the composition and phases of materials, (c) study the morphology and defects within materials, (d) conduct in situ experiments to observe changes in the microstructure under various conditions. In summary, TEM provides unparalleled insights into the microstructural characteristics of materials, making it essential for advanced research and development across multiple scientific disciplines.

3.6 Magnetic Property Characterization

Magnetic peroperties of the samples, for instance, the hysteresis loops of the materials are measured with ShB Hysteresis Loop Tracer and SQUID MPMS3 magnetometer (Quantum Design), first order reversal curve (FORC) distribution are measured with SQUID MPMS3 magnetometer, while the magnetic domains are characterized using magnetic force micrscopy (MFM) study.

3.6.1 ShB Hysteresis Loop Tracer

We have characterized the prepared samples in our magnetic characterization laboratory using an ShB instruments (Mesa 200HF) Magnetic Measurement System real time B-H loop tracer shown in the Figure 3.10(a) and schematic of ShB is shown in Figure 3.10(a). The mentioned instrument is a $B-H$ loop tracer (hence forth referred to simply as the ShB) which was initially used to characterise thin film samples. This instrument has the advantage of being a real time measurement at room temperature, allowing samples to be analysed quickly and inexpensively. All thin film samples could be analysed using this instrument.

We have diced the thin films to sample for a 2 cm $\times$ 2 cm size prior to analysis, as the SHB hysteresis loop tracer is calibrated for this size. This was done by dicing the substrate on a wafer dicing machine (DISCO DAD 2H/6T Dicer) prior to film deposition. The diced samples were then loaded onto the sample stage and inserted into the instrument. Various drive fields were applied to the samples with intensities of up to 1000 Oersted (Oe)/(0.1T) and the resulting magnetic induction (flux density) was measured.

3.6.2 SQUID Magnetometer for High-resolution Magnetic Measurement

The magnetic property characterization of the developed magnetic materials is performed in the Quantum Design (QD) *S*uperconducting *Q*uantum *I*nterference *D*evice (SQUID) magnetometer

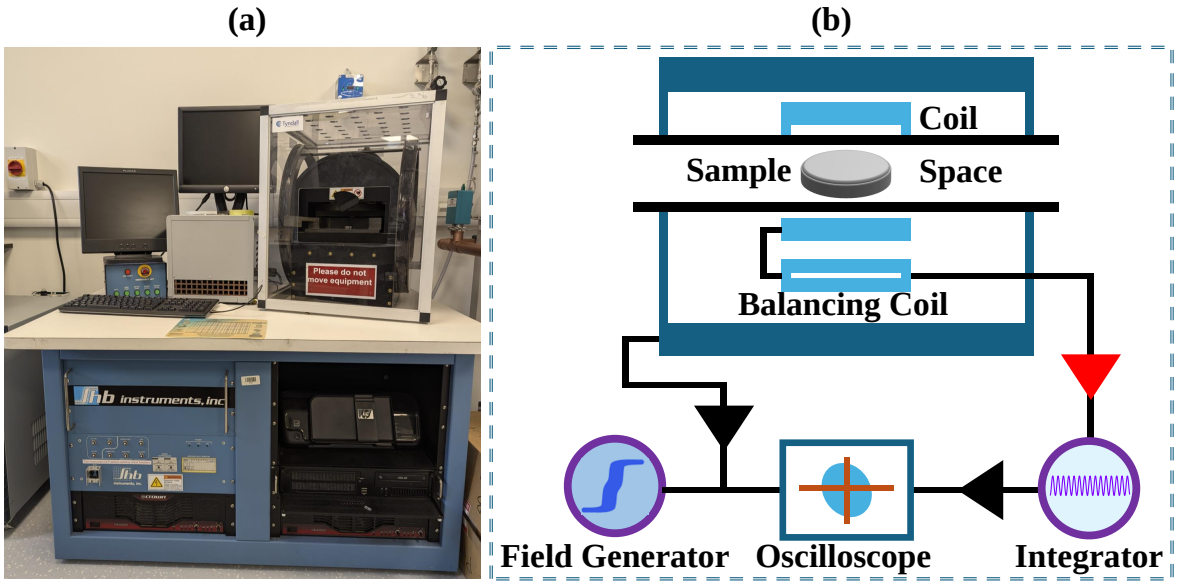


Figure 3.10: (a) Experimental setup of Mesa 200HF hysteresis loop tracer (ShB Instruments Inc.) in our laboratory (b) Schematic of hysteresis loop tracer (MESA 200 HF) by SHB Instruments Inc.

(field range: $\pm$7T and temperature range 1.8K$-$1000K using oven option) Magnetic Properties Measurements System (MPMS) (Model Number/Serial Number: MPMS3-349).

Figure 3.12 shows some snippets of "MultiVu" software exhibiting the procedure to measure magnetic moment of a sample at a specific temperature or magnetic field. The snippet shows that the measurement will be performed using emu units. A measurement could be started by clicking the "Measure" toolbar button or choosing the menu tiem from **Measure>Measure**, as highlighted in the figure, which opens the MPMS3 Measurement window. Following this, by choosing the required option, i.e., VSM/DC mode, the measurement could be done.

Figure 3.13(a) illustrates a simplified schematic of the SQUID MPMS3 detection hardware. The superconducting detection coils are arranged as a second-order gradiometer with counter-wound outer loops, making them largely unresponsive to uniform magnetic fields and linear magnetic field gradients. Thus, the detection coils generate a current only when there are magnetic field disturbances. Assuming the sample dimensions are much smaller than those of the detection coils, the induced current depends on the sample position. The general shape of this function is depicted in the figure, though it can vary slightly based on the sample's size and shape. This current is then inductively coupled to the SQUID, which acts as a highly sensitive current-to-voltage converter. While many details of the SQUID circuit are omitted for simplicity, it is important to note that the SQUID feedback nulls the current in the detection coils, meaning no actual current flows through them, and the feedback current provides the SQUID voltage for analysis.

After the deposition of the magnetic materials, the prepared thin films are diced into a maximum size of 4 mm x 4 mm, which is a prerequisite for performing any measurements in the SQUID MPMS3 system. This dicing can be done either by hand with a diamond cutter or using a dicing machine. Following this, we mount the sample properly on the sample holder (inside a straw for powder samples) and place it inside the SQUID chamber. The MPMS3 enables precise centring of the sample by conducting a DC scan along the entire length of the sample chamber. The system fits the scan data to an expected waveform to calculate the centre position. Significant deviations in the scan data from the fit function may indicate that the sample's size, shape, or magnetic properties are causing it to deviate from ideal point-like dipole behaviour. According to the design of the SQUID MPMS3, the ideal sample offset value for the system should be 66 ± 3

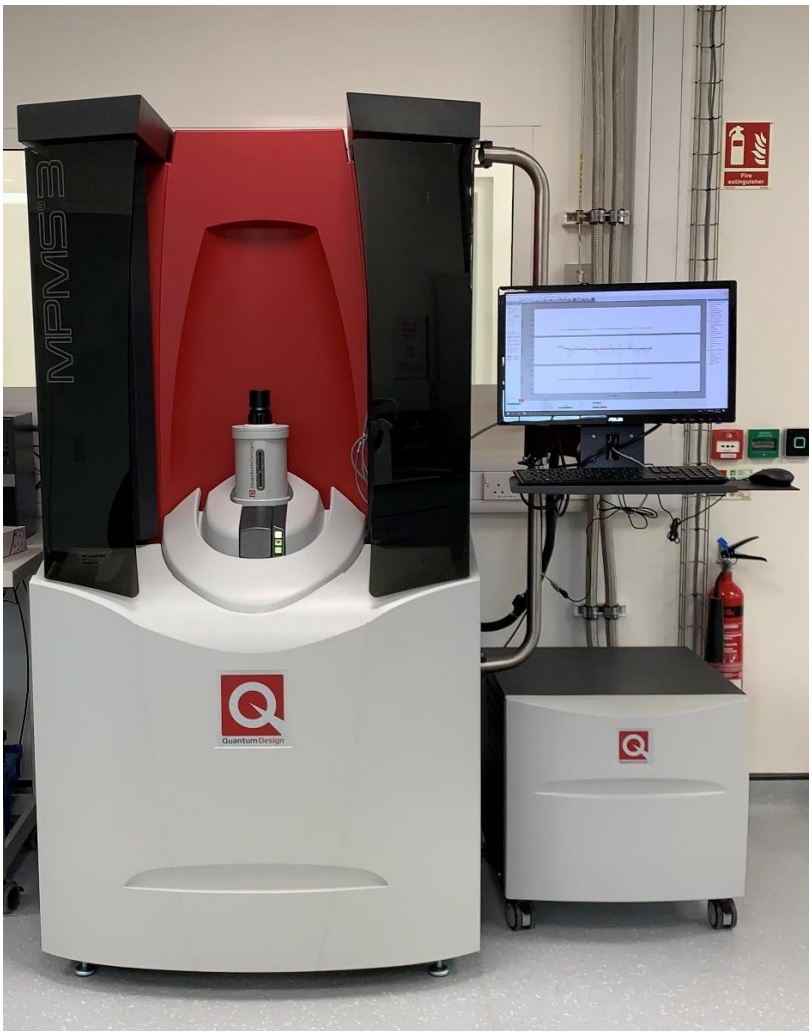


Figure 3.11: Experimental setup of MPMS3 SQUID magnetometer in our laboratory at Tyndall National Institute.

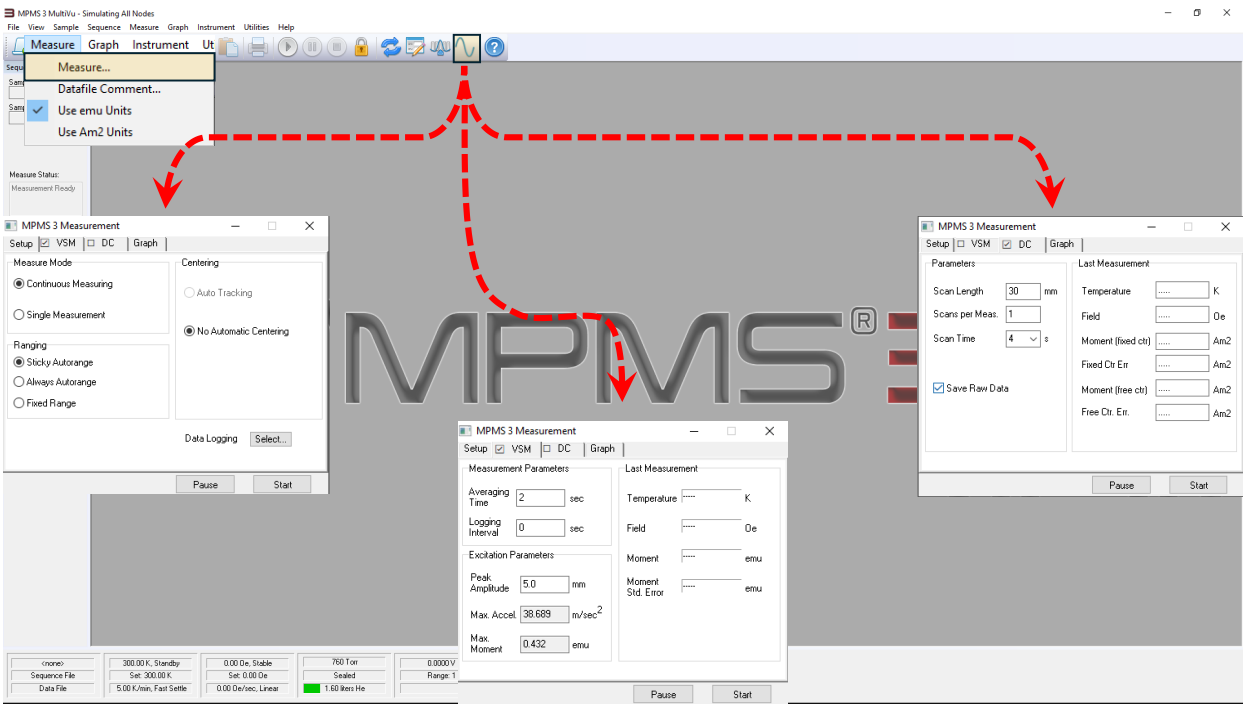


Figure 3.12: Snippets of Quantum Design MPMS3 SQUID magnetometer compatible "MultiVu" software.

mm. The sample offset value measures the distance from the bottom of the sample holder to the centre of the sample. An offset value of 66 mm indicates that there is no offset and the sample is in the exact centre position. Figure 3.13(b) illustrates a typical DC scan for the sample holder coordinates for the centre position.

In general, To measure the magnetic properties using the SQUID MPMS3 system, a standardized protocol is followed to ensure accurate and reliable results. Initially, thin films of magnetic materials are meticulously prepared and diced into uniform sizes, typically not exceeding 4 mm Œ 4 mm. Similarly, the substrate is prepared with equal care to match the dimensions of the samples. Once prepared, both the substrate and sample are thoroughly cleaned to remove any potential contaminants, ensuring the integrity of the measurements. The measurement procedure begins with system calibration and setup. The SQUID MPMS3 is powered on and allowed to stabilize, followed by necessary calibration steps as per the manufacturer's guidelines. The substrate is then placed into the sample holder within the system's sample chamber. Using the system's DC scan function, the substrate is centered to optimize measurement accuracy.

Firstly, the substrate alone is subjected to magnetic measurement under the desired experimental conditions, which typically include temperature and magnetic field strength variations. The resulting data provides a baseline for subsequent analysis. Next, the prepared sample, mounted on the substrate, is placed into the sample holder. Again, the sample's position is carefully centered

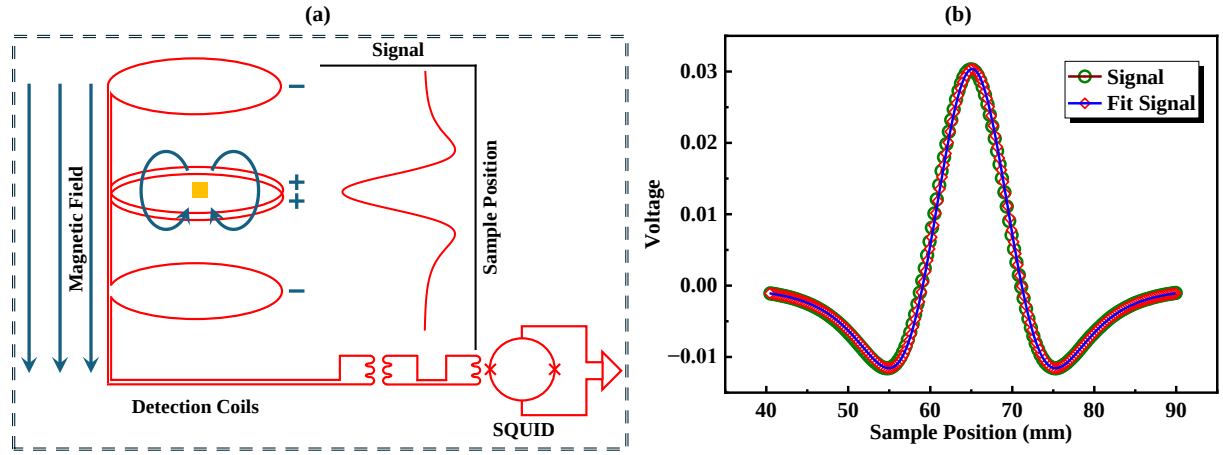


Figure 3.13: (a) Schematic of SQUID detection. (b) Sample offset value in mm to keep the sample holder in the center position.

using the system's DC scan feature to ensure consistent measurement conditions. Subsequently, the combined sample and substrate undergo magnetic measurement using the same parameters as the substrate alone. The data obtained from this measurement includes contributions from both the substrate and the magnetic sample. To isolate the magnetic properties of the ferromagnetic sample, the substrate data is subtracted from the combined data set during post-measurement analysis. This step reveals the specific magnetic contribution of the sample, crucial for accurate characterization. Following data analysis, results are documented in a comprehensive report that includes all measurement parameters, raw data, analysis procedures, and final findings. Any deviations or anomalies encountered during the measurements are also noted for thorough documentation. By adhering to this protocol, researchers can ensure systematic and reproducible measurements of magnetic properties using the SQUID MPMS3 system, facilitating reliable interpretation and comparison of experimental results.

For example, the following Figure 3.14(a) shows aforementioned different types of hysteresis loops[1] at room temperature for the sample grown on a diamagnetic substrate. The overall magnetic response, i.e., the response coming out from the magnetic substance and substrate is shown with blue line plots and the red line plots denote the substrate contribution while the actual magnetic behaviour is illustrated in the grey highlighted region with the green line plots. Figure 3.14(b) dictates the magnified version of the background subtracted actual magnetic behaviour (overall response - substrate contribution) from the material as highlighted in the Figure 3.14(a), in this case that is the mixture of ferrimagnetic and antiferromagnetic/altermagnetic [9, 10] contribution

[1]Measured with Quantum Design (QD) SQUID (Superconducting QUantum Interference Device) MPMS3 at Tyndall National Institute, University College Cork, Cork, Ireland.

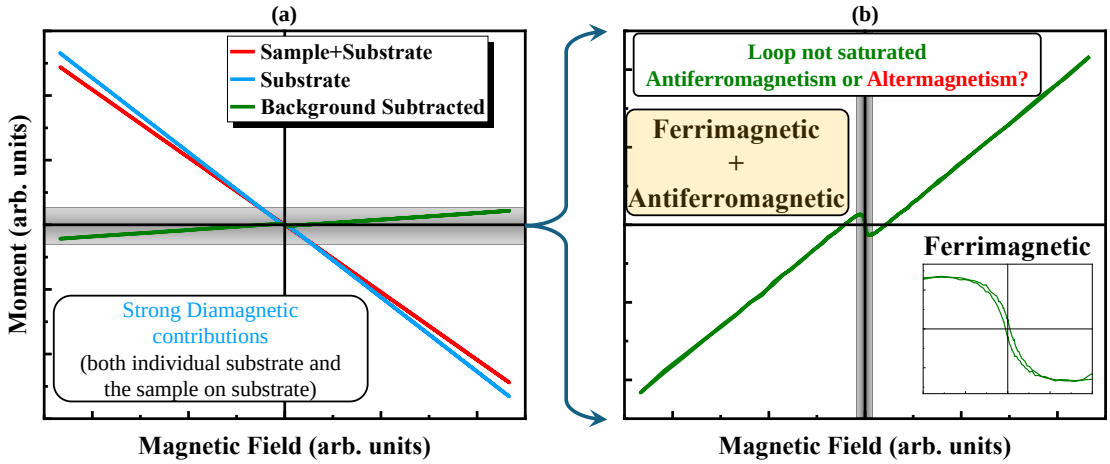


Figure 3.14: (a) At room temperature, different hysteresis loops of a thin magnetic material grown on a diamagnetic substrate. (b) Magnified version (obtained after subtracting the substrate contribution) shows the real/actual magnetic behaviour of deposited magnetic material.

coming out from the single starting material. Inset of Figure 3.14(b) confirms the ferrimagnetic nature presented in the sample.

3.6.3 First Order Reversal Curve

The FORC technique represents a significant advancement in understanding nanostructured magnetic materials, providing detailed insights into their magnetic interactions and domain behaviours crucial for developing next-generation magnonic devices. This method enables precise analysis of various magnetic interactions such as exchange coupling, dipolar interactions, and magnetostatic effects. Additionally, FORC offers valuable observations into domain wall dynamics, reversible and irreversible magnetization processes, and the spatial distribution of coercive fields within the material. It is particularly effective in identifying magnetic variations across different regions of a sample, essential for comprehending the performance of composite and heterogeneous materials.

The significance of FORC lies in its ability to offer comprehensive, multidimensional perspectives on magnetic behaviour, facilitating the optimization and design of magnetic materials for advanced applications. In nanostructured materials and integrated magnonic devices, FORC analysis provides critical advantages. By unraveling complex magnetic interactions and domain behaviours, researchers can customize materials for specific applications like data storage, sensors, and magnonic devices, enhancing overall design capabilities. Moreover, FORC aids in identifying and mitigating sources of magnetic noise and loss, thereby improving material and device efficiency, stability, and performance. Its insights into nanoscale magnetic phenomena contribute significantly to advancing fields such as spintronics and magnonics. Furthermore,

FORC serves as a vital diagnostic tool for assessing the quality and uniformity of magnetic materials, crucial for industrial applications and large-scale production efforts.

In the relevant FORC related studies associated with this thesis, we have utilised the FORCinel software [121] developed by Harrison and Feinberg to post-process the FORC diagrams and plot them in (H_C, H_U) plane. The software utilises an improved algorithm for generating FORC diagrams using a technique called LOESS (Locally Weighted Regression Smoothing). This technique is crucial in analyzing complex magnetic signals in rock and mineral samples, which are vital for research in geomagnetism and paleomagnetism.

FORCinel offers an enhanced smoothing algorithm that improves upon existing methods by allowing a constant smoothing factor across the entire range up to the $H_C = 0$ axis. This improvement includes permitting noninteger values for the smoothing factor, providing greater control over the degree of smoothing and assisting in the automatic selection of optimal smoothing parameters. Additionally, the algorithm is designed to automate extrapolation across gaps or undefined regions of FORC space. This capability helps eliminate artifacts caused by instrumental instabilities and allows specific regions to be masked for focused analysis. The FORCinel algorithm is implemented in a user-friendly software package featuring a graphical user interface built using Igor Pro software, which is accessible for download from multiple online sources.

The core of the improved algorithm is the Locally Weighted Regression Smoothing (LOESS), which differs from conventional FORC smoothing by fitting a second-order polynomial to magnetization data over a user-defined region in FORC space rather than a fixed grid. This approach offers greater flexibility in the smoothing process. FORC diagrams are produced by measuring the magnetization of a sample through a series of reversal curves. These curves are used to compute a mixed second derivative of the magnetization with respect to applied fields, and this derivative is displayed in a rotated coordinate system (H_C, H_U).

FORC diagrams are crucial diagnostic tools for studying magnetic interactions and grain distributions within rock samples, making this improved method valuable for researchers in rock magnetism and related fields. By providing a comprehensive, easy-to-use tool, FORCinel broadens access to advanced magnetic analysis techniques for the research community. The advancement of the FORCinel software and its underlying algorithm significantly enhance the accuracy and usability of FORC diagrams. The incorporation of LOESS smoothing and the ability to handle data anomalies and gaps make it a powerful tool for magnetic characterization. This new approach promises to facilitate more detailed and accurate magnetic analyses, benefiting a wide range of geophysical and geological research applications.

I have developed a Python program along with its executable file (.exe) in-house to make the program, platform independent but limited to Windows system only, and coined it as, *"PyFORC"*,

is developed to generate the multiVu compatible FORC measurement sequence with QD SQUID MPMS3 Magnetometer [1] and finally post-processing the measured FORC data for instance streamlined data analysis, data sorting and generating the graph.

3.6.4 Magnetic Force Microscopy (MFM)

Magnetic Force Microscopy (MFM), a specialized technique within the area of AFM, is designed to measure magnetic properties. As shown in Figure 3.15, MFM relies on several key components. The piezoscanner, a critical part of the device, holds the sample and allows for spatial movement in the x, y, and z directions, enabling accurate surface mapping. The MFM probe (Model no: MESP-RC-V2) is typically made from n-type antimony (Sb) doped silicon having resistivity with a range of 0.01 ω-cm to 0.025 ω-cm. This specific probe features a cantilever with dimensions of 125 µm in length, 35 µm in width, and 1.8 µm in thickness. It oscillates at a frequency of 150 kHz and has a spring constant of 5 N/m. The MESP-RC-V2 probe is designed with a reflective Co/Cr coating on its backside to enhance the laser signal used in detecting cantilever deflections, while the front side with magnetic co/Cr layer. This precise construction allows for highly sensitive and accurate measurements of the magnetic domain structures (amplitude and phase) along with simultaneous sample surface characteristics, contributing significantly to the reliability of MFM analyses. The MFM probe is affixed to a cantilever that is not itself magnetized. To magnetize the probe, the north pole of a strong magnet is brought very close (1-2 mm) to the tip and then slowly moved away horizontally.

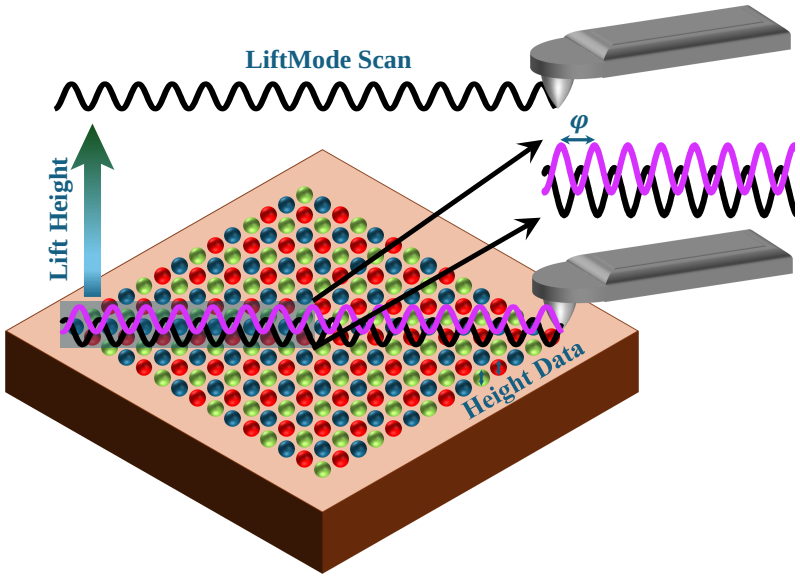


Figure 3.15: Schematic of working principle of MFM (magnetic force microscopy). Magnetic Forces cause the phase shift denoted by φ over different domains during the 'LiftMode Scan'.

During the MFM operation, the sample, which possesses magnetic properties, is mounted on

the piezoscanner. The cantilevers tip is positioned just above the sample surface. As the tip scans the sample, magnetic interactions between the tip and the sample cause the cantilever to bend. These deflections are due to the magnetic forces, which are stronger than the van der Waals forces also present between the atoms of the tip and the sample surface. The van der Waals forces, though weaker, still play a role in the interaction. As the tip moves vertically across the sample surface, it induces oscillations in the cantilever. These oscillations lead to changes in the angular deflection of a light beam that is reflected off the surface of the cantilever. An optical sensor, also known as a small displacement transducer, detects these deflections. The sensors readings are used to generate an image of the magnetic field distribution on the sample surface. MFM is essentially an AFM equipped with a magnetized tip. It measures the magnetic forces acting on the cantilever tip, allowing it to detect and image stray magnetic fields on the sample surface. This technique provides insight into both the magnetic properties and the physical topography of the sample, making it a versatile tool for comprehensive surface characterization. The combination of AFM and MFM enables researchers to analyse a wide range of surface characteristics, including both structural and magnetic properties, thereby enhancing the understanding of the material being studied.

3.7 Dynamic Characterization

The developed shiny and smooth nanostructured magnetic materials by DC electrodeposition technique are characterized using dynamic characterization techniques, namely, Brillouin Light Scattering (BLS) Study and Time-resolved Magneto-Optical Kerr Effect (TRMOKE) Study, respectively. The following sections describe a general trivia about both the techniques.

3.7.1 Brillouin Light Scattering (BLS) Study

The BLS spectra of thermally excited spin waves (SWs) were measured using a six-pass [(3+3)-pass] tandem Fabry-Perot interferometer. Since these spin waves are thermally excited and exist at room temperature, no external excitation, such as microwave or current, was needed for the measurements. Instead, the room temperature surface spin waves were detected as a BLS signal using a 532 nm wavelength laser as the incident light source. The experimental setup was configured to detect the backscattered light in the direction opposite to the incident light, facilitating accurate measurement of the spin waves. For the measurement of surface spin waves, specifically the Damon-Eshbach (DE) spin waves, the experiment was conducted in DE geometry. This involved applying an in-plane magnetic field greater than $\mu_0 M_S$ along the x-direction during

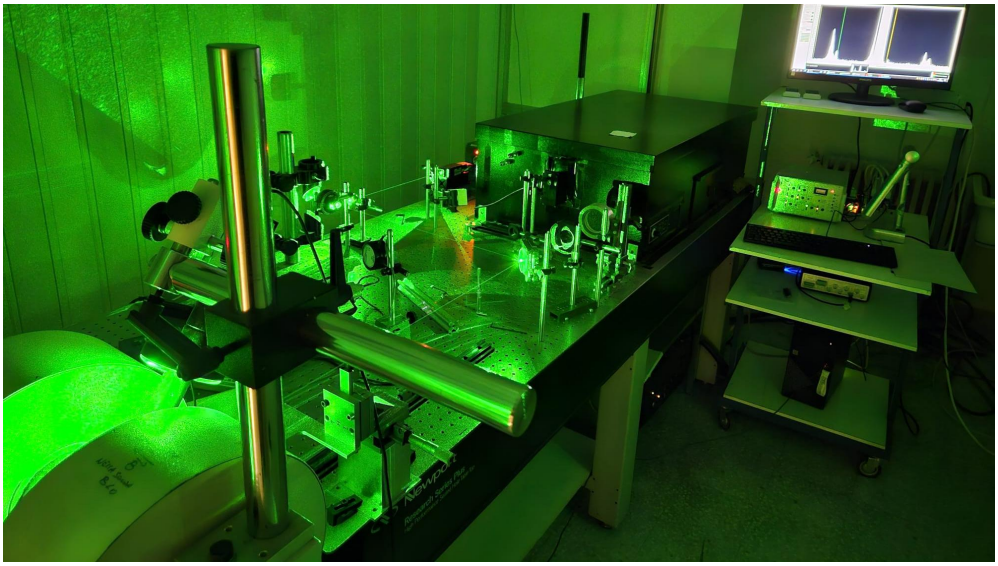


Figure 3.16: Experimental setup of the Brillouin Light Scattering (BLS) setup in the GHOST laboratory at CNR-IOM, Perugia, Italy.

the measurement. The strength of the applied magnetic field was sufficient to saturate the in-plane magnetization, ensuring the proper conditions for detecting DE spin waves. By utilizing this setup, the BLS technique effectively captured the characteristics of the thermally excited spin waves without the need for additional external excitation.

3.7.2 Time-resolved Magneto-Optical Kerr Effect (TRMOKE) Study

To investigate the ultrafast demagnetization and precessional magnetization dynamics of the sample, we employed the TR-MOKE technique in polar Kerr geometry using a two-color non-collinear pump-probe setup. A portion of the fundamental laser beam (wavelength = 800 nm, pulse width = 40 fs, repetition rate = 1 kHz) from a femtosecond regenerative amplifier (Libra, Coherent Inc.) is directed through a second harmonic generator to produce the pump beam (wavelength = 400 nm, pulse width $>$ 40 fs, repetition rate = 1 kHz) for excitation. Another fraction of the fundamental laser beam is utilized as the probe beam to monitor the magnetization dynamics. The time delay between the pump and probe beams is controlled by passing the probe beam through a motorized variable delay stage. During measurements, the pump beam fluence is significantly higher ($\sim$ 10 mJ/cm^2) than that of the probe beam ($\sim$ 1.5 mJ/cm^2). An external magnetic field is applied at an angle of $\sim 30^\circ$ [denoted as ξ in Figure 6.3(a)] to the sample plane, which is optimal for introducing a finite demagnetizing field in this sample. This tilt in magnetization is further altered by the pump pulse, initiating precessional dynamics within the sample. The probe beam strikes the sample perpendicularly with a spot diameter of approximately 100 μm, while the pump

beam is slightly defocused, with a spot diameter of about 250 μm, and is incident obliquely at around 45° to the sample plane, ensuring proper spatial overlap with the probe spot. An optical chopper operating at 373 Hz chops the pump beam, and the dynamic signal in the probe beam is detected via a Si detector using a lock-in amplifier in a phase-sensitive manner. Our experiment utilizes 4 ps and 2 ns time windows (representing the total duration of measurement of the time-resolved signal) to probe ultrafast demagnetization (temporal resolution = 25 fs) and damped precessional motion (temporal resolution = 5 ps), respectively.

Time-Resolved Magneto-Optical Kerr Effect (TRMOKE) and Brillouin Light Scattering (BLS) spectroscopy are crucial techniques for studying nanostructured magnetic materials. TRMOKE provides high temporal resolution in the picosecond to femtosecond range, essential for capturing ultrafast magnetic phenomena such as spin wave dynamics and rapid magnetization precession. This sensitivity to ultrafast processes makes TRMOKE invaluable for developing high-speed magnetic devices and exploring terahertz spintronics. Additionally, TRMOKE's integration with scanning microscopy allows high spatial resolution studies of magnetic domains, aiding in the development of nanoscale devices. Its non-destructive nature ensures sample integrity during repeated measurements, making it ideal for studying delicate or thin film samples. BLS spectroscopy, while providing lower temporal resolution compared to TRMOKE, excels in measuring spin wave frequencies and damping, offering critical insights into the magnetic material's behaviour under steady-state conditions. BLS is adept at examining the collective behaviour of magnons over larger areas, crucial for applications requiring an understanding of bulk properties, such as in designing magnetic thin films and multilayers. Both TRMOKE and BLS are non-destructive and contactless, preserving sample integrity. Together, these techniques provide a comprehensive understanding of magnetic materials, essential for advancing both fundamental research and technological applications in magnetism.

4

Fabrication of Nano-hetero-structured Magnetic Exchange Springs

This chapter is based on the following published paper in APL Materials [1][1] and the International Conference presentations[2],[3].

4.1 Introduction

In contrast to traditional single ferromagnetic (FM) thin films, multilayered nano-heterostructures (NHSs) with sandwich-like configurations exhibit enhanced properties, such as higher coercivity (H_C) and greater saturation magnetization (M_S), resulting in an increased energy product (BH_{max}). These NHSs, termed as exchange-spring (ES) systems [25, 73, 77], are highly relevant for advanced applications in data storage, spintronics, and beyond. A crucial aspect of the formation of ES NHSs is the relative thickness of the soft phase (L_S) compared to the domain wall width (δ_H) of the hard phase. Specifically, $L_S > 2\delta_H$ fosters ES behaviour, while $L_S \leq 2\delta_H$ results in a single unit behaviour, marked by a flat rectangular hysteresis loop indicative of exchange-coupled (EC) systems [26]. Significant research over the past three decades has been dedicated to exploring ES systems [2, 27, 101, 105, 122–132].

[1] Investigation of transverse exchange-springs in electrodeposited nano-heterostructured films through first-order reversal curve analysis, **A. Samanta**, S. Roy, ***APL Materials***, **12**(9), 091118, (2024)

[2] Exchange Spring Co-Rich CoP Nanomagnetic Thin Films (Oral), **A. Samanta**, S. Roy, *'Intermag 2021 Conference'*, (Oral Presentation), April 26-30, 2021.

[3] Structural and Magnetic Study of Single Nano-Hetero-Structured Co-Rich CoP Magnetic Thin Films (Oral Presentation), **A. Samanta**, S. Roy, *'2022 Joint MMM-Intermag Conference'*, New Orleans, January 10-14, 2022.

Given that soft and hard magnets interact through magnetic exchange interactions at the nanometre scale, the observation and analysis of domain structures are crucial for understanding their behaviour. Interfaces in the ES structures significantly impact exchange coupling and magnetic anisotropy. Analysing domain wall behaviour at these interfaces reveals the nature of exchange interactions that define functionality of the ES systems. The competition between in-plane (IP) anisotropy and out-of-plane (OOP) anisotropy within the material often results in stripe domain structures [133, 134]. Despite their importance, magnetic domain analyses in ES NHSs are underexplored, and it is expected that IP ES systems would lack periodic stripe domain patterns due to the absence of OOP anisotropy. A recent study discusses the competition between in-plane and out-of-plane anisotropy through the formation of helical anisotropy [135]. Helical anisotropy refers to a material structure where the direction of magnetic anisotropy follows a helical pattern, leading to unique and beneficial magnetic properties by balancing and enhancing the competition between in-plane and out-of-plane anisotropies. This controlled interplay significantly reduces magnetic losses and acoustic noise in rotating machines [135].

On the other hand, some OOP ES structures, featuring ferromagnetic and antiferromagnetic interactions, exhibit spin flop transitions [75]. These structures show maze-like domain patterns in strongly OOP systems such as [Co/Pd]-NiFe [136] and $L1_1$ CoPt-NiFe [137]. The domain behaviour of OOP [Co/Pt]/NiFe ES systems, however, remains unexplored [110]. When continuous thin films are nano-patterned to nano-meter or sub-micron dimensions, the resulting nano-modulation can dominate the film's uniaxial anisotropy, creating a competition between IP and OOP magnetic dipoles, thereby preventing vortex formation [138], although without forming the stripe domains. Notably, while the IP ES structures are well-studied, transverse ESs with OOP anisotropy are comparatively less explored [27, 75, 110, 139].

Here, first, the preparation of stress-free, shiny, fine-grained dispersed *"in situ"* magnetic nano-heterostructures (NHSs) of a single CoP film has been elucidated, still a less explored avenue to the research community. This is achieved through a modified stable acidic bath chemistry with controlled hydrogen evolution, a method not previously employed in the context of ES systems. This innovative approach offers a low-cost and high-yield alternative to traditional *ex situ* fabrication techniques, such as magnetron sputtering [110], annealing [140], ion-irradiation [125], and molecular beam epitaxy [75]. The electroplating technique used here allows for the creation of complex nano-topologies, which are crucial for the development of advanced magnetic materials [2, 46, 53, 111]. A significant contribution of this study is the demonstration of the transition from a non-ES state to a transverse-ES state within a single thin film driven by the non-collinearity of spin textures at room temperature, which reveals new insights into the magnetic behaviour of ES systems, particularly those influenced by out-of-plane (OOP) anisotropy. Additionally, first-

order reversal curve (FORC) measurements and analysis confirm that the developed ES system is driven by anisotropy induced by OOP anisotropy, leading to the formation of novel stripe domain patterns. These findings are further corroborated by micromagnetic simulations using MuMax^3 [24], providing a robust theoretical framework to support the experimental results.

4.2 Experimental Methods

The smooth, shiny, amorphous-nanocrystalline cobalt phosphorus (CoP) films by DC electrodeposition technique have been developed. The following chemicals and reagents, phosphorus acid, phosphoric acid, cobalt chloride hexahydrate, cobalt carbonate [2, 80], as mentioned in the Table 4.1, forms the required electrolytic plating bath. The developed thin films from the bath are quite stressed and rough possibly due the instability of the bath and the high surface tension between the working electrode (WE) and the electrolyte. Therefore, a surface tension reducing agent, glycine, have been added in order to stabilize the bath along with stress-relieving additives, naphthalene trisulfonic acid (NTA), saccharine [2] reduce the surface tension between the WE and electrolyte to the solution. Consequently, the stress-free, smooth, glossy thin films are developed (comparatively lower R_q values are mentioned in the Table 4.2). The modified and stable bath compositions are mentioned in the following Table 4.1.

TABLE 4.1: Plating bath composition and conditions

Component	Amount (g / 100 mL)	
	Old Bath [80]	New Bath
Phosphorus acid (H_3PO_3)	3.00	3.30
Phosphoric acid (H_3PO_4)	5.00	5.90
Cobalt chloride hexahydrate ($CoCl_2 \cdot 6H_2O$)	18.00	18.87
Cobalt carbonate ($CoCO_3$)	1.50	1.55
Glycine	—	1.15
Saccharine	—	1.51
NTA	—	1.52
Temperature	$345K$	$293K$
pH	0.75	$0.72 - 86$

The electrodeposition has been carried out by varying the current density from 5 mA/cm^2 to 40 mA/cm^2 and keeping the deposition time fixed for 120 minutes. The micro-structural and elemental characterization of the electrodeposited films have been performed using Zeiss scanning electron microscope (SEM)—energy dispersive X-ray spectroscopy (EDX) analysis (Oxford In-

struments). The XRD (X-Ray diffraction) patterns have been characterized in Panalytical X'Pert Pro MRD with Cu Kα radiation (40 kV, 50 mA) at a wavelength of 1.54 nm. The HR-TEM (high-resolution Transmission electron microscopy) characterization using JEOL TEM 2100. The HR-TEM lamella Cross sections were prepared using a Dual Beam focused ion beam (FIB) FEI Helios NanoLab 600i. A 50 nm C layer and 300 nm Pt layer were deposited within the DualBeam FIB by electron beam induced deposition and 2 um thick Pt layer with ion beam induced deposition. These three layers are for protection before the FIB milling process. The lamella was prepared and thinned down for the HR-TEM analysis. The thinning at 30 kV was finished with a final polishing at 5 kV (47 pA) to reduce the ion-beam induced damage to a less than 2 nm thin layer on both sides. Micro-structural analysis was performed using HR-TEM (Jeol 2100 transmission electron microscope; 200 kV using a double tilt sample holder. 3D Surface profiles (roughness) and magnetic force microscopy imaging (MFM) of the films were studied using a Bruker Dimension Icon AFM (atomic force microscopy).

The magnetic measurements were carried out using hysteresis loop tracer (MESA 200, ShB Instruments, USA) for $\pm$1000 Oe for the hysteresis loops and **S**uperconducting **QU**antum **I**nterference **D**evice (SQUID) magnetometer [Quantum Design Magnetic Property Measurement System (MPMS), Model: MPMS3] for the first-order reversal curve (FORC) measurements. A total of 200 FORCs were measured for each sample using the SQUID MPMS3 system. The required FORC measurement sequence and the subsequent data-processing were done by a code (Python) developed in-house, called "PyFORC", and subsequently its an executable file and the FORC diagrams in (H_C, H_U) plane were constructed utilizing FORCinel software [121]. Each of the FORC measurements involved saturating the sample and then measuring the moment from a reversal field H_R back to positive saturation field ($+H_S$), yielding a family of FORCs for different values of H_R with an increasing field of H_F spaced equally. Note that, H_F represents the applied magnetic field during each minor loop within the FORC measurement, whereas the field spacing refers to the incremental steps between successive applied fields in the FORC analysis. The following mixed second-order derivative expression obtained the FORC distribution, $\rho(H_R, H_F)$:

$$\rho\ (H_R, H_F) = -\frac{1}{2M_S}\left(\frac{\partial^2 M(H_R, H_F)}{\partial H_R \partial H_F}\right)$$

where M_S is the saturation magnetization. This eliminates the pure reversible components of magnetization (ρ=0), and any non-zero ρ corresponds to irreversible switching processes in the system [141–143]. The FORC distribution $\left[\rho\ (H_C, H_U)\right]$ is presented in the (H_C, H_U) plane, where $H_C = \frac{1}{2}(H_R - H_F)$ and $H_U = \frac{1}{2}(H_R + H_F)$ represent the local coercivity and the interaction or bias field, respectively.

4.3 *"In situ"* NHS formation by hydrogen evolution

The transfer of electrons in an electrochemical process, induces the chemical change, such as, the oxidation or reduction of a metal complex. Here, the anode represented by Co, undergoes oxidation process to form Co^{3+} ions via heterogeneous electron transfer. The schematic of this oxidation process is illustrated in Fig. 4.1(a). Conversely, the reduction process of reduced phosphorus (P) follows a reverse phenomenon, as depicted in Fig. 4.1(a) and in the later section.

We perform the widely used electrochemical technique of three-electrode cyclic voltammetry (CV) analysis, schematically illustrated in Fig. 4.1(b), in order to investigate the possible reaction processes. Here, a piece of $2 \times 2\ cm^2$ Si wafer, featuring top-conducting sputtered Ti/Au (20/200 nm) seed layers, serves as the working electrode (WE), and a Co-piece functions as the counter electrode (CE). The voltage of the working electrode is referenced to Ag/AgCl (reference electrode (RE), Fig. 4.1(b)).

TABLE 4.2: Experimentally obtained values of different structural, stoichiometric and magnetic parameters for various electrodeposited CoP thin films.

Current Density	Thickness	R_q	$\frac{R_q}{d} \times 100$	Stoichiometric	$H_C\ (kA/m)$		$B_S\ (T)$		$B_R\ (T)$		S(M_R/M_S)	
(mA/cm^2)	(μm)	(nm)	in %	Ratio	dir-X	dir-Y	dir-X	dir-Y	dir-X	dir-Y	dir-X	dir-Y
5.48	0.31	3.00	0.967	$Co_{86.80}P_{13.20}$	2.697	2.718	0.472	0.367	0.223	0.193	0.4724	0.5367
10.97	0.68	2.24	0.329	$Co_{87.10}P_{12.90}$	13.41	15.73	0.596	0.814	0.5134	0.701	0.8603	0.8601
16.46	5.06	10.03	0.198	$Co_{88.20}P_{11.80}$	15.31	15.74	1.801	1.587	1.487	1.343	0.8260	0.8464
21.95	11.38	11.54	0.101	$Co_{86.30}P_{13.70}$	12.88	12.96	0.881	0.677	0.780	0.616	0.8958	0.9094
27.44	12.44	12.24	0.098	$Co_{92.34}P_{7.76}$	13.60	13.60	0.987	0.803	0.888	0.728	0.8998	0.9072
32.92	13.36	12.30	0.092	$Co_{91.99}P_{8.07}$	18.18	18.28	1.000	0.936	0.900	0.840	0.8998	0.8982

The resulting CV curve obtained with 50 mV/s scan rate and shown in Fig. 4.1(c) unveils two cathodic current peaks and two anodic current peaks during the reduction (cathodic/negative) and oxidation (anodic/positive) scans, respectively, whereas, one of those two peaks in each cycle, is narrower than the other. Concerning the standard reduction potentials, E_0, the salient feature of the CV study is the decrease in the obtained reduction potentials, which happens because of adding saccharine and naphthalene-1,3,6-trisulfonic acid (NTA) in the solution. During the negative scan, in the cathode, (i) a sharp cathodic peak is obtained at $-0.17V$ due to the reduction of Co^{2+} in the bath, and (ii) a broad peak is obtained at $-0.37V$, which ranges from $-0.31V$ to $-0.42V$. The former cathodic peak at $-0.17V$ generates possibly due to a faster reduction of Co^{2+} to Co, and H_3PO_4 to H_3PO_3, while the latter one generates due to a slow reduction of H_3PO_4. In this region, the nascent generated H_3PO_3 and the raw H_3PO_3 present in the solution, reduce to H_3PO_2 and nonmetallic P, and then the H_3PO_2 also reduces to nonmetallic P. It was previously believed that the elemental Co and P together form the $Co-P$ amorphous alloy, which provides the low coercivity of the soft material [94].

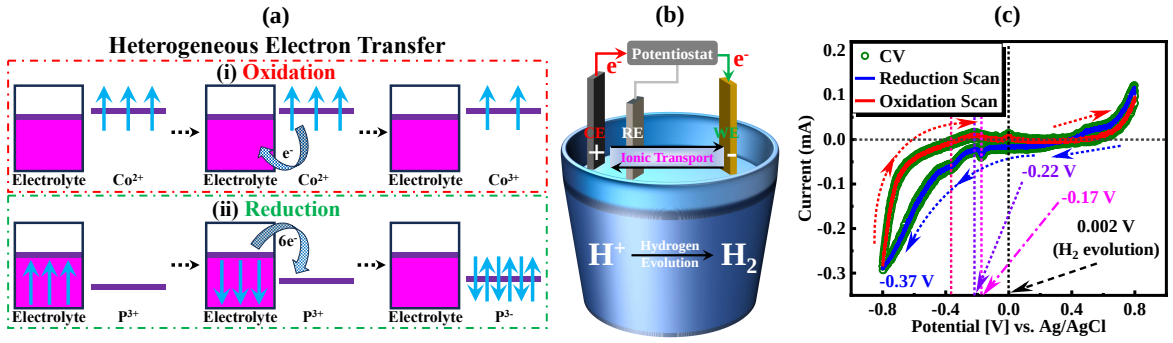


Figure 4.1: (a) Heterogeneous electron transfer: (i) oxidation of Co and (ii) reduction of P (b) The schematic of the electrochemically controlled NHS formation by hydrogen evolution. (c) A three electrode Cyclic Voltammogram curve recorded with standard Ag/AgCl electrode [1].

As the structural studies reveals two different phases present in a single nano-hetero-structured material, it is worth assuming that there should be two different phases. So, there must be a different electrochemical mechanism that favours forming a crystalline phase to serve as the source of high coercivity, simultaneously with the amorphous $Co-P$ alloy providing the low coercivity. Hence, we propose the following electrochemical mechanism in forming the nano-heterostructure from a single starting material.

During the cathodic scan, beyond those peaks, the potential sharply falls from $-0.50\ V$ to $-0.80\ V$ region due to the reduction of nonmetallic P to phosphine (PH_3) and splitting of water (H_2O) molecule. During the positive scan, in the anode, the peaks correspond to the liberation of O_2, H_2, and oxidation of H_3PO_3 to H_3PO_4. The small peak at $-0.002\ V$ corresponds to the evolution of hydrogen. This hydrogen evolution may cause bubbles and internal stress near the cathode. Although those stress-relieving additives were added to the bath, care was taken in such a way that the precipitates just disappeared from the bath and simultaneously ensured the existence of a little amount of stress. As literature study shows that internal stress causes the hydrogen evolution, the amount of NTA was adjusted to the bath in such a way that it ensured the hydrogen evolution. During the oxidation process, the anode (Co) dissolves in the solution and oxidizes to Co^{3+}, and forms an unstable metallic compound, $Co(PH_3)_3$. The nascent unstable metallic compound $[Co(PH_3)_3]$ then spontaneously forms the stable amorphous $Co-P$ alloys [144, 145].

The electron configuration of the elemental Co would be the $Co-hcp$ having the $[Ar]3d^74s^2$, and that of the CoP alloy would be the electron configuration of Co^{3+}, i.e., $[Ar]3d^54s^1$. According to Hunds rule, half/full$-$filled $-d$ orbital is more stable than other filled $-d$ orbital; hence, the Co^{3+} having the configuration of $3d^5$ has the stable electronic configuration. These two different phases, i.e., the $Co-hcp$ crystalline phase and the amorphous CoP phases, are separated (illustrated in FIG 4.1(a)) due to the hydrogen evolution developed by the stress. Since the Co^{3+} is

more stable than Co, the formation of $Co-P$ alloys will be preferred than the $Co-hcp$ structures, and hence, minor fraction of nanocrystalline $Co-hcp$ structures formed due to a faster reduction process of Co^{2+} to Co, as evidenced by the cathodic peak at $-0.17\ V$, would co-exist within the matrix of amorphous $Co-P$ alloys and help build the nano-hetero-structured thin film.

Continuous monitoring of the pH reveals that the pH of the solution increases after the deposition, as the concentration of $[H^{2+}]$ decreases due to hydrogen evolution and that of $[OH^-]$ increases because of water splitting, generation of PH_3 and elemental P. The electrochemical equations [146] involved in the formation of the NHS structures within the amorphous matrix influenced by the hydrogen evolution, as elucidated in the previous sections are summarized below:

$$Co^{2+} + 2e^- \rightleftharpoons Co \tag{1}$$

$$P + 3H_2O + 3e^- \rightleftharpoons PH_3 + 3OH^- \tag{2}$$

$$H_3PO_4 + 2H^+ + 2e^- \rightleftharpoons H_3PO_3 + H_2O \tag{3}$$

$$2H^+ + 2e^- \rightleftharpoons H_2 \tag{4}$$

$$H_3PO_3 + 2H^+ + 2e^- \rightleftharpoons H_3PO_2 + H_2O \tag{5}$$

$$2H_2O \rightleftharpoons O_2 + 4H^+ + 4e^- \tag{6}$$

$$HPO_3^{2-} + 2H_2O + 3e^- \rightleftharpoons P + 5OH^- \tag{7}$$

$$Co(Anode) \rightleftharpoons Co^{3+}(CoP) + 3e^- \tag{8}$$

$$H_3PO_2 + H^+ + e^- \rightleftharpoons P + 2H_2O \tag{9}$$

$$Co^{3+} + 3PH_3 \rightarrow Co(PH_3)_3 \rightarrow Co-P \tag{10}$$

$$2H_2O + 2e^- \rightleftharpoons H_2 + 2OH^- \tag{11}$$

4.4 Structural and Stoichiometry Analysis

Exploring the quantitative and qualitative analysis of phosphorus (P) in the electrodeposited thin film is of paramount importance due to its significant impact in the crystallinity of CoP thin film [2, 3]. Elemental analysis across various regions of the film confirms a consistent stoichiometry. The atomic percentages of cobalt (Co) and phosphorus (P) range from approximately 86 to 90 and 10 to 14, respectively (see Table 4.2). An EDX spectrum (Fig. 4.2(a)) validates the presence of Co and P, with the yellow line indicating the EDX linescan path on the film surface. The EDX linescan [Fig. 4.2(b)] further illustrates the homogeneity in composition, depicting Co and P distribution without any other impurity source. The red and green curves represent the linescan

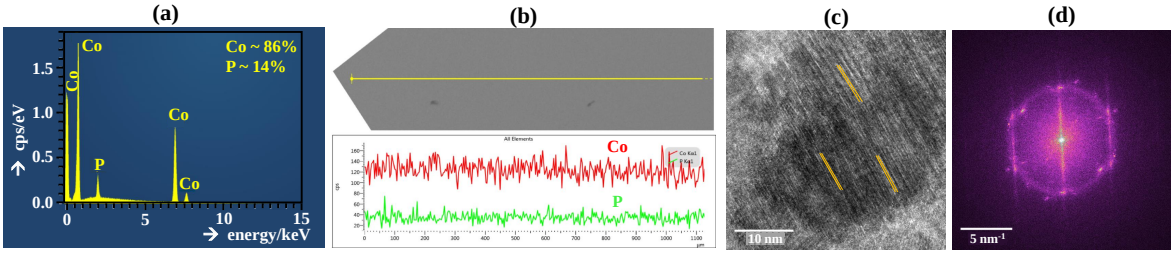


Figure 4.2: (a) Typical EDX spectrum showing the presence of Co and P in the films. (b) Top: EDX linescan path on the surface (yellow line). Bottom: Red curve denotes linescan for Co, and green curve for P. (c) A cross-sectional HR-TEM image of the film showing the striations in nm range formed due to stress caused by $H-$evolution. (d) FFT of the TEM image (c) confirms crystalline phases ($Co-hcp$) present in the amorphous CoP matrix [1].

for Co and P, respectively. Any non-identifiable topographic feature of the SEM figure [top image of the Fig. 4.2(b)] unveils the smooth, shiny, and fine-grained surface of the material.

The thicknesses of the electrodeposited films range from 0.31 μm to 14 μm are given in the Table 4.2. The nano-heterostructures, developed via electrodeposition technique favoured by hydrogen evolution, as explained earlier, have been experimentally observed by the cross-sectional HR-TEM [see Fig. 4.2(c)]. Here, the $2-5$ nm white lines in the HR-TEM image correspond to the $Co-hcp$ phases, and the rest of the black regions correspond to amorphous CoP (a few of the white lines are marked with orange lines) form the nano-hetero-structured system, where the crystalline $Co-hcp$ phases are embedded within the amorphous CoP matrix [2]. The crystallinity of the $Co-hcp$ phases are further confirmed by performing the Fast Fourier Transformation (FFT) of the TEM image, as shown in the Fig. 4.2(d).

Figure 4.3(a) illustrates the XRD pattern of the prepared amorphous CoP thin films. No additional peaks are detected beyond the three dominating substrate peaks: the peak near $2\theta = 69.22^\circ$ corresponds to the Si-wafer, while the other two peaks near $2\theta = 38^\circ$ and 83° originate from the top conducting seed layer of gold (Au), confirming the overall amorphous nature of the samples. However, the magnified XRD profiles in Fig. 4.3(b) and (c) reveal minor peaks at $2\theta = 44.3^\circ$ and 77.5°, indicating the presence of nanocrystalline $Co-hcp$ (002) and $Co-hcp$ (110) phases, respectively. Using the Scherrer equation, the mean grain size of the crystalline phase in the nano-hetero-structured film, depicted in Fig. 4.3(d), is calculated to be approximately (3.20 ± 0.57) nm, consistent with the $Co-hcp$ stripe thickness obtained from the HR-TEM.

We utilized atomic force microscopy (AFM) to determine the root mean square (RMS) roughness (R_q) of the topographic features, providing quantitative insights from the AFM images. The R_q values are listed in the third column of Table 4.2. The analysis of the results shows that the R_q value increases steadily with the current density during electrodeposition. When the deposition

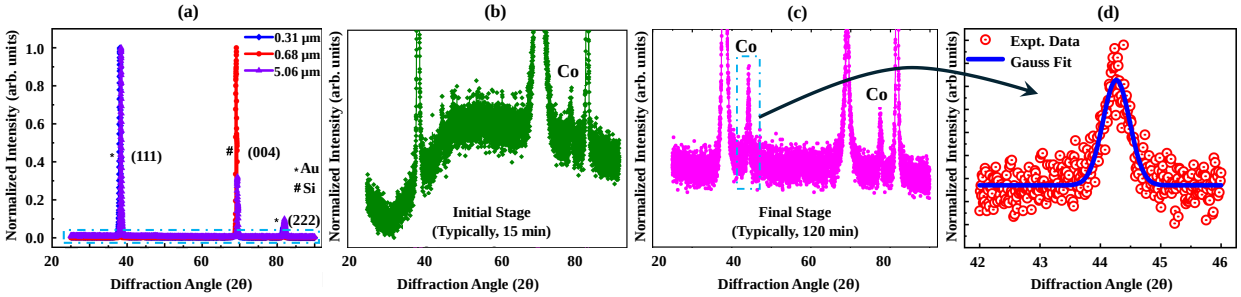


Figure 4.3: Structural characterization. (a) XRD spectra of the 0.31 μm, 0.68 μm, 5.06 μm thick films having three dominant substrate peaks confirming the overall amorphousness of the samples. The magnified XRD spectra of the highlighted region in (a) is shown in (b) for 0.31 μm film and in (c) for 0.68 μm film, respectively. (d) Gaussian Fit to the 44^o $Co-hcp$ peak as marked in (c) [1].

time is 120 minutes with a current density of approximately 33 mA/cm^2, the R_q value is about four times higher compared to around 5.5 mA/cm^2. However, it decreases by one order of magnitude in terms of the percentage of the overall thickness of the deposited film. This decrease indicates the effectiveness of the bath chemistry, including the proportion of stress-relieving additives, in the plating process. These minor changes are not visible in the SEM images. The significant variation in R_q, ranging from 2.24 nm to 12.30 nm, accompanied by a corresponding decrease in R_q/d from 0.329 to 0.198, suggests that roughness may contribute to the distribution of nucleation fields.

The spin orientations of the low current density sample (0.31 μm thick) and comparatively a higher current density sample are shown in Fig. 4.4(a) and (b), respectively. Both the figures reveal almost parallel periodic stripes within a certain region. The white and black stripe pairs in the figure reflect the regions with opposite magnetic orientation, i.e., upward, and downward directions. Though the spin stripes shown in Fig. 4.4(a) are almost straight and regular, however, a careful observation confirms that they are slightly bent locally. Generally, stripe domains manifests the competition between in-plane and out-of-plane (OOP) anisotropy present in the sample [133]. Coexistence of IP anisotropy simultaneously with the OOP anisotropy in an *in situ* amorphous-nano-hetero-structured thin film is elucidated elsewhere [2].

In a magnetic thin film with an OOP anisotropy, stray field or magnetostatic energy generated by the interaction between the dipoles favours IP anisotropy. So, in this *"in situ"* NHS system, the competition between IP anisotropy and OOP anisotropy acts as the driving force for stripe domains. As a result, periodic stripes formed where the magnetization rotates in the plane perpendicular to the thin film. This could be the characteristic signature of Transverse ES, which have been confirmed later by first-order reversal curve (FORC) measurements and micromagnetic simulations. However, it is worth mentioning here that the reverse might not be always true, i.e.,

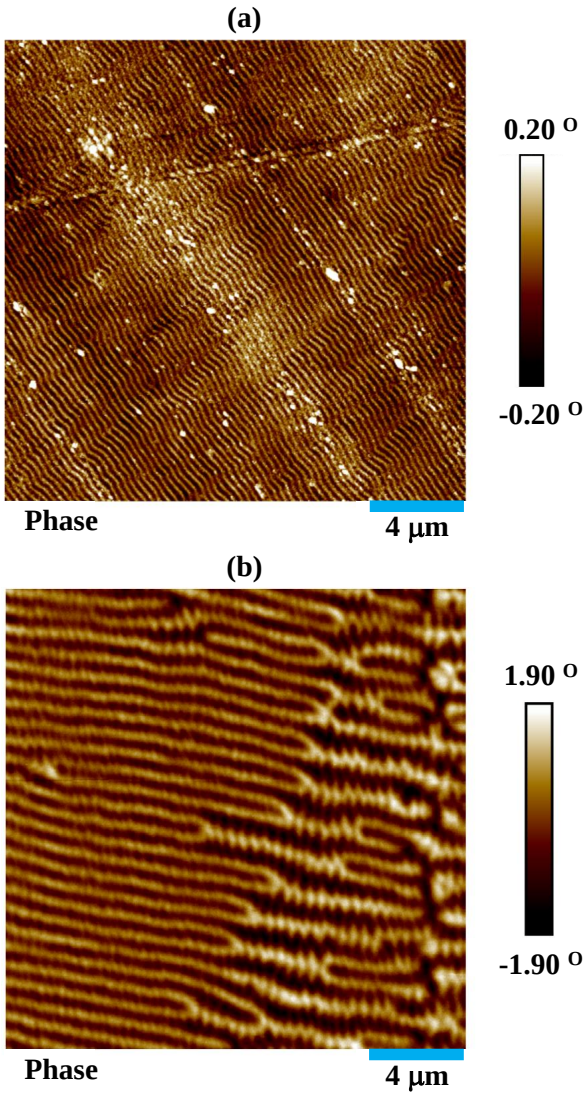


Figure 4.4: (a) Typical stripe domain structure in low current ($\sim 5.5\ mA/cm^2$) sample (thickness 0.31 μm). (b) Modified domains featuring corrugated stripes with domain branching in comparatively higher current $\sim 137\ mA/cm^2$ sample (thickness $\sim 5\mu$m). Both the scale bars are 4 μm and right side is the image colour scale [1].

the systems which exhibit stripe domains may not necessarily have transverse ES state.

Let us define a dimensionless material parameter, $Q = K/K_d$, where K is an appropriate anisotropy (uniaxial or crystalline or shape) constant, and K_d is the stray field energy constant. Usually, in a sample with stress-induced OOP anisotropy, the domain bifurcation is favoured with a comparatively lower Q value ($Q < 1$, i.e., $K_u < K_d$) [133]. From the Maxwell's equations, it has been seen that the lateral flux is zero, which results into generating the stray field energy. So, the magnetization flux which is entering the area at the base must be dissipated in the interior if

practically no flux leaves the finely divided surface. Also, the nucleation/branching of the domains is perhaps due to the tendency for the spin stripes to remain equidistant and stay in the minimized energy state [133].

Although the surface was uniform, due to the internal size of the striations (cross-sectionally) in the amorphous and nano-hetero-structure matrix, the two different phases just not only interact with each other but also they both interact with the out-of-plane anisotropy. The Q parameter of cobalt is too small for this effect, but surface anisotropy adds to the OOP anisotropy for very thin films, so that the effective Q becomes larger than unity [133], and the typical stripe domain gets modulated leading to the creation of novel corrugated stripe domains.

4.5 Static Magnetic Study

Fig. 4.5 shows the experimentally obtained normalized hysteresis loops along the direction X ($dir.X$) and direction ($dir.Y$) of those as-prepared materials, where $dir.X$ and $dir.Y$ represent that the measurements were done on the longitudinal and transverse directions, respectively. Hence, the X and Y directions are two mutually perpendicular directions on the sample plane, i.e., $dir.Y = dir.X + 90^o$. The interesting fact for all the normalized hysteresis loops is that both dir. X and dir. Y are practically equivalent, i.e., all the samples are assumed to be magnetically isotropic in the XY plane – a good agreement with the presence of a perpendicular anisotropy [147]. Fig. 4.5(a) unveils the coercivity of 0.31 μm thick is ~ 34 Oe $(2.697 kA/m)$. Three distinct regions are prominent in Fig. 4.5(a), i.e., (i) at the applied field below ~ 35 Oe $(2.785 kA/m)$, the loop shows hysteresis, (ii) a region at the applied field between 35 Oe to ~ 500 Oe $(\sim 40$ $kA/m)$, where magnetization changes almost linear with the applied field, and finally (iii) beyond ~ 500 Oe, an unchanged constant magnetization with the applied magnetic field, i.e., the magnetization has been saturated.

Generally, this kind of three slope hysteresis loop, particularly the region (ii), is the signature of thin films having a weak perpendicular anisotropy [148] that shows magnetic stripe domains, which has already been demonstrated in Fig. 4.4(a) and (b), respectively. However in this case, the in-plane (IP) anisotropy strongly dominates over the weak perpendicular anisotropy. When the sample thickness becomes 0.68 μm, the coercivity increased almost six times to reach ~ 200 Oe (15.951 kA/m) shown in Fig. 4.5(b). The observed increments in the thickness and coercivity are qualitatively consistent since nano-hetero-structures are formed in this case. Consequently, the staircase-like hysteresis loop has been obtained, a signature of ES structure with two distinguishable coercivities in a single amorphous/nano-hetero-structured material shown in Fig. 4.5(b). Here, the two different phases (namely, $Co-hcp$ and amorphous CoP) are non-

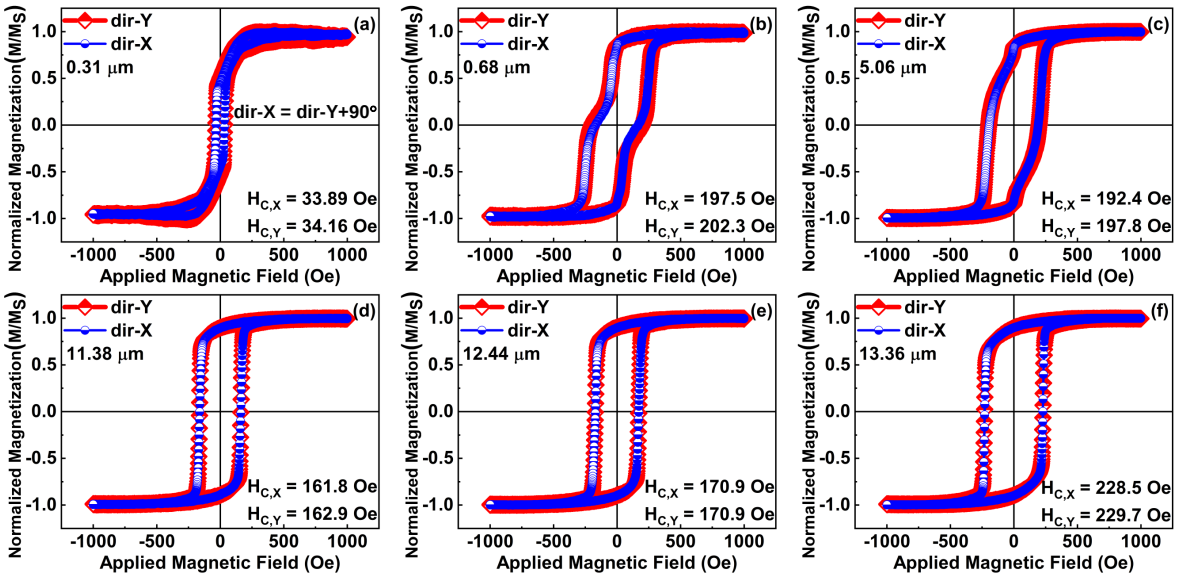


Figure 4.5: (a) Non-exchange-spring (ES) of 0.31 μm sample. (b) ES signature with 0.68 μm sample. (c) A small kink near $\sim$ 10 Oe observed when the thickness becomes 5.4 μm showing the OOP anisotropy starts dominating over the IP anisotropy. The ES state becomes a flat EC state, while the thickness is $\sim$ 11 μm in (d) due to the entire domination of the OOP anisotropy over the IP anisotropy. In (e), (f) the flat loops continue with the thicknesses 11.23 μm, 12.34 μm obtained, respectively. Here, for all the figures, $dir.Y = dir.X + 90^o$ [1].

rigidly coupled to each other through the magnetic exchange interaction and act as separate units in the same material. Neither IP nor OOP anisotropy dominates each other. Hence, with the application of an external magnetic field, both the phases reverse at the different magnetic fields. The amorphous CoP phases correspond to the lower coercivity, while the $Co-hcp$ phase corresponds to the relatively higher coercivity. While the thickness becomes 5.4 μm, the OOP anisotropy starts dominating over the IP anisotropy. Consequently, a small kink near 10 Oe exists along with the relatively higher coercivity of $\sim$ 180 Oe. The ES structure starts converting to EC structure giving rise to a flat hysteresis loop, while the thickness is $\sim$ 11 μm in Figure 4.5(d), as, in this case, the OOP anisotropy entirely dominates over the IP anisotropy, and both the phases act as a single unit. As a result, they reverse at the same field. In Fig. 4.5(e), (f), the flat nature of the hysteresis loops remains unaltered with the thicknesses $\sim$ 12 μm, $\sim$ 13 μm, respectively. As a result, high S value (M_R/M_S) is obtained for Fig. 4.5(b)-(f) as given in Table 4.2.

4.6 First-Order Reversal Curve (FORC) Measurement

So far, the static magnetic study illustrated the complex relationship between magnetization and the applied magnetic field resulting into the different hysteresis loops. However, they are not

capable of revealing the presence of magnetic exchange interaction between the phases in the system. For a deeper understanding of magnetic phase interactions at the nanoscale, the analysis has been extended to include minor hysteresis loop analysis, specifically through First-Order Reversal Curve (FORC) measurements presented on the (H_C, H_U) plane.

Figure 4.6(a) and (b) illustrate the FORC distributions of 0.31 μm and 0.68 μm films, respectively. Fig. 4.6(a) reveals only one peak at $H_C = \sim 35$ Oe centred at $H_U = 0$ Oe which signifies that there is no extra peak except the coercivity in the sample. On the contrary, the 4.6(b) unveils three distinct peaks, two on $H_C = 10$ Oe ('P1') and $H_C = \sim 280$ Oe ('P2') centred at $H_U = \sim -30$ Oe axis while the third one is centred at $H_U = -135$ Oe on $H_C = 160$ Oe ('P3'). The third peak, 'P3', arises in 0.68 μm film due to the interaction between the two other peaks present in the system while the peak, 'P3' is absent in the 0.31 μm film. Therefore, the 0.31 μm film is the non-exchange-spring (non-ES) sample while the 0.68 μm film becomes the (ES) sample. So, in the thicker samples which exhibited such staircase-like hysteresis loop, it is justifiably assumed that FORC distribution of the same would reveal similar pattern on (H_C, H_U) plane.

Though the FORC distribution revealed the magnetic exchange interaction between different phases, it fails to reveal the competition between IP (in-plane) anisotropy and OOP (out-of-plane) anisotropy. Since the signature of weak perpendicular anisotropy is observed with strong IP anisotropy in the 0.31 μm non-ES film, it is assumed that the OOP anisotropy of 0.68 μm ES film at some OOP angle might overcome the IP anisotropy and may exhibit transverse ES [27, 110] nature. Therefore, the minor loop measurement of hysteresis loop was further studied, i.e., FORC measurements of the 0.68 μm sample as a function of OOP angle exploring how such magnetic exchange interaction influences pivoting towards the transverse exchange-spring due to the influence of OOP anisotropy.

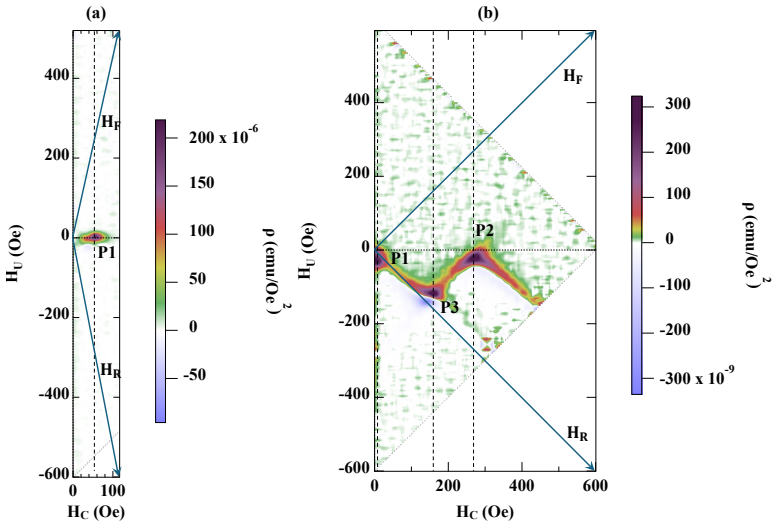


Figure 4.6: IP FORC measurement of (a) 0.31 μm and (b) 0.68 μm films in (H_C, H_U) plane [1].

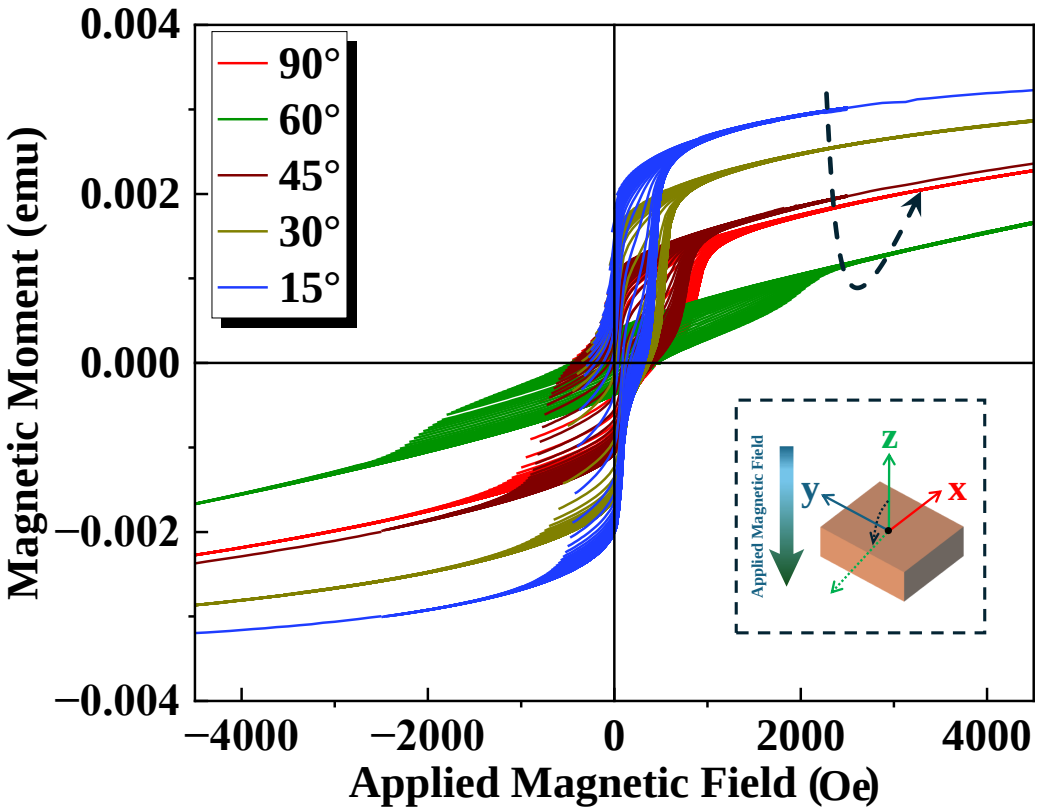


Figure 4.7: OOP Angle dependent raw FORC curves of 0.68 μm film. The inset shows the schematic of the sample and applied magnetic field orientation reveals that the OOP angle is varying along the z-direction while the applied magnetic field direction is fixed along the perpendicular direction [1].

The raw FORC data i.e., individual minor line of the full hysteresis loop for different angles particularly (15°, 30°, 45°, 60°, and 90°) are shown in Fig. 4.7. Though it has been observed initially (in the Fig. 4.5) that the ES film is magnetically isotropic on in-plane, the variation of the moments (first decrease to a certain point and then again start increasing, as highlighted with the arrow) in the OOP plane measurement suggests that the sample is magnetically anisotropic along the OOP direction. The 60° data shows that it has an elongated loop, which is possibly due to the dominance of strong OOP anisotropy over the IP one.

We have now presented the individual raw data, aiming to confirm the competition between in-plane (IP) and out-of-plane (OOP) anisotropy. In Fig. 4.8, the raw minor hysteresis loops of various angles are displayed, along with magnified versions near the ±0.0005 emu region inset at the bottom right of each figure, alongside their corresponding processed FORC distributions on the (H_C, H_U) plane. Notably, a distinct jump in the minor hysteresis loop was observed at the 60° angle, indicating the establishment of an anisotropy-driven metastable state. This phenomenon is consistent with previous findings, where the competition between IP and OOP anisotropy

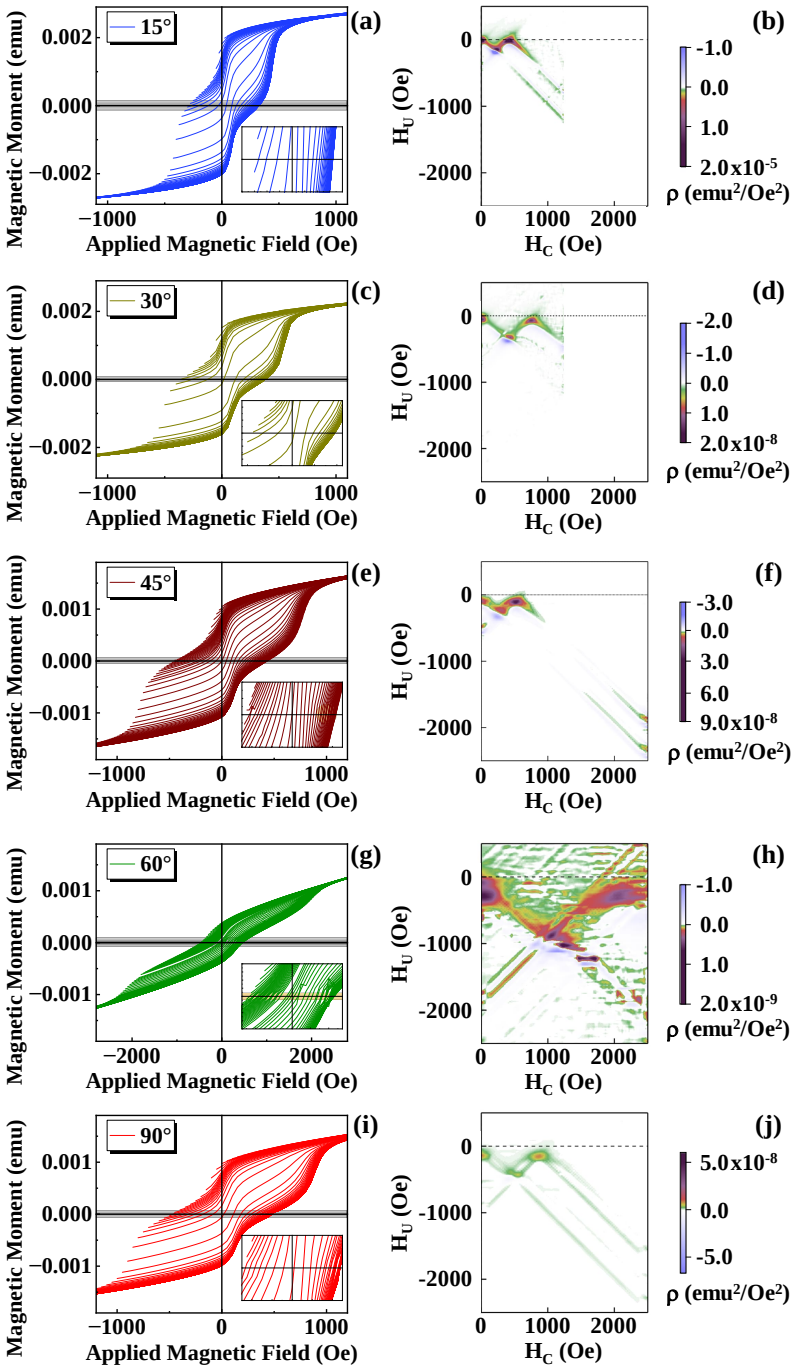


Figure 4.8: OOP angle dependent raw minor loops and its corresponding FORC distribution of 0.68μm film indicating transverse ES nature [1].

leads to a sudden jump in the hysteresis loop and the establishment of a metastable state [138]. Consequently, it could be inferred that between angles 60° to 90°, another phase contributes to the exchange-spring (transverse), which may be suppressed at other angles by a dominant phase.

Thus, in the case of such amorphous and nanocrystalline films, the in-plane exchange-spring may tend to convert to the transverse exchange-spring due to the effect of the emerging metastable state.

4.7 Micomagnetic Simulations

In order to elucidate the experimentally obtained results of the nano-hetero-structured thin films, micromagnetic simulation using MuMax^3 [24] was further performed. An external image as shown in Fig. 4.9(a) (nearest approximation) was utilized in simulation to make the geometry comparable to the experimentally obtained dispersed NHS. In the simulation, each of the dispersed black lines of average thickness 3.50 nm is assumed as crystalline $Co-hcp$ with OOP anisotropy along $(0,0,1)$ direction, while the remaining blank portion represents as amorphous CoP with IP anisotropy along $(1,1,0)$ direction. It is noted that $-X,Y,Z$ signify the $-x,y,z$ directions of the geometry, respectively. We considered different values for the typical magnetic material parameters like Saturation Magnetization (M_S), Exchange Stiffness Constant (A_{ex}), Anisotropy Constant (K_{u1}) as $815\times10^3\ A/m$, $10\times10^{-12}\ J/m$, $1.232\times10^3\ J/m^3$ for CoP and $1400\times10^3\ A/m$, $30\times10^{-12}\ J/m$, $520\times10^3\ J/m^3$ for $Co-hcp$, respectively. We considered the cell size in each direction lower than the exchange length $\left(l_{ex}=\sqrt{\frac{A_{ex}}{K_d}}=\sqrt{\frac{2A_{ex}}{\mu_0 {M_S}^2}}=8.45\ nm\right)$ [133] of the system ensuring inclusion of all exchange interactions properly. The simulations have been performed with cell size = $3\times3\times3\ nm^3$ and the simulation grid size = $512\times512\times128$, which results the final volume of the simulation = $1536\times1536\times384\ nm^3$. We note that, here, $-X,Y,Z$ signify the $-x,y,z$ directions of the geometry, respectively.

Figure 4.9(b) shows the typical three slope hysteresis loop as mentioned in the Fig. 4.5(a) obtained from the simulation. '*' marked positions in Fig. 4.9(b) and (d) are the nucleation state, the signature of the formation of the weak perpendicular anisotropy. The cross-sectional view of the macro-spin configuration of '*' marked position in Fig. 4.9(b) is shown in Fig. 4.9(c), where the red and green arrow represent moments along $+x$ and $-x$ directions, respectively. The cross-sectional view reveals that the slight distorted stripes are formed with alternate upward (white) and downward (black) moments throughout the cross-section, respectively.

To get more insight into the formation of the stripes in the simulation, the quality factor defined as $Q = K/K_d$ has been calculated, where K and K_d are the appropriate anisotropy and the stray field coefficient of the system, respectively. Since units of K and K_d are the same, Q is a dimensionless quantity. Theoretically, it has been proven that stripe formation is favoured by low or moderate Q values (i.e., $Q << 1$ or $Q \simeq 1$) of the system [133]. To validate the effect of the thickness of the NHS in the formation of stripes and its orientation, another sets of simulation

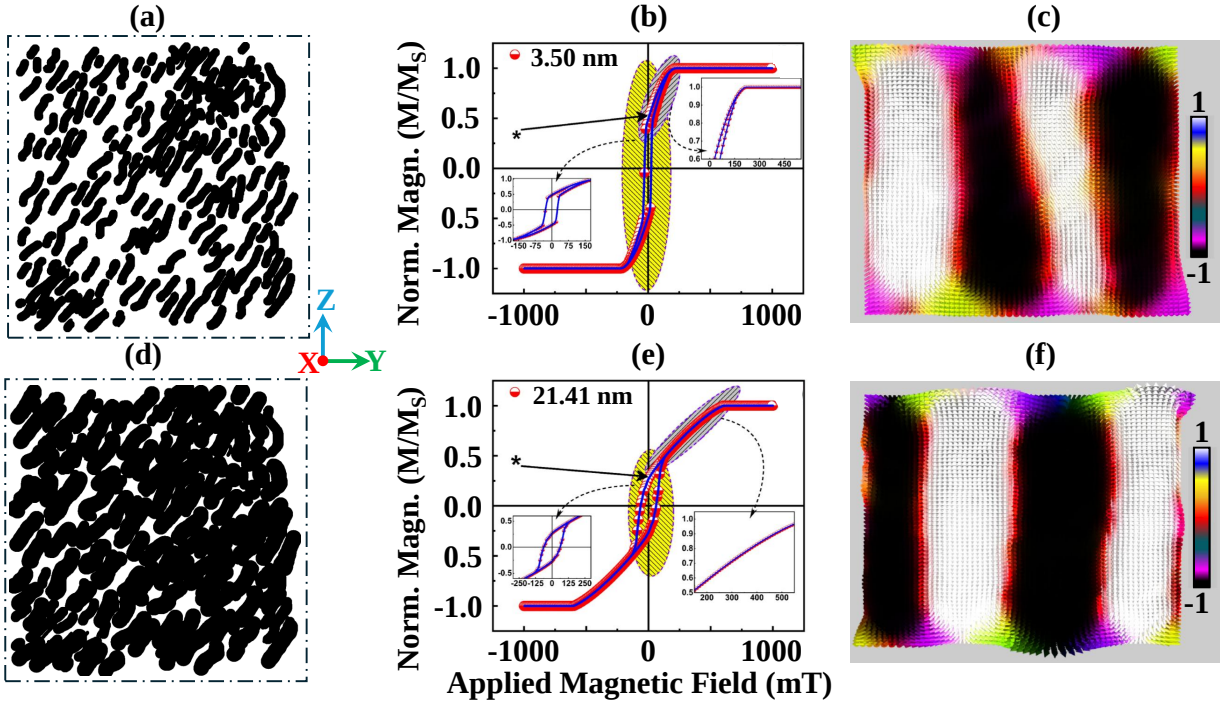


Figure 4.9: (a) An average of dispersed 3.50 nm thick NHS utilized as an input image in simulation at YZ plane. (b) Simulated three slope hysteresis loop with the complex geometry. (c) Cross-sectional macro-spin behaviour of '*' marked position in the hysteresis loop. (c) thick NHS. (d) ≈ 6 times dense 21.41 nm thick NHS utilized as an input image in YZ plane. (e) The simulated large hysteresis loop considering the NHS in (c). (f) the macro-spin behaviour as marked in (e) [1].

have been studied with different thickness of NHSs. By simulation, it has been identified that the critical limit of average thickness of NHS lies between 9.78 nm and 12.66 nm when the stripes change their orientation. Also, subsequently, enhancement in coercivity has been observed. Here, comparatively more denser 21.41 nm thick NHS beyond the obtained critical limit is considered, as shown in Fig. 4.9(d), while The rest of conditions during the simulations remains unchanged.

As discussed, the denser NHS results in the hysteresis loop with an enhanced coercivity, as shown in Fig. 4.9(e), which would also help to increase the energy product (BH_{max}) of the material. Interestingly, in comparison to the stripe domains in Fig. 4.9(c), a significant change in the stripe domains is visible as shown in Fig. 4.9(f), though both the macro-spin behaviours in Fig. 4.9(c) and (f) are taken at the same applied field value from the simulation. The upward and downward moments not only change their positions but also, the stripes of Fig. 4.9(f) are more aligned and straight than that of Fig. 4.9(c). The enhancement of the OOP anisotropy in the later case associated to the broadening the NHS widths might be responsible in stabilizing the stripe domains.

To quantify the variation of the stripe obtain from the simulations as shown in Fig. 4.9(c)

and (f), the variation of energies was calculated, such as exchange energy, anisotropy energy, demagnetization energy, total energy of those two NHSs as a function of applied magnetic field, as shown in Fig. 4.10 (a), (b), (c), (d), respectively. Since the width of the NHS increases in Fig. 4.9(d) compared to Fig. 4.9(a), the strength of the exchange interaction between the $(0,0,1)$ spins and the $(1,1,0)$ spins are much stronger in the NHS of Fig. 4.9(d) than that of Fig. 4.9(a). As a result, the exchange energy increases for the 21.41 nm width NHS compared to that of 3.50 nm NHS, as shown in Fig. 4.10(a). The Q parameter of OOP $Co-hcp$ is small ($Q \approx 0.4$), however, surface anisotropy plays a key role to increase the OOP anisotropy for 3.50 nm NHS, and as a result, the effective Q becomes larger than unity. However, the relative influence of surface anisotropy decreases with the increasing widths of the NHSs, which results into decrease in the anisotropy energy, as shown in the Fig. 4.10(b). Since the demagnetizing field/magnetostatic energy depends on the shape and volume, the demagnetization energy increases because of the increasing widths of the NHS, as shown in Fig. 4.10(c), which favours the formation of the stripe domains. However, beyond a critical thickness of the nano-heterostructure (here, greater than 12.66 nm), the contribution of the shape in demagnetization energy as shown in Fig. 4.10(c) becomes apparent with the change of the slope of the decrease and consequently the slope of the variation of the demagnetization energy for denser sample crosses over the slopes of the others. As shown in Fig. 4.10(d), the total energy for the denser NHS (Fig. 4.9(d)) is comparatively lower than the thinly dispersed NHS (Fig. 4.9(a)), which might be responsible in stabilization of the stripe domains.

The dimensionless parameter, Q plays an important role in determining the applicability of a material and explaining the formation of domain structures. Usually, the soft magnetic materials have $Q << 1$, while the condition, $Q >> 1$ favours a material to be a strong permanent hard magnet. As both the values of Q_{IP} and Q_{OOP} (0.003 and 0.422, respectively) satisfy the theoretical framework, here, stripe domains are formed in the simulation, as seen in Fig. 4.9(c) and (e). Since the recording media should have to be both permanent and easy to switch, materials should consist of neither high nor low anisotropy, i.e., moderate anisotropy value should be desirable. Though magnetic hardness is not directly related to the properties of high and low relative anisotropy, i.e., the high and low coercivity. In conjunction with the magnetic microstructure, other additional structural features such as lattice defects, grain boundaries, sample or particle size, and surface irregularities take play to determine the coercivity of the material. The intrinsic Q parameter determines the ease with which a desired magnetic hardness (or softness) can be achieved. Now,

Figure 4.10: Variation of simulated (a) exchange energy (b) anisotropy energy (c) demagnetization energy and (d) total energy as a function of applied magnetic field for different widths of the NHS [1].

if a system built with an intrinsic stripe domain structure, the Q value should satisfy the criteria, i.e., $Q < 1$ or $Q \approx 1$, i.e., with this $Q \approx 1$ condition, the desired criteria of the recording media have already been achieved. Moreover, the system does not require any external agitation such as ac demagnetization or thermal perturbations for modulating the parameters and thereby can serve as a building block for recording media [110, 133]. Additionally, the ES structures with non-collinear anisotropies, i.e., the transverse ES springs with canted interfacial moments can potentially be tuned to facilitate the absorbed spin current to exert even greater torque for optically induced magnetization precession in spin transfer torque (STT) devices, thus providing a path for improving the efficiency of such devices to a great extent[110, 133].

4.8 Conclusion

Utilizing the conventional DC electrodeposition technique, the nano-hetero-structured transverse exchange-spring (ES) amorphous/nanocrystalline magnetic thin films have been fabricated *in situ* from a single starting material through the electrochemical control of hydrogen evolution within the system. Our study offers an approach to prepare the transverse exchange-spring and exchange coupled (EC) structure in a cost-effective and scalable manner, opening the door to modify the bulk magnetic properties even in a single ferromagnetic thin film, and further the study of exchange-spring mechanism evolving to exchange coupled state via transverse exchange-spring in single amorphous/nanocrystalline film. The quasi-static magnetic properties of nano-hetero-structured CoP thin films characterized by magnetic stripe domains at remanence have been investigated both experimentally and by performing micromagnetic simulations. The signature of the stripe domains and its modification (the corrugated stripes) are prominently observed in the MFM and hysteresis loop measurements and supplemented by micromagnetic simulations. The existence of the OOP anisotropy in the system is confirmed by MFM, first-order reversal curve (FORC) measurements and micromagnetic simulations. Micromagnetic study further confirms that the thicknesses of the nano-hetero-structures influence the nature of the hysteresis in such amorphous/nanocrystalline film. The increment in the coercivity and energy product in the ES and EC structures, and the performed micromagnetic simulations demonstrated here, provide a wonderful opportunity to use these materials and their derivatives for next generation spintronic devices.

5

Spin Waves in Exchange Spring Nanomagnets

This chapter is based on the following paper published in Physical Review B [2][1,⋆] and the International Conference presentation[2,#].

5.1 Introduction

Conventional nanomagnetic thin films offer either high saturation magnetization with low coercivity (soft magnetic materials) or moderate saturation magnetization with a high coercivity (hard magnetic materials). However, such thin films can deliver the advantages of both the worlds simultaneously if they are consisted of alternate (bi/tri)−layers and exchange coupled at the manometer scale. Exchange Spring (ES) [25, 26, 73] nano-hetero-structured systems, in which both the hard and soft magnetic materials are tuned (compositions, thicknesses, and morphologies) at the nanometre scale to provide high energy product (BH_{max}) [26, 73, 149], has taken keen attention because of its potential applications in recording media [110], spintronics [150, 151], spin torque nano-oscillator (STNO) devices [152] etc. Formation of the ES systems is generally

[1] Spin waves in exchange nanoheterostructured amorphous/nanocrystalline films, **A. Samanta**, S. Roy, *Physical Review B* **107**, 214449 (2023); DOI: 10.1103/PhysRevB.107.214449

[2] Brillouin Light Scattering Study of Spin Waves in CoP Exchange Spring Thin Films (Oral Presentation), **A. Samanta**, G. Gubbiotti, S. Roy, *'Intermag 2021 Conference'*, (Virtual), April 26-30, 2021.

⋆,#These works were done in collaboration with Dr. Gianluca Gubbiotti, Istituto Officina dei Materiali - Consiglio Nazionale delle Ricerche (CNR-IOM), Perugia, Italy. Particularly, the corresponding BLS measurement work was performed at CNR-IOM, Perugia, Italy by Dr. Gianluca Gubbiotti. Arindam did the associated BLS analysis and wrote the paper.

favored by the critical conditions, i.e., the thickness (L_S) of the soft phase being larger than twice the domain wall width (δ_H) of the hard phase $L_S > 2\delta_H$ [26], where the soft and hard phases reverse at the distinguishable field at the same time and act like different units in the same system.

A flurry of research articles on these ES systems has been published in the last three decades [25–27, 73, 77, 101, 110, 123, 139, 149–152], and consequently, with various combinations of materials such as nanocomposite [77], bi-layer thin films [102, 122, 126, 131, 136, 153], magnetic tri-layer structure [154] in multiple systems have been studied. Several techniques, such as magnetron sputtering [74], molecular beam epitaxy (MBE) [75], and heat treatment, including rapid annealing [140], have been utilised for developing ES NHSs. However, those ES structures were constituted with the *"ex situ"* process of deposition of multi-nano-layer/structures and were studied mostly with static magnetic measurements [155]. Lately, ES systems have been studied through dynamic measurements [73, 103–105, 156, 157]. However, the ES system has not been reported to date in an in-situ single nano-hetero-structured (NHS) thin film prepared through the electrodeposition technique and characterized through their dynamic measurements. Here, it is worth mentioning that the term *"ex-situ"* means the bi/tri-layer structures are prepared with two/multiple different sources of materials (namely multiple targets in sputtering techniques), while the *"in-situ"* term signifies that a single source of materials (in an electroplating bath) could be sufficient to prepare bi/tri-layers nano-hetero-structures. For example, to prepare the $SmCo/Fe$ or $NiFe/[Co/Pt]$ ES structures, two different sputtering targets have been used. However, in this reported work, the NHSs have been prepared from a single bath itself, without requiring a second bath in the electrodeposition process for generating the bi-layer structures. We have chosen electroplating technique to fabricate ES NHS due to its low cost and high yield, which lends itself around complex nano-topologies [11, 53]. Though thin films of cobalt phosphorous alloys (CoP) have been prepared by electrodeposition technique, and have been extensively studied by several groups [46, 55–57, 80, 81, 84, 107, 108], however, the emergence of ES magnetic structure in an *"in situ"* amorphous and nanocrystalline CoP film as a result of self-organized process from a single bath electrochemical deposition technique has not been identified/studied and reported yet.

In this work, the ES magnetic structure is demonstrated in a stress-free, optically smooth nano-hetero-structure (NHS) of a single CoP thin film developed by a modified stable acidic bath chemistry in an electrodeposition process. Consequently, by performing the measurements with SEM and EDX (Zeiss-Oxford Instruments), XRD (Panalytical XPert Pro), and cross-sectional TEM (JEOL TEM 2100), the surface morphology at the micron to the nanometre scale, composition, and the cross-sectional NHSs of the thin films have been determined. Crossover from low coercivity non-ES system to the ES magnetic structures at room temperature has also been demonstrated using quasi-static magnetic measurements by hysteresis loop tracer (ShB MESA,

USA) and First Order Reversal Curve (FORC) measurements (Quantum Design PPMS Versalab, USA). Subsequently, the non-ES and ES structured CoP samples have been further studied by Brillouin light scattering (BLS) spectroscopy and investigated the effect of interfacial exchange energy.

Contextually, it is imperative to mention that the exchange energy plays a crucial role in realizing the exchange coupled nano-hetero-structured systems, irrespective of the ES or non-ES structures. Since thus prepared in-situ systems have significantly increased the number/volume of interfaces compared to the conventional multi-nano-layered systems, it is important to study the effect of the interfacial exchange coupling in the system. Brillouin light scattering (BLS) spectroscopy is a powerful technique to investigate the effect of such interfacial exchange coupling (J_{I}) in the NHS system.

5.2 Experimental Methods

The following chemicals and reagents [57] are used for preparing smooth, shiny, amorphous CoP thin film utilizing the electrodeposition technique at room temperature ($293K$): Phosphorous acid (3.30), Phosphoric acid (5.90), Cobalt chloride hexahydrate (18.87), Cobalt carbonate (1.55), Glycine (1.15), Saccharine (1.51), NTA (1.52)- values in the parenthesis are amount of the chemicals in g/100 mL. The pH of the bath is maintained between $\sim 0.72 - 0.86$.

The electrodeposition of amorphous CoP thin film using direct current (dc) plating on 2 cm $\times$ 2 cm Si-wafer with top conducting seed layer of 10 nm Ti & 200 nm Au has been carried out utilizing CHI 660B potentiostat. A constant dc of 40 mA has been applied for 15 and 60 minutes. The microstructural analysis and elemental characterization of the electrodeposited films have been performed using Zeiss Scanning Electron Microscope (SEM) and Energy Dispersive X-ray Spectroscopy (EDX) analysis (Oxford Instruments). The TEM lamella cross-sections were prepared using a Dual Beam focused ion beam (FIB) of FEI Helios NanoLab 600i. To protect from the FIB milling process, three layers of C/Pt/Pt have been deposited on the sample within the Dual Beam FIB (50nm/300 nm by electron beam induced deposition/ 2 μm by ion beam induced deposition). The lamella was prepared and thinned down for the TEM analysis. The thinning at 30 kV was finished with a final polishing at 5 kV (47 pA) to reduce the ion-beam induced damage to less than 2 nm thin layers on both sides. Ultrafine microstructural analysis was performed through TEM (Jeol 2100; 200 kV) using a double tilt sample holder. The X-Ray diffraction (XRD) patterns were measured through Panalytical X'Pert Pro setup with Cu K_α radiation (40 kV, 50 mA) at a wavelength of 0.154 nm to characterize the crystalline/amorphous structures.

The magnetic measurements of the deposited films have been carried out in a hysteresis Loop

tracer (MESA 200, ShB Instruments, USA). The First order reversal curves (FORC) measurements are done with Quantum Design Physical Property Measurement System (PPMS) Versalab (USA) with VSM-FORC option. The PPMS system has been used to measure a large number [229 for Sample 1 (here after as the non-ES sample) and 159 for Sample 2 (here after as the ES sample)] of FORCs. Typical FORC measurements are done as follows: First, the sample is saturated, and then the moment has been measured starting from a reversal field H_R back to positive saturation ($+H_{sat}$), that traces out a FORC. A family of FORCs has been yielded for different values of H_R, with equal field spacing (H_F). Following that, the FORC distribution is extracted by a mixed second-order derivative: $\rho(H_R,H_F) = -\frac{1}{2M_S}\left(\frac{\partial^2 M(H_R,H_F)}{\partial H_R \partial H_F}\right)$, where M_S is the saturation magnetization. The FORC measurement ensures that the pure reversible components of the magnetization are eliminated, and thus any non-zero ρ corresponds to irreversible switching processes present in the system [141–143]. Here, the FORC distribution $\left[\rho(H_C,H_U)\right]$ is presented on (H_C,H_U) plane, defining, $H_C = \frac{1}{2}(H_R - H_F)$ as the local coercivity, and $H_U = \frac{1}{2}(H_R + H_F)$ as the interaction field or bias field obtained by post-processing the raw data with FORCinel Software [121].

The Brillouin light scattering (BLS) spectroscopy [105, 156, 157] has been used to measure the thermally excited SWs in the frequency range between 1 and 50 GHz. The BLS measurement was operated using a single-mode diode-pumped solid state laser at wavelength, $\lambda = 532$ nm monochromatic laser light with an incidence angle of $\sim$ 10 degrees with respect to the sample normal, which results in a magnon wave number, $k_{||} = 2k_i.sin\theta = 4.1 \times 10^6$ rad/m, ($k_i = 2\pi/\lambda$). The backscattered light has been analysed utilizing a Six $(3+3)-$ pass Sandercock-type tandem Fabry-Perot interferometer. An external magnetic field (H) has been applied parallel to the film surface and perpendicular to the plane of incidence of the light, i.e., the Damon-Eshbach configuration.

5.3 Structural Characterization and Elemental Analysis

Initial instability of the electrolytic bath causes the development of quite stressed and rough thin films (R_q = $\sim$316 nm), even for the comparatively lower thicknesses ($\sim 0.50\ \mu m$) of the film, as shown in Figure 5.1(a). The possibility of such high stress might be the presence of high surface tension between the working electrode and the electrolyte, which causes the samples to be stressed with microcracks, rough and thus incompatible for the BLS measurements. A surface tension reducing agent - glycine, stress-relieving additives - a combination of naphthalene trisulfonic acid (NTA) and Saccharine [111, 158] have been added to the solution to stabilize the bath and to reduce the surface tension between the working electrode and electrolyte. Consequently,

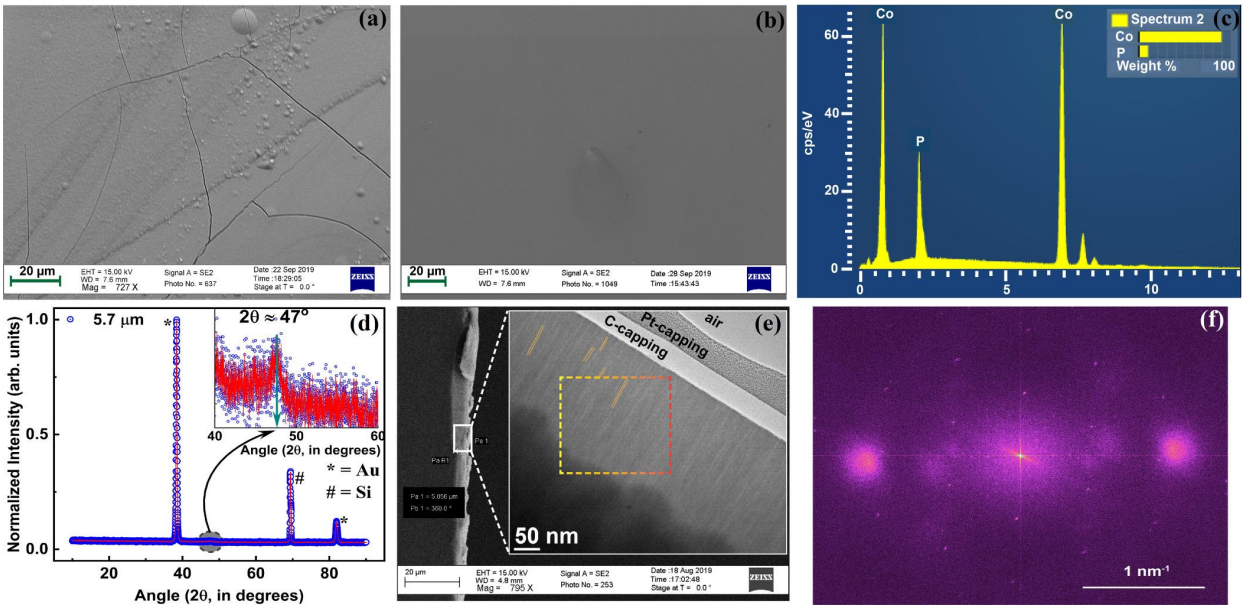


Figure 5.1: Typical SEM top surface morphology of (a) stressed thin film, (b) stress free thin film. (c) EDX spectrum of one of the samples. (d) XRD-spectrum of the sample. (e) Cross-sectional TEM micrograph of the electrodeposited CoP thin films showing the individual striations (white lines in the NHS) in (thickness 2-5 nm) nm range, typical and (f) FFT of the selected region of TEM as highlighted in (e) [2].

stress-free, smooth and glossy thin films have been developed even for the comparatively higher thicknesses ($\sim 1.4 - 5.7\ \mu m$) of the film. Figure 5.1(b) shows a typical stress free film of 1.4 μm thickness. The top surface quality of the film remains unaltered even for the 5.7 μm thick film.

Since phosphorous content in CoP thin film plays a crucial role to determine the crystallinity of CoP thin film, it is important to explore the qualitative and quantitative analysis of phosphorous in the electrodeposited thin film [159]. A typical example of the EDX spectra of CoP thin film (here, for 1.4 μm film) is shown in Figure 5.1(c), confirming the different dominant Co and P peaks. For example, the peaks at 0.77 keV, 6.93 keV, and 7.64 keV unveil the L_α, $K_{\alpha 1,2}$, and K_β peaks of 'Co', while the peak at 2.13 keV corresponds to the K_β peak of 'P', respectively. EDX study at different places of the film yields the similar stoichiometry of the thin films, i.e., the overall atomic percentage of cobalt (86%) and phosphorous (14%) in the CoP thin films remains almost invariant, which corroborates the homogeneity in the composition of the films. We have also observed that the deposited films retain their stoichiometry for a long deposition time. We have obtained this improvement due to the addition of the stabilizing agent in the plating bath, which restrains the bath from precipitating over a long period.

Figure 5.1(d) shows the XRD pattern of the prepared 5.7 μm nano-hetero-structured CoP thin film with the three dominating substrate peaks only, i.e., the peak near $2\theta = 69.22^o$ (Si-wafer) and the other two peaks near $2\theta = 38^o$ and 83^o (top conducting Au-seed layer), hence, the

gross amorphousness of the prepared samples has been verified. However, the magnified XRD profile (inset in Figure 5.1(d)) shows a minor and broad peak at $2\theta \sim 47^o$, which confirms that the samples also have a nanocrystalline Co-hcp (002) phase. Though, the overall XRD spectra with three dominant substrate peaks do not exhibit a significant difference, however, there is a subtle change observed in the magnified XRD spectra in terms of minor peaks, resulting into a subtle change in the nanocrystalline structure due to the increase in the film thickness. For the 1.4 μm thick film [not shown in the main manuscript], there were two minor peaks at $2\theta \approx 45^o$ and $2\theta = 77.5^o$, which signify the coexistence of nanocrystalline Co-hcp (002) and Co-hcp (110) phases, respectively.

Nano-hetero-structures/multi-nano-layers in the ES CoP system have been experimentally confirmed by the cross-sectional TEM as shown in Figure 5.1(e). Here, the white lines in the TEM image correspond to the $Co-hcp$ phases, and black regions correspond to amorphous CoP, where the individual striped nano-crystallites with 2-5 nm thicknesses ($Co-hcp$ phases), as measured from the TEM, are embedded within the amorphous matrix (CoP phase). The Fast Fourier Transformation (FFT) of the selected region of the TEM image in Figure 5.1(e) is shown in Figure 5.1(f) confirms the crystalline nature of the film which could be attributed to the nanocrystalline phases present in the sample.

However, from XRD [as shown in Figure 5.1(d)], for the 5.7 μm film, the relative intensity of Co-hcp (002) phases is increased compared to the Co-hcp (110) phases. Hydrogen evolution during electrodeposition might have favoured the formation of these hcp textures. The size of the crystalline phase in the nano-hetero-structured film as calculated utilizing the Scherrer equation [$\tau = \frac{\kappa \cdot \Lambda}{\beta \cdot cos\theta}$, where τ is the mean grain size, κ is a dimensionless shape factor with a value close to unity, Λ is the X-ray wavelength (1.54 Å), β is the line broadening at half the maximum intensity (FWHM) of the crystalline peak, and θ is the Bragg angle (in degrees)] is found to be $\approx (1.239 \pm 0.143)$ nm, which is in the same order of the Co-hcp stripe thickness obtained from the TEM. Therefore, while the surface morphology remains unaltered with the increase in overall thickness, a subtle nanocrystalline structural variation with enhanced out-of-plane (OOP) anisotropy (as detailed below) is observed. In order to investigate the nature of anisotropies present, it is needed to study the constituent energies of the system. The total energy (5.1) can be written as an integral over the sample volume [133]:

$$E_{total} = \int \left[w_{\text{ex}} + w_a + w_d + w_z + w_{me} \right] dV \tag{5.1}$$

where, 'w' denotes the corresponding energy density of the material. Symmetric exchange energy density, 'w_{ex}'$= A_{\text{ex}}.\nabla(\vec{m})^2 = A_{\text{ex}}.[\nabla(\vec{m}_x)^2 + \nabla(\vec{m}_y)^2 + \nabla(\vec{m}_z)^2]$ (A_{ex} be the exchange stiffness

constant). 'w_a' is the anisotropy energy density (due to crystallinity of the material). Stray field energy density or magnetostatic energy density, 'w_d'$= \int \left(\frac{1}{2}\mu_0 \vec{H}_d \cdot \vec{M}\right) dV$. '$w_z$' is external energy density or Zeeman energy density $= \mu_0 \vec{H} \cdot \vec{M}$, and the last term, '$w_{me}$' is the magnetoelastic (ME) energy density $= k.\lambda_s \cdot \sigma_p \cdot (S)^2$, where, $k =$ constant $(+ve)$, $\lambda_s =$ magnetostriction constant, $\sigma_p =$ the interfacial planar stress and 'S' is the squareness ratio $= M_R/M_S(+ve)$, here, M_R and M_S are remanent magnetisation and saturation magnetisation of the material, respectively.

In order to elucidate the origin of out-of-plane (OOP) anisotropy in the system, first, the magnetoelastic (ME) energy density is considered. A significant aspect of ME energy density, is that if λ_s and σ_p have opposite signs in the expression of the ME, i.e., $w_{me} = k.\lambda_s \cdot \sigma_p \cdot (S)^2$ the ME energy becomes negative (-ve); and that -ve ME energy density has the ability to produce an out-of-plane (OOP) anisotropy in the system [133]. In this ES system, the nano crystalline $Co-hcp$ phases are embedded in the amorphous CoP matrix. As shown in Figure 5.1(e), the inset in the TEM image shows that the thickness of $Co-hcp$ is around 2-5 nm. For $Co-hcp$, a positive value of λ_s $[(+2.50 \pm 0.20) \times 10^{-5}]$ [160] is expected above 2 nm thickness [147, 160]. Earlier, experimentally, it was shown that CoP thin films have a -ve λ_s value $[(-2.75 \pm 0.20) \times 10^{-6}]$ [90]. Hence, two different magnetostrictive material coexist in the nano-hetero-structured system, which might be responsible for the generation of the compressive stress in the system, i.e., $\sigma_P = -ve$. So, the ME becomes $-ve$ and thus helps generate the out-of-plane anisotropy in the system. Therefore, it is assumed that the nanocrystalline $Co-hcp$ (002) phases in the NHSs are responsible for the OOP anisotropies in the system, which get enhanced beyond 2 nm thickness with the simultaneous decrease in the content of nanocrystalline $Co-hcp$ (110) phases.

5.4 Static Magnetic Properties

Experimentally obtained normalized hysteresis loops along the direction X ($dir.1$) and direction Y ($dir.2$) of the *in-situ* NHS single CoP materials (measured by SHB instruments) have been shown in Figure 5.2; $dir.1$ and $dir.2$ represent the longitudinal and transverse directions, respectively. Hence, the X and Y directions are two mutually perpendicular directions on the sample plane, i.e., both the axes, $dir.1$ and $dir.2$ ($dir.2 = dir.1 + 90^o$), lie in-plane to the sample. The interesting fact for all the normalized hysteresis loops is that both dir. X and dir. Y are practically equivalent, i.e., all the samples are magnetically isotropic in the XY plane, and there is no identifiable easy or hard axis lying on the plane of the material. Previously, Ausanio et al. [147] showed that the magnetisation with OOP anisotropy was inclined at an angle with respect to the sample plane in case of isotropic hysteresis loops in the X and Y directions on the sample plane. Additionally, following the nature of the hysteresis loop as detailed below, it has been assumed that there must

be a weak OOP anisotropy present in the thinner non-ES sample.

Figure 5.2.(a) shows (1.4 μm film) low coercivity ($\sim$ 31 Oe) non-ES hysteresis loop, while that of Figure 5.2(b) (5.7 μm film) exhibits a high coercivity ($\sim$ 220 Oe) ES nature with steps in the hysteresis loops along with the low coercivities ($\sim$9 Oe and $\sim$31 Oe). Three distinct regions are prominent in the non-ES sample, i.e., (i) hysteresis at the applied field below $\sim$ 25 Oe, (ii) a linear region at the applied field between 25 Oe to $\sim$ 150 Oe, where the magnetisation changes almost linearly with the applied field, (iii) the saturation magnetisation beyond $\sim$ 150 Oe, whereas the region (ii), is a common signature of thin films having a weak perpendicular anisotropy [148]. Here, in the 1.4 μm thick sample, in-plane (IP) anisotropy arising out of the CoP amorphous phase strongly dominates over the weak perpendicular anisotropy arising out of the Co-hcp phase.

On the other hand, a staircase-like hysteresis loop, one of the signatures of ES structure, is obtained with two distinguishable coercivities in a single material (5.7 μm), as shown in Figure 5.2(b). In this case, the two different phases, $Co-hcp$ phase (corresponds to the relatively higher coercivity) and the amorphous CoP phase (corresponds to lower coercivity) are non-rigidly coupled to each other and act as separate units in the same material. Hence, with the application of an external magnetic field, both the phases reverse at the different magnetic fields, as neither IP nor OOP anisotropy dominates each other, i.e., the OOP anisotropy becomes comparable to the IP anisotropy in the ES system, however, the sample magnetization still lies in the plane of the material even if there is OOP anisotropies present in the system. As a result, a high S (M_R/M_S) value (0.8333) is obtained for 5.7 μm film, as shown in Figure 5.2(b) in comparison to the 'S' value (0.6234) of 1.4 μm film as shown in Figure 5.2(a).

The presence of different coercivities in 1.4 μm and 5.7 μm films is prominently visible in the corresponding differentials of the magnetisation values [dir-2 (typical)] as in Figure 5.2(c) and (d), respectively. It is interesting to note that the 1.4 μm film also has a smaller coercivity of $\sim$9 Oe along with $\sim$32 Oe, which is invisible as such in the normal hysteresis loop in Figure 5.2(a). This arises possibly due to the nano-hetero-structure, i.e., the presence of Co-hcp phase within the amorphous matrix, as shown in the insets of Figure 5.2(c). Similar characteristics, i.e., low coercivities of $\sim$9 Oe and $\sim$23 Oe and a comparatively higher coercivity of $\sim$242 Oe, are also observed for 5.7 μm film, as shown in the insets of Figure 5.2(d).

5.5 First—Order Reversal Curve (FORC) Distribution

In order to comprehend the magnetic phase interactions in the nanoscale regime, it has been further analyzed using minor hysteresis loop analysis, namely FORC measurements. The corresponding FORC distributions obtained with smoothing factor of 4 for 1.4 μm and 5.7 μm films on (H_C,H_U)

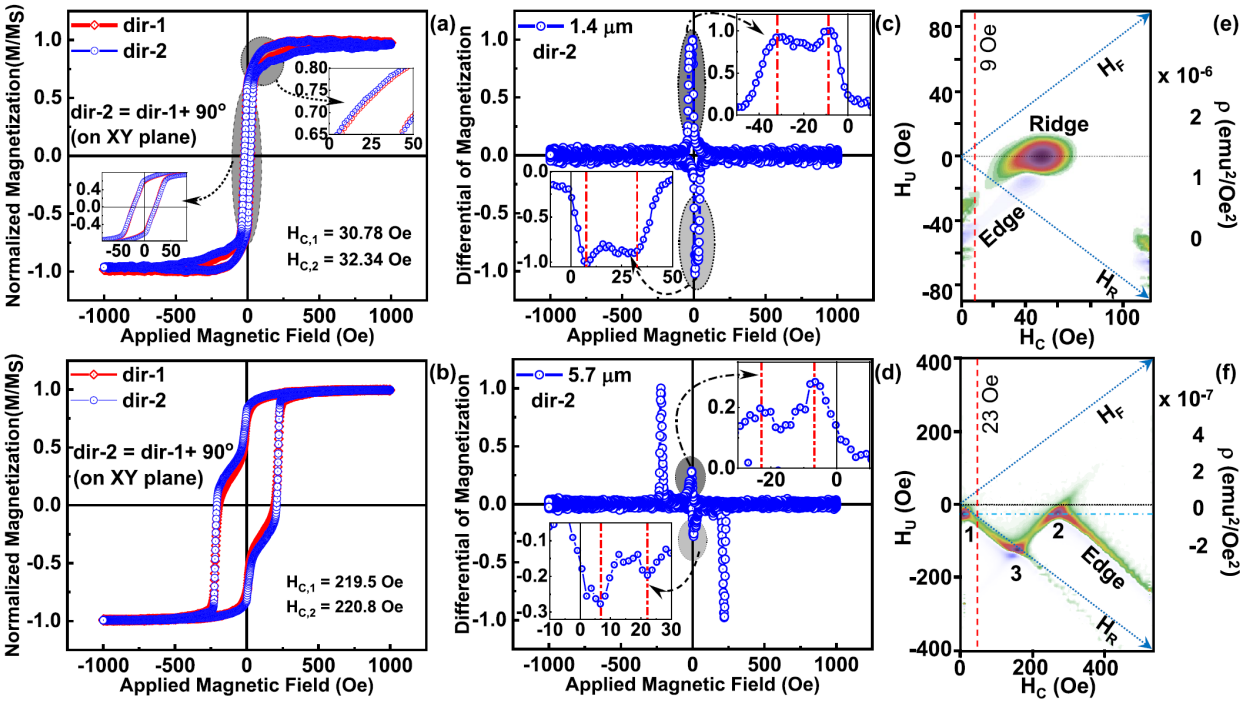


Figure 5.2: Hysteresis loop of the DC electrodeposited CoP thin films measured in ShB Hysteresis Loop tracer in XY plane; here, dir-2 = dir-1+ 90^o. The thickness of the films is (a) 1.4 μm, (b) 5.7 μm, for the electrodeposition time (a) 15 min, (b) 60 min, respectively. (c)-(d) Differential of magnetisation of the (a) 1.4 μm, (b) 5.7 μm thick thin films, respectively. Red dotted lines indicate different coercivities in the low field range. (e)-(f) The FORC distributions on (H_C, H_U) plane for non-ES and ES samples, respectively [2].

plane are portrayed in Figure 5.2(e) and (f), respectively, displaying completely two different reversal mechanisms present in the systems. The prominent feature of FORC distribution of 1.4 μm film is centered at H_U = 0 Oe and $H_C \sim 45$ Oe [Figure 5.2(e)], while that of the ∼9 Oe peak [as observed in Figure 5.2(c)] is invisible for 1.4 µm film. Again, the FORC distribution ensures the elimination of the pure reversible components of the magnetization. Hence, the peak at ∼9 Oe in 1.4 µm film must be the reversal phase of the system.

Figure 5.2(f) reveals a significant change for 5.7 μm film, i.e., now the center has shifted to -25 Oe along H_U axis at $H_C \sim 9$ Oe (peak 1). It is interesting to note that the $\sim$ 23 Oe peak [as observed in Figure 5.2(d)] is invisible in this case. Hence, the peak at ∼9 Oe in 5.7 µm film must be the irreversible phase present in the systems while that at $\sim$ 23 Oe confirms its reversible nature. The loop reaches the trough at $H_U \sim 135$ Oe and $H_C \sim 160$ Oe (peak 3), following that the next center arises again at $H_U = -25$ Oe and $H_C = 270$ Oe (peak 2), which necessarily means that a prominent different irreversible phase has been introduced into the system along with the reversible phase ($\sim$ 23 Oe). The shift in the FORC distribution on the H_C plane confirms the increment of the coercivity in the ES sample compared to the non-ES sample.

Additionally, the positive and negative signatures (edges) reveal the deviation of the hysteresis loop from an ideal hysteron. On the other hand, the complex FORC behaviour of the ES sample confirms that the phases interact strongly between them in the nano-level and are not independent as it is in non-ES sample, which are imperceptible from the conventional hysteresis loop. In an ES system, the soft phase should be fully reversible [26] and the hard phase should be irreversible [123] while they are only coupled via exchange interaction [26, 73, 123]. Though both reversible ($\sim$9 Oe) and irreversible ($\sim$45 Oe) phases present in the 1.4 μm film, however, lack of any exchange interaction between those phases, as evident from the absence of any interaction peak in Figure 5.2(e), make the sample non-ES system. On the contrary, the reversible $\sim$ 23 Oe and the irreversible $\sim$270 Oe phases are connected through a strong exchange interaction in the 5.7 μm film, as observed in Figure 5.2(f) (peak 3 of $\sim$160 Oe), make the 5.7 μm film as ES system. The tiny shift (-25 Oe) in the H_U value is due to the exchange interaction present in the ES system [141, 142] and this small amount of field might be due to the ES effect, as explained earlier.

The complex FORC behaviour of ES sample could be explained as follows. In FORC study, the magnetic field is first saturated and then reduced from that positive saturation to small negative fields, where the high coercivity phase (possibly Co-hcp, here) remains positively saturated while the low coercivity phase follows the field reversibly, which then relaxes to a positive orientation in the absence of a field due to the exchange coupling to the high coercivity phase. In the following sections, it has been elucidated analytically.

5.6 Analytical Formulation by Exchange Energy Calculation

To elucidate the enhancement of the exchange exchange energy further, the influence of nano-hetero-structure (NHS) has been considered in exchange energy. Considering the continuum approximation method [3], which excludes the discrete nature of the lattice, the Hamiltonian ($\hat{H}$) of the system is expressed as,

$$\hat{H} = N \sum_{<i,j>} J_{ij}(S_i \cdot S_j) \tag{5.2}$$

where, N is the number of atom present in the system, J_{ij} is the exchange constant or exchange integral, the symbol, $\sum_{<i,j>}$ denotes the sum over nearest-neighbours. Since this present system is ferromagnetic, it is assumed that the angles between the nearest-neighbour spins (θ_{ij}) are very small, i.e., $\theta_{ij} << 1$ for all i and j, which lead to the result that the spins are not aligned completely, and hence, the *Exchange energy* could be written as,

[3] *Chapter 4 & 5, Magnetism in Condensed Matter by Stephen Blundell, Oxford University Press*

$$E_{ex} = -NJ_{ij}S^2 \sum_{<i,j>} cos(\theta_{ij}) \tag{5.3}$$

for $\theta_{ij} << 1$, $cos(\theta_{ij}) \approx 1 - \theta_{ij}^2/2$. So, E_{ex} becomes,

$$E_{ex} = constant + \frac{NJ_{ij}S^2}{2} \sum_{<i,j>} \theta_{ij}^2 \tag{5.4}$$

Utilizing the notations from the Figure 5.3,

$$\theta_{ij} \approx |\vec{m}_i - \vec{m}_j| \approx |\vec{r}_{ij} \cdot \nabla|, \tag{5.5}$$

and considering $J_{ij} = J_1$, and $\vec{m} = \vec{M}/M_S$, $\vec{m}$ be the normalized unit vectors, where $\vec{M}$ is the magnetization and M_S is the Saturation Magnetization, the Energy term can be rewritten as.

$$E_{ex} = \frac{NJ_1S^2}{2} \sum_{<i,j>} [(\vec{r}_{ij} \cdot \nabla)m]^2 \tag{5.6}$$

While calculating the energy term, the constant term which only refers to the energy of the fully aligned state has been ignored. Thus, ignoring the discrete nature,

$$E_{ex} = A_{ex} \int_V \left[\nabla m_x^2 + \nabla m_y^2 + \nabla m_z^2\right] d^3r = A_{ex} \int_V \left[I\right] d^3r \tag{5.7}$$

where, I be the integral, i.e., $I = \nabla m_x^2 + \nabla m_y^2 + \nabla m_z^2$.

Here, $A_{ex} = 2NJ_1S^2z/a$ is known as the exchange stiffness of the material, a = nearest neighbour distance and z is the number of sites in the unit cell. A_{ex} has the typical values in the order of pJ/m (10^{12} J/m) range.

Now, if the next-nearest-neighbour exchange constant is considered, J_2 along with the term J_1, number of reduced moments having in-plane (IP) anisotropy is denoted as N_1 and that of out-of-plane (OOP) anisotropy is N_2, A_{ex}^1 and A_{ex}^2 are the exchange stiffness constant of the IP and OOP

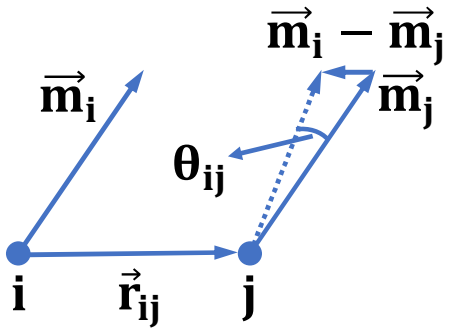


Figure 5.3: Representations of reduced moments m_i and m_j at neighbouring sites i and j separated by a vector $\vec{r}_{ij}$. The angles between the reduced moments, m_i, and m_j, is θ_{ij} [2].

anisotropies respectively, the energy value becomes,

$$E_{ex} = N_1 A_{ex}^1 \int_V I_1 d^3r + N_2 A_{ex}^2 \int_V I_2 d^3r \tag{5.8}$$

Considering the non-ES and ES systems in the studied samples, it can be comparatively said that the Exchange energy present in the thicker sample, here denoted as ES system (E_{ex}^{ES}) is greater than that in the non-ES system ($E_{ex}^{non\text{-}ES}$), as N_2^{ES} is greater than $N_2^{non\text{-}ES}$ due to the increase in the thicknesses of the individual striations of the grown NHS, i.e.,

$$\frac{E_{ex}^{ES}}{E_{ex}^{non\text{-}ES}} = \frac{N_1^{ES} A_{ex}^1 \int_V I_1 d^3r + N_2^{ES} A_{ex}^2 \int_V I_2 d^3r}{N_1^{non\text{-}ES} A_{ex}^1 \int_V I_1 d^3r + N_2^{non\text{-}ES} A_{ex}^2 \int_V I_2 d^3r} \tag{5.9}$$

$$\Rightarrow \frac{E_{ex}^{ES}}{E_{ex}^{non\text{-}ES}} > 1 \quad [as,\ N_2^{ES} > N_2^{non\text{-}ES}]. \tag{5.10}$$

As the E_{ex} term is independent of any overall thickness parameter, it could be mentioned that the evolution of ES is not directly related to the overall thickness of the film, rather, it depends on the thicknesses of the individual striations of the internal nano-hetero-structures grown inside the film. This enhanced exchange energy in the thicker samples being the exchange between relatively stronger out-of-plane (OOP) anisotropies of Co-hcp nano-striations and in-plane (IP) anisotropy of CoP amorphous matrix help create an exchange spring state with higher coercivity and signature step-hysteresis loop.

5.7 Brillouin Light Scattering Spectroscopy

Thermally excited magnons have been further studied using Brillouin Light Scattering (BLS) spectroscopy in understanding the ES nano-hetero-structured system, as BLS spectroscopy allows to measure the frequency of the thermally excited spin waves in the absence of any external stimuli such as microwave driving magnetic field, electric field, electrical current, or optical pumping [161, 162] compared to available techniques for dynamic measurements, e.g., vector-network analyzer Ferromagnetic Resonance (VNA-FMR) measurement [110, 163], time-resolved magneto-optic Kerr (TRMOKE) effect [110, 164, 165].

During a typical BLS measurement, a focused laser beam interacts with the sample, and the photons are inelastically scattered by the spin waves [166]. Momentum and energy conservation causes the annihilation of magnons (anti-Stokes process) and the creation of magnons (Stokes process). The linewidth of the inelastic peaks (i.e., the BLS spectra) relates to the magnetic inhomogeneity [167], while that of the elastic peak reveals the instrumental linewidth broadening

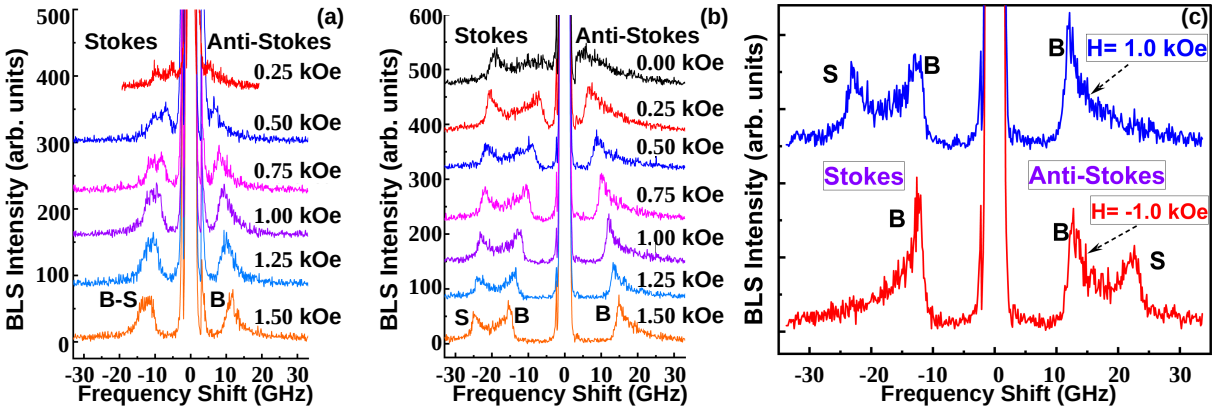


Figure 5.4: BLS Spectra of (a) non-ES (1.4 μm) and (b) ES (5.7 μm) CoP thin film at different in-plane bias magnetic fields measured from 1.50 kOe to 0.25 kOe [in (a)] and 0.00 kOe [in (b)] with the backscattering geometry.(c) BLS Spectra of 5.7 μm in a bias magnetic field of $+1.0$ and -1.0 kOe revealing the effect of the reversal of the magnetisation on the frequency position of the Damon-Eshbach wave [2].

[168]. Here, the BLS measurements have been performed by saturating the sample in 1.5 kOe magnetic field and reducing it down to 0.25 kOe, thus following the descending branch of the hysteresis loop as shown in Figure 5.2. In this field range, the magnetization is always saturated and parallel to the applied magnetic field. As the thickness of the striations of NHSs increases in the ES system compared to that of the non-ES sample, the laser light interacts more with the available spins in the ES system compared to the non-ES sample. This might be the reason behind the appearance of pronounced surface spin wave in the ES system. Sequences of BLS spectra measured at different H values are shown in Figure 5.4(a) and (b) for the 1.4 μm and 5.7 μm thick, thin films, respectively.

Spectra for the 1.4 μm films show almost similar characteristics (only one broad peak B, as mentioned in the figure) on both the sides of the spectra, whereas the 5.7 μm film consists of two well resolved distinct peaks (S and B, as mentioned in the figure) on the Stokes side of the spectra. Here, B stands for a band of bulk modes at the low frequency and S for the surface spin wave corresponds to the higher frequency (sharp peak), the so-called Damon-Eshbach (DE) surface spin wave [169]; which propagates in the film plane. The S mode is observed only on one side of the spectrum depending on the direction of the external magnetic field, which is the consequence of its nonreciprocal character within the micrometer thickness of the investigated films. A careful observation of the BLS spectra of the 1.4 μm film reveals that the peak shape on the Stokes side of the spectra is broadened compared to that of the anti-Stokes side for an applied bias field larger than 1 kOe. However, below 1 kOe, the DE/S mode is shouldered to the B mode, and a wide peak on the Stokes side has appeared due to the small frequency difference between the DE/S and B mode. This double peak structure could be ascribed to the hybridization between

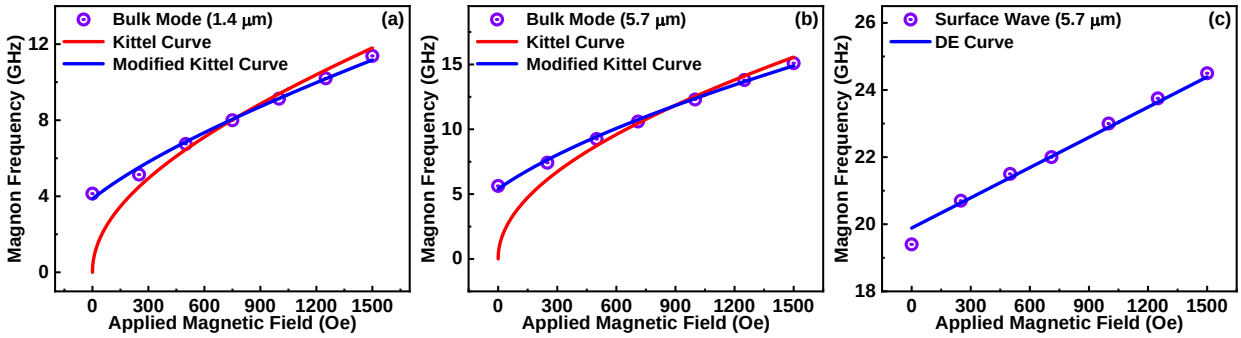


Figure 5.5: Spin wave frequencies of (a) bulk mode (1.4 μm non-ES film), (b) bulk mode of ES and (c) Damon-Eshbach surface wave as a function of magnetic field of 5.7 μm ES CoP thin film [2].

B and DE/S mode, as previously observed by Sandercock [169]. The S mode in 5.7 μm film is observed only on one side of the spectrum depending on the direction of the external magnetic field, which is the consequence of its nonreciprocal character within the micrometre thickness of the investigated films [169]. The BLS spectra, as shown in Figure 5.4(c), reveal the effect of magnetic field reversal at constant magnitude of 1.0 kOe, which unveils the predicted side change of Damon-Eshbach (DE) surface mode due to its non-reciprocal spatial localization.

Additionally, the external magnetic field-dependent BLS spectra for both the samples have been studied, which show an almost linear dependence of the mode frequencies vs the magnetic field intensity, as shown in Figure 5.5. A careful observation reveals the dissimilarity in the bulk mode frequencies of 1.4 μm and 5.7 μm thick samples, respectively. Figure 5.5(a) unveils that the bulk mode frequencies follow the typical Kittel curve (red curve in the figure) with the least deviation, however, below 9.26 GHz frequency in Figure 5.5(b), that deviate from the typical Kittel Curve, with a downward shift in frequency [where γ = gyromagnetic ratio, H = magnetic field, M_S = saturation magnetisation]. In order to fit the experimentally obtained bulk magnon frequencies, the typical Kittel formula has been modified by adding the exchange field, H_U, to the applied bias field, H, which results into H_{eff}, i.e., $H_{eff} = H + H_U$. Experimental data have been well fitted with the modified Kittel Curve (5.11) [169] (blue curve in the figure).

$$\omega_B = \gamma\sqrt{H_{eff}\cdot(H_{eff}+4\pi M_S)} \tag{5.11}$$

It is noted that in the low field regime (<200 Oe), the spectra could not be measured properly. So, in the subsequent paragraph, the H_U value from the DE mode have been reported, as shown in Figure 5.5(c), following the similar approach by Haldar et al. [105]. Further, the field evolution of the surface Damon-Eshbach mode have been analysed, as shown in Figure 5.5(c), by using the analytical formula [eq. (5.12)] valid for a semi-infinite medium [169]. The fitted line shows

almost linear frequency dependency of the DE mode with respect to the applied magnetic field.

$$\omega_{DE} = \gamma \cdot (H_{eff} + 2\pi M_S) \tag{5.12}$$

As observed from the FORC measurement [Figure 5.2(f)], a weak exchange coupling should exist between the multi-nano-layers of the nano-hetero-structure of the in-situ ES CoP thin film. Therefore, considering the exchange field, $H_U = -25.30$ Oe as input in the equation, the fitting yields gyromagnetic ratio, $\gamma = 30.02 \times 10^{-4}$ GHz/G and saturation magnetisation, $4\pi M_S = (13188 \pm 56)$ G [(12233 ± 376) G from bulk peak fitting]. There is a little misfit between the saturation magnetisation ($4\pi M_S$) values obtained from the bulk and surface peak fitting results, possibly due to the weak out-of-plane anisotropy present in the system or might be due to the thick sample and experimental limitation with the dynamic study. In BLS measurements, usually, the outermost layer ($\sim 15-20$ nm) of the samples can be probed while the quasi-static magnetic measurements probe the entire sample volume, thus providing information on the overall sample magnetic parameters [30]. Moreover, the gyromagnetic ratio (γ) is related to magneto-mechanical ratio (g) through, $\gamma = g(\frac{\mu_B}{\hbar})$, where, μ_B is Bohr magneton and $\hbar$ is the reduced Planck constant. So, $\gamma = 30.02 \times 10^{-4}$ GHz/G yields $g = 2.15$. Such slightly larger g values (i.e., $g > 2$) have been observed before [105] and could possibly be due to complex nano-hetero-structures. It is worth mentioning that the sharp and almost symmetric shape of the surface peak detected in the BLS spectra is due to the fact that for metallic (opaque) material the in-plane component of the wave vector is conserved in the scattering process and therefore fitting the surface peak by a Lorentzian (symmetric) curve is a valid assumption. On the other hand, the asymmetry in the shape of the bulk peak of the investigated CoP films is due to the concomitant effect of several factors.

For thick ferromagnetic films, the bulk mode (Perpendicular Standing Spin Waves, PSSW) have the perpendicular component of the wavevector ($k_\perp$) that is quantized according to the simple expression $k_\perp = n(\frac{\pi}{d})$, where d is the film thickness and n is an integer number. These modes have a stationary character with an oscillatory profile across the film thickness with a BLS intensity reduction, on increasing the mode number n [170]. Furthermore, on increasing d, these modes condensate toward the frequency value of the lowest order PSSW mode forming a continuous band of modes with an high density of magnonic states there. An additional effect is that, due to the finite penetration of light into an opaque material, in the direction perpendicular to the surface the laser light sees only a limited extent of the excitation with the result that from the uncertainty principle the wavevector component $k_\perp$ is not conserved. This spread is responsible for the fact that several PSSW modes enter into the scattering process [169] giving rise to the broad and asymmetric lineshape peaking at the low frequency.

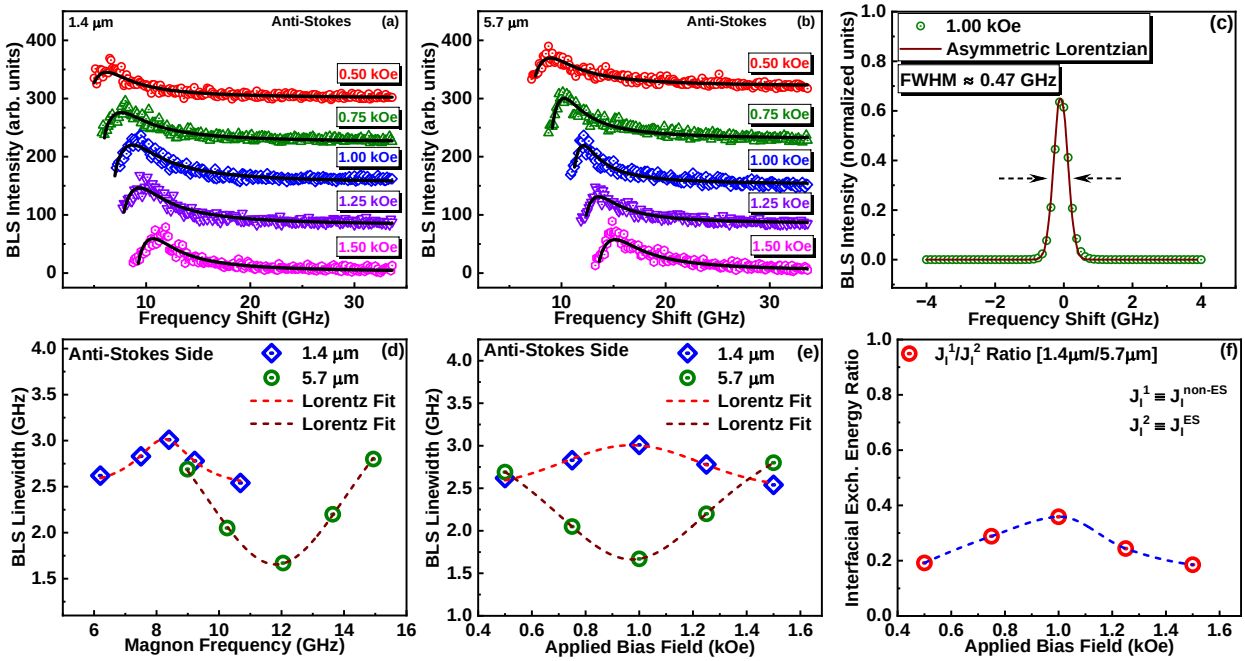


Figure 5.6: Lorentzian fittings of the anti-Stokes BLS peak as a function of magnetic field of (a) 1.4 μm non-ES and (b) 5.7 μm ES CoP thin film. (c) Lorentzian fitting to a typical elastic peak in the BLS spectra. BLS linewidth (Δf) as a function of (d) corresponding anti-Stokes magnon frequencies and. (e) applied bias magnetic field for 1.4 μm and 5.7 μm thick thin films. (f) The J_I^1/J_I^2 ratio as function of bias magnetic field. The symbols correspond to the experimental data while the lines joining the symbols are guide to eyes [2].

Considering all these effects, the theory from Michael Cottam [171] has been used for fitting the asymmetric peak lineshape associated to the bulk mode with light scattering from spin-waves in absorptive (opaque) magnetic materials. This theory introduced the concept of 'opacity broadening' contribution to the peak linewidth associated to a complex refractive index of the material.

The obtained BLS linewidths (Δf) of the corresponding bulk magnon frequency (f) peaks on the anti-Stokes side for 1.4 μm non-ES and 5.7 μm ES films, as shown in Figure 5.6(a) and (b) have been utilized to calculate the ratio of the interfacial exchange energy [J_I in equation (5.13)] for two different systems (i.e., ES and non-ES) [105]. An estimate of instrumental linewidth broadening, as shown in Figure 5.6(c), is obtained with the Lorentzian fitting to a 1.00 kOe elastic peak of the BLS spectra of 1.4 μm film [167, 168]. The fitting procedure yields the value of linewidth broadening of 0.47 GHz, which provides the lower limit of the linewidth measurement in the BLS spectra, and is uniformly present in the BLS signal for all the measurements. The anti-Stokes linewidths (Δf) as a function of magnon frequency, as shown in Figure 5.6(d) for 1.4 μm film, have reached the peak in the beginning and decreased gradually, while that of 5.7 μm film first hit a trough and then increased again. A similar behaviour in linewidth variation as a function

of applied bias magnetic field is observed, as shown in Figure 5.6(e). The reduction in the initial linewidth value obtained in the ES system compared to the non-ES system indicates a significant variation in the damping parameter with the evolution of ES spring morphology. Moreover, it is assumed that the interfacial exchange energy gradually becomes comparable with the exchange energy within the layer [73], resulting into a trough in the linewidth variation with the applied bias field in case of the ES sample; subsequently, the linewidth increases again while the interfacial exchange dominates over the exchange within the layer.

$$\Delta f = \frac{\gamma^2 < A_d > p < cos^2\alpha > \zeta}{A_{\text{ex}} \cdot f} \left(\frac{J_{\text{I}}}{t}\right)^2 \tag{5.13}$$

Since the data is not deconvoluted, the linewidth variation presented here, as shown in Figure 5.6(d) & (e), includes the contribution coming from instrumental broadening [168] and from the intrinsic spin-wave damping (Gilbert damping). The sharp decrease in linewidth with increasing frequency for the non-ES film indicates extrinsic contribution (interfacial roughness or structural inhomogeneity) to the magnetic inhomogeneity in this film [167].

Here, γ is the gyromagnetic ratio, $< A_d >$ is surface area, p is fraction of defects, α is the angle between the moments of two consecutive layers, ζ is a numerical factor, A_{ex} is exchange stiffness constant $= \frac{1}{2} \cdot D \cdot M_{\text{S}}$, J_{I} is the interfacial exchange energy, t = probed thickness in the BLS measurements. From BLS spectra of 1.5 kOe applied bias magnetic field data, the equation (5.13) yields the J_{I} values are approx. 3.68 erg/cm^2 and 10.12 erg/cm^2 for 1.4 μm and 5.7 μm films, respectively, with an assumption $< cos^2\alpha > = 0.5$ and the numerical factor ζ as 0.55 [105, 172]. The interfacial exchange energy ratio as a function of the applied bias magnetic field is shown in Figure 5.6(f)). Increment in the J_{I} value for 5.7 μm film with respect to that of 1.4 μm film reduces the interfacial exchange energy ratio, i.e., $J_{\text{I}}^{\text{non-ES}}/J_{\text{I}}^{\text{ES}}$ below unity (as $J_{\text{I}}^{\text{ES}} > J_{\text{I}}^{\text{non-ES}}$), which confirms that the strength of the exchange coupling in ES is greater than the non-ES film.

5.8 Conclusion

In summary, the optically smooth, nanohetero-structured, amorphous− nanocrystalline CoP thin films have been fabricated using the electrodeposition technique at room temperature and demonstrated the evolution of the ES state from the *in situ* non-ES state within such films starting in a single alloy material. The existence of the NHS in the system is confirmed by XRD, TEM and FFT of TEM. The static magnetic properties of nanohetero-structured CoP thin films characterized by magnetic hysteresis loop measurements show a signature of the ES nature in the system and has been further corroborated by FORC measurements. The existence of *in situ* ES systems has been

supplemented by dynamic characterization using BLS. Only bulk mode on both the Stokes and anti-Stokes sides of the relatively thinner film has appeared, and an additional peak appears, as a shoulder of the B mode, on the Stokes side of the spectra, which could probably be ascribed to the S mode that is hybridized with the B mode. On the other hand, in the relatively thicker system, well resolved distinct bulk and surface modes on the Stokes side and only bulk mode on the anti-Stokes side have appeared. The increment in the coercivity and interfacial exchange energy value in the 5.7 μm film compared to the 1.4 μm film demonstrated here confirms the presence of increased exchange interaction in 5.7 μm film compared to that in 1.4 μm film. Our study offers an approach to preparing the ES structure in a cost-effective and scalable manner, opening the door to modifying the magnetic properties even in a single ferromagnetic thin film. Thus, it provides a novel pathway to use these materials and their derivatives as next generation recording media and potentially for the next generation optically induced spin transfer torque (STT) devices.

6

Ultrafast demagnetization of nanostructured magnetic materials

This chapter is based on the following paper published in Journal of Materials Science [3] [1,⋆,#].

6.1 Introduction

High-frequency nano-structured magnetic films are crucial for cutting-edge applications, particularly in enhancing the performance of high-frequency integrated micro-inductors, coupled inductors, and micro-transformers with multi-nanomagnetic-layered cores. These components are essential in on-chip power supply systems, such as DC-DC switch-mode power converters, which are vital for the power delivery of next-generation microprocessors [11, 12]. Moreover, these films are pivotal in improving the efficiency of magneto-resistive random access memory (MRAM) switching [22, 39] and in the development of high-speed spintronic devices of the future.

Despite their potential, a significant challenge for high-frequency integrated magnetic devices is controlling eddy current losses, a typical energy dissipation mechanism in magnetic materials that converts energy into heat. To reduce these losses, especially in thicker magnetic materials that

[1] Ultrafast Demagnetization and Gilbert Damping in Electrodeposited CoP Film, S. Dutta, **A. Samanta**, S. N. Panda, S. Roy and A. Barman, *Journal of Materials Science*, **58**, 14817, 2023; DOI: 10.1007/s10853-023-08956-9.

⋆This work was done in collaboration with Professor Anjan Barman, S. N. Bose National Centre for Basic Sciences (SNBNCBS), Kolkata, India. Particularly, the corresponding TRMOKE measurement work was done at SNBNCBS, Kolkata, India by Soma Dutta under the supervision of Professor Anjan Barman. Arindam performed the static magnetic measurements and wrote the relevant sections.

#The relevant TRMOKE discussions will be included in Soma's thesis as well. Further TRMOKE data and analysis will be found in the above mentioned published paper.

are required for achieving reasonable power density, as well as to mitigate hysteresis and ferromagnetic resonance (FMR) losses, materials with higher resistivity, high saturation magnetization, low coercivity, and moderate anisotropy fields (H_K) are needed [40, 41]. FMR losses stem from spin motions, which might result from direct relaxation to the lattice or indirect relaxation through the excitation of non-uniform magnetization modes, such as spin waves [42]. Consequently, to develop GHz-level integrated magnetic devices that function effectively near the FMR frequency, it is vital to design and model these devices to investigate spin dynamics and relaxation at these frequencies [41, 42].

In prior work, electroplated inductors were fabricated using multi-nano-layered structures composed of CoP thin films. Phosphorus was incorporated to enhance resistivity and induce amorphousness in the material, making it suitable for integration into circuits [54]. Developing thicker nano-structured magnetic materials capable of functioning at high frequencies is essential for achieving high power densities in state-of-the-art applications. The electrodeposition technique is particularly advantageous in developing these films due to its cost-effectiveness, high yield, and adaptability to complex nano-topologies [53]. Although cobalt phosphorus (CoP) thin films have been prepared via electrodeposition and extensively investigated by various research teams [46, 55–57, 80, 81, 84, 107, 108], their ultrafast dynamic properties have not yet been thoroughly explored. Addressing the challenges and improving the performance of high-frequency integrated inductors, power systems, MRAM switches, and future spintronic devices necessitates investigating the ultrafast dynamics of magnetic materials. This involves understanding their responses to external stimuli and the relaxation processes of magnetisation, which provide valuable insights into their high-frequency performance.

The ultrafast control of magnetisation through femtosecond (fs) laser pulses reveals two significant magnetisation dynamics: ultrafast demagnetisation [32] and laser-induced magnetisation precession. These precessional dynamics facilitate the investigation of anisotropic magnetic properties through the frequencies of various dynamical modes, including the uniform Kittel mode, the perpendicular standing spin wave (PSSW) mode, and other dispersive modes within a continuous thin film, as well as the damping properties of these materials. Ultrafast spin dynamics are vital for high-speed information storage, initiated when a femtosecond laser pulse impacts a magnetic material, causing transient perturbations of its electron, spin, and lattice systems, leading to the field of femtomagnetism [173]. The system responds with rapid magnetisation reduction within femtoseconds, termed ultrafast demagnetisation. This is followed by quick relaxation via energy transfer from electrons and spins to the lattice, described by the phenomenological three temperature model (3TM). Several mechanisms have been proposed to explain ultrafast demagnetisation, including electron-magnon interaction [174], spin-flip (SF) scattering [175],

and spin-photon interaction [176]. Zhang and Hübner highlighted the role of spin-orbit coupling (SOC) in local angular momentum dissipation during ultrafast demagnetisation [112, 177]. More recently, superdiffusive spin transport has been proposed to elucidate enhanced magnetisation quenching in ferromagnetic/nonmagnetic bilayers following laser irradiation [178], and optical inter-site spin transfer has been suggested for multi-sub-lattice alloys and multilayer systems [179]. Although the precise mechanism of ultrafast demagnetisation remains under debate, the coexistence of multiple mechanisms [180, 181] has been demonstrated in different systems.

Increases in lattice temperature following fast relaxation lead to rapid changes in magneto-crystalline anisotropy, prompting magnetisation precession around an effective magnetic field. These precessional dynamics facilitate the exploration of various anisotropic magnetic properties through the frequencies of several dynamical modes, such as the uniform Kittel mode, PSSW mode, and other dispersive modes in a continuous thin film [182], as well as the damping properties of the magnetic material [183]. The Kittel mode, a coherent spin wave (SW) mode (wavevector, k=0), serves as the primary coherent channel for magnetisation relaxation in thin films. For thicker samples (greater than optical penetration depth), SWs excited by laser pulses propagate through the sample thickness and reflect from the substrate to form PSSW modes. SWs act as relaxation channels, helping to transition the system from a highly excited state back to equilibrium [184]. The natural relaxation of magnetisation precession is described by the Gilbert damping (α) parameter in the Landau-Lifshitz-Gilbert (LLG) equation [33, 185]. Intrinsic damping originates from SOC and the bandwidth of the d band in 3d ferromagnets [186]. Numerous intrinsic and extrinsic mechanisms, such as eddy currents [187], phonon drag [188], capping or doping with other materials, two-magnon scattering [189], and spin current injection [190], can influence damping. From an application standpoint, lower damping is critical for the long-distance propagation of spin waves and energy-efficient MRAM switching [22], while higher damping is essential for mitigating ringing after magnetic switching [191]. Therefore, the Gilbert damping constant is a crucial parameter for spintronics applications, necessitating its careful design and control in device engineering. Consequently, exploring ultrafast demagnetisation and spin relaxation, as well as precessional dynamics in soft magnetic materials, remains a significant area of research due to the fundamental physical mechanisms involved and their potential applications in future high-speed spin-based devices.

Understanding the ultrafast dynamics of magnetic materials provides insights into the mechanisms affecting their behaviour at high frequencies, which can be leveraged to optimise the design and performance of emerging technologies. For instance, studying spin dynamics and relaxation processes at ultrafast timescales reveals information about the behaviour of magnetic materials under rapid switching or dynamic conditions, common in high-frequency operations. This un-

derstanding guides the selection of magnetic materials with properties such as high saturation magnetisation, low coercive fields, and moderate anisotropy fields, and informs the engineering design of miniaturised devices, aiming to minimise losses and achieve efficient performance at higher operational frequencies.

At lower frequencies (sub-MHz—MHz level), operational frequency is not solely limited by eddy current losses or domain wall (DW) movement/rotation losses but also by spin losses and decreased permeability. As frequencies reach the GHz level, inhomogeneities in the material's magnetic ordering can lead to coexisting dynamical processes, such as DW-assisted and FMR-assisted responses, independent of the driving field's orientation. Additionally, from a practical device application perspective, examining the lifetime of spin wave modes is critical since eddy currents not only restrict wave lifetimes but also significantly alter their effective dispersion relations. Therefore, to accurately assess spin losses in highly miniaturised devices operating at ultra-high frequencies, a comprehensive understanding of high-frequency dynamics is essential.

In this study, all-optical time-resolved magneto-optical Kerr effect (TR-MOKE) magnetometry was employed to measure ultrafast demagnetisation and magnetisation precession in a soft ferromagnetic CoP alloy. By systematically varying the in-plane magnetisation orientation (φ) with respect to an externally applied magnetic field, it was found that the precessional frequency exhibits a dominant two-fold anisotropy superimposed with moderate four-fold anisotropy, whereas the Gilbert damping coefficient demonstrates a strong four-fold anisotropy. In contrast, ultrafast demagnetisation remains almost invariant with φ. Our results suggest that the anisotropic variation of precession frequency may result from SOC variation with φ, while the four-fold variation of damping, along with its high value, is attributed to the dephasing of the Kittel-like precessional mode with PSSW and other dissipative modes. In the highly nonequilibrium spin dynamics following laser excitation, SOC's role is nearly isotropic in contributing to ultrafast spin-flip scattering processes [192]. Higher damping is crucial for reducing resonance response in power supplies and mitigating noise, ringing, and oscillations produced by them.

6.2 Experimental Methods

In the preparation of smooth, shiny, amorphous cobalt phosphorus (CoP) thin films at room temperature ($293K$), the following chemicals and reagents are utilised via the electrodeposition method [57]: phosphorus acid (3.30), phosphoric acid (5.90), cobalt chloride hexahydrate (18.87), cobalt carbonate (1.55), glycine (1.15), saccharin (1.51), and naphthalene trisulfonic acid (NTA) (1.52). The values in parentheses indicate the concentration of each chemical in grams per 100 mL of solution. The electrolyte bath is maintained at a pH range of approximately 0.72

to 0.86. Initially, the bath exhibits instability, resulting in the formation of stressed and rough thin films due to high surface tension between the working electrode and the electrolyte. To counteract this, glycine is added to reduce surface tension, while NTA and saccharin are included as stress-relieving agents [111, 158]. This stabilisation process enables the development of stress-free, smooth, and glossy thin films. The electrodeposition process for the amorphous CoP film, with a thickness of 3.173 μm, employs pulse-reverse plating (PRP) on a 2 cm $\times$ 2 cm silicon wafer featuring a top conducting seed layer of 20 nm titanium and 200 nm gold. The CHI 660B potentiostat facilitates the deposition process using forward and reverse current pulses to achieve the desired film characteristics. The elemental composition and surface topology of the electrodeposited film are examined through energy-dispersive X-ray (SEM-EDX) spectroscopy and atomic force microscopy (AFM). The film's crystallinity and amorphous nature are evaluated using the X-ray diffraction (XRD) technique. In-plane magnetic hysteresis loop measurements are performed with a ShB MESA 200 hysteresis loop tracer (USA).

To investigate the ultrafast demagnetisation and precessional magnetisation dynamics of the film, the time-resolved magneto-optical Kerr effect (TR-MOKE) technique is utilised in polar Kerr geometry. This technique is based on a two-colour non-collinear pump-probe setup. A fraction of the fundamental laser beam (wavelength = 800 nm, pulse width = 40 fs, repetition rate = 1 kHz) from a femtosecond regenerative amplifier (Libra, Coherent Inc.) is directed through a second harmonic generator to create the pump beam (wavelength = 400 nm, pulse width $>$ 40 fs, repetition rate = 1 kHz) for sample excitation. Simultaneously, a smaller portion of the fundamental laser beam serves as the probe beam to detect magnetisation dynamics. The time delay between the pump and probe beams is controlled using a motorised variable delay stage. During measurements, the pump beam's fluence is kept significantly higher ($\sim$ 10 mJ/cm^2) than that of the probe beam ($\sim$ 1.5 mJ/cm^2).

An external magnetic field is applied at an angle of approximately 30° (indicated as ξ in Figure 6.3(a)) to the sample plane, creating a finite demagnetising field within the sample. The magnetisation tilt caused by this field is further altered by the pump pulse to initiate precessional dynamics within the sample. The probe beam is directed normally onto the sample with a spot diameter of approximately 100 μm, while the pump beam is slightly defocused to a spot diameter of around 250 μm and is incident obliquely at an angle of about 45° to the sample plane, ensuring proper spatial overlap with the probe spot. An optical chopper modulates the pump beam at a frequency of 373 Hz, and the dynamic signal in the probe beam is detected using a silicon detector in conjunction with a lock-in amplifier for phase-sensitive detection. In this experiment, time windows of 4 ps and 2 ns are utilised (the time window refers to the total duration for which the time-resolved signal is measured) to examine ultrafast demagnetisation (with a temporal reso-

lution of 25 fs) and damped precessional motion (with a temporal resolution of 5 ps), respectively.

6.3 Static Characterization

In determining the crystallinity or amorphousness of CoP thin film, phosphorous content plays a key role. Therefore, it is important to study the qualitative and quantitative analysis of phosphorous in the electrodeposited thin film. The energy dispersive x-ray (EDX) spectrum for the electrodeposited Si/Ti (20 nm)/Au (200 nm)/CoP (3.173 μm) sample as shown in Figure 6.1(a) confirms different Co and P peaks. For example, Cobalt L_α peak originates at 0.77 keV, K_α originates at 6.93 keV, and K_β is at 7.64, while the 2.13 keV peak is for the P- K_β peak. The EDX analysis confirms the presence of Co and P entities in the sample with $\sim$87% and $\sim$13%, respectively. The surface topography of the electrodeposited film is investigated using atomic force microscopy (AFM) as shown in Figure 6.1(b). From the AFM image, the average roughness of the surface have been extracted as $\sim$ 4 nm. The surface roughness is slightly higher than typical films deposited by physical vapor deposition techniques, but it is substantially small relative to the film thickness (3.173 μm) signifying the efficacy of the bath chemistry (proportion of stress relieving additives etc.) in the plating process.

The crystal structure of this electrodeposited sample is characterized by x-ray diffraction (XRD) technique using a 40 kV x-ray source (Rigaku: SmartLab) as shown in Figure 6.1(c). Four characteristic peaks can be observed at 2θ values of of 38.2°, 44.6°, 61.7° and 69.1° which could be assigned to Au (111) [193], Co (111) [194], Si (004) [195] and Si (004) [196] plane,

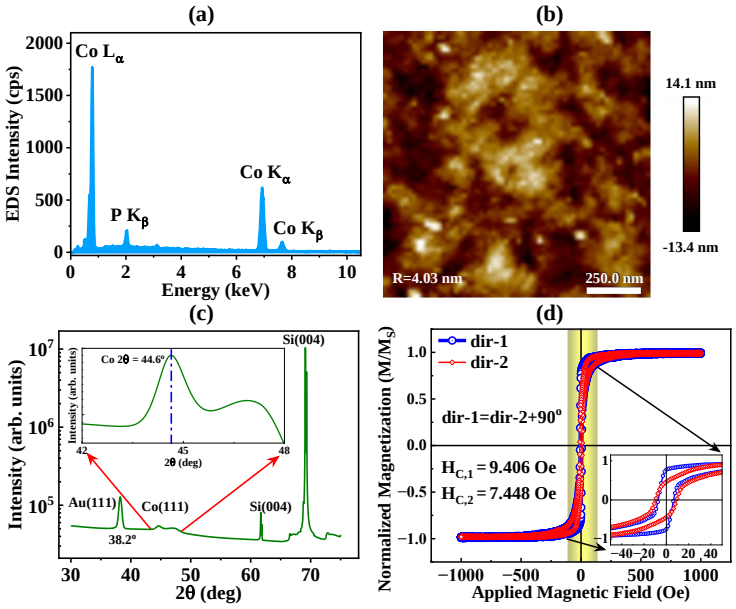


Figure 6.1: (a) Typical EDX spectrum of the sample at room temperature showing the presence of Co and P. (b) AFM image showing the surface topography. (c) X-ray diffraction pattern showing the amorphous property with nanocrystalline Co-fcc phase. (d) Typically measured in-plane hysteresis loop of one of the samples at two different in-plane directions showing anisotropic nature of the sample, here, dir.-2 = dir.-1 + 90°. Inset: magnified hysteresis loop [3].

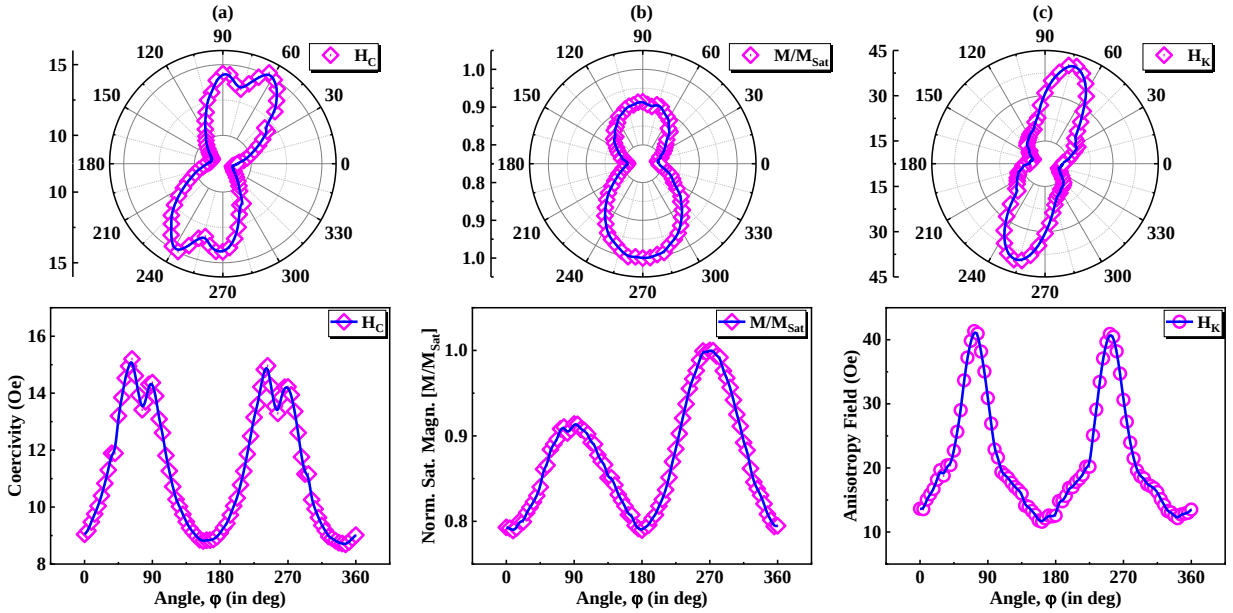


Figure 6.2: The variation of the (a) coercive field (H_C), (b) saturation magnetization (M_{Sat}) and (c) anisotropy field (H_K) of the material as a function of angle (in degrees). The top row exhibits the polar plot of the corresponding parameters [3].

respectively. The very small standard diffraction peak of Co suggests mainly the face-centred cubic structure (fcc) of Co [194]. This peak is not sharp because of the amorphous nature of the material in presence of P. Therefore, the system could be considered as a nano-hetero-structured system where tiny nanocrystalline Co-fcc phases are embedded in the amorphous CoP phase.

Figure 6.1(d) shows the experimentally obtained normalized in-plane hysteresis loops along the direction X (dir.-1) and direction Y (dir.-2) of the CoP thin films. Here, dir.-1 and dir.-2 are the longitudinal and transverse directions, respectively, i.e., both the axes, dir.-1 and dir.-2 ($dir.-2 = dir.-1+90^o$), lie in-plane to the sample. The magnified hysteresis loop from -50 Oe to $+50$ Oe range in the inset shows that the loops along X and Y directions are different, i.e., the sample should have an identifiable anisotropy.

In order to investigate the anisotropy present in the system, an in-plane angle dependent magnetic study has been performed. The variation of the coercive field (H_C), saturation magnetization (M_{Sat}) and anisotropy field (H_K) of the material as a function of angle (ϕ, in degrees) is shown in Figure 6.2. Figure 6.2(a) reveals a prominent four-fold symmetry in H_C while Figure 6.2(b) and Figure 6.2(c) reveal mostly two-fold symmetry in M_{Sat} and H_K, respectively. However, H_K shows a complex angular variation as explained below. Here, it has been noted that each of the corresponding symmetry axes lies in different directions. For example, the two symmetry axes in H_C are aligned with the $60^\circ - 240^\circ$ and $90^\circ - 270^\circ$ axes. The M_{Sat} symmetry axes lie

along $90^\circ - 270^\circ$ axis where the amplitude of M_{Sat} along the 270° direction is comparatively greater than that along the 90°, which suggests that an asymmetric behaviour is also observed in the magnetization along with a two-fold symmetry. It could be assumed that the Cobalt (Co) nano-crystallites grown within the amorphous matrix might have a preferred growth orientation. Therefore, Spin-Orbit Coupling (SOC) could exhibit a greater effect along a particular direction (here, along the 270° angle) compared to the other direction (90° angle).

The H_{K} symmetry axis shows a strong alignment with the $75^\circ - 255^\circ$ axis and weaker alignments along $30^\circ - 210^\circ$ and $135^\circ - 315^\circ$ axes. Since the $75^\circ - 255^\circ$ axis has a strong influence in the angular distribution of H_{K}, that axis accordingly develops a two-fold symmetry. However, considering other weaker alignments along $30^\circ - 210^\circ$ and $135^\circ - 315^\circ$ axes, the H_{K} symmetry does not fall into a simple two-fold or four-fold symmetry pattern – this suggests the complex anisotropy behaviour for the anisotropy field present in the material, which could be influenced by several factors, such as nanocrystalline structure, different magnetostriction of Co-fcc and amorphous CoP phases etc [90, 147, 160].

6.4 TRMOKE Measurement of Ultrafast Spin Dynamics

The ultrafast spin dynamics of this electrodeposited film has been measured using an all-optical time-resolved magneto-optical Kerr effect (TR-MOKE) magnetometry [183] in a non-collinear optical pump-probe geometry. The experimental measurement geometry in polar TR-MOKE configuration is shown in Figure 6.3(a). The optical pump-probe technique uses femtosecond (fs) laser pulses (pump) to excite the sample and to probe the ensuing dynamics in terms of the polar Kerr rotation (θ_k) of the sample as a function of the time delay between the pump and probe pulses. In the polar Kerr geometry, θ_k is proportional to the change of the out-of-plane component of the magnetization. Figure 6.3(b) shows a typical TR-MOKE trace from CoP containing three different temporal regimes. When a femtosecond laser is incident on a ferromagnetic sample placed in an external magnetic field, a rapid quenching of magnetization is observed just after the zero delay (i.e., when pump and probe beams are incident simultaneously on the sample). This phenomenon is known as ultrafast demagnetization. This is followed by a fast remagnetization within a few picoseconds (ps) due to spin-lattice relaxation. Change in the lattice temperature changes magnetocrystalline anisotropy which acts as a pulsed magnetic field and triggers the precession of magnetization of the sample. The heat diffusion from lattice to surroundings corresponds to longer relaxation within hundreds of ps time range. In this time scale the magnetization precession damps out.

After subtraction of a bi-exponential background from the precessional oscillation in the Kerr

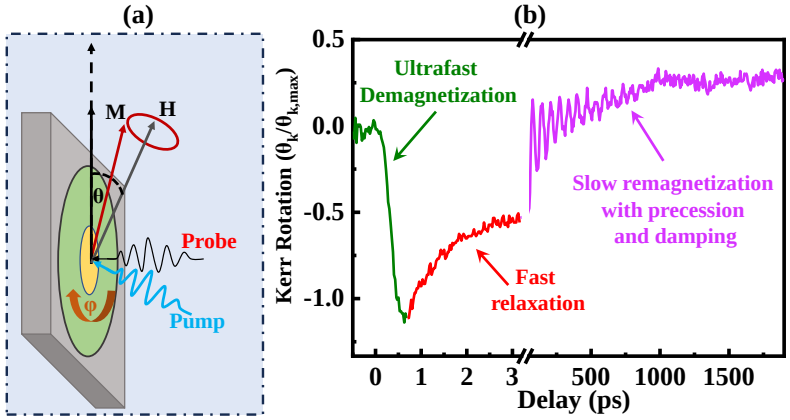


Figure 6.3: (a) Schematic of experimental geometry, sample is in x-y plane and x-z is the plane of the laser beam and (b) typical TR-MOKE data from Si/Ti (20 nm)/Au (200 nm)/CoP (3.173 μm) sample at an external bias magnetic field of 1.35 kOe. The three important temporal regimes at pump fluence of 10 mJ/cm^2 are indicated in the graph [3].

rotation data, a damped oscillatory motion is obtained. Figure 6.4(a) shows the damped Kerr oscillation in the polar Kerr geometry at an external magnetic field of 1.35 kOe for three different in-plane angles of 45°, 90° and 150° w.r.t. the x axis along the x-y sample plane in clock-wise direction. The precessional oscillation is fitted to the equation,

$$\theta_k = \sum_{i=1}^{n} A_i e^{-t/\tau_i} sin(2\pi f_i t + \delta_i) \tag{6.1}$$

where, n is the number of modes, and A_i, τ_i, f_i and δ_i are initial precessional amplitude, decay time, resonance frequency and initial phase shift of the i^{th} mode. When there is more than one clear SW modes ($1 \leq n \leq 3$), this expression is used to fit the time-resolved magnetization curves. The frequency of precession can be extracted by performing the fast Fourier transform (FFT) of the Kerr rotation data. Figure 6.4(b) shows the FFT spectra containing the magnetic modes corresponding to those three different in-plane angles. From these three angles it could be observed that there is frequency shift in magnetic modes from one angle to another. This gives a signature of the existence of magnetic anisotropy in the system. Also, it has been observed that FFT spectrum for 90° orientation contains a single clear peak whereas other two angles contain two dominant peaks.

To investigate the anisotropic magnetic behaviour more precisely, the magnetic modes have been investigated by continuously rotating the in-plane bias-field angle (φ) at 15° interval at an external magnetic field of constant magnitude of 1.35 kOe at pump fluence of 10 mJ/cm^2. Figure 6.4(c) displays that the most dominated precessional mode shows a combination of two-fold and four-fold anisotropy terms. Thus, its frequency (f) variation with φ have been fitted using the following equation (6.2) [197]:

$$f = \frac{\gamma}{2\pi}\left[H + \frac{2K_2}{M_S}\cos 2\varphi - \frac{4K_4}{M_S}\cos 4\varphi + \frac{2A}{M_S}\left(\frac{n\pi}{d}\right)^2\right]$$
$$\times \left[H + 4\pi M_S + \frac{2K_2}{M_S}\cos^2 2\varphi - \frac{4K_4}{M_S}(3+\cos 4\varphi) + \frac{2A}{M_S}\left(\frac{n\pi}{d}\right)^2\right] \quad (6.2)$$

where f is the precessional frequency, $\gamma = \frac{g\mu_B}{\hbar} = 1.76 \times 10^7$ rad/(s.G) is the gyromagnetic ratio, H is the bias magnetic field and M_S is the saturation magnetization. K_2 and K_4 indicate the two-fold and four-fold anisotropy constants. A, d and n are exchange stiffness constant, thickness of the film and order of PSSW mode, respectively. Here, $n = 0$ have been fixed, since the most dominating mode here is the uniform Kittel mode. The estimated value of M_S is obtained as ~1350

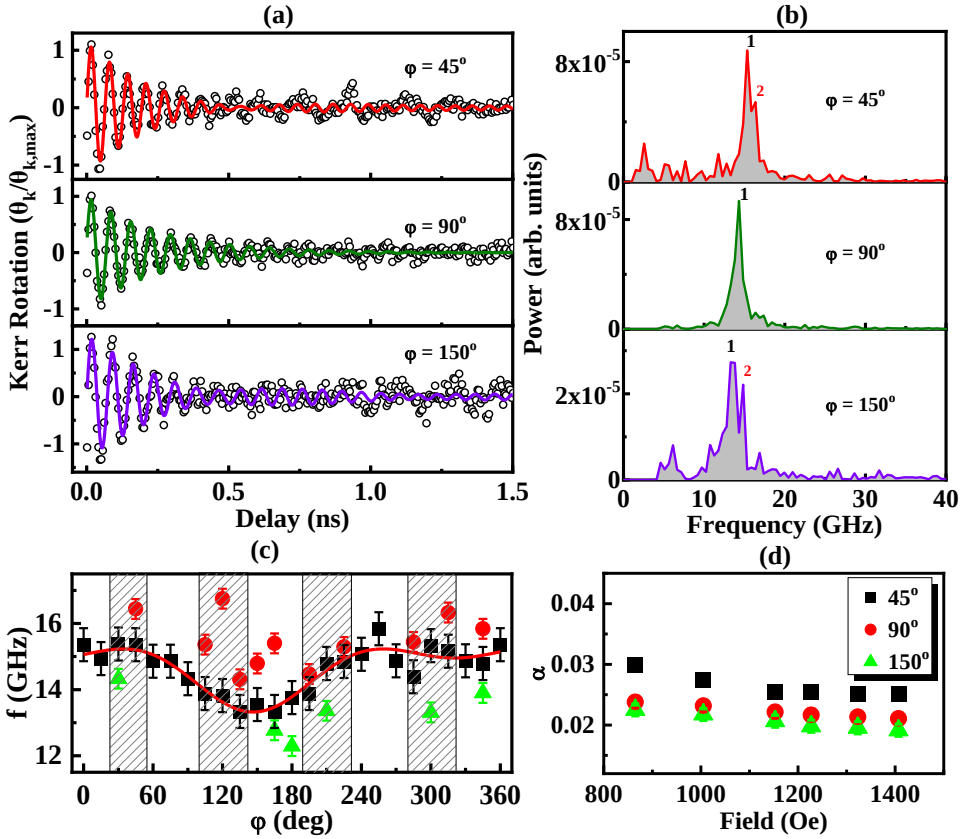


Figure 6.4: (a) Background subtracted time-resolved Kerr rotation data for external magnetic field of 1.35 kOe applied along three different in-plane angles (45°, 90° and 150°, respectively w.r.t. the x axis along x-y plane) at a fixed pump fluence of 10 mJ/cm^2. The solid lines are fitted curves using the damped sine function. (b) FFT spectra corresponding to three different angles showing the magnetic modes. (c) In-plane angle dependent precessional frequency at the same external magnetic field of 1.35 kOe. The solid line is fitted the Kittel mode. i.e., Eq. (6.2). (d) Bias field dependent Gilbert damping constant of the Kittel mode at $\varphi = 45°, 90°$ and 150° reveals the suppression of extrinsic effects at higher field [3].

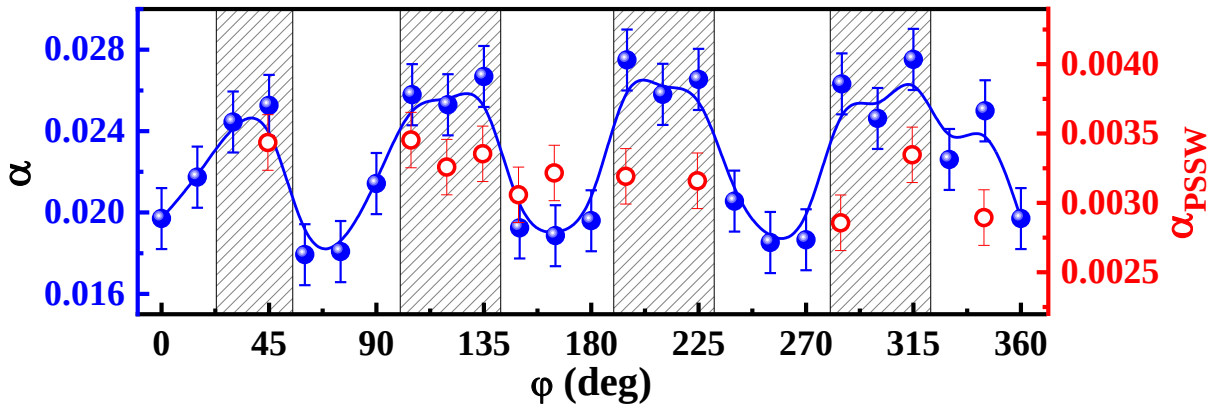


Figure 6.5: The variation of α of Kittel modes (solid blue scattered points) and PSSW modes (open red scattered points) with different in-plane angles at an external bias magnetic field of 1.35 kOe with the pump fluence of 10 mJ/cm^2. Blue solid line is guide to eye [3].

emu/cc, which matches closely with the reported value for bulk Co [198]. We have cross checked this value from another independent measurement of the magnetic hysteresis loop measured along the hard axis of the sample and obtained the value of M_S as $\sim$ 1129 emu/cc. The slightly lower value of M_S obtained from the hysteresis loop tracer can be attributed to the errors in evaluating the sample volume. The value of uniaxial anisotropy constant is found to be 1.1×10^5 erg/cc superposed with a weaker four-fold anisotropy constant of 0.3×10^5 erg/cc. Additionally, the value of uniaxial anisotropy, K_2 can be calculated from the hard-axis hysteresis loop using the expression: $K_2 = \frac{1}{2} H_S M_S$. Here the saturation field, $H_S \sim 200$ Oe and saturation magnetization $M_S \sim 1129$ emu/cc. The value of K_2 is calculated to be $\sim 1.13 \times 10^5$ erg/cc, in good agreement with the value obtained from the fit.

We have extracted the effective Gilbert damping (α) coefficient of the Kittel modes by using the expression:

$$\alpha = \frac{1}{\gamma\tau\,(H + H_1 + H_2)} \tag{6.3}$$

where $H_1 = \frac{K_2}{M_S}\cos 2\varphi - \frac{2K_4}{M_S}\cos 4\varphi$ and $H_2 = 2\pi M_S + \frac{K_2}{M_S} cos^2 2\varphi - \frac{2K_4}{M_S}(3 + \cos 4\varphi)$. Here, τ is the decay time of the magnetization precession and other parameters have their usual meaning. The effective damping consists of both intrinsic and extrinsic contributions. The damping as a function of H is plotted in Figure 6.4(d) for three different values of φ. Effective α is found to decrease with increasing frequency and becomes nearly constant for $H > 1.15$ kOe, as reported previously. This means a field above 1.15 kOe is high enough to suppress all extrinsic effects contributing to the damping.

To investigate the anisotropic behaviour of damping, the angular dependence of effective damping was extracted, as shown in Figure 6.5 corresponding to the Kittel mode and the PSSW

mode of Figure 6.4(c). Large in-plane four-fold anisotropic behaviour of damping is observed for the Kittel mode. Angular regimes with higher damping value are marked by black shade in Figure 6.5, those regimes are containing richer number of modes along with the Kittel mode as illustrated in Figure 6.4(c). Enhancement of α at some angles is found to be due to the mutual dephasing of PSSW and the low frequency mode with the Kittel mode which opens up additional energy dissipation channels [184]. The damping parameter corresponding to the PSSW mode (α_{PSSW}) wherever present is shown in Figure 6.5 with open circle symbol. The anisotropic behaviour of α has been theoretically predicted previously based on breathing Fermi-surface model [199, 200]. This has been shown experimentally not only in ferromagnetic metals [201], but also in alloys [202]. The electrodeposited CoP film shows $\sim$ 80% two-fold and $\sim$ 20% four-fold anisotropy in precession frequency coupled with a four-fold anisotropic damping. Such anisotropic GHz-frequency precessional dynamics can be crucial for various high-frequency applications such as frequency selectivity can be achieved without replacing the magnetic film and only by rotating the film for any input information for radio frequency signals and spintronic resonators [203]. Moreover, anisotropy of damping will enable to design future spintronic devices. The higher damping of the CoP film will be useful for increasing the switching speed for high-speed magnetic recording devices and to reduce the noise in power supply devices.

6.5 Conclusion

In summary, the time-resolved spin dynamics in electrochemically deposited CoP alloy film is experimentally investigated using the all-optical TR-MOKE magnetometry to explore possible anisotropy in magnetization precession and damping as well as ultrafast demagnetization w.r.t. in-plane magnetization orientation of the sample. We observed that the magnetization precession frequency obeys a stronger two-fold anisotropy superposed with a weaker four-fold anisotropy, while the Gilbert damping follows a four-fold anisotropic nature. This typical anisotropic precession frequency may stem from the variation of spin-orbit coupling (SOC) at equilibrium. The strong four-fold anisotropic Gilbert damping can be attributed to the additional dissipation channel due to the presence of PSSW mode and another lower-frequency mode along with the Kittel mode, causing mutual dephasing of precession. Our work provides important experimental results regarding to ultrafast demagnetization and Gilbert damping in a new soft magnetic system for possible future applications and opening new avenues for further investigation.

7 Magnon Microwave Antenna (MMA)

This chapter is based on the following paper published in IEEE Transactions on Electron Devices [4][1] and the International Conference presentation[2].

7.1 Introduction

The emergence of the Internet of Things (IoT) devices develops a great interest in microwave based technologies [115, 116, 204], in applications such as, autonomous driverless/autopilot cars, efficient radars/antennae etc., which rely on generation of microwave frequencies with a relatively lower power consumption, strong signal amplitude, and good frequency stability. These high-end features become the prerequisite of the advanced systems to perform necessary operations smoothly. However, conventional voltage controlled oscillators (VCO) typically consume a large amount of power to perform the operations [205]. Previously, spin torque oscillators (STO) have been investigated as source of microwaves, as STOs are, in general, highly tunable and offer small chip size compared to existing VCOs [117, 206], however, suffers from weak output signal. To circumvent this issue, an array with synchronized phase-locking STOs have been studied. Additionally, the synchronization time of such phase-locking STOs is extremely short, and in practical applications the synchronization of the STOs itself becomes one of the biggest challenge, which limits their utilization for cutting-edge IoT applications. Additionally, some electric/magnetic field as an external bias is required in controlling the STOs [15, 207].

Lately, Fabiha et al. used tripartite coupling between phonon-magnon-photon to demonstrate

[1] Generation of Microwaves With Tuneable Frequencies in Ultracompact "Magnon Microwave Antenna" via Phonon-Magnon-Photon Coupling, **A. Samanta**, S. Roy, *IEEE Transaction on Electron Devices*, **70** (1), 335-342, 2023; DOI: 10.1109/TED.2022.3221026

[2] Power–Phase Relation in Ultra-compact "Magnon Microwave Antenna" for Generation of Microwaves with Tuneable Frequencies (Poster), **A. Samanta**, S. Roy, *"68th MMM Conference"*, Dallas, Oct. 30–Nov. 3, 2023

spin-wave based nano-antenna [20]. In this work, a spin-wave (SW) based "Magnon Microwave Antenna" (MMA) was demonstrated [4] for microwave generation via non-volatile domain configuration induced by tripartite phonon-magnon-photon coupling in an array of magnetostrictive nanowires (NWs) patterned on a piezoelectric substrate. Since domains are modified at the cost of energy, here, the required energy has been provided to the NWs in the form of an external stress launched by a surface acoustic wave (SAW) in the piezoelectric substrate along the longitudinal direction. However, no external bias field is required as in other devices, e.g., STO-based or conventional domain wall based oscillators or straintronic microwave oscillator. [116, 208–214].

7.2 COMSOL Design of MMA

The proposed tripartite coupling based MMA consists of magnetostrictive NWs (FeGa) patterned on the piezoelectric $LiNbO_3$ substrate, which relies on two different working principles, first, phonon-magnon coupling and then the magnon-photon coupling. This section first describes MMA design in 2D cross-sectional model with COMSOL Multiphysics® [118] [as in Figure 7.1(a)] and then estimates the SAW resonance frequency generated from the system. In order to implement the necessary design and simulations, the Piezoelectric effect and Magnetostriction physics interfaces from Structural Mechanics module along with AC/DC module of COMSOL Multiphysics have been employed.

In simulation, two of the aluminum (Al) electrodes separated by a distance of $\sim 3.6\ \mu m$ and placed along the longitudinal direction of the substrate have been considered as terminal ports to apply voltage into the device for generating the SAW from the piezoelectric substrate. The

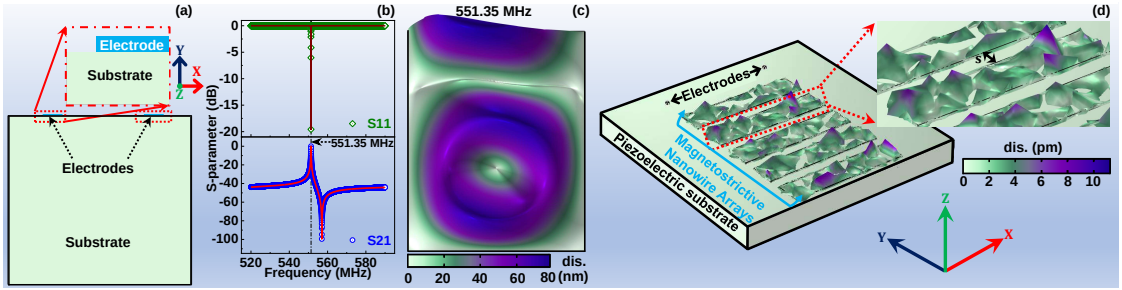


Figure 7.1: COMSOL design of the magnon microwave antenna with magnetostrictive nanowires: (a) 2D cross-sectional model in COMSOL to calculate the generated SAW frequency. Substrate width $-9\ \mu$m, thickness $-10\ \mu$m; Aluminium (Al) electrodes (the magnified version of the highlighted region) width $-1\ \mu$m and thickness -5 nm. (b) S_{11} and S_{21} parameters confirm the surface acoustic wave (SAW) resonance frequency at 551.35 MHz. (c) Deformed shape plot of the resonance SAW mode confirms the maximum penetration depth of the SAW. (d) The magnetostriction effect in nanowires shows some mechanical displacement of NWs caused by the SAW [4].

reflection coefficients, namely, S_{11} and S_{21} parameters, as shown in Figure 7.1(b), obtained from the COMSOL simulation estimates the SAW resonance frequency as 551.35 MHz. The orientation confirms that the generated SAW propagates along the longitudinal directions (i.e., X-direction). It is worth mentioning that this resonance frequency has been considered as input in micromagnetic simulation with MuMax^3 [24].

It is imperative to calculate the amount of power that is coupled to the SAW, which could be further utilized in estimation of the stress generated upon launching of SAW. In order to do that, the similar approach by De et al. [215] and Drobitch et al. [216] have been considered. Here, the S_{11} parameter in Figure 7.1(b) has been calculated considering an ideal scenario, i.e., any loss from the substrate has been neglected, that estimates the reflection coefficient of the system. The S_{11} value of ≈ -19.56 dB gives the reflection coefficient of the system as ≈ 0.011. Here, in the simulation, the input power (P_I) is 6.5×10^{-5} W. Therefore, the power coupled into the SAW is $P_C = (1-r) \cdot P_I \approx 6.43 \times 10^{-5}$ W.

The corresponding stress profile at 551.35 MHz, generated due to SAW is shown in the Figure 7.1(c), which estimates the penetration depth on the surface as 80 nm. Hence, the thicknesses of the NWs should be smaller than 80 nm to ensure that all of the strain generated in the substrate due to the SAW is transferred to the NWs. Since the nanomagnet thickness in this study is 40 nm, it could be assumed that the generated strain has been transferred fully to the NWs producing the required magnetization, as confirmed in the Figure 7.1(d). The maximum mechanical displacement of the NWs caused by the strain from SAW is 10 pm. The following sections provide the deeper insight into the detailed magnetization study and the spin-wave (magnonic) modes of MMA.

7.3 Micromagnetic Simulations of MMA

We have performed the micromagnetic simulations using MuMax^3 [24] by discretizing the NWs into the cell sizes of $2 \times 2.5 \times 2.5$ nm^3 solving the Landau-Lifshitz-Gilbert (LLG) equation [equation (7.1) and (7.2)]. Here, $\vec{m}$ is the unit vector of local magnetization, $\gamma_0 = \mu_0|\gamma|$, γ - gyromagnetic ratio (GHz/T), $\vec{H}_{\text{eff}}$ is the effective magnetic field originates from demagnetization energy, exchange energy, magnetic and shape anisotropy, α is the Gilbert damping factor, μ_0 is the free space permeability, M_S is the saturation magnetization (A/m).

$$\frac{\partial \vec{M}}{\partial t} = |\gamma| \vec{M} \times H_{\text{eff}} + \frac{\alpha}{M_S} \left[\vec{M} \times \frac{\partial \vec{M}}{\partial t} \right] \tag{7.1}$$

$$H_{\text{eff}} = -\frac{1}{\mu_0} \cdot \left[\frac{\partial E}{\partial \vec{M}} \right] \tag{7.2}$$

We have considered the following material parameters of FeGa [217], saturation magnetiza-

tion M_S = 1.32 MA/m, exchange stiffness constant A_{ex} = 16 pJ/m, initial exchange anisotropy constant $K_{u1,i}$ = 0 J/m^3, before applying external stress (σ). Since MuMax^3 does not include external stress directly [24], the stress has been applied as magnetoelastic anisotropy, $K_{me} = \frac{3}{2}\lambda_s \cdot \sigma(t)$, where λ_s is saturation magnetostriction constant of FeGa (400 ppm) and $\sigma(t)$ is the generated time-varying sinusoidal stress due to the launch of SAW [218]. So, the external stress reforms the uniaxial anisotropy value as $K_{u1,eff} = K_{u1,i} + K_{me}$ [217] $\Rightarrow K_{u1,eff} \approx \frac{3}{2}\lambda_s \cdot \sigma_0 \sin(2\pi f t)$ [218]. The stress field has further been calculated according to the following equation: $H_S(t) = \frac{3}{2} \cdot H_0 \cdot \sin(2\pi f t)$, where, $H_0 = \left(\frac{\lambda_s \cdot \sigma_0}{\mu_0 \cdot M_S}\right)$ is the amplitude of the stress field ($H_S(t)$) due to SAW. Here, $\sigma_0 = \sqrt{P_{A,max} \cdot Z_{max}}$ and $Z_{max} = \sqrt{C_{\varepsilon 11} \cdot \rho}$; Z_{max}, $C_{\varepsilon 11}$ (202.897×10^9 Pa) and ρ (4.7×10^6 g/m^3) are characteristic acoustic impedance, the first diagonal element of the elasticity tensor and the density of the $LiNbO_3$ substrate, respectively. The power coupled into the SAW per unit area along the normal to the direction of propagation, $P_{A,max} = P_C/A_{max}$, where P_C is the power coupled into the SAW ($\approx$ 0.99 mW as calculated earlier) and A_{max} is the area (8×10^{-14} m^2) normal to the direction of propagation of the SAW [calculated as the width of the electrodes (1 μm) times the penetration depth of the SAW (80 nm)]. Therefore, $P_{A,max}$ becomes 8×10^8 W/m^2, $Z_{max} = 9.786 \times 10^8$ N$\cdot$S/m^3 and $\sigma_0 = 1.25 \times 10^9$ Pa. Hence, the amplitude of $H_S(t)$, i.e., H_0 is 452144 A/m = 5681 Oe.

Here, the cell size lies below exchange length ($l_{ex} = \sqrt{\frac{2A_{ex}}{\mu_0 M_S^2}} \approx 4.24$ nm), which further ensures the inclusion of all of the exchange interactions. MuMax^3 determines the macro-spin configuration at every coordinate point within the NW and it produces the vector files containing the magnetization distribution over the simulating magnetic object. Simulations are performed with the typical dimensions NWs are $512 \times 120 \times 40$ nm^3 length [(l) $\times$ width (w) $\times$ thickness (h)] as depicted in Figure 7.2(a) with different 's' value (20 nm - 160 nm), where, the effective magnetic fields generated by the effect of the shape anisotropy, dipole coupling and strain have been considered. This study has been performed at 0 K, a widely used method in micromagnetic modelling of strain-mediated structures, to ignore the switching errors [219].

It is important to note that transverse stress applied along the Y direction helps developing the multi-domain configurations (as shown in Figure 7.2(b)) along the cross-section of the NWs out of initial random magnetization configuration (as shown in Figure 7.2(a)). Due to the SAW, the smaller multi-domains in Figure 7.2(b) start rotating into one direction in forming a large size single domain state along longitudinal direction (Figure 7.2(c)), which helps to generate the microwave. In the process of the creation or annihilation of domains, demagnetization energy has taken an important role. In general, dipolar energy or demagnetizing energy of any system could be stored by forming multiple domains in the system. Therefore, the energy should be minimized in the studied systems as well. Consequently, the initial magnetization was also considered as

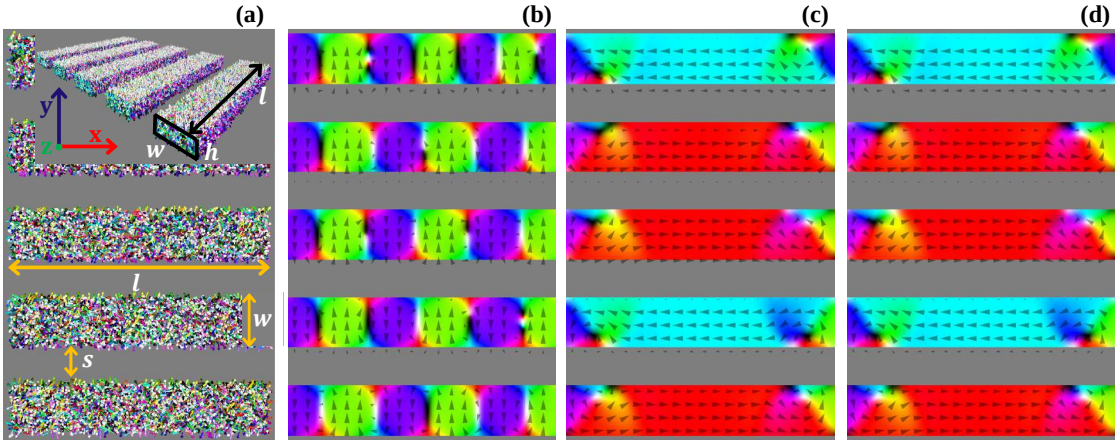


Figure 7.2: Micromagnetic modelling of NWs: (a) Initial random magnetization configuration. l, w are length, width of each of the NWs along the x, y directions, respectively, and s is the separation between the NWs along y direction of 40 nm thick NWs. (b) Multidomain state in presence of transverse stress along Y. (c) Single domain state upon launching of the SAW along X. (d) Final spin configuration after completion of 20 ns simulation confirms that the domain configurations are non-volatile in nature [4].

random magnetization (Figure 7.2(a)). For s = 90 nm figuration, the demagnetization energy of the initial random magnetization state is 4484.20 aJ. The demagnetization energy becomes 818.32 aJ while the system has been broken into multi-domain state (Figure 7.2(b)). The multi-domain state has been diminished upon launching of the SAW. The energy associated with the SAW further helps to minimize the demagnetization energy of the system. In this case, the demagnetization energy of the single-domain state (Figure 7.2(c)) is minimized to 337.83 aJ.

It is worth mentioning that such kind of change in domain wall motion with SAW is promising for wireless energy harvesting applications, such as for power-hungry IoT devices [220]. Another important aspect of this present study is that the SAW engineered single domain state is nonvolatile in nature, as evidenced in Figure 7.1(d), after a 20 ns long simulation. These single domain nanomagnets remain in its own state until they are reset by application of stress or a strong external magnetic field to the initial multi-domain state, which makes the single domain state nonvolatile, that could be useful in energy efficient logic applications, low-power computing applications, as well [221], however, that is out of the scope in present study.

7.4 Simulated Magnetization Oscillations

In electrically connected series or parallel Spin Torque Oscillator (STO) [222], each of the individual NWs is connected through interdigitated electrodes delineated by lithography. However, the MMA provides the liberty to connect them without any electrical connection, rather they are

connected via the dipolar interaction between them and the strength of the dipolar coupling could be considered analogous to the electrical resistance in the electrically connected STOs [222]. Since the SAW has been launched along the longitudinal (x) direction, the NWs could be considered to be connected magnetically in parallel combination via dipolar coupling between them as analogous to the electrical STOs and it is important to mention that the demagnetization energy along with the exchange energy plays a crucial role in stabilizing the magnetization oscillations. So, there must be a trade off between the demagnetization energy and the exchange energy of the systems. Therefore, it is worth mentioning that in the absence of the SAW, the system might excite at its intrinsic spin wave mode due to strong magnetostatic interaction between the neighbouring elements or in presence of SAW, new extrinsic modes might occur at the SAW frequencies which are not resonant with the intrinsic modes [215].

We have shown the calculated magnetization components, M_X, M_Y and M_Z, as a function of the increasing separation value ('s') between the NWs in Figure 7.2(a), (b), (c), respectively, where M_X, M_Y and M_Z represent the calculated magnetization components along the major, minor axes and normal to the plane component of the NW, respectively. To find the optimum separation for effective synchronization, the SAW with 0.5 GHz frequency has been launched first, as obtained from the COMSOL simulation shown in Figure 7.1(b). Both the configurations with the smallest and largest separations between the NWs, i.e., 20 nm and 160 nm, give a desynchronized oscillations in all the directions, i.e., along the x, y and z directions, respectively, as evidenced in Figure 7.3(a), (b), (c). Hence, these configurations have failed to generate a proper synchronized auto-oscillations in the microwave antenna, which has been evidenced from the multiple peaks in the corresponding Fast Fourier Transform (FFT) spectra, in Figure 7.4(a), (b), (c), of the corresponding damped magnetization curves, respectively. However, the configuration with moderate separation, i.e., the NWs separated with 90 nm distance, provides the required optimum magnetization output (M_X and M_Y) with proper synchronized auto-oscillations, i.e., an undamped sinusoidal response along x and y directions, respectively. In addition, the sinusoidal M_Z component in this configuration seems to be suffered from a slight damping. It is important to notice that the magnetization oscillation amplitudes decrease almost by one order of magnitude from M_X to M_Z.

7.5 Simulated Power Spectra Analysis

The FFT of the magnetization components, M_X, M_Y, M_Z yields the corresponding power spectra of each configuration. The obtained Power-Frequency spectra of $M_X/M_Y/M_Z$ by FFT as a function of 's' value between the NWs are shown in Figure 7.4(a)/(b)/(c), respectively. The corresponding

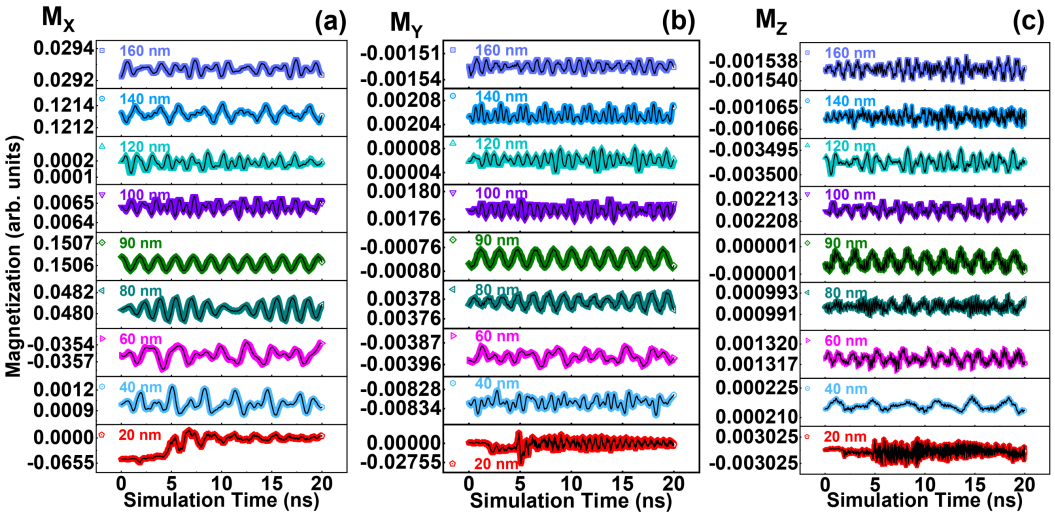


Figure 7.3: Calculated magnetization oscillations as a function of spacing between the NWs in MMA along x, y, z directions in (a), (b), (c), respectively, while the exciting SAW frequency remain kept constant at 0.5 GHz throughout the simulations [4].

insets in each stack show the magnified frequency spectra of the highlighted region of the parent power spectra ($0-50$ GHz range). The $s = 20$ nm configuration shows only a single peak (the power is in 10^{-2} order of magnitude), however, any effect from the SAW might have been neglected as its magnetization is noisy, and not synchronized in any direction at all, as evidenced in Figure 7.4(a)/(b)/(c). At this configuration, the intrinsic shape anisotropy and the strength of the magnetostatic interaction are more prominent [overall demagnetization energy (~ 297 aJ) is greater than the exchange energy (~ 200 aJ)] that obstruct to synchronize with the launched SAW frequency and trigger incoherent magnetization precession inside the nanomagnets and hence the power is concentrated at low frequency (that is the natural frequency of the system), which arises due to the array geometry itself [215]. For $s = 40$ nm configuration, there are four peaks in the corresponding spectrum, which means that at least two NWs are synchronized along x direction. However, the power at this configuration becomes three orders of magnitude smaller (the power is in 10^{-5} order of magnitude) than that in 20 nm configuration, as in the case of 40 nm configuration, the exchange energy (~ 375 aJ) dominates over the demagnetizing energy of the system. As a result, new extrinsic modes generate upon launching of SAW.

Upon increasing the separation between the NWs, some of the peaks start merging as the number of peaks is decreased as depicted in the Figure 7.4. For $s = 60$ nm, there are three different peaks, which necessarily signifies that at least three NWs are synchronized. For $s = 80$ nm, the number of the synchronized NWs are four, however, the $s = 90$ nm configuration generates only a single frequency where each of the five NWs is properly synchronized giving rise to the

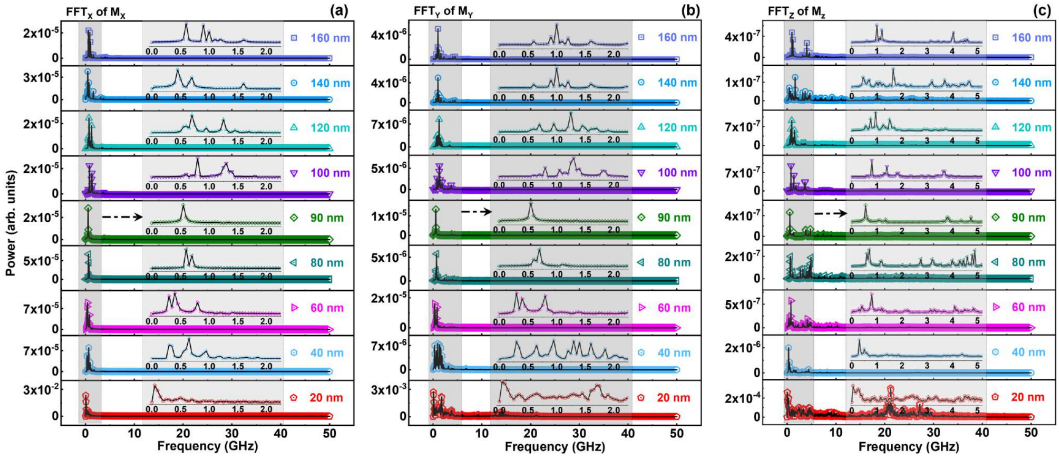


Figure 7.4: Power distribution as a function of spacing between NWs along x, y, z directions in (a), (b), (c), respectively. Corresponding insets reveal magnified frequency spectra (0-2.5(5) GHz range) of M_X & $M_Y(M_Z)$ of the highlighted region at left side of the parent Power-Frequency spectra (0-50 GHz range) [4].

optimum output. Here, this synchronized frequency for $s = 90$ nm configuration was denoted as the 'peak frequency', f_p, and the 's' value as s_{op}, i.e., the optimum separation value for effective synchronization of each of the NWs. Upon further increasing the separation value destroys the synchronized state as evidenced in the Figure 7.4. In addition, the Power-Frequency spectra along the minor direction also show similar kind of behaviour, i.e., only $s = 90$ nm separation gives a proper synchronized signal along y direction. So, it could be mentioned that the frequency response are identical along the major and minor directions, respectively, i.e., the MMA could be exploited bidirectionally for required applications. However, the magnitude in FFT_Y becomes almost half of that in FFT_X.

On the other hand, FFT_Z in Figure 7.4(c) confirms that it is extremely hard to synchronize the NWs at any separation value studied here in the out-of-plane (Z) direction; even the s_{op} configuration has some other weaker (power) higher bands (frequency) over f_p. The time varying strain generated in the magnetostrictive nanomagnet due to the surface acoustic waves (SAW) modulate the overall precessional dynamics, which in turn give rise to the hybrid magnetodynamical modes along out-of-plane component [223] - this might be the reason behind the higher band along z direction. Here, it is worth mentioning that the power of the resonance peak, 'f_p' of M_X is approximately two (six) times larger than that of M_Y (M_Z) oscillations. Hence, the spin-wave is composed mostly of the longitudinal oscillations in the component of the magnetization along the major axis while the SAW is also propagating along the same direction.

Domains of all these studied phonon-magnon-photon coupling based "Magnonic Microwave Antennas" (MMAs) are observed to be non-volatile in nature (as shown in Figure 7.2). However, it is imperative to mention that there is a significant difference in the non-volatility of the domains

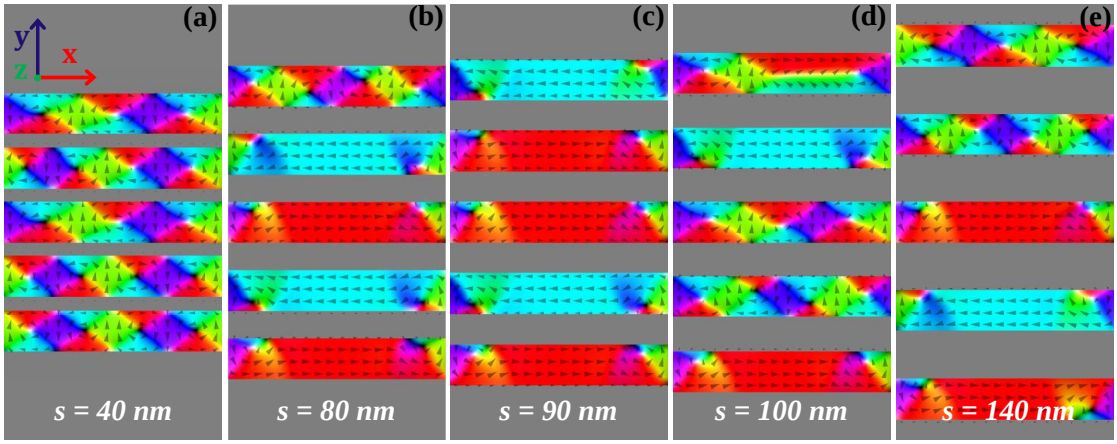


Figure 7.5: (a)-(e) Final spin configuration of the NWs after completion of 20 ns of micromagnetic simulation showing the non-volatility nature of the domains for the separation values, 40 nm, 80 nm, 90 nm, 100 nm and 140 nm, respectively [4].

for different separation values, as shown in Figure 7.5(a)-(e). For example, domains of all of the nanowires for s = 40 nm configuration are organized in a diamond orientation, while for s = 80 nm, domains of one nanowire is found in such diamond orientation, as shown in Figure 7.5(a) and (b), respectively. Similarly, diamond domain orientations are found in several NWs for s = 100/140 nm configurations as shown in Figure 7.5(d)/(e), respectively. However, for s = 90 nm configuration, a single domain with the aforementioned non-volatile configurations is found as shown in Figure 7.5(c), which might be the possible reason behind synchronization of all of the NWs and providing only a single peak output frequency, where efficient coupling between the launched SAW (phonon) and generated SW (magnon) has been occurred.

The calculated phase and power profiles of the spin waves at the dominant peak frequency (i.e., 0.55 GHz) are shown in Figure 7.6(a) and (b), respectively (obtained after post-processing of the magnetization data with python). The phase profile shows that the profile at the 0.55 GHz frequency is almost uniform while the power profile at this frequency exhibits a complex

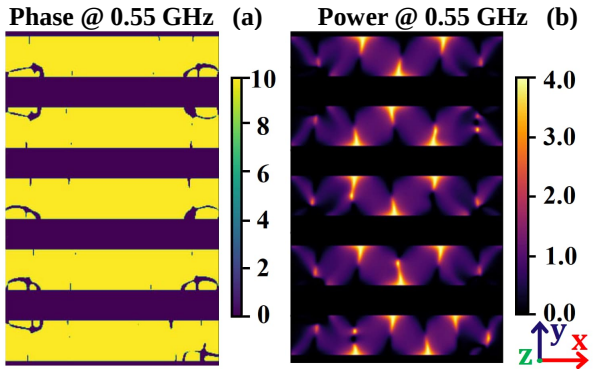


Figure 7.6: (a) The phase and (b) power profiles of the spin waves at the dominant frequency, i.e., the 0.55 GHz mode showing the uniformity of the profile. The color bars are shown at the right side of each of the figures [4].

propagation mode. Therefore, the power in the spin wave at s = 90 nm configuration is mostly concentrated in the longitudinal magnetization oscillations.

7.6 Frequency Tunability

In order to obtain the tunability, the array of NWs in the MMA was further patterned by keeping s_{op} unaltered at 90 nm along the transverse direction to develop a matrix of nanodots in the MMA with 25 elements of dimensions $90 \times 120\ nm^2$ separated at a horizontal distance of 15 nm as shown in the Figure 7.7. The Figure 7.7(a) shows the initial random magnetization configuration of the matrix of nanodots constituting the MMA, each of which becomes a multidomain state, as shown in Figure 7.7(b) upon applying a transverse stress in the matrix. [previously, similar effects for the nanowires in the MMA were observed as in Figure 7.2(b)]. After launching the SAW on the substrate, the multidomain states transform into multi-vortex states, as shown in Figure 7.7(c). Interestingly, it is observed, as shown in Figure 7.7(d), that the matrix of nanodots in the MMA retains their initial multi-vortex state (that has been obtained after launching the SAW on the substrate) even after completion of 20 ns of simulation demonstrating their non-volatility nature.

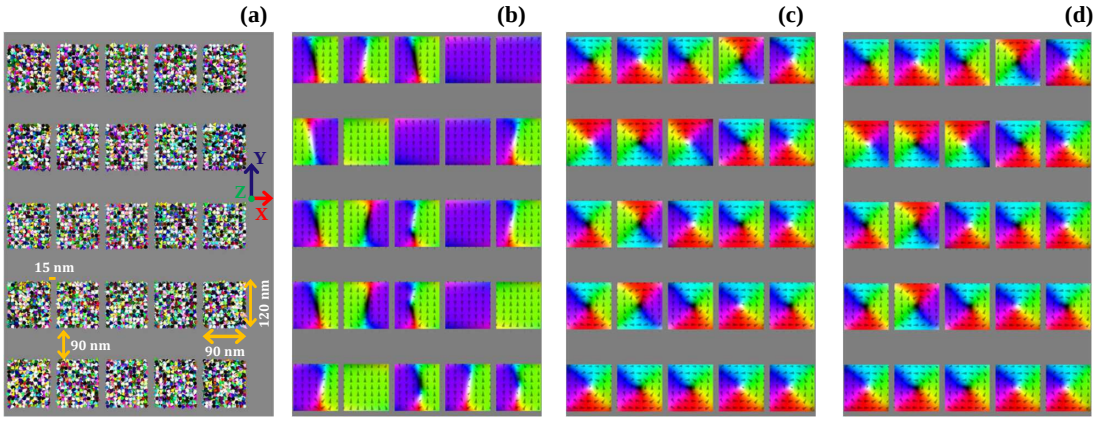


Figure 7.7: Micromagnetic modeling of the patterned matrix of nanodots in the MMA (a) Initial random magnetization configuration of the arrays. (b) Obtained Multidomain configuration in each of the nanodots in presence of a transverse stress along Y direction. (c) The multidomain structures in (b) are diminished upon launching of the 0.5 GHz SAW along X direction. (d) Final spin configuration of the NWs after completion of 20 ns simulation showing the non-volatility nature of the domains [4].

Due to further patterning of the NWs in MMA as shown in Figure 7.7(a), instead of generating the mutually synchronized auto-oscillations in the nanowires, the magnetization auto-oscillations along *x*/*y*/*z* directions become non-linear with time and exhibits a quasi-stable fluctuation as evidenced from Figure 7.8(a)/(b)/(c), respectively. The M_X component has a prominent beating period of ~ 6 ns. This non-linear auto-oscillation generates $1.5/1.4$ GHz microwave frequencies

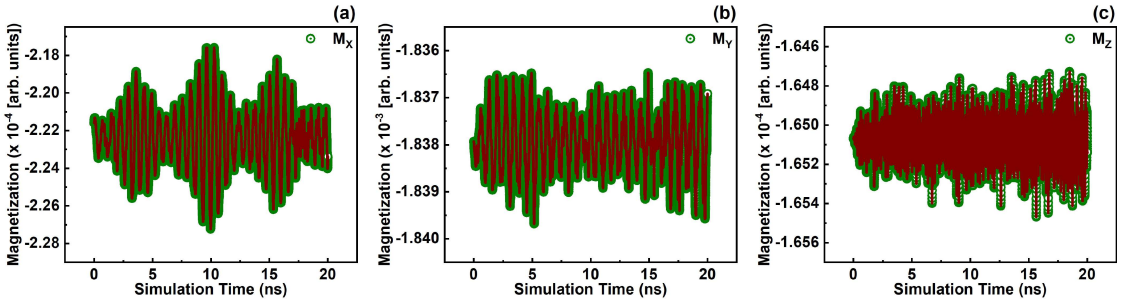


Figure 7.8: Calculated oscillations in the magnetization components, M_X, M_Y, M_Z, in a matrix of nanodots in the MMA along x-, y-, z- directions in (a), (b), (c), respectively, while the exciting SAW frequency remain kept constant at 0.5 GHz throughout the simulations [4].

as shown in FFT_X/FFT_Y in Figure 7.9(a)/(b) along with some other bands (4.8 GHz in FFT_X or 6.3 GHz in FFT_Y) with smaller amplitudes along the $x-$ and $y-$ directions, respectively. However, the FFT_Z as shown in Figure 7.9(c) shows a multiband ($1.4-30$ GHz) frequency spectra, where both the 27.25 GHz and the 4.8 GHz frequencies have almost same amplitudes.

It is also worth mentioning that the generated frequencies are greater than the SAW frequency, i.e., the nano-matrix has its own magnonic modes due to the rich spin-wave properties, which is determined by the exchange energy and the demagnetizing energy. Here, the exchange energy in this matrix of nanodots in the MMA (393 aJ) is almost double than the nanowires of MMA (187 aJ), while the demagnetization energy of the matrix of nanodots in the MMA (238 aJ) becomes smaller than that of the nanowires of MMA (337 aJ). So, there must be a trade off between the demagnetization energy and the exchange energy of the systems. In the latter case, the unique frequency tuneability seems to be governed by the particular exchange coupling modification in the vicinity of the each of the dots within the nano-matrix in the MMA. Overall, depending upon the requirement, this novel ultra-compact MMA could be designed to generate desired

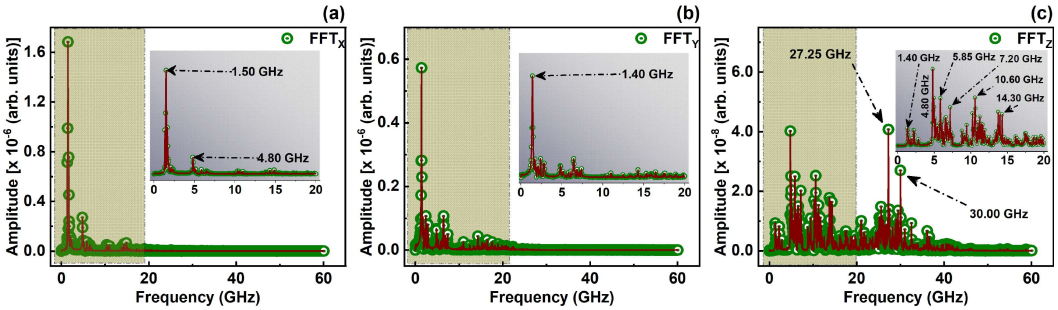


Figure 7.9: Power distribution of the patterned a matrix of nanodots in the MMA along $x-$, $y-$, $z-$ directions in (a), (b), (c), respectively. In each of the Graph, the corresponding insets reveal the magnified frequency spectra ($0-20$ GHz range) of M_X, M_Y, M_Z of the highlighted region at left side of the parent Power-Frequency spectra ($0-60$ GHz range) [4].

frequencies and the generated non-volatile spin textures of the nanowires/nanodots can also be useful in energy-efficient logic and low-power computing applications.

The generated spin waves further radiate electromagnetic waves (photon) into the surrounding space, and which could be captured with a horn-antenna/spectrum analyser for desired applications [216]. The phonons, due to the launched SAW on the piezoelectric substrate, first get coupled into the generated magnons within the nanomagnets and following that, the magnons further couple into the photons, i.e., the tripartite coupling between phonon-magnon-photon takes place, which could be exploited to generate desired microwave frequencies.

7.7 Conclusion

In conclusion, a tripartite coupling has been investigated between phonons (SAW), magnons (SW) and photons (EM wave) in ultra-compact SW dependent 'Magnon Microwave Antenna' (MMA) developed with magnetostrictive NWs on the piezoelectric substrate while generating microwaves with tunable frequencies. Initially, SAW is launched onto the piezoelectric substrate, which stimulates the magnetization precession of the NWs. As a result, the magnons (SW) have been generated within the NWs, which in turn causes the radiation of EM wave into the surroundings. The generated radiation can be collected by a horn antenna for applications. Hence, these MMA are based on the tripartite coupling which provides an advantage to utilize themselves over the electromechanical resonance based antennas. In addition, these novel structure gives the liberty to further miniaturize the overall existing size of the devices.

8 Tunability of Magnon Power-Phase Distribution for Reservoir Computing

This chapter is based on the following submitted paper [5][1].

8.1 Introduction

A spin wave (SW) is a collective excitation of the magnetic moments in a magnetic material, which is when quantized is referred as magnon [6]. Such spin waves are often used to transfer and process information in a manner similar to electromagnetic waves, as used in electronic devices. Generally, the power of a spin wave is related to the number of spins involved in the excitation and their collective behavior. The phase of a spin wave, on the other hand, refers to the relative timing or position of the spins within the wave. The power−phase relation of spin waves, denoting the connection between intensity and phase, unveils essential insights into the nuanced characteristics of these propagating waves. The correlation between power and phase is pivotal, as understanding the interdependence between power and phase is integral to deciphering the intricate dynamic behavior of spin waves from fundamental perspective, ultimately guiding the design and optimization in terms of their application in cutting-edge technologies.

Notably, the modern era has developed a great interest in microwave-based technologies due to the emergence of the Internet of Things (IoT) devices. Such advanced devices are based on the generation of microwave frequencies that have a relatively lower power consumption, however, still possess a strong signal amplitude, and good frequency stability. The advanced systems

[1]Tunable power-phase distributions in phonon-magnon coupled magnon microwave antenna for reservoir computing, **A. Samanta**, S. Roy, *Physical Review Applied*, **22**, 054076, 2024; DOI: 10.1103/PhysRevApplied.22.054076

require these high-end characteristics to perform their necessary operations seamlessly. However, traditional voltage controlled oscillators (VCOs) usually require a significant amount of electrical power to carry out their operations. Previously, spin torque oscillators (STO) have been explored as a potential source of microwaves due to their high tunability and small chip size compared to existing VCOs [117, 206]. However, they suffered from a weak output signal, which led to the investigation of an array of synchronized phase-locking STOs as a solution to this problem. Nevertheless, these phase-locking STOs have an extremely short synchronization time, and also synchronizing itself becomes a significant challenge in practical applications, limiting their use for cutting-edge IoT applications. Moreover, controlling the STOs requires an external bias in the form of an electric or magnetic field [15, 207]. Therefore, researchers are looking for bias-field free cutting-edge devices, as a solution. Spin wave based devices could be a potential solution in circumventing those issues, as such devices deal with spins of electrons [224] and the generated effective internal magnetic field [225] of the material.

A spin wave based nanomagnetic antenna is an integrated magnetic device that is constituted of patterned magnetostrictive (MS) materials on the piezoelectric (PE) substrate having dimensions in the order of tens of nanometers, potentially which could be used in a variety of applications, including ultra-compact transceivers, sensing and microwave applications etc. While such SW/magnon based nano-patterned magnetic antenna is operated in the microwave frequency range is known as Magnon Microwave Antenna (MMA) [4]. Since the MMA have been designed with magnetic nano-hetero-structures, i.e., patterned arrays of MS nanowires (NWs) on the PE substrate, the operation of MMA is based on the interaction between the phonons (generated from piezoelectric layer), magnon (originated from magnetic nano-patterns) and photons (electromagnetic radiation in the space). It is noted that the phonons, magnons and photons are the quantized acoustic waves, spin waves and electromagnetic waves, respectively. When the MMA is subjected to an alternating external electric field, a sinusoidal stress has been generated in the PE layer, that travels along the surface of the PE substrate and acts as a surface acoustic wave (SAW). The developed SAW (here, 0.5 GHz frequency) has then been transferred to the patterned MS NWs which in turn excites the magnetization in the same to form collective spin wave excitations (magnon) (of the similar SAW frequency) via the coupling of the phonons in the SAW to magnons in the spin wave [215]. Subsequently, the generated SWs further radiates the EM waves (photons) at the SAW frequency as the spin waves get coupled to the electromagnetic radiative modes via magnon-photon coupling and which can be used to transfer information and energy in the nanoscale regime [4, 20].

Here, it is worth mentioning that the moments in the MS NWs of the MMA experience effective internal magnetic field arising from the dipolar interaction and exchange interaction, which

accordingly shows a sustained magnetization precession about the effective internal magnetic field. Moreover, nanomagnetic antennas have several advantages over the conventional electrical antennas, including high miniaturization, improved directivity, higher magnetic confinement, and lower power consumption [205]. The small size and high efficiency of such nanomagnetic antennas make them well-suited for use in wide range of applications, including communication systems, sensing systems, microwave based technologies, etc. [116].

In the process of microwave generation through magnon microwave antenna (MMA), it is identified in the previous work that there are creation and annihilation of domains within the consisting magnetostrictive nanowires/nanodots on the piezoelectric substrate [4]. The creation of domain, i.e., the multidomain state is generated due to the application of transverse stress along the y-direction. Following that, when surface acoustic wave (SAW) is applied along the longitudinal direction (i.e., x-axis), the multidomain state gets converted into a single domain state, i.e., the corresponding domains are annihilated. However, such an important journey towards generating microwaves though the creation and annihilation of domains empowered by phonon-magnon coupling has overlooked the correlation of magnonic power profile and phase distributions at the operating frequency, which are extremely crucial for evaluating the performance of magnetic materials and devices, and accordingly to optimize their design for specific magnon based applications. It is also imperative to note that our digital modern era is shaped by the vast expanse of a large volume of data and lately developed artificial intelligence (AI). Consequently, the focus on enhancing speed, performance, miniaturization, and energy efficiency becomes paramountly important [38, 226–228].

In that context, the most significant hurdle in the realm of modern electronics revolves around the pursuit of energy-efficient solutions tailored for information processing endeavors, particularly while dealing with noisy or incomplete dataset(s) [38]. On such occasion, a suitable high-end computing algorithm, such as, the artificial neural network (ANN) needs to undergo a lots of rigorous training, else it would take more time to solve the given task. A potential promising avenue is the adoption of physical reservoir computing (RC) [226], a novel approach that capitalizes on the inherent nonlinearity and recurrence found in the dynamical ANN systems, colloquially referred to as the reservoir, to serve as a formidable computational resource. This innovative paradigm not only challenges the conventional norms of computing but also beckons towards a future where the intricacies of dynamical systems become the backbone of efficient and powerful information processing, where such RC typically does not require any such rigorous training. We investigate into the complex linear as well as non-linear dynamics of spin waves and their associated power and phase distribution within a SAW driven phonon-magnon coupling based MMA. Furthermore, it describes the possibility to tune the domains vis-à-vis corresponding power-phase distributions

in presence of an external bias magnetic field, which in turns offers an opportunity to utilize these MMA for reservoir computing as elucidated subsequently.

8.2 SAW Analysis: COMSOL Simulation

First, some typical nano-patterned MMAs have been designed in COMSOL [118] to obtain the SAW frequency, which have been further used as input in micromagnetic simulation with MuMax^3 [24]. The schematic of the MMA as shown in Fig. 8.1(a) is composed of *FeGa* MS NWs shaped in particular patterns onto a PE $LiNbO_3$ substrate. To carry out the design and simulations, the COMSOL Multiphysics software's structural mechanics module is used in conjunction with the AC/DC module. This combination enabled the incorporation of both the piezoelectric effect and magnetostriction physics interfaces. The S_{11} and S_{21} parameters estimate the SAW frequency as 550.75 MHz, which propagates along the longitudinal directions. The COMSOL simulation estimated the penetration depth of the surface acoustic wave (SAW) as 45 nm as shown in Fig. 8.1(c). Therefore, the thickness of the nanowire/nanodots is limited below 45 nm to ensure that the entire stress has been transferred into the nanowires/nanodots to excite the magnetization and accordingly the spin waves properly [4, 20].

We now calculate the amount of power that is coupled to the SAW, which could be further utilized in estimation of the stress generated upon launching of SAW. In order to do that, the similar approach by De et al. [215] and Drobitch et al. [216] have been considered. Here, the S_{11} parameter in Fig. 8.1(b) has been calculated considering an ideal scenario, i.e., any loss from the substrate has been neglected, that estimates the reflection coefficient of the system. The

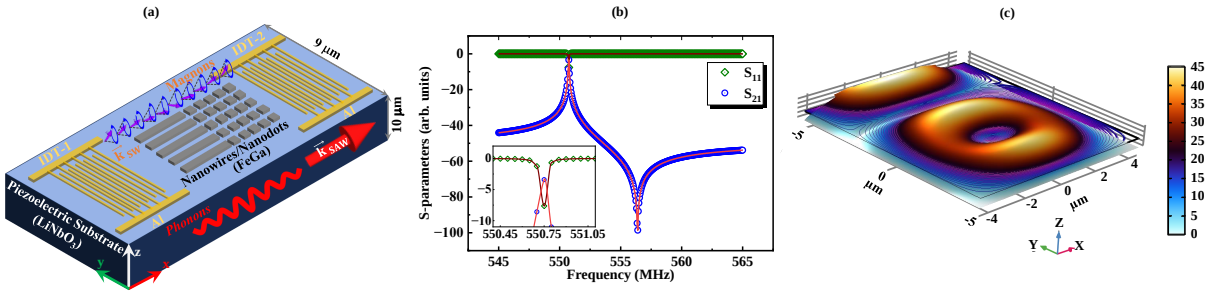


Figure 8.1: (a) 3D schematic of the magnon microwave antenna (MMA) with magnetostrictive (FeGa) nanowires (NWs). $\vec{k}_{SAW}$ and $\vec{k}_{SW}$ are the wave vectors associated with the SAW and the SW, respectively. Here, the width and thickness of the piezoelectric substrate ($LiNbO_3$) are 9 μm and 10 μm and that of the interdigitated transducer electrodes [*IDT-1* and *IDT-2* in the schematic] of *Al* (stands for Aluminum) are 1 μm and thickness 100 nm, respectively. (b) S_{11} and S_{21} parameters confirm the resonance frequency of SAW at 550.75 MHz. (c) Deformed shape plot at the resonance SAW mode estimates the penetration depth of 45 nm [5].

S_{11} value of ≈ -7.56 dB gives the reflection coefficient of the system as ≈ 0.175. Here, in the simulation, the input power (P_I) is 10×10^{-3} W. Therefore, the power coupled into the SAW is $P_C = (1-r) \cdot P_I \approx 8.25 \times 10^{-3}$ W.

The velocity of acoustic waves in $LiNbO_3$ typically ranges from 3 to 6 km/s [4, 20]. For the calculations, an approximate average velocity of 5.5 km/s has been used. This assumption leads to the maximum penetration depth, λ_{max} of 10 μm, considering operating frequency at ~550 MHz. Therefore, the SAW cross-sectional area becomes, $A_{max} = \lambda_{max}$ times width of the electrode $= 1 \times 10^{-11}$ m^2. Hence, the power coupled with the SAW is, $P_{C,max} = P_C / A_{max} = 8.25 \times 10^8$ W/m^2.

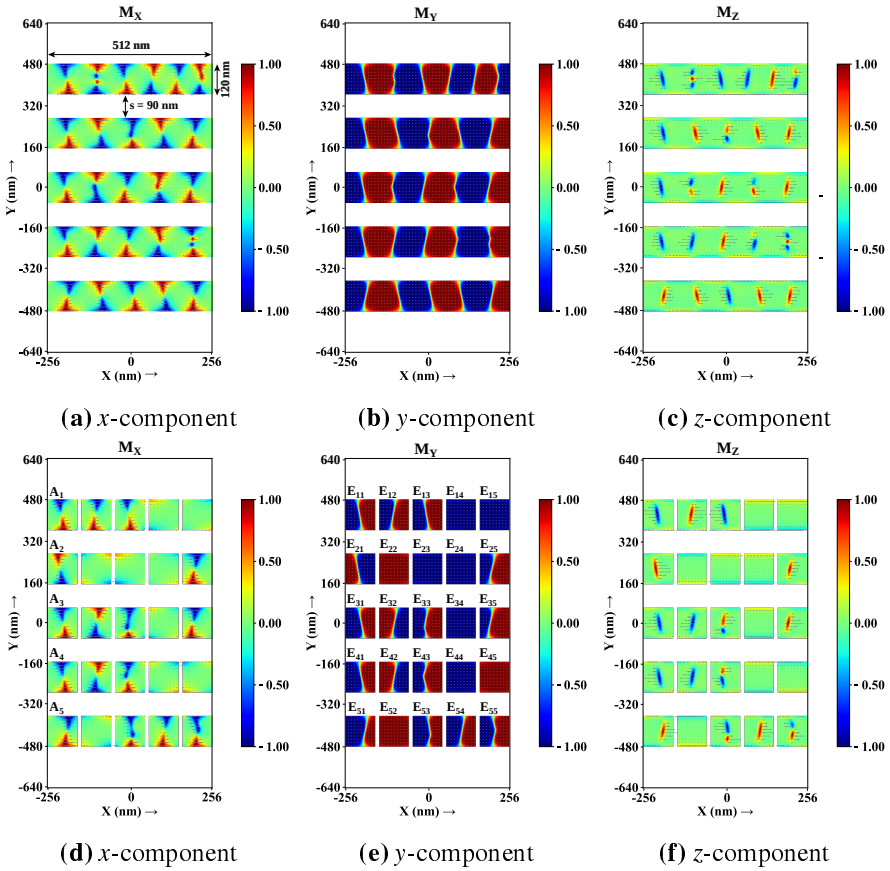
8.3 Spin Wave Analysis: MuMax^3 Simulation

The micromagnetic simulations using MuMax^3 [24] have been performed by discretizing the nanowires (NWs)/nanodots (NDs) into the cell sizes of $2 \times 2.5 \times 2.5$ nm^3. MuMax^3 solves the Landau-Lifshitz-Gilbert (LLG) equation [see equation (8.1) and (8.2)] and determines the macro-spin configuration at every coordinate point within the NWs/NDs and it produces the vector files containing the magnetization distribution over the simulating magnetic object. The following material parameters of FeGa [217], saturation magnetization $M_S = 1.32$ MA/m, exchange stiffness constant $A_{ex} = 16$ pJ/m, initial exchange anisotropy constant $K_{u1,i} = 0$ J/m^3, before applying external stress (σ_{stress}) are used in the simulation. We note that the effective internal magnetic fields is generated due to the effect of the shape anisotropy, dipole coupling and strain. This micromagnetic modeling of strain-mediated structures have been conducted at 0K to neglect switching defects, a widely used method [219].

$$\frac{\partial \vec{M}}{\partial t} = |\gamma| \vec{M} \times H_{\text{eff}} + \frac{\alpha}{M_S} \left[\vec{M} \times \frac{\partial \vec{M}}{\partial t} \right] \tag{8.1}$$

$$H_{\text{eff}} = -\frac{1}{\mu_0} \cdot \left[\frac{\partial E}{\partial \vec{M}} \right] \tag{8.2}$$

Here, the cell size lies below exchange length ($l_{ex} = \sqrt{\frac{2A_{ex}}{\mu_0 M_S^2}} \approx 3.82\, nm$), which further ensures the inclusion of all of the exchange interactions. Simulations performed with the typical dimensions of NWs are $512 \times 120 \times 40$ nm^3 (length $\times$ width $\times$ thickness) with different separation values (denoted as 's') (from 20 nm to 160 nm). Here, the cell size lies below exchange length ($l_{ex} = \sqrt{\frac{2A_{ex}}{\mu_0 M_S^2}} \approx 3.82\, nm$), which further ensures the inclusion of all of the exchange interactions. Simulations are performed with the typical dimensions NWs are $512 \times 120 \times 40$ nm^3 (length $\times$ width $\times$ thickness) with different separation values (denoted as 's') (from 20 nm to 160 nm).



(a) x-component **(b)** y-component **(c)** z-component

(d) x-component **(e)** y-component **(f)** z-component

Figure 8.2: For separation, 's' = 90 nm configuration, (a) $x-$, (b) $y-$ and (c) $z-$ components of the multidomain state in presence of the transverse stress along the y-direction and for nanodots that are in (d), (e) and (f), respectively. Length and width of the individual nanowires remain constant throughout the study at 512 nm and 120 nm, respectively. For the nanodots, while the separation along y-axis (vertical direction) is 90 nm that along the x-axis (horizontal direction) is 14 nm. Here, A_1 to A_5 denote the nanodot array while the E_{ij} denotes the individual nanodot elements for i^{th} row and j^{th} column, where $i, j = 5$ [5].

A typical example with 's' = 90 nm separated nanowire array/nanodots matrix is shown in Fig. 8.2(a)/(b)/(c) and (d)/(e)/(f), respectively. The spatial distributions of the $x-$, $y-$, $z-$ components reveal different domain configuration along the respective directions. The multidomain state predominantly forms along the $y-$ direction, where up (brown) and down (blue) spins are separated with the domain walls, as expected given the application of transverse stress along the $y-$ direction. On the other hand, the $x-$ and $z-$ components primarily consist of in-plane spins (greens region with zero magnitude), while they are separated by either alternate down (blue) and up (brown) spins along the edges (for $x-$ directions) or by alternate up (red) and down (blue) spins within the nanowires (for $z-$ directions), respectively. However, the spatial distributions for the nanodot matrix exhibit a drastic variation in domain configuration compared to that of the continuous nanowires, as shown in Fig 8.2(d)/(e)/(f).

Let us consider the domains of the $x-$ component (for the dot-matrix). The first three elements (E_{1j}, $j = 1-3$) of the A_1 array of the matrix have a similar domain configuration with in-plane spins edged by down (blue) and up (brown) spins on the top and bottom sides, while the last two consist mostly of in-plane spins. Similar domain configurations are formed for the other arrays as well. The M_Z domain structure also mostly formed with consistent in-plane spins, where some of the elements are centered by either up spins or down spins. However, the multidomain state with up/down spins separated by domain wall also forms for the M_Y component along the $y-$ direction. Interestingly, there are some elements which are dominated with either up spin or down spins. For example, elements, E_{14}, E_{15}, E_{23}, E_{24}, E_{34}, E_{44} are strongly dominated by down spin configuration, while elements, E_{22}, E_{45} and E_{52} are strongly dominated by up spin configuration; which might be the one of the reasons behind such complex magnetization oscillations observed along the $x-$, $y-$ and $z-$ directions (as shown later in Fig. 8.7(a), (b) and (c), respectively).

Following similar approach by Fabiha et. al. [20], the stress has also been incorporated in the anisotropy (K_{u1}) and calculated as $K_{\text{stress}}=-\frac{3}{2}\lambda_S \cdot \sigma_{\text{Stress}} \cdot \sin(2\pi f_0 t)$, where $\frac{3}{2}\lambda_S$ is the saturation magnetostriction constant of FeGa [400×10^6] [217, 218] and σ_{stress} is the effective stress acting on the magnetostrictive material due to launching of the surface acoustic wave (SAW) and f_0 is the resonance frequency of the SAW (550 MHz). Therefore, the effective anisotropy value is $K_{\text{eff}}=K_{u1,i}+K_{\text{stress}}$. Thus, the local magnetic field generated within the system is calculated as $H_{\text{stress}}(t)=H_0 \cdot \sin(2\pi f_0 t)$, where, H_0 is the amplitude of the stress field $= \left(\frac{\lambda \cdot \sigma_{\text{Stress}}}{\mu_0 \cdot M_S}\right)$ generated due to the SAW; here, $\sigma_{\text{stress}}=\sqrt{2 \cdot P_{C,\max} \cdot Z_{\max}}$ and $Z_{\max}=\sqrt{C_{11} \cdot \rho}$, where $Z_{\max}$, C_{11} (202.897×10^9 Pa) and ρ (4.7×10^6 g/m^3) are characteristic acoustic impedance, the first diagonal element of the elasticity tensor and the density of the $LiNbO_3$ substrate, respectively. Thus, $Z_{\max}=9.786 \times 10^8$ N$\cdot$S/m^3 and $\sigma_{Stress}=1.27 \times 10^9$ Pa are obtained. Hence, the amplitude of the stress field, $H_{\text{Stress}}(t)$ is $H_0 = 306252$ A/m ~ 3864 Oe.

In case of 's' = 20 nm configuration, a dominant peak is observed at a 50 MHz frequency, as depicted in Fig. 8.3. This observation implies inadequate coupling of the Surface Acoustic Wave (SAW) at this frequency with the spin waves. Examining the FFT in Fig. 8.3, the configurations for 's' = 40 nm, 60 nm, 140 nm, and 160 nm display three distinct peaks. Specifically, for 's' = 40 nm, the central peak is at 650 MHz, accompanied by two subbands at 300 MHz and 950 MHz. Similarly, 's' = 60 nm is centered at 400 MHz with subbands at 300 MHz and 800 MHz. Moving on, 's' = 140 nm dominates at 500 MHz, featuring two upper subbands at 700 MHz and 1600 MHz, while 's' = 160 nm is centered at 900 MHz with subbands at 600 MHz and 1000 MHz. Among the other configurations with two peaks, 's' = 80 nm has peaks at 600 MHz and 700 MHz, 's' = 100 nm has peaks at 800 MHz and 1300 MHz, and 's' = 120 nm exhibits peaks at 700 MHz and 1250 MHz. Notably, the 's' = 90 nm configuration stands alone at 550 MHz without any

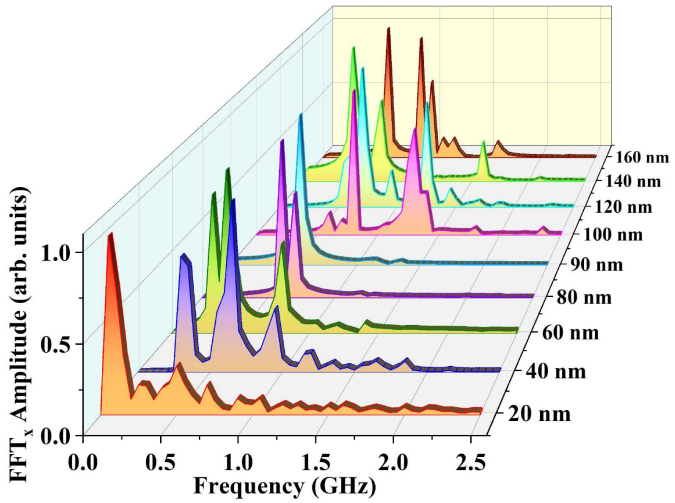


Figure 8.3: Variation of the power distribution obtained from fast Fourier Transformation (FFT) of magnetization as a function of NW spacing [5].

subbands, indicating effective coupling of the SAW with the generated spin waves. Consequently, this 's' = 90 nm configuration yields an optimum synchronized output with sustained oscillation [4]. Appearance of multiple peaks/single peak in the FFT power spectra is further explained later.

Contextually, the demagnetization energy (E_{demag}), the exchange energy (E_{exch}) and the total energy (E_{total}) values of the different geometrical configuration for different magnetization configurations (namely, multidomain state and the stable single domain state) are summarized in Table 8.1. For all geometrical configurations, the exchange energy of the initial random magnetization state (not shown here) is three order of magnitude greater than the multidomain state and the single domain state, which is expected as in random distribution the neighboring moments within each NW are coupled randomly through strong exchange interaction. Since there is no external magnetic field applied, the Zeeman energy is zero and hence not considered. Moreover, the magnetic dipoles tend to align in a way that minimizes the overall energy of the system. This interaction contributes to the stabilization of the aligned magnetic moments within a domain.

With the introduction of a Surface Acoustic Wave (SAW) in the longitudinal direction ($x-$ direction here), one can consider the magnetic interconnection between the neighboring nanowires (NWs) as a parallel combination through dipolar coupling, akin to how electrical Spin Transfer Oscillators (STOs) function through resistive connection. It's crucial to emphasize the vital roles played by demagnetization energy and exchange energy in maintaining stable magnetization oscillations. Therefore, finding a suitable equilibrium or a trade off between these energy components is imperative for these systems [4].

Each of the individual nanowire (five here) in the MMA is observed almost in single domain state (as shown in Fig. 8.2) for the s = 90 nm configuration while the other configurations (s = 20 nm to 160 nm, other than the 90 nm configuration; not shown here) all the nanowires failed to form such single domain state like the earlier. Throughout the study here, each of the studied

magnetostrictive nanowires has a high aspect ratio (AR) of ~ 4.2, defined as length:width (512 nm:120 nm), which is kept constant. We note that the demagnetization energy plays an important role in stabilizing the domains [6, 133], which is the case in this study due to such high aspect ratio. Therefore, the tiny spacing between the neighboring nanowires (s = 20 nm to 160 nm) comes into the picture and determines the domain configuration. Each of the nanowires would experience the exchange energy due to small separation between them. Hence, the demagnetization energy or the dipole interaction (due to the high aspect ratio) competes with the exchange energy.

The separation value with a particular aspect ratio in a NW/ND array not only contributes to the exchange energy, also it contributes to the demagnetization energy. Moreover, it is well known that in a magnetic system domains are formed at the cost of energy. Fig. 8.4 depicts the ratio of exchange energy (E_{exch}) to demagnetization energy (E_{demag}), i.e., [$E_{\text{exch}}/E_{\text{demag}}$], which confirms the previous statement. In the process of forming such single domain states in each of the nanowires, both E_{exch} (818.31 aJ) and E_{demag} (806.63 aJ) become comparable to each other. Compared to the continuous nanowire arrays, a completely dissimilar trend for the nanodot matrix is observed, as the ratio for single domain state and the multidomain state lies on the opposite end, i.e., the demagnetizing energy of the single domain state is dominated by the exchange energy while for the multi domain state the demagnetizing energy strongly dominates over the exchange energy. However for other configurations, the exchange energy seems to be surpassed by the demagnetization energy. Thus, such stable single domain state was not observed. Accordingly, sustained oscillations in the magnetization responses are observe, as elucidated in the following paragraph.

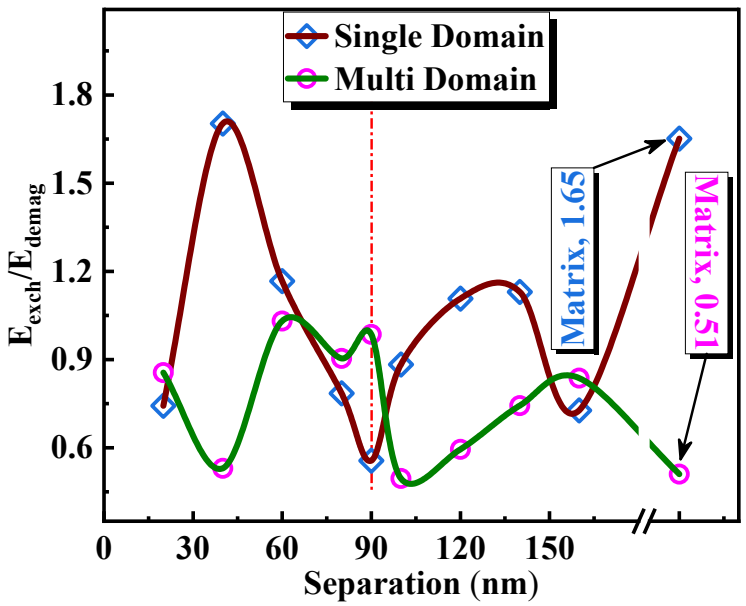


Figure 8.4: Variation of the exchange energy ratio to the demagnetizing energy as a function of spacing between the NWs for the single domain state and multidomain state, respectively. The same for the nanodot matrix is annotated on the graph [5].

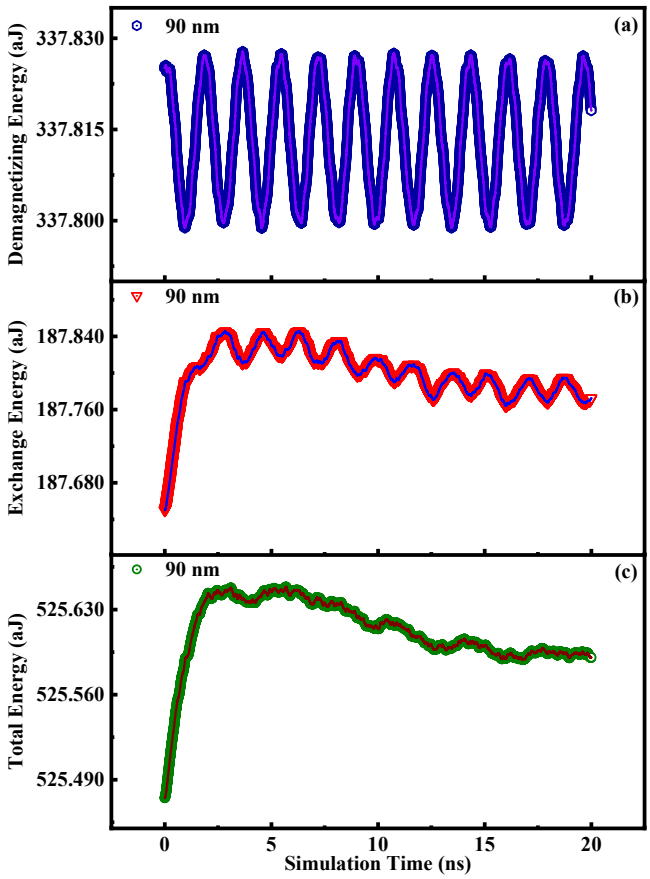


Figure 8.5: Variation of the (a) Demagnetization Energy, (b) Exchange Energy, (c) Total Energy, as a function of simulation time of the MMA at 90 nm separation ensuring efficient coupling for the auto-oscillation and mutually synchronized state of the NWs [5].

Both the exchange energy and the demagnetization energy terms are related to the oscillations of the magnetization with the following equations, symmetric exchange energy density, $w_{\text{ex}} = A_{\text{ex}}.\int \nabla(\vec{m})^2 = A_{\text{ex}}.\int [\nabla(\vec{m}_x)^2 + \nabla(\vec{m}_y)^2 + \nabla(\vec{m}_z)^2]$ (A_{ex}, exchange stiffness constant), and the stray field energy density or magnetostatic energy density, $w_{\text{d}} = \int \left(\frac{1}{2}\mu_0 \vec{H}_{\text{d}} \cdot \vec{M}\right) dV$, respectively, where, 'w' denotes the corresponding energy density of the material [2, 133]. The total energy variation as shown in Fig. 8.5(c) first saturates at 4.5 ns, which remain almost unaltered up to 5.5 ns and then starts decreasing continuously. The exchange energy has perhaps a greater influence in the total energy of the system as the demagnetization energy varies sinusoidally which is free from any damping over the studied time span. Such sinusoidal variation of demagnetization energy might be responsible for such stable overall magnetization oscillations. Since the single domain in each of the nanowires has its own directions, it is imperative to check the magnetization oscillations for each of the nanowires, as elucidated later.

Figure 8.6(a), (b), (c) show the magnetization oscillations of individual NWs (where, each of the NWs are labeled as 1-5 in order from top to bottom as shown in Fig. 8.2(a)) along $x-$, $y-$ and $z-$ directions, respectively. We observe that each of the NW oscillates in their own way, however, they are synchronized to the overall magnetization. Here, [in Fig. 8.6(a)/(b)/(c)], only

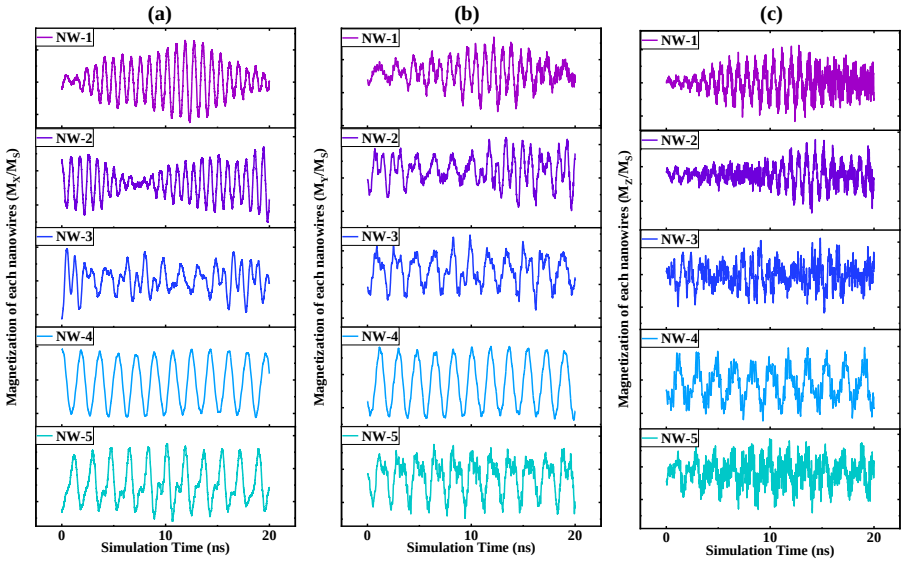


Figure 8.6: The (a) M_X, (b) M_Y and (c) M_Z components of each nanowire for 90 nm configuration, respectively while, the top row highlights the overall magnetization of the whole system [5].

the magnetization oscillation of the NW-4 is similar to the overall magnetization oscillations of the system, i.e., synchronized properly with the input. In this case, the relationship between the input (surface acoustic waves) and the output (magnetization oscillations of overall system/NW-4) follows almost a linear pattern. On the other hand, the other nanowires (namely, NW-1, 2, 3 & 5) show drastically different magnetization oscillations. The amplitude of them increases/decreases in a random manner, signifying the possibility of introducing frequency mixing, i.e., the interaction between different frequencies results in the generation of new frequencies, which are not present in the original input. Therefore, it is worth assuming that the system hints towards the generation of non-linear dynamics within each of the nanowires and that non-linear spin wave behavior may introduce complexities such as higher harmonics, different mode coupling, and frequency mixing, which might be beneficial for reservoir computing as further described in section 8.7. Since the NW-4 is synchronized with the output possibility of its detection of the task/signal will be the least, whereas, the possibility of its detection in the NW-3 might be the highest. Similar scenario is observed for the nanodot array. The overall magnetization oscillation for nanodots even does not synchronize with that of the individual arrays, as shown in Fig. 8.7. Therefore, it might be the best for probabilistic computing. Though, the proposed MMA has the potential for such probabilistic computing, a detailed explanation from that aspect is out of the scope of this present study.

The power spectra obtained through Fast Fourier Transform (FFT) is depicted in Fig. 8.3. At the 20 nm and 40 nm configurations, the dominance (as explained in Section 8.6) of intrinsic shape anisotropy and the strength of magnetostatic interaction is notable. In these cases, the overall demagnetization energy surpasses the exchange energy, hindering synchronization with

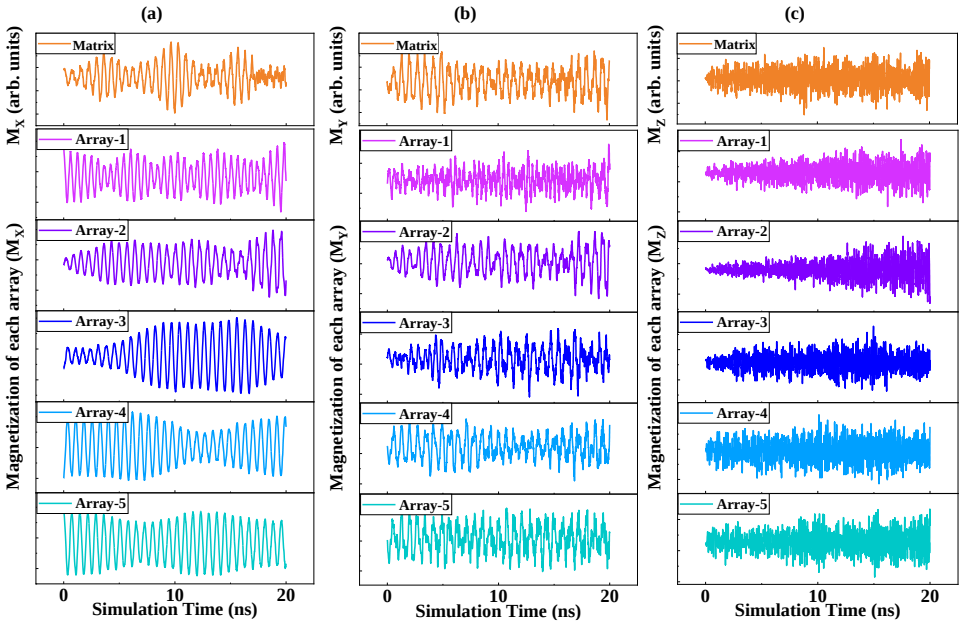
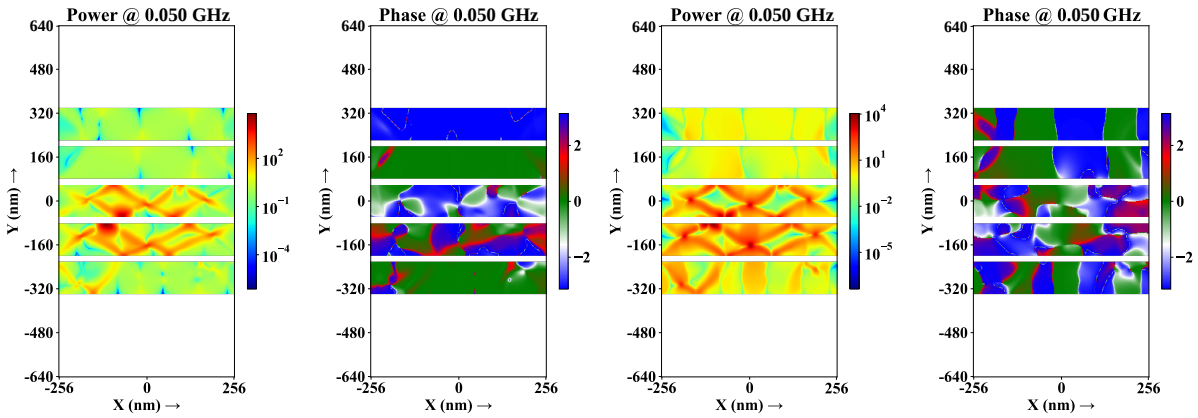


Figure 8.7: For the nanodot array, the (a) M_X, (b) M_Y and (c) M_Z components of each array, respectively while, the top row depicts the overall magnetization responses arising from the whole system [5].

the launched Surface Acoustic Wave (SAW) frequency. Consequently, incoherent magnetization precession, intrinsic to the array, occurs within the nanomagnets. This leads to power distribution at both lower and higher frequencies, potentially influenced by the array geometry [215].

In the case of the 20 nm configuration, with only one peak, it can be inferred that no nanowires are synchronized with each other. The x-component of magnon power distribution (refer to Fig. 8.8(a)) illustrates that the highest power is localized predominantly between NW-3 and NW-4 at two points (dark red region), indicating non-uniform distribution. Notably, systems tend to stay in the lowest energy state, and the complex canted power profile in NW-3 and NW-4 suggests that, while traveling longitudinally, the magnon path bifurcates towards the edge of the nanowire (potentially due to the system's exchange energy) and reunites, returning from the edge to the middle of the nanowire (possibly due to strong dipolar interaction) to minimize the system's energy. Consequently, the relatively higher power (orange region) in NW-3 and NW-4 follows a zigzag path, forming a tetrahedron shape (henceforth mentioned as, diamond shape), where the lower power is surrounded by higher power. Other nanowires exhibit a moderate power distribution (green-yellow region) with some lower edges (sharp blue lines in NW-1, 2, and 5) between them, highlighting complexity in the phase profile. In general, the propagating spin waves (here the red region; traveling longitudinally) involve a coherent movement of the phase of the spin precession across space, while standing spin waves (here green-yellow region; almost constant) involve a stationary pattern of spin precession.

NW-1 exhibits a phase distribution of 180° ($\equiv \pi$ rad), while NW-2 and NW-5 have a 0° phase. This suggests that NW-2 is in phase with the input Surface Acoustic Wave (SAW), while NW-1 is



(a) x-component **(b)** y-component

Figure 8.8: Magnon power profile and phase distribution for 's'=20 nm configuration showing out of synchronized state [5].

out of phase. A closer examination reveals alternating sharp blue edges with changes in direction. Considering the $y-$ direction, it is horizontally divided into two parts, i.e., the quantization number is $n_y = 2$. The blue region, representing the lowest magnon power, implies an attempt to distribute energy associated with magnon power among neighboring nanowires. Consequently, a zigzag pattern is observed, possibly due to the coexistence of propagating spin waves and standing spin waves (as explained earlier) preventing synchronization between neighboring nanowires along the longitudinal direction. On the contrary, the y-component in Fig. 8.8(b) displays complex quantization. For example, NW-1 and NW-2 are vertically divided with $n_x = 5$ and 3, respectively, while NW-3 and NW-4 are horizontally divided with quantization number $n_y = 2$. Notably, NW-5 first follows a zigzag path and then divides horizontally with quantization number $n_x = 3$. The phase distribution of the y-component for NW-1 and NW-2 does not exhibit clear synchronization, as they are well-separated with π rad and 0 rad. However, unlike the x-component, NW-1 and NW-2 are in the same phase. Similar behavior is observed for NW-5 as well. However, NW-3 and NW-4 show a random phase distribution.

In the x-component, NW-3 exhibits a tiny region with no phase (green with 0 rad) surrounded by a $-\pi/2$ rad phase region, while in NW-4, it is a $\pi/2$ phase region. A similar pattern is observed for the y-component. Since the gap in both cases of phase distribution is extremely small, it could be considered that those positions in the two NWs (NW-3 and NW-4) are synchronized. However, such synchronization is challenging to control, as the spin wave in this case is mainly influenced by the array geometry. In the case of the 40 nm configuration, there are three peaks in the corresponding spectrum, indicating that at least two nanowires (NWs) are synchronized along the x direction simultaneously, as observed in Fig. 8.9(a). For instance, NW-4 and NW-5 appear

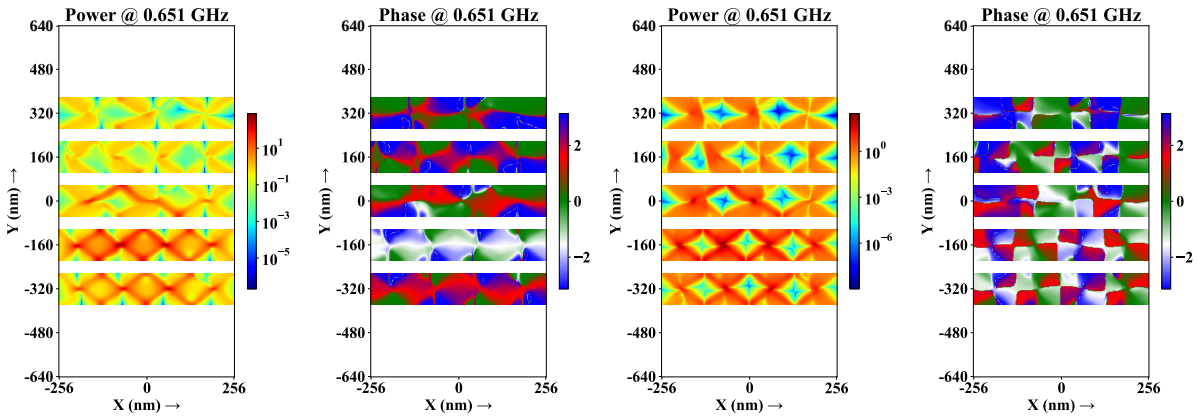
to be synchronized, although there is a noticeable difference in the amplitude of power between them. Compared to the 20 nm configuration, the power of the central peak is lower, signifying that the exchange energy dominates over the demagnetizing energy of the system this time, as evidenced in Table 8.1. Consequently, the launching of Surface Acoustic Wave (SAW) gives rise to new extrinsic modes.

TABLE 8.1: The demagnetization energy, exchange energy, and total energy values of the different spatial configuration as a function of different magnetization configurations, namely, multidomain state and single domain state.

Separation (nm)	Demagnetization energy (aJ)		Exchange energy (aJ)		Total energy (aJ)	
	Multi-domain state	Single domain state	Multi-domain state	Single domain state	Multi-domain State	Single domain State
20	892.15	261.13	763.35	193.92	1655.55	455.05
40	1014.14	220.26	537.30	374.71	1578.43	594.97
60	823.06	266.48	848.26	310.87	1671.32	577.35
80	850.15	290.80	768.28	228.09	1618.43	518.89
90	818.32	337.83	806.63	187.65	1624.94	525.47
100	1123.28	311.42	556.18	275.07	1679.46	586.49
120	1072.01	270.75	637.34	299.86	1709.34	570.61
140	937.79	262.14	696.88	296.42	1634.68	558.57
160	870.78	318.55	728.56	231.44	1599.34	549.99
Array	1022.31	238.27	521.37	393.48	1543.68	631.76

The associated phase and power profiles of the spin waves of the M_X and M_Y components, at the central peak frequency (i.e., 0.65 GHz) are shown in Fig. 8.9(a) and (b), respectively (obtained after post-processing of the magnetization data with python). For NW-1 and 2, the power is distributed diagonally (towards higher region) from its respective origin (lower region). The power in NW-3 traverses along the zigzag path (and a weak diamond shape distribution), possible due to the competition between exchange energy and the demagnetizing energy. The NW-4 and 5 show previously explained diamond shape distribution for the x-component. In this studied nanowire system, the quantization numbers provide insight into the distribution of power along different directions. Notably, $n_y = 2$ suggests a vertical quantization of power, while varying values of n_x along the horizontal direction (e.g., $n_x = 4$ for NW-1 and NW-2, $n_x = 5$ for NW-4 and NW-5) indicate different modes of power confinement. The complexity observed in NW-3, where n_x is unidentifiable due to a complex pattern, hints at intricate power distribution characteristics. The phase profile at a specific frequency reveals a complex propagation mode of spin waves, indicative of collective spin excitations. Particularly, at a 40 nm configuration, the power in the spin wave is not confined to a single frequency, suggesting a broader distribution across frequencies. This multifaceted analysis underscores the nuanced behavior of spin waves in nanowires, influenced by their geometry and material properties, with implications for diverse frequency modes and intricate power distribution patterns.

Now, the power profile and phase distribution for 's' = 90 nm configuration along $x-$ and $y-$ directions are discussed, as shown in Fig. 8.10(a)/(b), which reveals that the power at 0.55

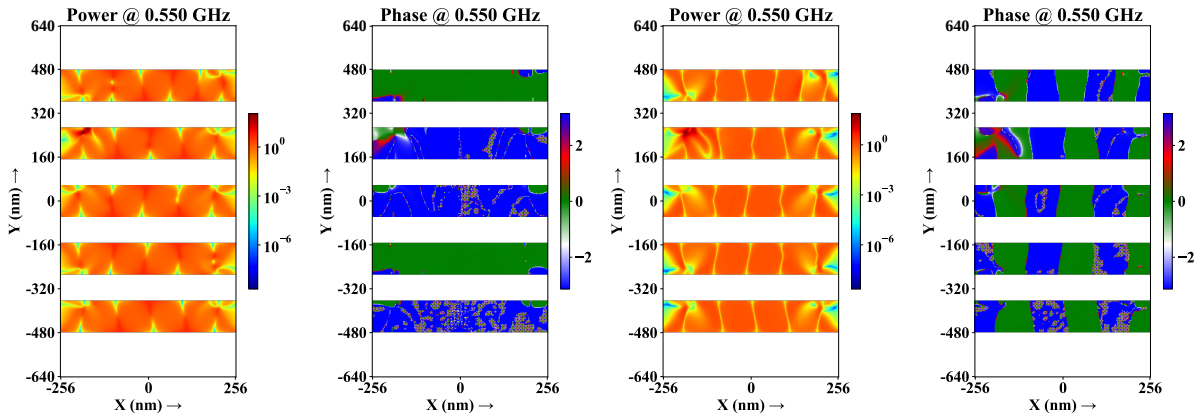


(a) x-component **(b)** y-component

Figure 8.9: Magnon power profile and phase distribution for 's'=40 nm configuration showing partially synchronized state [5].

GHz is evenly distributed between the five nanowires. Since the power shows almost uniform distribution the magnon power is concentrated at this particular frequency only and as a result, a synchronized single peak is observed in the FFT power spectra as shown in Fig. 8.3. A closure insight reveals that the power suffers a tiny edge effect (green-yellow region, i.e., comparatively the lower power region) in its magnon power distribution [Fig. 8.10a], which allows the spin wave to travel throughout the nanowire along the longitudinal direction. Since all the nanowires are synchronized no diamond shape is observed. Accordingly, both the quantization number, n_x and n_y become 1 for this case. The phase distribution shows that the NW-1 and 2 have π phase difference while the NW-2 and 3 seem to be mostly in same phase. Similarly, NW-3 and 5 have π phase difference compared to NW-4. As explained earlier, there exist local synchronization in phase for some of the positions in the individual nanowires (e.g., NW-2, 3 and 5). Interestingly, the uniform power distribution throughout the five nanowire for the y-component as shown in the Fig. 8.10b shows quantization number $n_y = 1$ and $n_x = 5$. This time the edge effect appears on the extreme left and right of the each of the nanowires. Each of the nanowires are in phase along the y-direction. However, in each of the nanowires there is π phase difference between the adjacent portions.

Now, the power distributions and phase profiles of the arrays of the nanodot matrix are considered, as shown in Fig. 8.11 where each of the elements is separated horizontally by 14 nm distance and vertically by the optimum separation, 90 nm, at which sustained synchronized oscillations in the nanowires are obtained. Most of the magnon power (red/brown) is distributed evenly throughout each of the elements of the nanodot matrix, as shown in Fig. 8.11a. However, a closure insight reveals that comparatively lower magnon power (either green/yellow or yellow-



(a) x-component **(b)** y-component

Figure 8.10: Magnon power profile and phase distribution for 's' = 90 nm showing the synchronized state with uniform distribution [5].

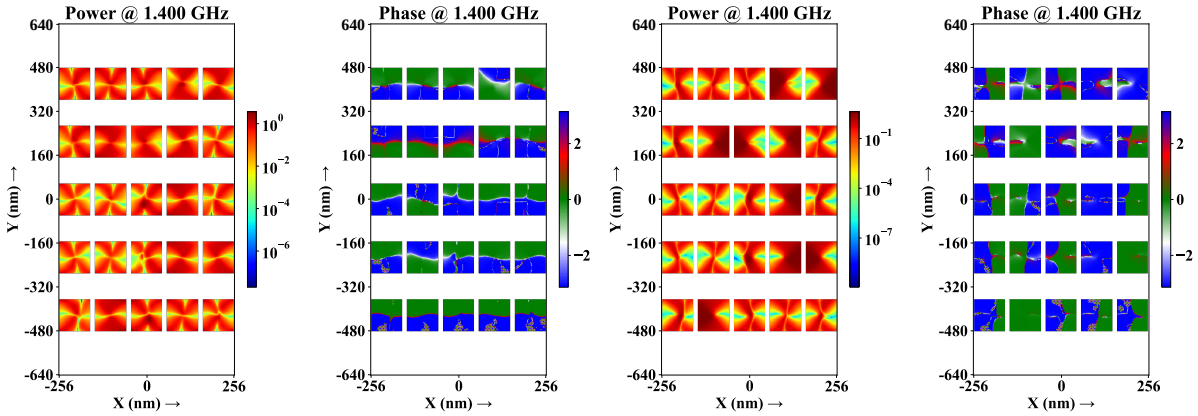
green mixture) edged along each direction (top, right, bottom and left) of the nanodots creates an inverse tetrahedron structure. Therefore, they do not have such straight quantization numbers, n_x or n_y. However, some of the elements, e.g., E_{14}, E_{15}, E_{22}, E_{23}, E_{24}, E_{34}, E_{44}, E_{45} and E_{52} form a mirrored conical pattern lacking comparatively lower powers along the top and bottom directions.

On the other hand, the phase profile exhibits significant interesting distribution. For instance, the top (green, i.e., 0 phase) and bottom (blue, π phase) halves of the $E_{1j}, j = 1-3$ elements are in same phase while E_{14} and E_{15} elements are inversely synchronized separated by tiny phase either $\pi/2$ (red) or $-\pi/2$ (white) phases. Similar kind of synchronization is observed for the other arrays due to the appearance of such $\pi/2$ (red)/$-\pi/2$ (white) separation between the green (0 phase) or blue (π phase). Similar kind of almost evenly distributed magnon power is observed for the $y-$ component as well, as shown in Fig. 8.11b. Instead of the lower power distribution along the four directions, this time, the magnon power is almost equally halved in the right and left directions only, resulting into the quantization number, $n_x = 2$ for each element and accordingly the formation of the conical shapes. However, interestingly, those elements which lack lower magnon power distributions along the $x-$ direction on the top and bottom parts, i.e., the elements E_{14}, E_{15}, E_{22}, E_{23}, E_{24}, E_{34}, E_{44}, E_{45} and E_{52} exhibit a comparatively higher magnon power distribution in any one half of the elements.

It is interesting to note that a higher value of n_x/n_y for the phase spectra results in a greater displacement of magnon intensity toward the periphery of the nanowire or nanodots. This phenomenon can be intuitively explained by the decrease in exchange energy. By maintaining an expansive region surrounding the circular core (might be a 'vortex') with the comparatively lower amplitude, a pronounced deviation of neighboring spins in close proximity to the vortex core is

mitigated, consequently leading to an overall reduction in the total energy [229].

An intriguing observation is that the spin waves observed here are not propagating; instead, they are localized at the center of each element. This localization might be attributed to the formation of vortices, favored by the strong demagnetization energy characteristic of the multidomain state. As the nanowires are patterned into nanodots, the demagnetization energy strongly dominates over the exchange energy of the multidomain state. While the exchange energy of the single domain state surpasses the demagnetization energy (as seen in Fig. 8.4), it proves insufficient to induce the movement of the spin wave. Consequently, the stationary nature of the spin wave is observed, primarily influenced by the matrix (nanodots) geometry.



(a) *x*-component **(b)** *y*-component

Figure 8.11: Magnon power profiles and phase distribution for the array configuration showing complex synchronization state within the nanoelements of the matrix.

Power and phase profile of the spin wave show complicated spin wave distribution, i.e., the spin wave has propagation mode as well as standing mode. The propagating spin waves are longitudinally traversing across the continuous nanowires. Note that, instead of following an undeviating path, it follows a zigzag track. Interestingly, along with such propagating mode, localized edge modes as well as bullet modes appeared/co-existed on such zigzag spin wave track (Fig. 8.11a). The edge mode appears alternatively at certain intervals, however, it fails to last throughout the cross section, i,e., it vanishes within the middle of the nanowires. In some cases, they formed bullet mode in the middle of the nanowire. However, a closure observation of the power spectra on the other hand reveals that the intensity of the propagating spin wave is smaller compared to that of the edge/bullet modes.

Additionally, since there is no direct external bias magnetic field applied in this study, the fundamental *Kittel Mode* would disappear from the system, as in *Kittel Mode*, spins generally precess around the external magnetic field and the frequency has a strong field dependency.

Therefore in the absence of an external magnetic field, such studied nano-hetero-structured (NHS) systems (magnetostrictrive materials patterned on the piezoelectric substrate) show spin precession due to the periodic sinusoidal strain caused by the surface acoustic wave, which are influenced by the saturation magnetization, nanomagnet dimensions, separation between the neighboring nanowires. Accordingly, those aforementioned material and system properties further determine array parameters (namely, dipolar coupling field and demagnetizing energy). Thus, spin waves in those systems are often defined as the intrinsic spin wave dynamics [215]. So, the spin wave generated in such cases is due to the effective coupling between the launched SAW and the generated SW. Therefore, whenever any other frequencies are obtained other than the SAW frequency (here 550 MHz) there might be dependency of some other parameters, e.g., demagnetizing energy and exchange energy [4, 20, 215]. In fact the competition between such different energies play a crucial role in stabilizing the multidomain from the initial random magnetization state to a single domain state and subsequently, magnetization oscillation within the nanomagnet. Absence of fundamental *Kittel* mode leads to the frequency locking state of the MMA as explained in the following section 8.4.

8.4 Frequency Locking at Optimum Separation for effective synchronization

Injection locked studies within the electrically tunable spin torque oscillators (STOs) are usually performed to measure the mutually synchronized response of STOs to an external radio-frequency (rf) signal. Typically, during the injection locking experiments, an rf current (I_{rf}) in addition to the optimized external bias electric current (I_{dc}) is passed through the coupled oscillators, where the frequency of the I_{rf} is fixed at the resonance frequency/peak frequency [230]. As mentioned earlier, the MMAs do not require any external bias alternating magnetic field, the working prin-

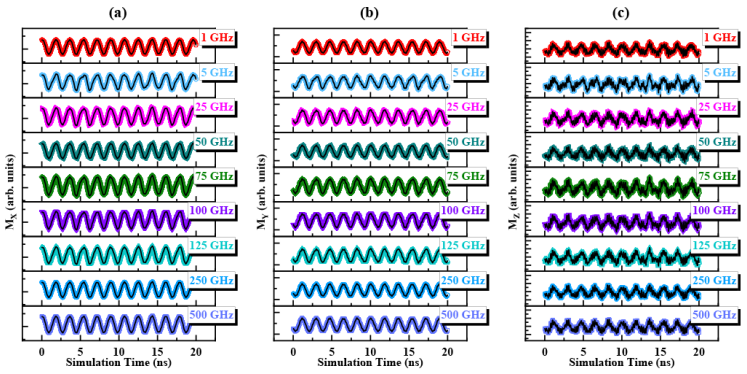


Figure 8.12: Magnetization dynamics along $x-$, $y-$, $z-$ directions as a function of SAW frequency altered from 1 GHz to 500 GHz with included with 0.5 GHz parent frequency. The inter-distance between the neighbouring five NWs remain constant at 90 nm to ensure sufficient exchange coupling and the dipolar interaction [5].

ciple of the MMA differs compared to the aforementioned electrically tunable STOs, accordingly giving rise to the occurrence of a different injection locking phenomena here; this could be ascribed as frequency locking. Recently, it is experimentally observed that the SAW frequency could be manipulated in the piezoelectric substrate/magnetostrictive nano-matrix hetero-structure by applying an ultrashort laser pulse [231, 232], which necessarily modulates the precessional dynamics and accordingly the phonon-magnon coupling (SAW-SW interaction) [223]. We have considered to perform the frequency locking response study by adding an additional external sine pulse with different frequencies varied between $1-500$ GHz to the mutually synchronized frequency (i.e., 0.55 GHz) at the optimum configuration as shown in Fig. 8.12. Following that, the discussed frequency locking states of the MMA configured with 90 nm configuration have been studied.

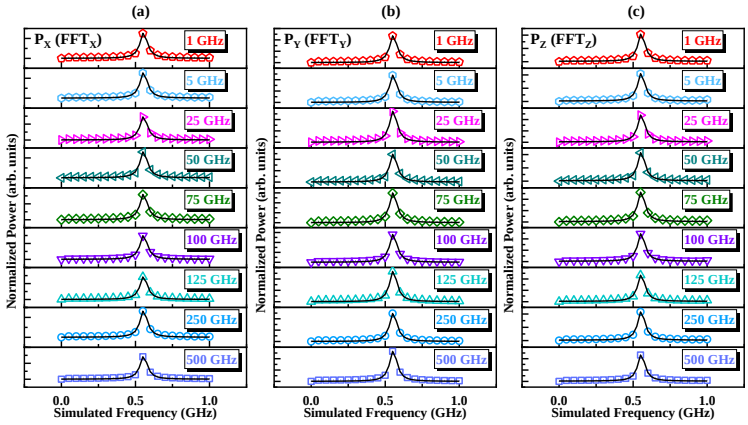


Figure 8.13: Power distribution of the frequency locked states as a function of frequency along $x-$, $y-$, $z-$ directions, respectively [5].

The power distribution of the injection locked MMAs with different frequencies reveals an almost constant omnidirectional synchronized peak at ~ 0.55 GHz (f_{sync}) as depicted in Fig. 8.13 (a), (b), (c), respectively. Hence, that f_{sync} peak might be intrinsic to the optimized geometry configuration [223, 233]. However, the power of the resonance frequencies follows the similar order, $P_X > P_Y > P_Z$, where, P_X, P_Y, P_Z are the obtained power of the resonance frequencies from the corresponding FFT of M_X, M_Y, M_Z, respectively. It is important to mention again that these MMA operates without the requirement of any external alternating bias magnetic field, which appears due to the absence of the fundamental Kittel mode in the MMA. Moreover, the array geometry parameters or the material parameters remain constant at the optimized 90 nm configuration, which might be responsible for establishing the frequency locking states between the neighbor nanowires in the MMA. Due to the frequency locking state the overall locking range gets enhanced (1-500 GHz) for the synchronized MMA as compared to the individual nanowire (0.5 GHz). Interestingly, auto-oscillations of the mutually synchronized states remain uninterrupted over the whole frequency range. However, a longer time of simulation is required

in confirming the stability of the frequency-locking state.

8.5 Time-domain stability of MMA

Now, the time-domain stability of the frequency-locked synchronized MMA was examine. Figure 8.14(a), (c) and (e) show the oscillations of the calculated magnetizations along $x-$, $y-$, $z-$, respectively, over the 20 ns and 50 ns stable time-domain trace for the optimized configuration of the MMA. The corresponding FFT of the calculated oscillations of the magnetizations has been performed in order to calculate the resonance frequency (f_{sync}) of the signal, which is shown in Fig. 8.14 (b), (d) and (f). It is observed that over the longer time span the oscillations (in every direction) become more stable compared to that in the shorter span. Moreover, the power of the 50 ns oscillation (in every direction) increases significantly. Since the MMA does not depend on any external alternating bias magnetic field, an increased power along every direction have been achieved independently.

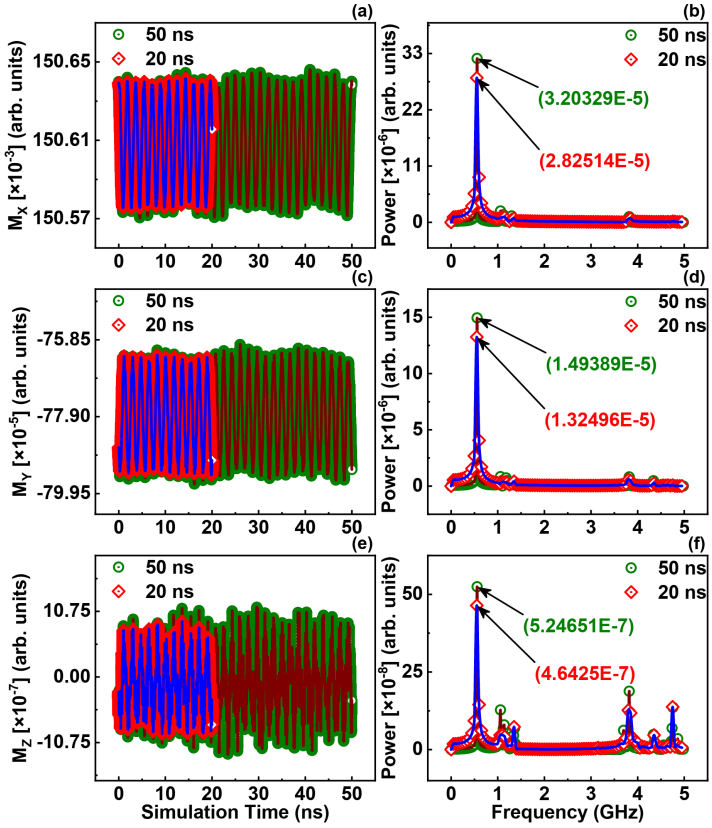


Figure 8.14: Comparison between 20 ns and 50 ns long simulation to verify the time domain stability of MMA. The calculated oscillations of the components of the magnetizations along longitudinal, transverse, and out-of-plane direction in (a), (c), and (e), respectively. The corresponding FFT spectra yield the auto-oscillation resonance peaks of the mutually synchronized MMA in (b), (d), (f), respectively [5].

Therefore, this present investigation offers a quite better energy efficient external bias field free performance over the conventional electronic devices. Moreover, when these structures emit the

electromagnetic radiation into the surrounding space that could be captured by a horn antenna [20] and could be used in other applications as well, such as, energy harvesting. While the microwave applications is the outcome of the phonon-magnon interaction, the following photon emission (EM wave radiation) induced by phonon-magnon coupling would be beneficial for wireless energy harvesting due to abundance of Wi-Fi, mobile, and other communication signals.

It's noteworthy to highlight that the observed alteration in domain wall motion induced by Surface Acoustic Waves (SAW) holds promise for applications in wireless energy harvesting, particularly beneficial for power-intensive Internet of Things (IoT) devices [220]. Another crucial aspect of this present investigation is the nonvolatility of the SAW-engineered single domain state (not shown here). The single domain nanomagnets maintain their state persistently until reset by either stress application or the application of a robust external magnetic field to revert to the initial multidomain state. This nonvolatility presents opportunities for energy-efficient logic applications and low-power computing [221], although this aspect is beyond the current scope of this present study.

8.6 Static Magnetic Study

The preceding sections comprehensively elucidate the spin wave power-phase distribution/synchronization properties within the nanowires of the MMA under bias field-free conditions. However, investigating into its fundamental static properties in the presence of an external magnetic field is worthwhile, as it may uncover potential applications for other magnetoelectronic devices [234]. Moreover, it is well known that switching mechanism is very sensitive to the thickness to width ratio of the nanowires. While the thickness is $\leq$ 40 nm, previously for a patterned $Ni_{80}Fe_{20}$ nanowires, it was reported that coherent spin rotation dominates in the reversal mechanism [235]. So, additional simulations were conducted to analyze the hysteresis loop under two conditions: (i) before applying the SAW [Fig. 8.15(a)-(d)] and (ii) after applying the SAW [Fig. 8.15(e)-(h)]. All MMA configurations, namely, 20 nm, 90 nm, 160 nm, and the nanodot array, are initially saturated by applying an external magnetic field of magnitude 3 T ($\equiv$ 30000 Oe). Subsequently, the hysteresis loops are simulated. It is noteworthy that, for the first condition (where the multidomain state is formed before the application of SAW), the magnetic field is applied along the transverse (i.e., $y-$) direction, and for the second condition, i.e., where the multidomain state transitions to the single domain state after the application of SAW, the magnetic field is applied along the longitudinal (i.e., $x-$) direction.

A significant contrast is evident in the simulated hysteresis loops before and after the application of Surface Acoustic Wave (SAW) conditions. First, considering the conditions before

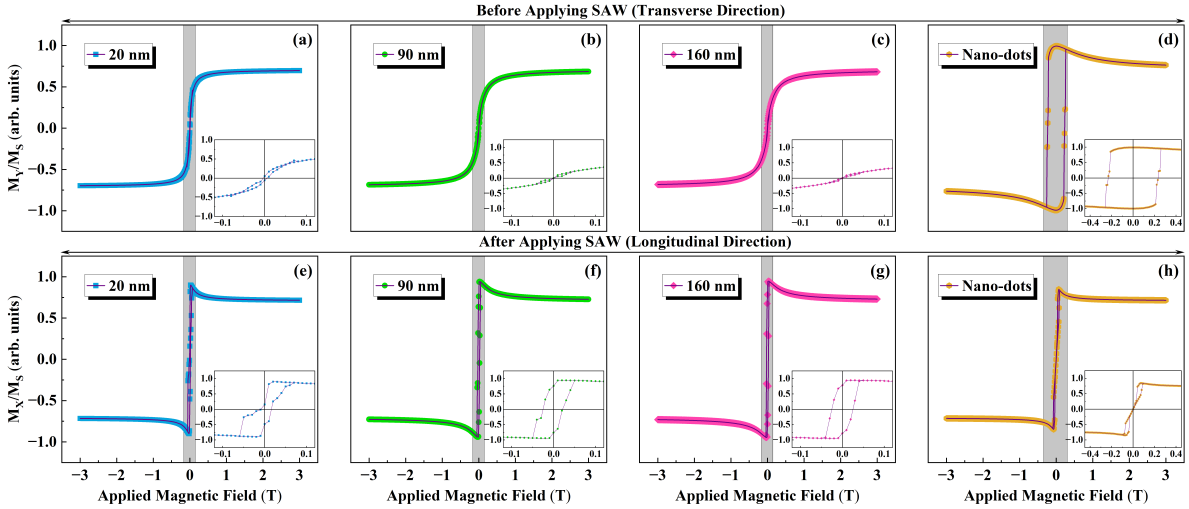


Figure 8.15: Simulated hysteresis loops of 20 nm, 90 nm, 160 nm separated NWs (a)-(c) and the nanodots (d) before applying the SAW along transverse ($y-$) direction, while the same for the same configurations, (e)-(h) after the application of the SAW along longitudinal ($x-$) direction [5].

applying SAW, the hysteresis loops of the 20 nm [Fig. 8.15(a)], 90 nm [Fig. 8.15(b)], and 160 nm [Fig. 8.15(c)] configurations exhibit a negligible coercive field (S-type), indicating that the y-axis serves as the easy axis for these nanowires. However, when the nanowires are patterned into nanodots, the hysteresis loop becomes rectangular [Fig. 8.15(d)], with a comparatively larger coercive field of approximately 230 Oe. In this case, an almost rectangular hysteresis loop is observed, marked by a sharp drop in magnetization at an external field of -230 Oe.

The observed drastic variation in hysteresis loops could be attributed to demagnetizing energy or dipolar magnetic coupling. The overall demagnetization energy values summarized in Table 4.1 reveal comparable values for some nanowire configurations and the nanodot configuration. Interestingly, the hysteresis loops confirm that the overall value alone does not contribute significantly to the phenomenon; instead, its spatial distribution plays a crucial role in complex spin wave distribution. Given the studied film thickness of 40 nm, it is reasonable to assume that a coherent magnetization rotation reversal mode mechanism takes place, leading to the observed hysteresis loop for patterned nanodot arrays.

After the application of SAW conditions, the hysteresis loops for 20 nm, 90 nm, and 160 nm configurations are drastically different from that of the nanodot array. The 20 nm and 90 nm configurations exhibit a step in the hysteresis loop, while the 160 nm configuration shows a quasi-rectangular hysteresis loop. All of them display a comparatively larger coercive field. Nevertheless, the nanodot array now changes to an almost zero coercivity hysteresis loop with negligible remanence, as shown in Fig. 8.15(h). Notably, all nanowire dimensions (length = 512 nm, width = 120 nm, and thickness = 40 nm) are greater than the exchange length (3.82 nm,

as calculated earlier) of FeGa. Therefore, deviations from uniform magnetization are expected. Since the thickness-to-width ratio ($40/120 = 0.33$) is ≤ 0.5, no reversal mode would be present in the system [236, 237]. The origin of such a hysteresis loop for square nanodots can be elucidated from the perspective of domain formation, as explained below.

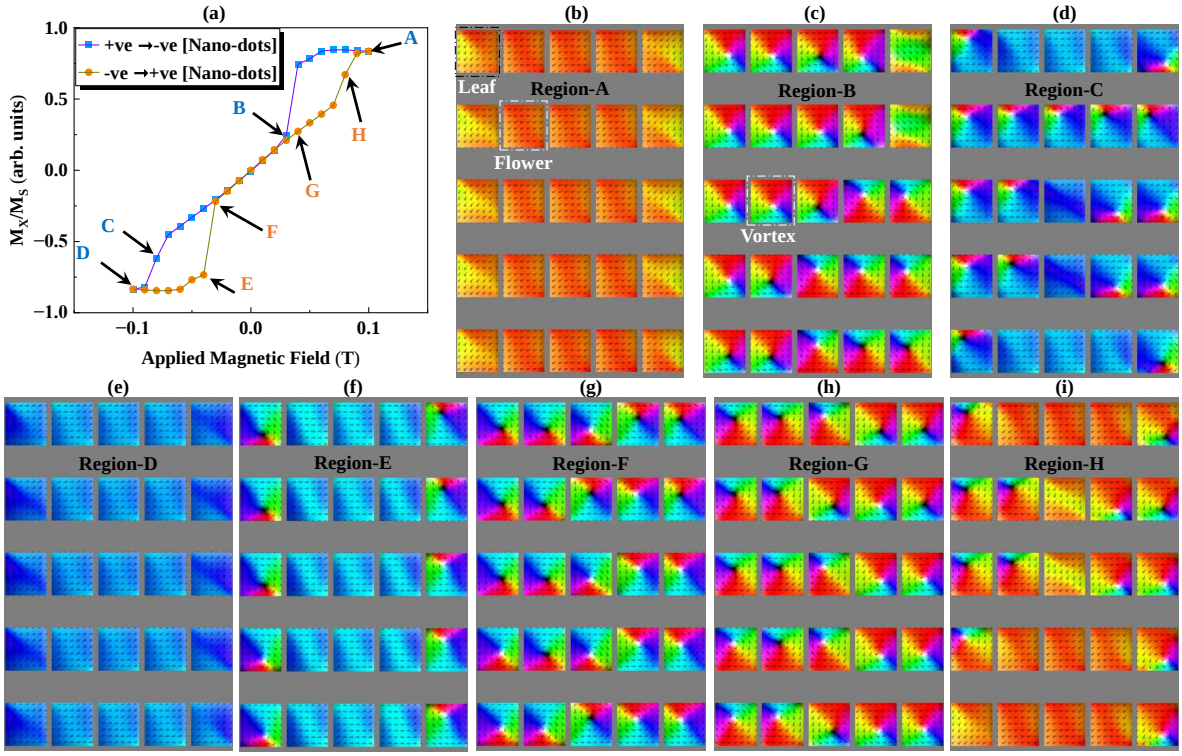


Figure 8.16: Magnified (for field range ± 0.1 T) simulated hysteresis loop for the square nanodot matrices after applying the SAW along longitudinal ($x-$) direction, where 'A'-'H' signifying the different position of magnetic field which are shown in (b)-(i), respectively. *'Flower'* (parallel to the longitudinal axis), *'Leaf'* (domains parallel to the diagonal of the nanodots), *'Vortex'* (flux closure of the magnetization) are highlighted to signify different domain states originated in the square nanodot matrix [5].

Figure 8.16(a) displays the magnified hysteresis loop (± 0.1 T, magnetization saturation already occurs at this field) for the square nanodots matrix, while Figs. 8.16(b)-(h) illustrate various magnetic domain configurations corresponding to different magnetic field values along the hysteresis loop. The blue curve with square dots represents the field variation from $+0.1$ T to -0.1 T, while the orange curve with circular dots depicts the field reversal from -0.1 T to $+0.1$ T. Previous studies have indicated that exchange and demagnetization energy play a more crucial role than anisotropy energy in stabilizing domains [238]. In this context, the domain configurations primarily consist of different orientations, namely the *'Flower'*, *'Leaf'*, and *'Vortex'* states [238], highlighted in Fig. 8.16(b) and 8.16(c).

When the domains are parallel to the longitudinal axis, they are referred to as the *'flower'*

state, while those parallel to the diagonal are known as the *'leaf'* state. For *'vortex'* states, the domains are arranged in magnetization flux closure states. Typically, a significant difference between magnetostatic energy and exchange energy is observed for a *flower* state and a *leaf* state [238], with magnetostatic energy considered dominant over the exchange energy. However, a less variation in exchange and magnetostatic energy is observed for a *vortex* state. Subsequent sections elucidate the different domain states formed at varying applied magnetic fields.

Figure 8.16(b) illustrates a mixture of domain states at the +0.1 T applied magnetic field (position 'A' in Fig. 8.16(a)), where both *leaf* and *flower* states coexist. As the field is reduced to +0.03 T after remanence, the *leaf* and *flower* states begin to transition toward *vortex* states [position 'B'; Fig. 8.16(c)]. The E_{15} and E_{25} elements indicate the formation of 'S'-type domains, which can be considered a pre-*vortex* state at that field. When the magnetic field is further reduced to −0.08 T, the domain configuration of position 'C' in Fig. 8.16(d) shows that the *leaf* states change their orientation, attempting to align themselves with the direction of the applied magnetic field. However, this field is insufficient to orient the *vortex* states into either *leaf* or *flower* states. All domains fully convert to a mixed *leaf* and *flower* state, where the states (position 'D') align in the reversed field direction, as depicted in Fig. 8.16(e), towards the opposite direction of the domains in Fig. 8.16(b).

Now, if the opposite direction is considered, i.e., when the field is reversed from −0.1 T to +0.1 T. As the field increases to −0.04 T, the domain configuration (position 'E') in Fig. 8.16(f) shows a coexistence of *vortex* and *flower* states. *vortex* states are generated on the edge elements, while *leaf* states lie in the middle elements. Upon further increasing the field to −0.03 T, the domain configuration (position 'F') in Fig. 8.16(g) reveals that *vortex* states are generated within each of the elements. As the field is further increased to +0.04 T, the domain configuration (position 'G') in Fig. 8.16(h) shows that *vortex* states remain in the *vortex* state. However, a closer look reveals that they now try to orient towards the positive side of the applied magnetic field. This subtle variation can be identified by the element color distribution; *vortex* states in position 'F' were inclined towards the negative direction (identified by its mostly bluish nature), whereas *vortex* states in 'G' are aligned towards the positive direction (identified by its strong reddish nature).

Before saturation, the domain state of position 'H' in Fig. 8.16(i) shows that *leaf* states are now coexisting with the *vortex* states. When the matrix is fully saturated with a +0.1 T magnetic field, the domain configurations again become similar to that of Fig. 8.16(b). On the contrary, for continuous nanowires are mostly formed with *flower* state (not shown here) thus signifying the dominance of magnetostatic energy contribution over the exchange energy. Since these complex mixtures of domain states (*flower*, *leaf*, *vortex*) are formed in the square nanodots

array, it is crucial to note that the energies are distributed throughout the elements in a similarly complex fashion. Since external applied bias magnetic fields can switch between different states it introduces tunability in domain states at the cost of external bias magnetic fields. Now, the following section 8.7 elucidates the opportunity to utilize these MMA in the prospect of reservoir computing [227, 228].

8.7 Prospects of Reservoir Computing

Initially, the nonvolatility of the domains under bias-field free condition was explored in section 8.3. Subsequently,the nonlinear behaviour for all the configurations (except the 90 nm configuration) were explored , where the output frequencies deviate from the input frequency. Notably, the 90 nm configuration exhibited the linear behaviour, synchronizing the output with the input frequency. The associated rich spin wave power-phase profiles revealed the intricate complex behaviour in phase space with higher n_x or n_y, as explained.

On the other hand, the preceding section 8.6 uncovered the potential to tune the domains within the nanowires/nanodots in presence of an external bias magnetic field. Hence, the same SAW excitation treatment should preserve the altered domain configuration of an external magnetic

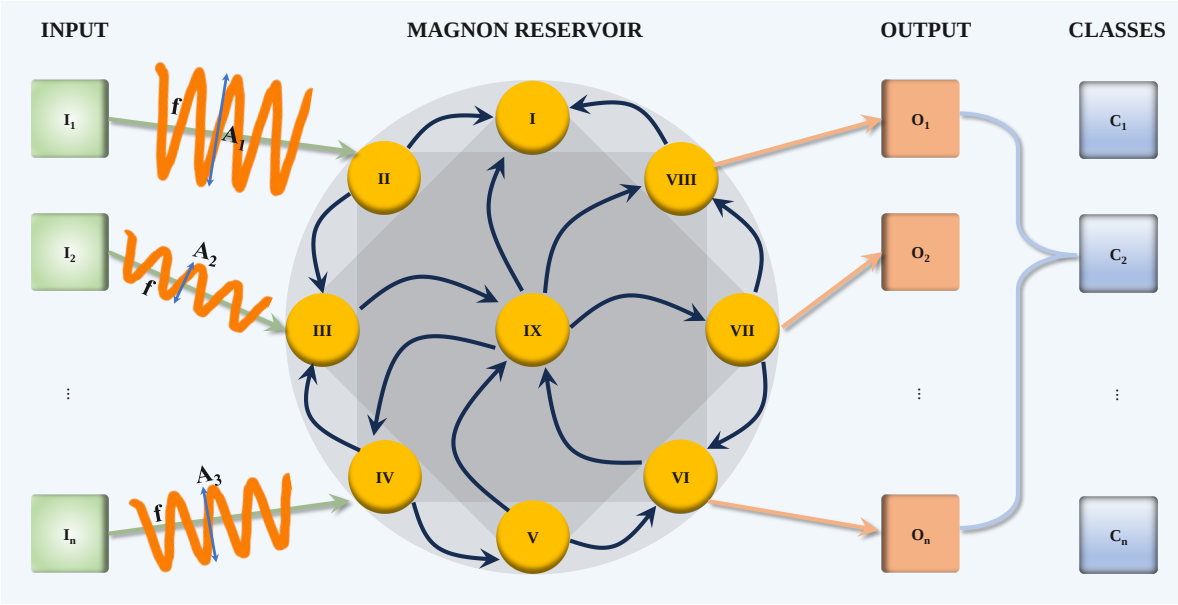


Figure 8.17: Illustration of reservoir computing to handle the amplitude variation (from A_1 to A_n) at the constant input frequency (f). I_{1-n} are the inputs to the magnon reservoir with the different sets of nanowires/nanodots array configurations (e.g., I to IX are such nine arrays). The reservoir yield the results into different outputs, O_{1-9} and subsequently, categorized into different classes, C_{1-n} depending upon the results [5].

field induced domain. However, a distinct power-phase behaviour is expected to occur due to the modifications induced by the external bias magnetic field. Moreover, it is note that the external bias magnetic field influences the operating oscillation frequency following the well-known *Kittel* formula, $f_\kappa = \sqrt{H_{ext} \cdot (H_{ext} + 4\pi M_{Sat})}$. This establishes the foundation for reservoir computing by generating different frequencies (say, f_1 and f_2) at varying H_{ext} values, thus facilitating signal mapping in high-dimensional phase space, a fundamental aspect of reservoir computing [38]. Therefore, the MMA could be beneficial for reservoir computing as per the approach where individual frequencies are provided to the input [38, 226].

While the ability to tune domains exists in the presence of external bias magnetic fields and subsequently the frequencies, the primary approach revolves around bias field-free conditions. Here, an alternate approach has been propose to perform the reservoir computing as illustrated in the schematic in Fig. 8.17. A frequency dependent vowel recognition study by coupled spin torque oscillators (STNOs) array [239] has been introduced recently. However, in reality while speaking, not only the frequency, but also the amplitude of vowels varies based on each individual person. Hence, a different perspective is proposed, where the required magnon reservoir assembly is placed in such a way that it could handle the amplitude variation at the operating frequency. Here, I_1, I_2 ... I_n are the inputs to the magnon reservoir with the different sets of nanowires/nanodots array configurations (e.g., I to IX represent such nine array combinations) operating at the same frequency (f) while its amplitude varies from A_1 to A_n. The reservoir yield the results into different outputs, O_1, O_2 ... O_n and subsequently, categorised into different classes, C_1, C_2 ... C_n depending upon the results. Therefore, this present approach offers further advancement over the prior work in understanding the concept of reservoir computing. A comprehensive study of reservoir computing based on MMA will be presented in future work.

8.8 Stress Induced Frequency Tuning

In the previous section, it was demonstrated that an additional external sine pulse fails to disrupt synchronization and frequency tunability. However, by keeping the input frequency constant and varying the stress value, it was observed that the frequency-locked state disappears, allowing for tunability and introducing non-linearity into the system. Notably, since MuMax^3 does not directly incorporate stress, stress has been modeled as a function of the anisotropy value. The stress-induced variations in magnetization oscillation and the corresponding frequency distribution are shown in Figure 8.18(a) and (b), respectively. Values of $K = 100, 300, 600, 800, 900, 1000$ reveal proper synchronized sinusoidal oscillation, while values of $K = 200, 400, 500, 700$ exhibit disrupted synchronization and introduce inherent non-linearity into the system. We further ex-

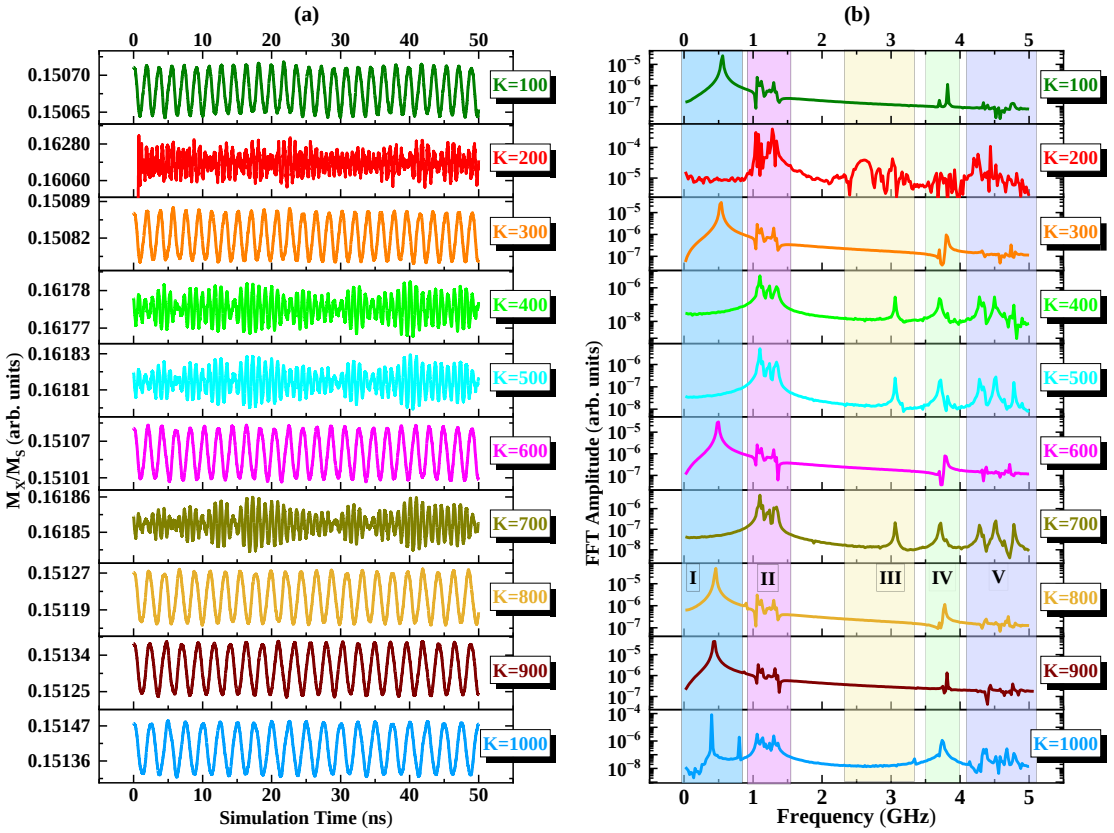


Figure 8.18: Variation of (a) magnetization oscillation and (b) its corresponding frequency as a function of applied stress [5].

plored the synchronization behavior by performing the FFT of the magnetization oscillation. The frequency spectra revealed five distinct regions: *I* (from 0 to 0.75 GHz), *II* (from 0.8 to 1.5 GHz), *III* (from 2.3 to 3.5 GHz), *IV* (from 3.5 to 4.0 GHz), and *V* (from 4.2 to 5.0 GHz), as highlighted in Figure 8.18(b). Most operating frequencies lie in region *I*, where the highest FFT amplitude is observed. A closer insight to the region *I* reveals that the frequency decreases with increasing stress. Region *IV* exhibits similar frequency tunability. However, regions *II* and *V* show contrasting behavior, indicating synchronization in the system. Notably, for $K = 200, 400, 500, 700$, the operating frequency shifts to region *II*. Region *III* displays irregularity; for instance, $K = 200$ shows higher amplitude and different behavior compared to the others. Therefore, this stress variation offers simultaneous frequency synchronization and tunability, which is advantageous for reservoir computing.

Tunability of hyper parameters in the software-based machine learning is capable of performing different computational tasks. However, the 'physical' reservoir computing schemes lack such critical functionality, which utilizes nonlinear and history-dependent responses of physical

systems for data processing. Here, it is proposed to utilize the complex nonlinearities present in the modulated spin waves, generated out of the synchronization and desynchronization behaviour within the different nanowires/nanodots matrices. The required functional tunability could potentially be addressed with amplitude dependent training of different combination of NWs/NDs parameters, such as NWs/NDs dimensions, topologies, material parameters and array matrices. Additionally, the combination of complex nonlinear magnon power-phase distributions can potentially be leveraged in reconfiguration of the key reservoir properties, such as nonlinearity, memory capacity, and complexity that would be capable of optimizing the computational performance across a diverse task set.

8.9 Conclusion

In conclusion, this present investigation focused on the power and phase profiles of spin waves within magnetostrictive nanowires (NWs) forming a nano-patterned "Magnon Microwave Antenna" (MMA) on a piezoelectric substrate under bias-field free conditions. In order to stimulate the magnetization precession within the NWs, surface acoustic waves (SAW) onto the piezoelectric substrate were launched. The power-phase analysis revealed complex quantization numbers for various NW configurations, indicating intricate synchronization processes within the nanowires/nanodots. The ability to control and manipulate spin waves at both power and phase levels is pivotal for practical applications. Notably, the MMA, operating without an external bias magnetic field, lacks the fundamental Kittel mode, enabling the establishment of a frequency-locking state up to 500 GHz. This frequency-locked MMA demonstrated high stability in the time domain over an 80 ns simulation time span. Static magnetic studies unveiled square hysteresis loops or stepped hysteresis loops under different conditions (pre and post SAW application). The subsequent domain analysis confirmed the generation of three distinct domain states – *flower*, *leaf*, and *vortex* states – in the square nanodot array. Moreover, it demonstrated that the non-volatile domains generated under bias-field free conditions could be tuned by applying an external magnetic field, presenting an opportunity for cutting-edge magnonic applications. Furthermore, an alternative approach has been introduced for on-chip reservoir computing operating at the same frequency with varying amplitude. This innovative structure not only underscores the flexibility for further miniaturization of existing device sizes but also represents a noteworthy contribution to the evolving landscape of spintronics applications and development of energy-efficient and multifunctional magnonic devices.

9 Conclusions

In this thesis, various aspects of nano-hetero-structured transverse exchange spring (ES) amorphous/nanocrystalline magnetic thin films fabricated using the conventional DC electrodeposition technique have been investigated. These studies focused on fabricating and understanding the magnetic properties, dynamic behaviour, and practical applications of these films. The research presented here provides significant insights and opens new avenues for future spintronic and magnonic devices. We have successfully fabricated optically smooth, nano-hetero-structured, amorphous-nanocrystalline CoP thin films at room temperature using the electrodeposition technique.

Through careful control of hydrogen evolution within the system, we achieved the *"in situ"* formation of transverse exchange spring (ES) structures from a single starting material. The nano-hetero-structured nature of the films was confirmed using XRD, TEM, and FFT of TEM. The quasi-static magnetic properties of these CoP thin films were characterized by magnetic stripe domains at remanence, observed through MFM and hysteresis loop measurements. The presence of out-of-plane (OOP) anisotropy was confirmed by MFM, FORC measurements, and micromagnetic simulations. These studies revealed that the thickness of the nano-hetero-structures significantly influences the nature of the hysteresis in such films, demonstrating an increase in coercivity and energy product in ES and EC structures. This opens the door to modifying bulk magnetic properties in single ferromagnetic thin films, providing a scalable and cost-effective approach for advanced magnetic materials.

The time-resolved spin dynamics in the CoP alloy films were investigated using all-optical TR-MOKE magnetometry. This study explored the anisotropy in magnetization precession, damping, and ultrafast demagnetization concerning the in-plane magnetization orientation. The magnetization precession frequency exhibited a strong two-fold anisotropy superposed with a weaker four-fold anisotropy, while the Gilbert damping followed a four-fold anisotropic nature. These

anisotropic behaviours were attributed to variations in spin-orbit coupling (SOC) at equilibrium and the presence of multiple modes causing mutual dephasing of precession. The ultrafast demagnetization time was found to be nearly invariant with the in-plane magnetization orientation, indicating a negligible role of anisotropic SOC in highly non-equilibrium states post-laser excitation.

For cutting-edge applications, we investigated the tripartite coupling between phonons (SAW), magnons (SW), and photons (EM waves) in ultra-compact SW-dependent "Magnon Microwave Antenna" (MMA). Developed with magnetostrictive nanowires (NWs) on a piezoelectric substrate, this system demonstrated the ability to generate microwaves with tunable frequencies. The power-phase analysis of spin waves within the NWs revealed complex synchronization processes and indicated the potential for bias-field-free operation with frequency locking up to 500 GHz. Static magnetic studies revealed distinct domain states (flower, leaf, and vortex) in the square nanodot array, and these non-volatile domains could be tuned by applying an external magnetic field. This ability to control and manipulate spin waves and domain states at both power and phase levels is crucial for practical applications in magnonic devices. Furthermore, we proposed an alternative approach for on-chip reservoir computing introducing amplitude dependent training, highlighting the flexibility for miniaturizing existing devices and contributing to the development of energy-efficient and multifunctional magnonic devices.

In conclusion, our comprehensive study has demonstrated the fabrication, characterization, and application potential of nano-hetero-structured amorphous-nanocrystalline CoP thin films. By investigating both static and dynamic magnetic properties and exploring advanced applications in spintronics and magnonics, this work provides a robust foundation for future research and development in these fields. The novel approaches and findings presented here underscore the potential of these materials for next-generation recording media, spintronic devices, and energy-efficient magnonic applications.

10 Future Work

The future work aims to further understand the dynamic and static magnetic properties of exchange spring systems and nano-modulated magnetic thin films. This will involve several experimental and simulation based approaches.

First, systematic angle dependent Brillouin Light Scattering (BLS) will be employed to observe the frequency response with different angles of incidence, ranging from in-plane to out-of-plane orientations. This study would aim to investigate deviations from the Kittel like curve, as the Kittel formula is expected to be violated or require modification with proper approximations for exchange spring systems due to the complex interplay of exchange interactions and anisotropy.

Second, polar time-resolved magneto-optical Kerr effect (TRMOKE) measurements will be conducted to explore the effects of canted states on magnetization dynamics. This will include magnetic field dependent TRMOKE study beyond saturation magnetization to observe the presence of magnetization precession. Additionally, the dependence of magnetic field on the frequency and amplitude of precession will be studied, with the parameters extracted from fitted curves.

Lastly, micromagnetic simulations using MuMax^3 will be carried out to model the behaviour of the magnetic thin films. Micromagnetic simulations are crucial for understanding the magnetic properties at the nanoscale and can complement experimental observations. The following Figure 10.1 exhibits some of the proposed designs to incorporate nonlinearity in magnon power-phase distributions in order to not only miniaturize the overall device but also make the MMA compatible for reservoir computing. Future simulations will cover several key areas such as simulating the hysteresis loop of the films to understand the magnetic reversal processes and coercivity in nano-modulated cobalt based films and its derivatives. This will provide insights into the energy barriers and stability of different magnetic states. At different stages of magnetization, the macrospin configurations to identify the formation and evolution of magnetic domains and vortices will be examined. This will help us understand the interplay between exchange interactions and

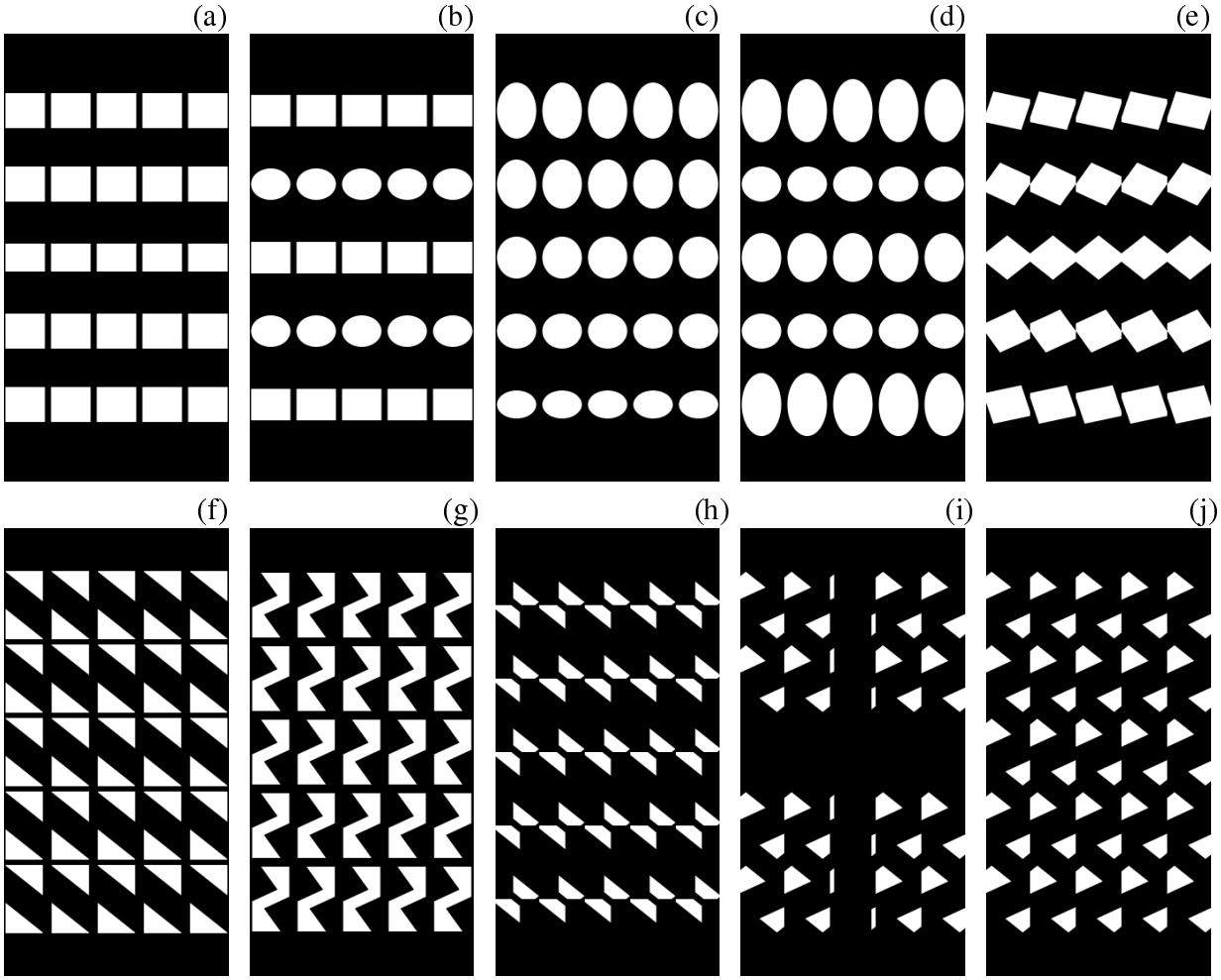


Figure 10.1: Several proposed design of nanostructured MMA to incorporate further nonlineaity in magnon power-phase distribution, which would eventually make the MMA compatible for reservouir computing.

anisotropy in these complex systems. Moreover, the simulations will help further to investigate the angle dependence of the magnetostatic energy in the films. By modulating the nanostructure and orientation, we could aim to understand how the energy landscape changes and how this affects the magnetic properties and stability of the films.

These combined experimental and simulation studies will provide a comprehensive understanding of the magnetic behaviour of nano-hetero-structured films. The insights gained will be crucial for developing next-generation spintronic and magnonic devices, offering enhanced performance and new functionalities. This research will pave the way for innovative applications in data storage, magnetic sensing, and energy-efficient computing technologies.

References

[1] Arindam Samanta and Saibal Roy. Investigation of transverse exchange-springs in electrodeposited nano-heterostructured films through first-order reversal curve analysis. *APL Materials*, 12(9):091118, 09 2024. ISSN 2166-532X. doi: 10.1063/5.0223485. URL https://doi.org/10.1063/5.0223485.

[2] Arindam Samanta, Gianluca Gubbiotti, and Saibal Roy. Spin waves in exchange spring nanoheterostructured amorphous/nanocrystalline films. *Physical Review B*, 107:214449, Jun 2023. doi: 10.1103/PhysRevB.107.214449. URL https://link.aps.org/doi/10.1103/PhysRevB.107.214449.

[3] Soma Dutta, Arindam Samanta, Surya Narayan Panda, Saibal Roy, and Anjan Barman. Ultrafast demagnetization and Gilbert damping in electrodeposited CoP film. *Journal of Materials Science*, 58(37):14817–14830, 2023. ISSN 1573-4803. doi: 10.1007/s10853-023-08956-9. URL https://doi.org/10.1007/s10853-023-08956-9.

[4] Arindam Samanta and Saibal Roy. Generation of Microwaves With Tuneable Frequencies in Ultracompact Magnon Microwave Antenna via Phonon-Magnon-Photon Coupling. *IEEE Transactions on Electron Devices*, 70(1):335–342, Jan 2023. ISSN 1557-9646. doi: 10.1109/TED.2022.3221026. URL https://doi.org/10.1109/TED.2022.3221026.

[5] Arindam Samanta and Saibal Roy. Tunable power-phase distributions in a phonon-magnon-coupled magnon microwave antenna for reservoir computing. *Physical Review Applied*, 22:054076, Nov 2024. doi: 10.1103/PhysRevApplied.22.054076. URL https://link.aps.org/doi/10.1103/PhysRevApplied.22.054076.

[6] Stephen Blundell. *Magnetism in Condensed Matter*. Oxford University Press, 10 2001.

doi: 10.1093/oso/9780198505921.001.0001. URL https://doi.org/10.1093/oso/9780198505921.001.0001.

[7] R Skomski. Nanomagnetics. *Journal of Physics: Condensed Matter*, 15(20):R841, may 2003. doi: 10.1088/0953-8984/15/20/202. URL https://dx.doi.org/10.1088/0953-8984/15/20/202.

[8] S. D. Bader. Colloquium: Opportunities in nanomagnetism. *Rev. Mod. Phys.*, 78:1–15, Jan 2006. doi: 10.1103/RevModPhys.78.1. URL https://link.aps.org/doi/10.1103/RevModPhys.78.1.

[9] Libor Šmejkal, Jairo Sinova, and Tomas Jungwirth. Emerging Research Landscape of Altermagnetism. *Phys. Rev. X*, 12:040501, Dec 2022. doi: 10.1103/PhysRevX.12.040501. URL https://link.aps.org/doi/10.1103/PhysRevX.12.040501.

[10] Igor Mazin. Editorial: Altermagnetism—A New Punch Line of Fundamental Magnetism. *Phys. Rev. X*, 12:040002, Dec 2022. doi: 10.1103/PhysRevX.12.040002. URL https://link.aps.org/doi/10.1103/PhysRevX.12.040002.

[11] N. Wang, T. ODonnell, S. Roy, M. Brunet, P. McCloskey, and S.C. O'Mathúna. High-frequency micro-machined power inductors. *Journal of Magnetism and Magnetic Materials*, 290-291:1347–1350, 2005. ISSN 0304-8853. doi: https://doi.org/10.1016/j.jmmm.2004.11.434. URL https://www.sciencedirect.com/science/article/pii/S0304885304016956.

[12] Cian Ó Mathúna, Ningning Wang, Santosh Kulkarni, and Saibal Roy. Review of Integrated Magnetics for Power Supply on Chip (PwrSoC). *IEEE Transactions on Power Electronics*, 27(11):4799–4816, Nov 2012. ISSN 1941-0107. doi: 10.1109/TPEL.2012.2198891. URL https://doi.org/10.1109/TPEL.2012.2198891.

[13] A. V. Chumak, V. I. Vasyuchka, A. A. Serga, and B. Hillebrands. Magnon spintronics. *Nature Physics*, 11(6):453–461, 2015. ISSN 1745-2481. doi: 10.1038/nphys3347. URL https://doi.org/10.1038/nphys3347.pdf.

[14] Andrii V. Chumak, Alexander A. Serga, and Burkard Hillebrands. Magnon transistor for all-magnon data processing. *Nature Communications*, 5, 08 2014. ISSN 2041-1723. doi: 10.1038/ncomms5700. URL https://doi.org/10.1038/ncomms5700.

[15] D. A. Allwood, G. Xiong, C. C. Faulkner, D. Atkinson, D. Petit, and R. P. Cowburn. Magnetic Domain-Wall Logic. *Science*, 309(5741):1688–1692, 2005. ISSN 0036-8075.

doi: 10.1126/science.1108813. URL https://science.sciencemag.org/content/309/5741/1688.

[16] Supriyo Bandyopadhyay and Marc Cahay. *Introduction to Spintronics (2nd ed.)*. CRC Press, 2015. URL https://doi.org/10.1201/b19103.

[17] S. A. Wolf, D. D. Awschalom, R. A. Buhrman, J. M. Daughton, S. von Molnár, M. L. Roukes, A. Y. Chtchelkanova, and D. M. Treger. Spintronics: A Spin-Based Electronics Vision for the Future. *Science*, 294(5546):1488–1495, 2001. doi: 10.1126/science.1065389. URL https://www.science.org/doi/abs/10.1126/science.1065389.

[18] Ruyi Chen, Chong Chen, Lei Han, Peisen Liu, Rongxuan Su, Wenxuan Zhu, Yongjian Zhou, Feng Pan, and Cheng Song. Ordered creation and motion of skyrmions with surface acoustic wave. *Nature Communications*, 14(1):4427–836, 2023. ISSN 2041-1723. doi: 10.1038/s41467-023-40131-1. URL https://doi.org/10.1038/s41467-023-40131-1.

[19] J. Puebla, Y. Hwang, S. Maekawa, and Y. Otani. Perspectives on spintronics with surface acoustic waves. *Applied Physics Letters*, 120(22):220502, 06 2022. ISSN 0003-6951. doi: 10.1063/5.0093654. URL https://doi.org/10.1063/5.0093654.

[20] Raisa Fabiha, Jonathan Lundquist, Sudip Majumder, Erdem Topsakal, Anjan Barman, and Supriyo Bandyopadhyay. Spin Wave Electromagnetic Nano-Antenna Enabled by Tripartite Phonon-Magnon-Photon Coupling. *Advanced Science*, 9(8):2104644, 2022. doi: https://doi.org/10.1002/advs.202104644. URL https://onlinelibrary.wiley.com/doi/abs/10.1002/advs.202104644.

[21] W. A. Challener, Chubing Peng, A. V. Itagi, D. Karns, Wei Peng, Yingguo Peng, XiaoMin Yang, Xiaobin Zhu, N. J. Gokemeijer, Y.-T. Hsia, G. Ju, Robert E. Rottmayer, Michael A. Seigler, and E. C. Gage. Heat-assisted magnetic recording by a near-field transducer with efficient optical energy transfer. *Nature Photonics*, 3, 04 2009. ISSN 1749-4893. doi: 10.1038/nphoton.2009.26. URL https://doi.org/10.1038/nphoton.2009.26.

[22] H. C. Yuan, S. H. Nie, T. P. Ma, Z. Zhang, Z. Zheng, Z. H. Chen, Y. Z. Wu, J. H. Zhao, H. B. Zhao, and L. Y. Chen. Different temperature scaling of strain-induced magneto-crystalline anisotropy and Gilbert damping in Co_2FeAl film epitaxied on GaAs. *Applied Physics Letters*, 105(7):072413, 2014. doi: 10.1063/1.4893949. URL https://doi.org/10.1063/1.4893949.

[23] Sumio Ikegawa, Frederick B. Mancoff, Jason Janesky, and Sanjeev Aggarwal. Magnetoresistive Random Access Memory: Present and Future. *IEEE Transactions on*

Electron Devices, 67(4):1407–1419, April 2020. ISSN 1557-9646. doi: 10.1109/TED.2020.2965403. URL https://doi.org/10.1109/TED.2020.2965403.

[24] Arne Vansteenkiste, Jonathan Leliaert, Mykola Dvornik, Mathias Helsen, Felipe Garcia-Sanchez, and Bartel Van Waeyenberge. The design and verification of MuMax^3. *AIP Advances*, 4(10):107133, 2014. doi: 10.1063/1.4899186. URL https://doi.org/10.1063/1.4899186.

[25] E. F. Kneller and R. Hawig. The exchange-spring magnet: a new material principle for permanent magnets. *IEEE Transactions on Magnetics*, 27(4):3588–3560, July 1991. doi: 10.1109/20.102931. URL https://doi.org/10.1109/20.102931.

[26] Eric E Fullerton, J.S Jiang, and S.D Bader. Hard/soft magnetic heterostructures: model exchange-spring magnets. *Journal of Magnetism and Magnetic Materials*, 200(1):392 – 404, 1999. ISSN 0304-8853. doi: https://doi.org/10.1016/S0304-8853(99)00376-5. URL http://www.sciencedirect.com/science/article/pii/S0304885399003765.

[27] G. B. G. Stenning, G. J. Bowden, S. A. Gregory, P. A. J. de Groot, G. van der Laan, L. R. Shelford, P. Bencok, P. Steadman, A. N. Dobrynin, and T. Hesjedal. Transverse magnetic exchange springs in a $DyFe_2/YFe_2$ superlattice. *Phys. Rev. B*, 86:174420, Nov 2012. doi: 10.1103/PhysRevB.86.174420. URL https://link.aps.org/doi/10.1103/PhysRevB.86.174420.

[28] A A Serga, A V Chumak, and B Hillebrands. YIG magnonics. *Journal of Physics D: Applied Physics*, 43(26):264002, Jun 2010. doi: 10.1088/0022-3727/43/26/264002. URL https://dx.doi.org/10.1088/0022-3727/43/26/264002.

[29] B. Divinskiy, H. Merbouche, V. E. Demidov, K. O. Nikolaev, L. Soumah, D. Gouéré, R. Lebrun, V. Cros, Jamal Ben Youssef, P. Bortolotti, A. Anane, and S. O. Demokritov. Evidence for spin current driven Bose-Einstein condensation of magnons. *Nature Communications*, 12, 11 2021. ISSN 2041-1723. doi: 10.1038/s41467-021-26790-y. URL https://doi.org/10.1038/s41467-021-26790-y.

[30] G. Gubbiotti, G. Carlotti, J. Weston, G. Zangari, D.C. Crew, and R.L. Stamps. Asymmetry in the static and dynamic magnetic properties of a weak exchange spring trilayer. *Journal of Magnetism and Magnetic Materials*, 286:479–483, 2005. ISSN 0304-8853. doi: https://doi.org/10.1016/j.jmmm.2004.09.140. URL https://www.sciencedirect.com/science/article/pii/S0304885304010303.

[31] Andrei Kirilyuk, Alexey V. Kimel, and Theo Rasing. Ultrafast optical manipulation of magnetic order. *Rev. Mod. Phys.*, 82:2731–2784, Sep 2010. doi: 10.1103/RevModPhys.82.2731. URL https://link.aps.org/doi/10.1103/RevModPhys.82.2731.

[32] E. Beaurepaire, J.-C. Merle, A. Daunois, and J.-Y. Bigot. Ultrafast spin dynamics in ferromagnetic nickel. *Phys. Rev. Lett.*, 76:4250–4253, May 1996. doi: 10.1103/PhysRevLett.76.4250. URL https://link.aps.org/doi/10.1103/PhysRevLett.76.4250.

[33] T.L. Gilbert. A phenomenological theory of damping in ferromagnetic materials. *IEEE Transactions on Magnetics*, 40(6):3443–3449, Nov 2004. ISSN 1941-0069. doi: 10.1109/TMAG.2004.836740.

[34] Yaroslav Tserkovnyak, Arne Brataas, Gerrit E. W. Bauer, and Bertrand I. Halperin. Nonlocal magnetization dynamics in ferromagnetic heterostructures. *Rev. Mod. Phys.*, 77:1375–1421, Dec 2005. doi: 10.1103/RevModPhys.77.1375. URL https://link.aps.org/doi/10.1103/RevModPhys.77.1375.

[35] V.V. Kruglyak and R.J. Hicken. Magnonics: Experiment to prove the concept. *Journal of Magnetism and Magnetic Materials*, 306(2):191–194, 2006. ISSN 0304-8853. doi: https://doi.org/10.1016/j.jmmm.2006.02.242. URL https://www.sciencedirect.com/science/article/pii/S0304885306005889.

[36] Silvia Tacchi, Jorge Flores-Farías, Daniela Petti, Felipe Brevis, Andrea Cattoni, Giuseppe Scaramuzzi, Davide Girardi, David Cortés-Ortuño, Rodolfo A. Gallardo, Edoardo Albisetti, Giovanni Carlotti, and Pedro Landeros. Experimental Observation of Flat Bands in One-Dimensional Chiral Magnonic Crystals. *Nano Letters*, 23(14):6776–6783, 2023. doi: 10.1021/acs.nanolett.2c04215. URL https://doi.org/10.1021/acs.nanolett.2c04215.

[37] L Perez, C Aroca, P Sanchez, E Lopez, and M.C Sanchez. Planar fluxgate sensor with an electrodeposited amorphous core. *Sensors and Actuators A: Physical*, 109(3):208 – 211, 2004. ISSN 0924-4247. doi: https://doi.org/10.1016/j.sna.2003.08.015. URL http://www.sciencedirect.com/science/article/pii/S0924424703005491.

[38] Dmytro D. Yaremkevich, Alexey V. Scherbakov, Luke De Clerk, Serhii M. Kukhtaruk, Achim Nadzeyka, Richard Campion, Andrew W. Rushforth, Sergey Savelev, Alexander G. Balanov, and Manfred Bayer. On-chip phonon-magnon reservoir for neuromorphic computing. *Nature Communications*, 14:8296, 12 2023. ISSN 2041-1723. doi: 10.1038/s41467-023-43891-y. URL https://doi.org/10.1038/s41467-023-43891-y.

[39] Dmytro Apalkov, Alexey Khvalkovskiy, Steven Watts, Vladimir Nikitin, Xueti Tang, Daniel Lottis, Kiseok Moon, Xiao Luo, Eugene Chen, Adrian Ong, Alexander Driskill-Smith, and Mohamad Krounbi. Spin-Transfer Torque Magnetic Random Access Memory (STT-MRAM). *J. Emerg. Technol. Comput. Syst.*, 9(2), may 2013. ISSN 1550-4832. doi: 10.1145/2463585.2463589. URL https://doi.org/10.1145/2463585.2463589.

[40] S. X. Wang, N. X. Sun, M. Yamaguchi, and S. Yabukami. Properties of a new soft magnetic material. *Nature*, 407:150–151, 2000. ISSN 1476-4687. doi: https://doi.org/10.1038/35025142. URL https://doi.org/10.1038/35025142.

[41] V Korenivski. GHz magnetic film inductors. *Journal of Magnetism and Magnetic Materials*, 215-216:800–806, 2000. ISSN 0304-8853. doi: https://doi.org/10.1016/S0304-8853(00)00292-4. URL https://www.sciencedirect.com/science/article/pii/S0304885300002924.

[42] H. Suhl. Theory of the magnetic damping constant. *IEEE Transactions on Magnetics*, 34(4):1834–1838, July 1998. ISSN 1941-0069. doi: 10.1109/20.706720. URL https://doi.org/10.1109/20.706720.

[43] Pavel Ripka. *Magnetic Sensors and Magnetometers, Second Edition*. Artech, 2021. ISBN 9781630817435. URL https://ieeexplore.ieee.org/document/9538838.

[44] B. G. Park, J. Wunderlich, X. Martí, V. Holý, Y. Kurosaki, M. Yamada, H. Yamamoto, A. Nishide, J. Hayakawa, H. Takahashi, A. B. Shick, and T. Jungwirth. A spin-valve-like magnetoresistance of an antiferromagnet-based tunnel junction. *Nature Materials*, 10, 05 2011. ISSN 1476-4660. doi: 10.1038/nmat2983. URL https://doi.org/10.1038/nmat2983.

[45] R. Skomski, P. Manchanda, P. Kumar, B. Balamurugan, A. Kashyap, and D. J. Sellmyer. Predicting the Future of Permanent-Magnet Materials. *IEEE Transactions on Magnetics*, 49(7):3215–3220, July 2013. ISSN 0018-9464. doi: 10.1109/TMAG.2013.2248139. URL https://doi.org/10.1109/TMAG.2013.2248139.

[46] Paul McCloskey, Brice Jamieson, Terence ODonnell, Donald Gardner, Michael A. Morris, and Saibal Roy. Electrodeposited amorphous CoP based alloy with improved thermal stability. *Journal of Magnetism and Magnetic Materials*, 322(9):1536 – 1539, 2010. ISSN 0304-8853. doi: https://doi.org/10.1016/j.jmmm.2009.07.059. URL http://www.sciencedirect.com/science/article/pii/S0304885309007951.

[47] Peng Zhang. CHAPTER 5 - Microprocessors. In Peng Zhang, editor, *Advanced Industrial Control Technology*, pages 155–214. William Andrew Publishing, Oxford, 2010. ISBN 978-1-4377-7807-6. doi: https://doi.org/10.1016/B978-1-4377-7807-6.10005-1. URL https://www.sciencedirect.com/science/article/pii/B9781437778076100051.

[48] M. Saidani and M. A. M. Gijs. High-quality radio-frequency inductors on silicon using a hybrid ferrite technology. *Applied Physics Letters*, 84(22):4496–4498, 05 2004. ISSN 0003-6951. doi: 10.1063/1.1756677. URL https://doi.org/10.1063/1.1756677.

[49] Yide Zhang, Shihe Wang, and Danny Xiao. Insulator coated magnetic nanoparticulate composites with reduced core loss and method of manufacture thereof, April 13 2004. URL https://patents.google.com/patent/US6720074B2. US Patent 6,720,074.

[50] Tingchuan Zhou, Ying Liu, Peng Cao, Jiao Du, Zifeng Lin, Renquan Wang, Lichuan Jin, Lixian Lian, and Vincent G. Harris. Cold Sintered MetalCeramic Nanocomposites for High-Frequency Inductors. *Advanced Electronic Materials*, 6(12):2000868, 2020. doi: https://doi.org/10.1002/aelm.202000868. URL https://onlinelibrary.wiley.com/doi/abs/10.1002/aelm.202000868.

[51] Zao Ni, Jing Zhan, Qiang Fang, Xin Wang, Zitao Shi, Yi Yang, Tian-Ling Ren, Albert Wang, Yuhua Cheng, Jianjun Gao, Xinxin Li, and Chen Yang. Design and Analysis of Vertical Nanoparticles-Magnetic-Cored Inductors for RF ICs. *IEEE Transactions on Electron Devices*, 60(4):1427–1435, April 2013. ISSN 1557-9646. doi: 10.1109/TED.2013.2245418. URL fttps://doi.org/10.1109/TED.2013.2245418.

[52] J. Zhan, C. Yang, X. Wang, Q. Fang, Z.T. Shi, Y. Yang, T.-L. Ren, A. Wang, Y.H. Cheng, and L.-T. Liu. Stacked-spiral RF inductors with vertical nanoparticle magnetic core for radio-frequency integrated circuits in CMOS. *Sensors and Actuators A: Physical*, 195: 231–238, 2013. ISSN 0924-4247. doi: https://doi.org/10.1016/j.sna.2013.02.030. URL https://www.sciencedirect.com/science/article/pii/S0924424713001271.

[53] S. Roy, A. Connell, M. Ludwig, N. Wang, T. ODonnell, M. Brunet, P. McCloskey, C. ÓMathúna, A. Barman, and R.J. Hicken. Pulse reverse plating for integrated magnetics on Si. *Journal of Magnetism and Magnetic Materials*, 290-291:1524 – 1527, 2005. ISSN 0304-8853. doi: https://doi.org/10.1016/j.jmmm.2004.11.566. URL http://www.sciencedirect.com/science/article/pii/S030488530401830X.

[54] Paul McCloskey, Donald S Gardner, Brice Jamieson, Saibal Roy, and Terence O'donnell. Forming electroplated inductor structures for integrated circuits. US Patent 8,029,922,

2011. URL https://patents.google.com/patent/US20090169874. Current Assignee: INTEL Corporation.

[55] L Perez, O de Abril, M.C Sanchez, C Aroca, E Lopez, and P Sanchez. Electrodeposited amorphous CoP multilayers with high permeability. *Journal of Magnetism and Magnetic Materials*, 215-216:337 – 339, 2000. ISSN 0304-8853. doi: https://doi.org/10.1016/S0304-8853(00)00151-7. URL http://www.sciencedirect.com/science/article/pii/S0304885300001517.

[56] I. Lucas, L. Perez, C. Aroca, P. Sanchez, E. Lopez, and M.C. Sanchez. Magnetic properties of CoP alloys electrodeposited at room temperature. *Journal of Magnetism and Magnetic Materials*, 290-291:1513 – 1516, 2005. ISSN 0304-8853. doi: https://doi.org/10.1016/j.jmmm.2004.11.563. URL http://www.sciencedirect.com/science/article/pii/S030488530401827X.

[57] Paul McCloskey, Brice Jamieson, Terence ODonnell, Donald Gardner, Michael A. Morris, and Saibal Roy. High-frequency nanostructured magnetic materials for integrated inductors. *Journal of Magnetism and Magnetic Materials*, 320(20):2509 – 2512, 2008. ISSN 0304-8853. doi: https://doi.org/10.1016/j.jmmm.2008.04.141. URL http://www.sciencedirect.com/science/article/pii/S0304885308003946.

[58] Yi Li, Wei Zhang, Vasyl Tyberkevych, Wai-Kwong Kwok, Axel Hoffmann, and Valentine Novosad. Hybrid magnonics: Physics, circuits, and applications for coherent information processing. *Journal of Applied Physics*, 128(13):130902, 10 2020. ISSN 0021-8979. doi: 10.1063/5.0020277. URL https://doi.org/10.1063/5.0020277.

[59] L. J. Cornelissen, J. Liu, R. A. Duine, J. Ben Youssef, and B. J. van Wees. Long-distance transport of magnon spin information in a magnetic insulator at room temperature. *Nature Physics*, 11, 12 2015. ISSN 1745-2481. doi: 10.1038/nphys3465. URL https://doi.org/10.1038/nphys3465.

[60] Benedetta Flebus, Dirk Grundler, Bivas Rana, YoshiChika Otani, Igor Barsukov, Anjan Barman, Gianluca Gubbiotti, Pedro Landeros, Johan Akerman, Ursula Ebels, Philipp Pirro, Vladislav E Demidov, Katrin Schultheiss, Gyorgy Csaba, Qi Wang, Florin Ciubotaru, Dmitri E Nikonov, Ping Che, Riccardo Hertel, Teruo Ono, Dmytro Afanasiev, Johan Mentink, Theo Rasing, Burkard Hillebrands, Silvia Viola Kusminskiy, Wei Zhang, Chunhui Rita Du, Aurore Finco, Toeno van der Sar, Yunqiu Kelly Luo, Yoichi Shiota, Joseph Sklenar, Tao Yu, and Jinwei Rao. The 2024 magnonics roadmap. *Journal of*

Physics: Condensed Matter, 36(36):363501, Jun 2024. doi: 10.1088/1361-648X/ad399c. URL https://dx.doi.org/10.1088/1361-648X/ad399c.

[61] J. J. Viennot, M. C. Dartiailh, A. Cottet, and T. Kontos. Coherent coupling of a single spin to microwave cavity photons. *Science*, 349(6246):408–411, 2015. doi: 10.1126/science.aaa3786. URL https://www.science.org/doi/abs/10.1126/science.aaa3786.

[62] S. S. P. Parkin, K. P. Roche, M. G. Samant, P. M. Rice, R. B. Beyers, R. E. Scheuerlein, E. J. OSullivan, S. L. Brown, J. Bucchigano, D. W. Abraham, Yu Lu, M. Rooks, P. L. Trouilloud, R. A. Wanner, and W. J. Gallagher. Exchange-biased magnetic tunnel junctions and application to nonvolatile magnetic random access memory (invited). *Journal of Applied Physics*, 85(8):5828–5833, 04 1999. ISSN 0021-8979. doi: 10.1063/1.369932. URL https://doi.org/10.1063/1.369932.

[63] Kamalika Nath, P C Mahato, Amit D Lad, Moniruzzaman Shaikh, Kamalesh Jana, Deep Sarkar, Rajdeep Sensarma, G Ravindra Kumar, and S S Banerjee. Macroscopic, layered onion shell like magnetic domain structure generated in YIG films using ultrashort, megagauss magnetic pulses. *New Journal of Physics*, 23(8):083027, Aug 2021. doi: 10.1088/1367-2630/ac1807. URL https://dx.doi.org/10.1088/1367-2630/ac1807.

[64] S. Tacchi, S. Fin, G. Carlotti, G. Gubbiotti, M. Madami, M. Barturen, M. Marangolo, M. Eddrief, D. Bisero, A. Rettori, and M. G. Pini. Rotatable magnetic anisotropy in a $Fe_{0.8}Ga_{0.2}$ thin film with stripe domains: Dynamics versus statics. *Phys. Rev. B*, 89:024411, Jan 2014. doi: 10.1103/PhysRevB.89.024411. URL https://link.aps.org/doi/10.1103/PhysRevB.89.024411.

[65] Maximilian O. Besenhard, Alec P. LaGrow, Aden Hodzic, Manfred Kriechbaum, Luca Panariello, Giorgio Bais, Katerina Loizou, Spyridon Damilos, M. Margarida Cruz, Nguyen Thi Kim Thanh, and Asterios Gavriilidis. Co-precipitation synthesis of stable iron oxide nanoparticles with NaOH: New insights and continuous production via flow chemistry. *Chemical Engineering Journal*, 399:125740, 2020. ISSN 1385-8947. doi: https://doi.org/10.1016/j.cej.2020.125740. URL https://www.sciencedirect.com/science/article/pii/S1385894720318684.

[66] Dmitry Bokov, Abduladheem Turki Jalil, Supat Chupradit, Wanich Suksatan, Mohammad Javed Ansari, Iman H. Shewael, Gabdrakhman H. Valiev, and Ehsan Kianfar. Nanomaterial by Sol-Gel Method: Synthesis and Application. *Advances in Materials Science and Engineering*, 2021(1):5102014, 2021. doi: https://doi.org/10.1155/2021/5102014. URL https://onlinelibrary.wiley.com/doi/abs/10.1155/2021/5102014.

[67] Soumen Rakshit, Krishna Gopal Mondal, Paresh Chandra Jana, Tapanendu Kamilya, and Satyajit Saha. Structural and optical properties of chemically synthesized copper oxide nanoparticles and their photocatalytic application. *Journal of Materials Science: Materials in Electronics*, 34, 11 2023. ISSN 1573-482X. doi: 10.1007/s10854-023-11593-2. URL https://doi.org/10.1007/s10854-023-11593-2.

[68] Yong X. Gan, Ahalapitiya H. Jayatissa, Zhen Yu, Xi Chen, and Mingheng Li. Hydrothermal Synthesis of Nanomaterials. *Journal of Nanomaterials*, 2020(1):8917013, 2020. doi: https://doi.org/10.1155/2020/8917013. URL https://onlinelibrary.wiley.com/doi/abs/10.1155/2020/8917013.

[69] Soumen Rakshit, Paresh Chandra Jana, and Tapanendu Kamilya. Green Synthesis of Copper Nanoparticles by Using Plant Extracts and their Biomedical Applications An Extensive Review. *Current Nanomaterials*, 8(2):110–125, 2023. ISSN 2405-4615/2405-4623. doi: 10.2174/2405461507666220516092814. URL http://www.eurekaselect.com/article/123574.

[70] Zhi-Chao Meng, Li-Yin Gao, and Zhi-Quan Liu. Synthesis of Cu Nanowires by Template Electrodeposition and Their Application in Pressure Sensors. *Journal of Electronic Materials*, 52, 05 2023. ISSN 1543-186X. doi: 10.1007/s11664-023-10317-w. URL https://doi.org/10.1007/s11664-023-10317-w.

[71] Juhi Jannat Mim, Mehedi Hasan, Md Shakil Chowdhury, Jubaraz Ghosh, Md Hosne Mobarak, Fahmida Khanom, and Nayem Hossain. A comprehensive review on the biomedical frontiers of nanowire applications. *Heliyon*, 10(8):e29244, 2024. ISSN 2405-8440. doi: https://doi.org/10.1016/j.heliyon.2024.e29244. URL https://www.sciencedirect.com/science/article/pii/S2405844024052757.

[72] Chou-Yi Hsu, Ahmed Mahdi Rheima, Zainab sabri Abbas, Muhammad Usman Faryad, Mustafa M. Kadhim, Usama S. Altimari, Ashour H. Dawood, Alaa dhari jawad al-bayati, Zainab Talib Abed, Rusul Saeed Radhi, Asala Salam Jaber, Safa K. Hachim, Farah K. Ali, Zaid H Mahmoud, Ghobad Behzadi pour, and Ehsan Kianfar. Nanowires Properties and Applications: A Review Study. *South African Journal of Chemical Engineering*, 46: 286–311, 2023. ISSN 1026-9185. doi: https://doi.org/10.1016/j.sajce.2023.08.006. URL https://www.sciencedirect.com/science/article/pii/S102691852300077X.

[73] Eric E. Fullerton, J. S. Jiang, M. Grimsditch, C. H. Sowers, and S. D. Bader. Exchange-spring behavior in epitaxial hard/soft magnetic bilayers. *Phys. Rev. B*, 58:12193–12200,

Nov 1998. doi: 10.1103/PhysRevB.58.12193. URL https://link.aps.org/doi/10.1103/PhysRevB.58.12193.

[74] F. Magnus, R. Moubah, A. H. Roos, A. Kruk, V. Kapaklis, T. Hase, B. Hjörvarsson, and G. Andersson. Tunable giant magnetic anisotropy in amorphous SmCo thin films. *Applied Physics Letters*, 102(16):162402, 2013. doi: 10.1063/1.4802908. URL https://doi.org/10.1063/1.4802908.

[75] G. B. G. Stenning, A. R. Buckingham, G. J. Bowden, R. C. C. Ward, G. van der Laan, L. R. Shelford, F. Maccherozzi, S. S. Dhesi, and P. A. J. de Groot. Exchange-spring-driven spin flop in an $ErFe_2/YFe_2$ multilayer studied by x-ray magnetic circular dichroism. *Phys. Rev. B*, 84:104428, Sep 2011. doi: 10.1103/PhysRevB.84.104428. URL https://link.aps.org/doi/10.1103/PhysRevB.84.104428.

[76] Jing Yu, Wei Han, Abdulsalam Aji Suleiman, Siyu Han, Naihua Miao, and Francis Chi-Chung Ling. Recent Advances on Pulsed Laser Deposition of Large-Scale Thin Films. *Small Methods*, n/a(n/a):2301282, 2023. doi: https://doi.org/10.1002/smtd.202301282. URL https://onlinelibrary.wiley.com/doi/abs/10.1002/smtd.202301282.

[77] Hao Zeng, Jing Li, J. P. Liu, Zhong L. Wang, and Shouheng Sun. Exchange-coupled nanocomposite magnets by nanoparticle self-assembly. *Nature*, 420, November 2002. ISSN 1476-4687. doi: 10.1038/nature01208. URL https://doi.org/10.1038/nature01208.

[78] A Brenner and GE Riddell. Nickel plating on steel by chemical reduction. *Plating and surface finishing*, 85(8):54–56, 1946. URL https://nvlpubs.nist.gov/nistpubs/jres/37/jresv37n1p31_A1b.pdf.

[79] Abner Brenner, Dwight E. Couch, and Eugenia Kellogg Williams. Electrodeposition of Alloys of Phosphorus with Nickel or Cobalt. *Plating and surface finishing*, 44:109–122, January 1950. URL https://nvlpubs.nist.gov/nistpubs/jres/44/jresv44n1p109_A1b.pdf.

[80] J. Riveiro and M. Sanchez-Trujillo. Magnetic anisotropy of electrodeposited Co-P amorphous alloys. *IEEE Transactions on Magnetics*, 16(6):1426–1428, November 1980. ISSN 0018-9464. doi: 10.1109/TMAG.1980.1060883. URL https://doi.org/10.1109/TMAG.1980.1060883.

[81] J. Riveiro and G. Rivero. Multilayered magnetic amorphous Co-P films. *IEEE Transactions on Magnetics*, 17(6):3082–3084, November 1981. ISSN 0018-9464. doi: 10.1109/TMAG.1981.1061623. URL https://doi.org/10.1109/TMAG.1981.1061623.

[82] J. Riveiro, M. Sanchez, and G. Rivero. Electrodeposited Amorphous Co-P alloys with variable magnetic anisotropy. *IEEE Transactions on Magnetics*, 17(3):1282–1285, May 1981. doi: 10.1109/TMAG.1981.1061210. URL https://doi.org/10.1109/TMAG.1981.1061210.

[83] J M Riveiro, M S Guijarro, G Rivero, and M C Sanchez. Magnetic domains in multilayered amorphous Co-P alloys. *Journal of Physics D: Applied Physics*, 15(1):145–152, Jan 1982. doi: 10.1088/0022-3727/15/1/016. URL https://doi.org/10.1088%2F0022-3727%2F15%2F1%2F016.

[84] J.M. Riveiro. Annealing effects in electrodeposited amorphous Co-P alloys. *Journal of Magnetism and Magnetic Materials*, 27(1):119 – 123, 1982. ISSN 0304-8853. doi: https://doi.org/10.1016/0304-8853(82)90291-8. URL http://www.sciencedirect.com/science/article/pii/0304885382902918.

[85] J. P. Sinnecker, J. M. García, A. Asenjo, M. Vázquez, and A. García-Arribas. Giant magnetoimpedance in CoP electrodeposited microtubes. *Journal of Materials Research*, 15(3):751755, 2000. doi: 10.1557/JMR.2000.0108. URL https://doi.org/10.1557/JMR.2000.0108.

[86] J.M Garcia, A Asenjo, J.P Sinnecker, and M Vazquez. Correlation between GMI effect and domain structure in electrodeposited CoP tubes. *Journal of Magnetism and Magnetic Materials*, 215-216:352 – 354, 2000. ISSN 0304-8853. doi: https://doi.org/10.1016/S0304-8853(00)00156-6. URL http://www.sciencedirect.com/science/article/pii/S0304885300001566.

[87] J.M Garcia, J.P Sinnecker, A Asenjo, and M Vázquez. Enhanced magnetoimpedance in CoP electrodeposited microtubes. *Journal of Magnetism and Magnetic Materials*, 226-230:704 – 706, 2001. ISSN 0304-8853. doi: https://doi.org/10.1016/S0304-8853(00)01142-2. URL http://www.sciencedirect.com/science/article/pii/S0304885300011422.

[88] J. M. Garcia, A. Asenjo, M. Vázquez, A. M. Yakunin, A. S. Antonov, and J. P. Sinnecker. Determination of closure domain penetration in electrodeposited microtubes by combined magnetic force microscopy and giant magneto-impedance techniques. *Journal of Applied*

Physics, 89(7):3888–3891, 2001. doi: 10.1063/1.1346998. URL https://doi.org/10.1063/1.1346998.

[89] C. Favieres, C. Aroca, M. C. Sanchez, and V. Madurga. Continuous change of surface magnetization direction from perpendicular to planar in soft magnetic CoP multilayers. *Journal of Applied Physics*, 91(12):9995–10002, 2002. doi: 10.1063/1.1479480. URL https://aip.scitation.org/doi/abs/10.1063/1.1479480.

[90] D. Ciudad, J. L. Prieto, I. Lucas, C. Aroca, and P. Sanchez. Optimization of magnetic properties of electrodeposited CoP multilayers for sensor applications. *Journal of Applied Physics*, 101(4):043907, 2007. doi: 10.1063/1.2654476. URL https://doi.org/10.1063/1.2654476.

[91] I. Lucas, L. Perez, M. Plaza, O. de Abril, and M.C. Sanchez. Pinning field and coercivity in CoP alloys. *Journal of Magnetism and Magnetic Materials*, 316(2):462 – 464, 2007. ISSN 0304-8853. doi: https://doi.org/10.1016/j.jmmm.2007.03.173. URL http://www.sciencedirect.com/science/article/pii/S0304885307004763.

[92] Yanqiu Li, Liangliang Li, and James Cai. Multi-pulse electrodeposition of soft magnetic thin film Co-P for embedded inductor application. In *2010 11th International Conference on Electronic Packaging Technology High Density Packaging*, pages 220–224, Aug 2010. doi: 10.1109/ICEPT.2010.5582436. URL https://doi.org/10.1109/ICEPT.2010.5582436.

[93] I. Kosta, E. Vallés, E. Gómez, M. Sarret, and C. Müller. Nanocrystalline CoP coatings prepared by different electrodeposition techniques. *Materials Letters*, 65(19):2849 – 2851, 2011. ISSN 0167-577X. doi: https://doi.org/10.1016/j.matlet.2011.06.026. URL http://www.sciencedirect.com/science/article/pii/S0167577X11006628.

[94] Mai Thanh Tung, Le Thi Thu Hang, Le Anh Tuan, Nguyen Hoang Nghi, and Manh-Huong Phan. Influence of electrodeposition parameters on the magnetic and magneto-impedance properties of CoP/Cu wires. *Physica B: Condensed Matter*, 442:16 – 20, 2014. ISSN 0921-4526. doi: https://doi.org/10.1016/j.physb.2014.02.022. URL http://www.sciencedirect.com/science/article/pii/S0921452614001094.

[95] Irene Lucas, David Ciudad, Manuel Plaza, Sandra Ruiz-Gómez, Claudio Aroca, and Lucas Pérez. Assessment of Layer Thickness and Interface Quality in CoP Electrodeposited Multilayers. *ACS Applied Materials & Interfaces*, 8(29):18930–18934, 2016. doi: 10.1021/acsami.6b02577. URL https://doi.org/10.1021/acsami.6b02577.

[96] Jiahong Wang, Danni Liu, Hao Huang, Na Yang, Bo Yu, Min Wen, Xin Wang, Paul K. Chu, and Xue-Feng Yu. In-Plane Black Phosphorus/Dicobalt Phosphide Heterostructure for Efficient Electrocatalysis. *Angewandte Chemie International Edition*, 57(10):2600–2604, 2018. doi: 10.1002/anie.201710859. URL https://onlinelibrary.wiley.com/doi/abs/10.1002/anie.201710859.

[97] Ralph Skomski and J. M. D. Coey. Giant energy product in nanostructured two-phase magnets. *Phys. Rev. B*, 48:15812–15816, Dec 1993. doi: 10.1103/PhysRevB.48.15812. URL https://link.aps.org/doi/10.1103/PhysRevB.48.15812.

[98] T. Schrefl, H. Kronmüller, and J. Fidler. Exchange hardening in nano-structured two-phase permanent magnets. *Journal of Magnetism and Magnetic Materials*, 127(3):L273 – L277, 1993. ISSN 0304-8853. doi: https://doi.org/10.1016/0304-8853(93)90042-Z. URL http://www.sciencedirect.com/science/article/pii/030488539390042Z.

[99] R. Skomski. Aligned twophase magnets: Permanent magnetism of the future? (invited). *Journal of Applied Physics*, 76(10):7059–7064, 1994. doi: 10.1063/1.358027. URL https://doi.org/10.1063/1.358027.

[100] Eric E. Fullerton, C. H. Sowers, J. P. Pearson, S. D. Bader, X. Z. Wu, and D. Lederman. A general approach to the epitaxial growth of rareearthtransitionmetal films. *Applied Physics Letters*, 69(16):2438–2440, 1996. doi: 10.1063/1.117663. URL https://doi.org/10.1063/1.117663.

[101] F. Magnus, M. E. Brooks-Bartlett, R. Moubah, R. A. Procter, G. Andersson, T. P. A. Hase, S. T. Banks, and B. Hjörvarsson. Long-range magnetic interactions and proximity effects in an amorphous exchange-spring magnet. *Nature Communications*, 7:ncomms11931, June, 13 2016. ISSN 2041-1723. doi: 10.1038/ncomms11931. URL https://doi.org/10.1038/ncomms11931.

[102] K. A. Thórarinsdóttir, T. Hase, B. Hjörvarsson, and F. Magnus. Amorphous exchange-spring magnets with crossed perpendicular and in-plane anisotropies. *Phys. Rev. B*, 103:014440, Jan 2021. doi: 10.1103/PhysRevB.103.014440. URL https://link.aps.org/doi/10.1103/PhysRevB.103.014440.

[103] S. Tacchi, T. N. Anh Nguyen, G. Carlotti, G. Gubbiotti, M. Madami, R. K. Dumas, J. W. Lau, Johan Åkerman, A. Rettori, and M. G. Pini. Spin wave excitations in exchange-coupled [Co/Pd]-NiFe films with tunable tilting of the magnetization. *Phys. Rev. B*, 87:144426, Apr 2013. doi: 10.1103/PhysRevB.87.144426. URL https://link.aps.org/doi/10.1103/PhysRevB.87.144426.

[104] S Tacchi, T N Anh Nguyen, G Gubbiotti, M Madami, G Carlotti, M G Pini, A Rettori, V Fallahi, R K Dumas, and Johan Åkerman. [Co/Pd]-CoFeB exchange spring magnets with tunable gap of spin wave excitations. *Journal of Physics D: Applied Physics*, 47(49): 495004, Nov 2014. doi: 10.1088/0022-3727/47/49/495004. URL https://doi.org/10.1088/0022-3727/47/49/495004.

[105] Arabinda Haldar, Chandrima Banerjee, Pinaki Laha, and Anjan Barman. Brillouin light scattering study of spin waves in NiFe/Co exchange spring bilayer films. *Journal of Applied Physics*, 115(13):133901, 2014. doi: 10.1063/1.4870053. URL https://doi.org/10.1063/1.4870053.

[106] J. F. McNulty, E.-M. Anton, B. J. Ruck, M. Suzuki, M. Mizumaki, and H. J. Trodahl. Tunable magnetic exchange springs in semiconductor GdN/NdN superlattices. *Phys. Rev. B*, 100:094441, Sep 2019. doi: 10.1103/PhysRevB.100.094441. URL https://link.aps.org/doi/10.1103/PhysRevB.100.094441.

[107] Paul McCloskey, Terence O'Donnell, Brice Jamieson, Donald Gardner, Michael A. Morris, and Saibal Roy. Electrochemical Fabrication of Multi-Nanolayers. In Mahmood Aliofkhazraei and Abdel Salam Hamdy Makhlouf, editors, *Handbook of Nanoelectrochemistry: Electrochemical Synthesis Methods, Properties and Characterization Techniques*, pages 1–27. Springer International Publishing, Cham, 2016. ISBN 978-3-319-15207-3. doi: 10.1007/978-3-319-15207-3_1-2. URL https://doi.org/10.1007/978-3-319-15207-3_1-2.

[108] Mir Saman Safavi and Frank C. Walsh. Electrodeposited Co-P alloy and composite coatings: A review of progress towards replacement of conventional hard chromium deposits. *Surface and Coatings Technology*, 422:127564, 2021. ISSN 0257-8972. doi: https://doi.org/10.1016/j.surfcoat.2021.127564. URL https://www.sciencedirect.com/science/article/pii/S0257897221007386.

[109] H. A. Dürr, G. Y. Guo, G. van der Laan, J. Lee, G. Lauhoff, and J. A. C. Bland. Element-Specific Magnetic Anisotropy Determined by Transverse Magnetic Circular X-ray Dichroism. *Science*, 277(5323):213–215, 1997. ISSN 0036-8075. doi: 10.1126/science.277.5323.213. URL https://science.sciencemag.org/content/277/5323/213.

[110] Maciej Dąbrowski, Andreas Frisk, David M. Burn, David G. Newman, Christoph Klewe, Alpha T. NDiaye, Padraic Shafer, Elke Arenholz, Graham J. Bowden, Thorsten Hesjedal, Gerrit van der Laan, Gino Hrkac, and Robert J. Hicken. Optically and Microwave-Induced Magnetization Precession in [Co/Pt]/NiFe Exchange Springs. *ACS Applied Materials &*

Interfaces, 12(46):52116–52124, 2020. doi: 10.1021/acsami.0c14058. URL https://doi.org/10.1021/acsami.0c14058.

[111] Dhiman Mallick, Kankana Paul, Tuhin Maity, and Saibal Roy. Magnetic performances and switching behavior of Co-rich CoPtP micro-magnets for applications in magnetic MEMS. *Journal of Applied Physics*, 125(2):023902, 2019. doi: 10.1063/1.5063860. URL https://doi.org/10.1063/1.5063860.

[112] W. Hübner and G. P. Zhang. Ultrafast spin dynamics in nickel. *Phys. Rev. B*, 58:R5920–R5923, September 1998. doi: 10.1103/PhysRevB.58.R5920. URL https://link.aps.org/doi/10.1103/PhysRevB.58.R5920.

[113] M. Aeschlimann, M. Bauer, S. Pawlik, W. Weber, R. Burgermeister, D. Oberli, and H. C. Siegmann. Ultrafast Spin-Dependent Electron Dynamics in fcc Co. *Phys. Rev. Lett.*, 79:5158–5161, Dec 1997. doi: 10.1103/PhysRevLett.79.5158. URL https://link.aps.org/doi/10.1103/PhysRevLett.79.5158.

[114] G. Malinowski, F. Dalla Longa, J. H. H. Rietjens, P. V. Paluskar, R. Huijink, H. J. M. Swagten, and B. Koopmans. Control of speed and efficiency of ultrafast demagnetization by direct transfer of spin angular momentum. *Nature Physics*, 4(11):855 – 858, 2008. doi: 10.1038/nphys1092. URL https://doi.org/10.1038/nphys1092.

[115] H. Harada and M. Fujise. Feasibility study on a highly mobile microwave-band broad-band telecommunication system. *IEEE Transactions on Intelligent Transportation Systems*, 3(1):75–88, March 2002. ISSN 1558-0016. doi: 10.1109/6979.994797.

[116] Sabpreet Bhatti and S. N. Piramanayagam. High Amplitude Microwave Generation Using Domain Wall Motion in a Nanowire. *physica status solidi (RRL) Rapid Research Letters*, 13(3):1800479, 2019. doi: https://doi.org/10.1002/pssr.201800479. URL https://onlinelibrary.wiley.com/doi/abs/10.1002/pssr.201800479.

[117] Dinesh Kumar, K. Konishi, Nikhil Kumar, S. Miwa, A. Fukushima, K. Yakushiji, S. Yuasa, H. Kubota, C. V. Tomy, A. Prabhakar, Y. Suzuki, and A. Tulapurkar. Coherent microwave generation by spintronic feedback oscillator. *Scientific Reports*, 6(1):30747, 2011. doi: 10.1038/srep30747. URL https://doi.org/10.1038/srep30747.

[118] COMSOL AB. COMSOL Multiphysics® Version 6.0., 2022. URL www.comsol.com.

[119] G. S. Abo, Y. Hong, J. Park, J. Lee, W. Lee, and B. Choi. Definition of Magnetic Exchange Length. *IEEE Transactions on Magnetics*, 49(8):4937–4939, Aug 2013. doi: 10.1109/TMAG.2013.2258028. URL https://doi.org/10.1109/TMAG.2013.2258028.

[120] Noémie Elgrishi, Kelley J. Rountree, Brian D. McCarthy, Eric S. Rountree, Thomas T. Eisenhart, and Jillian L. Dempsey. A Practical Beginners Guide to Cyclic Voltammetry. *Journal of Chemical Education*, 95(2):197–206, 2018. doi: 10.1021/acs.jchemed.7b00361. URL https://doi.org/10.1021/acs.jchemed.7b00361.

[121] Richard J. Harrison and Joshua M. Feinberg. FORCinel: An improved algorithm for calculating first-order reversal curve distributions using locally weighted regression smoothing. *Geochemistry, Geophysics, Geosystems*, 9(5), 2008. doi: 10.1029/2008GC001987. URL https://agupubs.onlinelibrary.wiley.com/doi/abs/10.1029/2008GC001987.

[122] Harsh Deep Chopra, Matthew R. Sullivan, A. Ludwig, and E. Quandt. Magnetoelastic and magnetostatic interactions in exchange-spring multilayers. *Phys. Rev. B*, 72:054415, Aug 2005. doi: 10.1103/PhysRevB.72.054415. URL https://link.aps.org/doi/10.1103/PhysRevB.72.054415.

[123] Joseph E. Davies, Olav Hellwig, Eric E. Fullerton, J. S. Jiang, S. D. Bader, G. T. Zimányi, and Kai Liu. Anisotropy dependence of irreversible switching in $Fe/SmCo$ and $FeNi/FePt$ exchange spring magnet films. *Applied Physics Letters*, 86(26):262503, 2005. doi: 10.1063/1.1954898. URL https://doi.org/10.1063/1.1954898.

[124] D. Suess. Multilayer exchange spring media for magnetic recording. *Applied Physics Letters*, 89(11):113105, 2006. doi: 10.1063/1.2347894. URL https://doi.org/10.1063/1.2347894.

[125] Jeffrey McCord, Ludwig Schultz, and Jürgen Fassbender. Hybrid Soft-Magnetic Lateral Exchange Spring Films Prepared by Ion Irradiation. *Advanced Materials*, 20(11):2090–2093, 2008. doi: https://doi.org/10.1002/adma.200700623. URL https://onlinelibrary.wiley.com/doi/abs/10.1002/adma.200700623.

[126] Yuzi Liu, Y. Q. Wu, M. J. Kramer, Y. Choi, J. S. Jiang, Z. L. Wang, and J. P. Liu. Microstructure analysis of a $SmCo/Fe$ exchange spring bilayer. *Applied Physics Letters*, 93(19):192502, 2008. doi: 10.1063/1.2978325. URL https://doi.org/10.1063/1.2978325.

[127] Debangsu Roy and P. S. Anil Kumar. Enhancement of $(BH)_{max}$ in a hard-soft-ferrite nanocomposite using exchange spring mechanism. *Journal of Applied Physics*, 106(7):073902, 2009. doi: 10.1063/1.3213341. URL https://doi.org/10.1063/1.3213341.

[128] P. Krone, D. Makarov, T. Schrefl, and M. Albrecht. Exchange coupled composite bit patterned media. *Applied Physics Letters*, 97(8):082501, 2010. doi: 10.1063/1.3481668. URL https://doi.org/10.1063/1.3481668.

[129] S. Sawatzki, R. Heller, Ch. Mickel, M. Seifert, L. Schultz, and V. Neu. Largely enhanced energy density in epitaxial $SmCo_5$/Fe/$SmCo_5$ exchange spring trilayers. *Journal of Applied Physics*, 109(12):123922, 2011. doi: 10.1063/1.3596756. URL https://doi.org/10.1063/1.3596756.

[130] Wenjing Si, G. P. Zhao, N. Ran, Y. Peng, F. J. Morvan, and X. L. Wan. Deterioration of the coercivity due to the diffusion induced interface layer in hard/soft multilayers. *Scientific Reports*, 5, 2015. URL https://doi.org/10.1038/srep16212.

[131] David J. Carnevale, Michael Shatruk, and Geoffrey F. Strouse. Ligand Passivated CoreShell FePt@Co Nanomagnets Exhibiting Enhanced Energy Product. *Chemistry of Materials*, 28 (15):5480–5487, 2016. doi: 10.1021/acs.chemmater.6b02062. URL https://doi.org/10.1021/acs.chemmater.6b02062.

[132] Q. Zhao, X.X. He, F.J. Morvan, X.F. Zhang, G.P. Zhao, Z.B. Li, L.F. Li, and Y.L. Liu. Interface layer thickness dependence of magnetic properties of SmCo/Fe exchange-spring multilayers: An analytical micromagnetic approach. *Journal of Magnetism and Magnetic Materials*, 495:165858, 2020. ISSN 0304-8853. doi: https://doi.org/10.1016/j.jmmm.2019.165858. URL http://www.sciencedirect.com/science/article/pii/S0304885319311473.

[133] Alex Hubert and Rudolf Schäfer. *Magnetic domains: the analysis of magnetic microstructures*. Springer Science & Business Media, 2008.

[134] Olav Hellwig, Andreas Berger, Jeffrey B. Kortright, and Eric E. Fullerton. Domain structure and magnetization reversal of antiferromagnetically coupled perpendicular anisotropy films. *Journal of Magnetism and Magnetic Materials*, 319(1):13–55, 2007. ISSN 0304-8853. doi: https://doi.org/10.1016/j.jmmm.2007.04.035. URL https://www.sciencedirect.com/science/article/pii/S030488530700649X.

[135] S. Dobák, J. Füzer, I. Petryshynets, P. Kollár, and F. Ková. Enhanced soft-to-hard magnetic switching ratio in grain-oriented FeSi cores induced by helical anisotropy. *Applied Physics Letters*, 123(24):242406, 12 2023. ISSN 0003-6951. doi: 10.1063/5.0166910. URL https://doi.org/10.1063/5.0166910.

[136] T. N. Anh Nguyen, Y. Fang, V. Fallahi, N. Benatmane, S. M. Mohseni, R. K. Dumas, and Johan Åkerman. [Co/Pd]NiFe exchange springs with tunable magnetization tilt angle. *Applied Physics Letters*, 98(17):172502, 2011. doi: 10.1063/1.3580612. URL https://doi.org/10.1063/1.3580612.

[137] P. Saravanan, Jen-Hwa Hsu, C. L. Tsai, C. Y. Tsai, Y. H. Lin, C. Y. Kuo, J.-C. Wu, and C.-M. Lee. Interplay between out-of-plane anisotropic L11-type CoPt and in-plane anisotropic NiFe layers in CoPt/NiFe exchange springs. *Journal of Applied Physics*, 115(24):243905, 2014. doi: 10.1063/1.4885452. URL https://doi.org/10.1063/1.4885452.

[138] Tuhin Maity, Shunpu Li, Lynette Keeney, and Saibal Roy. Ordered magnetic dipoles: Controlling anisotropy in nanomodulated continuous ferromagnetic films. *Phys. Rev. B*, 86:024438, July 2012. URL https://link.aps.org/doi/10.1103/PhysRevB.86.024438.

[139] G. B. G. Stenning, G. J. Bowden, S. A. Gregory, J.-M. L. Beaujour, P. A. J. de Groot, G. van der Laan, L. R. Shelford, P. Bencok, P. Steadman, A. N. Dobrynin, and T. Hesjedal. Magnetic reversal in a YFe_2 dominated $DyFe_2/YFe_2$ multilayer film. *Applied Physics Letters*, 101(7):072412, 2012. doi: 10.1063/1.4746749. URL https://doi.org/10.1063/1.4746749.

[140] J. P. Liu, C. P. Luo, Y. Liu, and D. J. Sellmyer. High energy products in rapidly annealed nanoscale Fe/Pt multilayers. *Applied Physics Letters*, 72(4):483–485, 1998. doi: 10.1063/1.120793. URL https://doi.org/10.1063/1.120793.

[141] Dustin A. Gilbert, Gergely T. Zimanyi, Randy K. Dumas, Michael Winklhofer, Alicia Gomez, Nasim Eibagi, J. L. Vicent, and Kai Liu. Quantitative Decoding of Interactions in Tunable Nanomagnet Arrays Using First Order Reversal Curves. *Scientific Reports*, 4 (1):4204, 2014. ISSN 2045-2322. doi: 10.1038/srep04204. URL https://doi.org/10.1038/srep04204.

[142] Dustin A. Gilbert, Peyton D. Murray, Julius De Rojas, Randy K. Dumas, Joseph E. Davies, and Kai Liu. Reconstructing phase-resolved hysteresis loops from first-order reversal curves. *Scientific Reports*, 11:4018, 2021. ISSN 2045-2322. doi: 10.1038/s41598-021-83349-z. URL https://doi.org/10.1038/s41598-021-83349-z.

[143] R. Egli. VARIFORC: An optimized protocol for calculating non-regular first-order reversal curve (FORC) diagrams. *Global and Planetary Change*, 110:302–320, 2013. ISSN 0921-8181. doi: 10.1016/j.gloplacha.2013.08.003. URL https://www.sciencedirect.com/

science/article/pii/S0921818113001744. Magnetic iron minerals in sediments and their relation to geologic processes, climate, and the geomagnetic field.

[144] Yue Zeng and Shaomin Zhou. In situ surface Raman study of the phosphorus incorporation mechanism during electrodeposition of NiP alloys. *Journal of Electroanalytical Chemistry*, 469(1):79–83, 1999. ISSN 1572-6657. doi: https://doi.org/10.1016/S0022-0728(99)00179-5. URL https://www.sciencedirect.com/science/article/pii/S0022072899001795.

[145] K. SRIDHARAN and K. SHEPPARD. Electrochemical characterization of Fe-Ni-P alloy electrodeposition. *Journal of Applied Electrochemistry*, 27(1):1198–1206, 1997. ISSN 1572-6657. doi: https://doi.org/10.1023/A:1018475718629. URL https://doi.org/10.1023/A:1018475718629.

[146] Grace Baysinger, Lev I Berger, RN Goldberg, HV Kehiaian, K Kuchitsu, G Rosenblatt, DL Roth, and D Zwillinger. *CRC handbook of chemistry and physics*. CRC Press, 96th (internet version 2016) edition, Internet version 2016.

[147] G Ausanio, V Iannotti, L Lanotte, M Carbucicchio, and M Rateo. Weak stripe domains in Co/Fe multilayers. *Journal of Magnetism and Magnetic Materials*, 226-230:1740–1742, 2001. ISSN 0304-8853. doi: https://doi.org/10.1016/S0304-8853(00)00878-7. URL https://www.sciencedirect.com/science/article/pii/S0304885300008787.

[148] Yuqin Sun, Weidong Li, Parul Dhagat, and Charles R. Sullivan. Perpendicular anisotropy in granular CoZrO films. *Journal of Applied Physics*, 97(10):10N301, 2005. doi: 10.1063/1.1851711. URL https://doi.org/10.1063/1.1851711.

[149] J S Jiang and S D Bader. Rational design of the exchange-spring permanent magnet. *Journal of Physics: Condensed Matter*, 26(6):064214, Jan 2014. doi: 10.1088/0953-8984/26/6/064214. URL https://doi.org/10.1088/0953-8984/26/6/064214.

[150] Chandrima Banerjee, Semanti Pal, Martina Ahlberg, T. N. Anh Nguyen, Johan Åkerman, and Anjan Barman. All-optical study of tunable ultrafast spin dynamics in [co/pd]/nife systems: the role of spin-twist structure on gilbert damping. *RSC Adv.*, 6:80168–80173, 2016. doi: 10.1039/C6RA12227B. URL http://dx.doi.org/10.1039/C6RA12227B.

[151] T. N. Anh Nguyen, R. Knut, V. Fallahi, S. Chung, Q. Tuan Le, S. M. Mohseni, O. Karis, S. Peredkov, R. K. Dumas, Casey W. Miller, and J. Åkerman. Depth-Dependent Magnetization Profiles of Hybrid Exchange Springs. *Phys. Rev. Applied*, 2:044014, Oct

2014. doi: 10.1103/PhysRevApplied.2.044014. URL https://link.aps.org/doi/10.1103/PhysRevApplied.2.044014.

[152] Sheng Jiang, Sunjae Chung, Quang Tuan Le, Ping Kwan Johnny Wong, Wen Zhang, and Johan Åkerman. Field-Free High-Frequency Exchange-Spring Spin-Torque Nano-Oscillators. *Nano Letters*, 23(4):1159–1166, 2023. doi: 10.1021/acs.nanolett.2c03613. URL https://doi.org/10.1021/acs.nanolett.2c03613.

[153] Kwanghyo Son and Gisela Schütz. Fabrication and temperature-dependent magnetic properties of large area L10-FePt/Co exchange-spring magnet nanopatterns. *Physica E: Low-dimensional Systems and Nanostructures*, 115:113687, 2020. ISSN 1386-9477. doi: https://doi.org/10.1016/j.physe.2019.113687. URL http://www.sciencedirect.com/science/article/pii/S1386947719306563.

[154] F Magnus, U B Arnalds, H Palonen, G K Pálsson, H Ali, K Leifer, and B Hjörvarsson. Tuneable exchange-spring stiffness in amorphous magnetic trilayer structures. *Journal of Physics: Condensed Matter*, 33(44):445803, Aug 2021. doi: 10.1088/1361-648x/ac1c2c. URL https://doi.org/10.1088/1361-648x/ac1c2c.

[155] R. Pellicelli, C. Pernechele, M. Solzi, M. Ghidini, F. Casoli, and F. Albertini. Modeling and characterization of irreversible switching and viscosity phenomena in perpendicular exchange-spring Fe-FePt bilayers. *Phys. Rev. B*, 78:184434, Nov 2008. doi: 10.1103/PhysRevB.78.184434. URL https://link.aps.org/doi/10.1103/PhysRevB.78.184434.

[156] Giovanni Carlotti and Gianluca Gubbiotti. Magnetic properties of layered nanostructures studied by means of Brillouin light scattering and the surface magneto-optical Kerr effect. *Journal of Physics: Condensed Matter*, 14(35):8199–8233, Aug 2002. doi: 10.1088/0953-8984/14/35/303. URL https://doi.org/10.1088/0953-8984/14/35/303.

[157] G. Gubbiotti, A. Sadovnikov, E. Beginin, S. Sheshukova, S. Nikitov, G. Talmelli, I. Asselberghs, I. P. Radu, C. Adelmann, and F. Ciubotaru. Magnonic band structure in CoFeB/Ta/NiFe meander-shaped magnetic bilayers. *Applied Physics Letters*, 118(16):162405, 2021. doi: 10.1063/5.0047737. URL https://doi.org/10.1063/5.0047737.

[158] Santosh Kulkarni and Saibal Roy. Deposition of thick Co-rich CoPtP films with high energy product for magnetic microelectromechanical applications. *Journal of Magnetism and Magnetic Materials*, 322(9):1592 – 1596, 2010. ISSN 0304-8853. doi: https://doi.org/10.1016/j.jmmm.2009.09.032. URL http://www.sciencedirect.com/science/article/pii/S0304885309009196.

[159] Juan F. Callejas, Carlos G. Read, Eric J. Popczun, Joshua M. McEnaney, and Raymond E. Schaak. Nanostructured Co2P Electrocatalyst for the Hydrogen Evolution Reaction and Direct Comparison with Morphologically Equivalent CoP. *Chemistry of Materials*, 27(10): 3769–3774, 2015. doi: 10.1021/acs.chemmater.5b01284. URL https://doi.org/10.1021/acs.chemmater.5b01284.

[160] Hiroshi Takahashi, Shigeru Tsunashima, Satoshi Iwata, and Susumu Uchiyama. Measurement of Magnetostriction Constants in (111)-Oriented Polycrystalline PdCo Alloy and Multilayered Films. *Japanese Journal of Applied Physics*, 32(Part 2, No. 9B):L1328–L1331, Sep 1993. doi: 10.1143/jjap.32.l1328. URL https://doi.org/10.1143/jjap.32.l1328.

[161] Samiran Choudhury, Avinash Kumar Chaurasiya, Amrit Kumar Mondal, Bivas Rana, Katsuya Miura, Hiromasa Takahashi, YoshiChika Otani, and Anjan Barman. Voltage controlled on-demand magnonic nanochannels. *Science Advances*, 6(40):eaba5457, 2020. doi: 10.1126/sciadv.aba5457. URL https://www.science.org/doi/abs/10.1126/sciadv.aba5457.

[162] S Tacchi, G Gubbiotti, M Madami, and G Carlotti. Brillouin light scattering studies of 2D magnonic crystals. *Journal of Physics: Condensed Matter*, 29(7):073001, Dec 2016. doi: 10.1088/1361-648x/29/7/073001. URL https://doi.org/10.1088/1361-648x/29/7/073001.

[163] A. F. Franco, C. Gonzalez-Fuentes, J. Åkerman, and C. Garcia. Anisotropy constant and exchange coupling strength of perpendicularly magnetized CoFeB/Pd multilayers and exchange springs. *Phys. Rev. B*, 95:144417, Apr 2017. doi: 10.1103/PhysRevB.95.144417. URL https://link.aps.org/doi/10.1103/PhysRevB.95.144417.

[164] S. N. Panda, S. Mondal, J. Sinha, S. Choudhury, and A. Barman. All-optical detection of interfacial spin transparency from spin pumping in β-Ta/CoFeB thin films. *Science Advances*, 5(4):eaav7200, 2019. doi: 10.1126/sciadv.aav7200. URL https://www.science.org/doi/abs/10.1126/sciadv.aav7200.

[165] L. R. Shelford, Y. Liu, U. Al-Jarah, P. A. J. de Groot, G. J. Bowden, R. C. C. Ward, and R. J. Hicken. Ultrafast Optical Parametric Pumping of Magnetization Reorientation and Precessional Dynamics in $DyFe_2/YFe_2$ Exchange Springs. *Phys. Rev. Lett.*, 113:067601, Aug 2014. doi: 10.1103/PhysRevLett.113.067601. URL https://link.aps.org/doi/10.1103/PhysRevLett.113.067601.

[166] Manuel Cardona and Gernot Güntherodt, editors. *Light scattering from spin waves in thin films and layered magnetic structures*, pages 303–335. Springer Berlin Heidelberg, Berlin, Heidelberg, 1989. ISBN 978-3-540-45998-9. doi: 10.1007/BFb0051993. URL https://doi.org/10.1007/BFb0051993.

[167] Jaivardhan Sinha, Chandrima Banerjee, Avinash Kumar Chaurasiya, Masamitsu Hayashi, and Anjan Barman. Improved magnetic damping in CoFeB|MgO with an N-doped Ta underlayer investigated using the Brillouin light scattering technique. *RSC Adv.*, 5:57815–57819, 2015. doi: 10.1039/C5RA06925D. URL https://dx.doi.org/10.1039/C5RA06925D.

[168] W. F. Oliver, C. A. Herbst, S. M. Lindsay, and G. H. Wolf. A general method for determination of Brillouin linewidths by correction for instrumental effects and aperture broadening: Application to highpressure diamond anvil cell experiments. *Review of Scientific Instruments*, 63(3):1884–1895, 1992. doi: 10.1063/1.1143299. URL https://doi.org/10.1063/1.1143299.

[169] J. R. Sandercock and W. Wettling. Light scattering from surface and bulk thermal magnons in iron and nickel. *Journal of Applied Physics*, 50(B11):7784–7789, 1979. doi: 10.1063/1.326763. URL https://aip.scitation.org/doi/abs/10.1063/1.326763.

[170] R.J. Hicken, D.E.P. Eley, M. Gester, S.J. Gray, C. Daboo, A.J.R. Ives, and J.A.C. Bland. Brillouin light scattering studies of magnetic anisotropy in epitaxial Fe/GaAs films. *Journal of Magnetism and Magnetic Materials*, 145(3):278–292, 1995. ISSN 0304-8853. doi: 10.1016/0304-8853(94)01626-7. URL https://www.sciencedirect.com/science/article/pii/0304885394016267.

[171] M G Cottam. Lineshape calculations for light scattering from spin-waves in absorptive magnetic materials. *Journal of Physics C: Solid State Physics*, 11(1):165, Jan 1978. doi: 10.1088/0022-3719/11/1/026. URL https://dx.doi.org/10.1088/0022-3719/11/1/026.

[172] S. M. Rezende, A. Azevedo, M. A. Lucena, and F. M. de Aguiar. Anomalous spin-wave damping in exchange-biased films. *Phys. Rev. B*, 63:214418, May 2001. doi: 10.1103/PhysRevB.63.214418. URL https://link.aps.org/doi/10.1103/PhysRevB.63.214418.

[173] Uwe Bovensiepen. Magnetism in step with light. *Nature Physics*, 5:461 – 463, January 2009. ISSN 1745-2481. doi: 10.1038/nphys1322. URL https://doi.org/10.1038/nphys1322.

[174] E. Carpene, E. Mancini, C. Dallera, M. Brenna, E. Puppin, and S. De Silvestri. Dynamics of electron-magnon interaction and ultrafast demagnetization in thin iron films. *Phys. Rev. B*, 78:174422, Nov 2008. doi: 10.1103/PhysRevB.78.174422. URL https://link.aps.org/doi/10.1103/PhysRevB.78.174422.

[175] B. Koopmans, J. J. M. Ruigrok, F. Dalla Longa, and W. J. M. de Jonge. Unifying Ultrafast Magnetization Dynamics. *Phys. Rev. Lett.*, 95:267207, Dec 2005. doi: 10.1103/PhysRevLett.95.267207. URL https://link.aps.org/doi/10.1103/PhysRevLett.95.267207.

[176] Jean-Yves Bigot, Mircea Vomir, and Eric Beaurepaire. Coherent ultrafast magnetism induced by femtosecond laser pulses. *Nature Physics*, 5:515–520, July 2009. doi: 10.1038/nphys1285. URL https://doi.org/10.1038/nphys1285.

[177] G. P. Zhang and W. Hübner. Laser-Induced Ultrafast Demagnetization in Ferromagnetic Metals. *Phys. Rev. Lett.*, 85:3025–3028, October 2000. doi: 10.1103/PhysRevLett.85.3025. URL https://link.aps.org/doi/10.1103/PhysRevLett.85.3025.

[178] M. Battiato, K. Carva, and P. M. Oppeneer. Superdiffusive Spin Transport as a Mechanism of Ultrafast Demagnetization. *Phys. Rev. Lett.*, 105:027203, July 2010. doi: 10.1103/PhysRevLett.105.027203. URL https://link.aps.org/doi/10.1103/PhysRevLett.105.027203.

[179] M. Hofherr, S. Häuser, J. K. Dewhurst, P. Tengdin, S. Sakshath, H. T. Nembach, S. T. Weber, J. M. Shaw, T. J. Silva, H. C. Kapteyn, M. Cinchetti, B. Rethfeld, M. M. Murnane, D. Steil, B. Stadtmüller, S. Sharma, M. Aeschlimann, and S. Mathias. Ultrafast optically induced spin transfer in ferromagnetic alloys. *Science Advances*, 6(3):eaay8717, 2020. doi: 10.1126/sciadv.aay8717. URL https://www.science.org/doi/abs/10.1126/sciadv.aay8717.

[180] Soma Dutta, Surya Narayan Panda, Jaivardhan Sinha, Samiran Choudhury, and Anjan Barman. Role of Spin Transport through the $\beta - Ta/Co_{20}Fe_{60}B_{20}$ Interface on its Ultrafast Demagnetization: Implications for Ultra-High-Speed Spin-Orbitronic Devices. *ACS Applied Nano Materials*, 5(12):17995–18003, 2022. doi: 10.1021/acsanm.2c03968. URL https://doi.org/10.1021/acsanm.2c03968.

[181] Wei Zhang, Qian Liu, Zhe Yuan, Ke Xia, Wei He, Qing-feng Zhan, Xiang-qun Zhang, and Zhao-hua Cheng. Enhancement of ultrafast demagnetization rate and Gilbert damping driven by femtosecond laser-induced spin currents in $Fe_{81}Ga_{19}/Ir_{20}Mn_{80}$ bilayers. *Phys.*

Rev. B, 100:104412, Sep 2019. doi: 10.1103/PhysRevB.100.104412. URL https://link.aps.org/doi/10.1103/PhysRevB.100.104412.

[182] M. van Kampen, C. Jozsa, J. T. Kohlhepp, P. LeClair, L. Lagae, W. J. M. de Jonge, and B. Koopmans. All-Optical Probe of Coherent Spin Waves. *Phys. Rev. Lett.*, 88:227201, May 2002. doi: 10.1103/PhysRevLett.88.227201. URL https://link.aps.org/doi/10.1103/PhysRevLett.88.227201.

[183] Anjan Barman and Jaivardhan Sinha. *Spin Dynamics*. Springer International Publishing, 2018. ISBN 978-3-319-66296-1. doi: 10.1007/978-3-319-66296-1_2. URL https://doi.org/10.1007/978-3-319-66296-1.

[184] Sucheta Mondal, Abhishek Talapatra, J. Arout Chelvane, Jyoti Ranjan Mohanty, and Anjan Barman. Role of magnetic anisotropy in the ultrafast magnetization dynamics of Gd-Fe thin films of different thicknesses. *Phys. Rev. B*, 100:054436, Aug 2019. doi: 10.1103/PhysRevB.100.054436. URL https://link.aps.org/doi/10.1103/PhysRevB.100.054436.

[185] D. TER HAAR, editor. *18 - ON THE THEORY OF THE DISPERSION OF MAGNETIC PERMEABILITY IN FERROMAGNETIC BODIES*, pages 101–114. Pergamon, 1965. ISBN 978-0-08-010586-4. doi: https://doi.org/10.1016/B978-0-08-010586-4.50023-7. URL https://www.sciencedirect.com/science/article/pii/B9780080105864500237.

[186] P. He, X. Ma, J. W. Zhang, H. B. Zhao, G. Lüpke, Z. Shi, and S. M. Zhou. Quadratic Scaling of Intrinsic Gilbert Damping with Spin-Orbital Coupling in $L1_0$ FePdPt Films: Experiments and Ab Initio Calculations. *Phys. Rev. Lett.*, 110:077203, Feb 2013. doi: 10.1103/PhysRevLett.110.077203. URL https://link.aps.org/doi/10.1103/PhysRevLett.110.077203.

[187] Pavol Krivosik, Nan Mo, Sangita Kalarickal, and Carl E. Patton. Hamiltonian formalism for two magnon scattering microwave relaxation: Theory and applications. *Journal of Applied Physics*, 101(8):083901, 2007. doi: 10.1063/1.2717084. URL https://doi.org/10.1063/1.2717084.

[188] B. Heinrich, J. F. Cochran, and K. Myrtle. The exchange splitting of phonon assisted microwave transmission at 9.5 GHz. *Journal of Applied Physics*, 53(3):2092–2094, 1982. doi: 10.1063/1.330708. URL https://doi.org/10.1063/1.330708.

[189] K. Lenz, H. Wende, W. Kuch, K. Baberschke, K. Nagy, and A. Jánossy. Two-magnon scattering and viscous Gilbert damping in ultrathin ferromagnets. *Phys. Rev. B*, 73:144424, Apr 2006. doi: 10.1103/PhysRevB.73.144424. URL https://link.aps.org/doi/10.1103/PhysRevB.73.144424.

[190] Surya Narayan Panda, Sudip Majumder, Arpan Bhattacharyya, Soma Dutta, Samiran Choudhury, and Anjan Barman. Structural Phase-Dependent Giant Interfacial Spin Transparency in W/CoFeB Thin-Film Heterostructures. *ACS Applied Materials & Interfaces*, 13(17):20875–20884, 2021. doi: 10.1021/acsami.1c03776. URL https://doi.org/10.1021/acsami.1c03776.

[191] Th. Gerrits, H. A. M. van den Berg, J. Hohlfeld, L. Bär, and Th. Rasing. Ultrafast precessional magnetization reversal by picosecond magnetic field pulse shaping. *Nature*, 418(6897):509 – 512, Aug 2002. ISSN 1476-4687. doi: 10.1038/nature00905. URL https://doi.org/10.1038/nature00905.

[192] H. Xia, Z. R. Zhao, F. L. Zeng, H. C. Zhao, J. Y. Shi, Z. Zheng, X. Shen, J. He, G. Ni, Y. Z. Wu, L. Y. Chen, and H. B. Zhao. Giant anisotropic Gilbert damping versus isotropic ultrafast demagnetization in monocrystalline $Co_{50}Fe_{50}$ films. *Phys. Rev. B*, 104:024404, Jul 2021. doi: 10.1103/PhysRevB.104.024404. URL https://link.aps.org/doi/10.1103/PhysRevB.104.024404.

[193] Xingguang Zhang, Xuebin Ke, and Huaiyong Zhu. Zeolite-Supported Gold Nanoparticles for Selective Photooxidation of Aromatic Alcohols under Visible-Light Irradiation. *Chemistry A European Journal*, 18(26):8048–8056, 2012. doi: https://doi.org/10.1002/chem.201200368. URL https://chemistry-europe.onlinelibrary.wiley.com/doi/abs/10.1002/chem.201200368.

[194] Xianxia Yuan, Xin-Xin Hu, Xin-Long Ding, Hai-Chuan Kong, Hao-Dong Sha, He Lin, Wen Wen, Guangxia Shen, Zhi Guo, Zi-Feng Ma, and Yong Yang. Effects of cobalt precursor on pyrolyzed carbon-supported cobalt-polypyrrole as electrocatalyst toward oxygen reduction reaction. *Nanoscale Research Letters*, 8(1):478, 2003. doi: 10.1186/1556-276X-8-478. URL https://doi.org/10.1186/1556-276X-8-478.

[195] K. J. Roe, M. W. Dashiell, J. Kolodzey, P. Boucaud, and J.-M. Lourtioz. Molecular beam epitaxy growth of $Ge_{1-y}C_y$ alloys on Si (100) with high carbon contents. *Journal of Vacuum Science & Technology B: Microelectronics and Nanometer Structures Processing, Measurement, and Phenomena*, 17(3):1301–1303, 1999. doi: 10.1116/1.590745. URL https://avs.scitation.org/doi/abs/10.1116/1.590745.

[196] C Pakpum. Preparation of copper thin film mask by sputtering technique assisted by polymer mask photolithography. *IOP Conference Series: Materials Science and Engineering*, 213(1):012023, jun 2017. doi: 10.1088/1757-899X/213/1/012023. URL https://dx.doi.org/10.1088/1757-899X/213/1/012023.

[197] A. Barman, V. V. Kruglyak, R. J. Hicken, A. Kundrotaite, and M. Rahman. Anisotropy, damping, and coherence of magnetization dynamics in a 10 μm square Ni81Fe19 element. *Applied Physics Letters*, 82(18):3065–3067, 2003. doi: 10.1063/1.1572969. URL https://doi.org/10.1063/1.1572969.

[198] S. P. Vernon, S. M. Lindsay, and M. B. Stearns. Brillouin scattering from thermal magnons in a thin Co film. *Phys. Rev. B*, 29:4439–4442, Apr 1984. doi: 10.1103/PhysRevB.29.4439. URL https://link.aps.org/doi/10.1103/PhysRevB.29.4439.

[199] D. Steiauf, J. Seib, and M. Fähnle. Unified theory of near-adiabatic magnetization dynamics for collinear and noncollinear magnetization. *Phys. Rev. B*, 78:020410, Jul 2008. doi: 10.1103/PhysRevB.78.020410. URL https://link.aps.org/doi/10.1103/PhysRevB.78.020410.

[200] Keith Gilmore, M. D. Stiles, Jonas Seib, Daniel Steiauf, and Manfred Fähnle. Anisotropic damping of the magnetization dynamics in Ni, Co, and Fe. *Phys. Rev. B*, 81:174414, May 2010. doi: 10.1103/PhysRevB.81.174414. URL https://link.aps.org/doi/10.1103/PhysRevB.81.174414.

[201] Yi Li, Fanlong Zeng, Steven S.-L. Zhang, Hyeondeok Shin, Hilal Saglam, Vedat Karakas, Ozhan Ozatay, John E. Pearson, Olle G. Heinonen, Yizheng Wu, Axel Hoffmann, and Wei Zhang. Giant Anisotropy of Gilbert Damping in Epitaxial CoFe Films. *Phys. Rev. Lett.*, 122:117203, Mar 2019. doi: 10.1103/PhysRevLett.122.117203. URL https://link.aps.org/doi/10.1103/PhysRevLett.122.117203.

[202] Shuang Qiao, Wei Yan, Shuaihua Nie, Jianhua Zhao, and Xinhui Zhang. The in-plane anisotropic magnetic damping of ultrathin epitaxial Co_2FeAl film. *AIP Advances*, 5(8): 087170, 2015. doi: 10.1063/1.4929765. URL https://doi.org/10.1063/1.4929765.

[203] Nathan Leroux, Arnaud De Riz, Dédalo Sanz-Hernández, Danijela Markovi, Alice Mizrahi, and Julie Grollier. Convolutional neural networks with radio-frequency spintronic nano-devices. *Neuromorphic Computing and Engineering*, 2(3):034002, jul 2022. doi: 10.1088/2634-4386/ac77b2. URL https://dx.doi.org/10.1088/2634-4386/ac77b2.

[204] Kaibin Huang and Xiangyun Zhou. Cutting the last wires for mobile communications by microwave power transfer. *IEEE Communications Magazine*, 53(6):86–93, June 2015. ISSN 1558-1896. doi: 10.1109/MCOM.2015.7120022.

[205] Francesco Chicco, Alessandro Pezzotta, and Christian C. Enz. Analysis of power consumption in LC oscillators based on the inversion coefficient. In *2017 IEEE International Symposium on Circuits and Systems (ISCAS)*, pages 1–4, May 2017. doi: 10.1109/ISCAS.2017.8050648. URL doi.org/10.1109/ISCAS.2017.8050648.

[206] Q. Mistral, Joo-Von Kim, T. Devolder, P. Crozat, C. Chappert, J. A. Katine, M. J. Carey, and K. Ito. Current-driven microwave oscillations in current perpendicular-to-plane spin-valve nanopillars. *Applied Physics Letters*, 88(19):192507, 2006. doi: 10.1063/1.2201897. URL https://doi.org/10.1063/1.2201897.

[207] Johan Åkerman. Toward a Universal Memory. *Science*, 308(5721):508–510, 2005. ISSN 0036-8075. doi: 10.1126/science.1110549. URL https://science.sciencemag.org/content/308/5721/508.

[208] R. Sbiaa, M. Al Bahri, and S.N. Piramanayagam. Domain wall oscillation in magnetic nanowire with a geometrically confined region. *Journal of Magnetism and Magnetic Materials*, 456:324–328, 2018. ISSN 0304-8853. doi: https://doi.org/10.1016/j.jmmm.2018.02.057. URL https://www.sciencedirect.com/science/article/pii/S0304885317332900.

[209] Michele Voto, Luis Lopez-Diaz, and Eduardo Martinez. Pinned domain wall oscillator as a tuneable direct current spin wave emitter. *Scientific Reports*, 7(1):13559, 2017. ISSN 2045-2322. doi: 10.1038/s41598-017-13806-1. URL https://doi.org/10.1038/s41598-017-13806-1.

[210] Ben Van de Wiele, Sampo J. Hämäläinen, Pavel Balá, Federico Montoncello, and Sebastiaan van Dijken. Tunable short-wavelength spin wave excitation from pinned magnetic domain walls. *Scientific Reports*, 6(1):21330, 2016. ISSN 2045-2322. doi: 10.1038/srep21330. URL https://doi.org/10.1038/srep21330.

[211] Arindam Samanta and Saibal Roy. Generation of High Amplitude Microwaves in Nanowires Induced by Domain Wall Motion. In 15^{th} *Joint MMM-Intermag Conference*, number HOH-03 in Magnetization Dynamics, page 432, January 2022.

[212] A. Dec and K. Suyama. Microwave MEMS-based voltage-controlled oscillators. *IEEE Transactions on Microwave Theory and Techniques*, 48(11):1943–1949, Nov 2000. ISSN 1557-9670. doi: 10.1109/22.883875.

[213] S. M. Mohseni, S. R. Sani, J. Persson, T. N. Anh Nguyen, S. Chung, Ye. Pogoryelov, and Johan Åkerman. High frequency operation of a spin-torque oscillator at low field. *physica status solidi (RRL) Rapid Research Letters*, 5(12):432–434, 2011. doi: https://doi.org/10.1002/pssr.201105375. URL https://onlinelibrary.wiley.com/doi/abs/10.1002/pssr.201105375.

[214] Md Ahsanul Abeed, Justine L. Drobitch, and Supriyo Bandyopadhyay. Microwave Oscillator Based on a Single Straintronic Magnetotunneling Junction. *Phys. Rev. Applied*, 11:054069, May 2019. doi: 10.1103/PhysRevApplied.11.054069. URL https://link.aps.org/doi/10.1103/PhysRevApplied.11.054069.

[215] Anulekha De, Justine Lynn Drobitch, Sudip Majumder, Saswati Barman, Supriyo Bandyopadhyay, and Anjan Barman. Resonant amplification of intrinsic magnon modes and generation of new extrinsic modes in a two-dimensional array of interacting multiferroic nanomagnets by surface acoustic waves. *Nanoscale*, 13:10016–10023, 2021. doi: 10.1039/D1NR01177D. URL http://dx.doi.org/10.1039/D1NR01177D.

[216] Justine Lynn Drobitch, Anulekha De, K. Dutta, Pratap Kumar Pal, Arundhati Adhikari, Anjan Barman, and Supriyo Bandyopadhyay. Extreme Subwavelength Magnetoelastic Electromagnetic Antenna Implemented with Multiferroic Nanomagnets. *Advanced Materials Technologies*, 5(8):2000316, 2020. doi: https://doi.org/10.1002/admt.202000316. URL https://onlinelibrary.wiley.com/doi/abs/10.1002/admt.202000316.

[217] Dhritiman Bhattacharya, Md Mamun Al-Rashid, Noel D'Souza, Supriyo Bandyopadhyay, and Jayasimha Atulasimha. Incoherent magnetization dynamics in strain mediated switching of magnetostrictive nanomagnets. *Nanotechnology*, 28(1):015202, Nov 2016. doi: 10.1088/0957-4484/28/1/015202. URL https://doi.org/10.1088/0957-4484/28/1/015202.

[218] Mohammad Salehi Fashami, Jayasimha Atulasimha, and Supriyo Bandyopadhyay. Magnetization dynamics, throughput and energy dissipation in a universal multiferroic nanomagnetic logic gate with fan-in and fan-out. *Nanotechnology*, 23(10):105201, Feb 2012. doi: 10.1088/0957-4484/23/10/105201. URL https://doi.org/10.1088/0957-4484/23/10/105201.

[219] Zhuyun Xiao, Roberto Lo Conte, Cai Chen, Cheng-Yen Liang, Abdon Sepulveda, Jeffrey Bokor, Gregory P. Carman, and Robert N. Candler. Bi-directional coupling in strain-mediated multiferroic heterostructures with magnetic domains and domain wall motion. *Scientific Reports*, 8(1):5207, 2018. doi: 10.1038/s41598-018-23020-2. URL https://doi.org/10.1038/s41598-018-23020-2.

[220] Sabpreet Bhatti, Chuang Ma, Xiaoxi Liu, and S. N. Piramanayagam. Stress-Induced Domain Wall Motion in FeCo-Based Magnetic Microwires for Realization of Energy Harvesting. *Advanced Electronic Materials*, 5(1):1800467, 2019. doi: https://doi.org/10.1002/aelm.201800467. URL https://onlinelibrary.wiley.com/doi/abs/10.1002/aelm.201800467.

[221] Vimal Sampath, Noel DSouza, Dhritiman Bhattacharya, Gary M. Atkinson, Supriyo Bandyopadhyay, and Jayasimha Atulasimha. Acoustic-Wave-Induced Magnetization Switching of Magnetostrictive Nanomagnets from Single-Domain to Nonvolatile Vortex States. *Nano Letters*, 16(9):5681–5687, 2016. doi: 10.1021/acs.nanolett.6b02342. URL https://doi.org/10.1021/acs.nanolett.6b02342.

[222] Raghav Sharma, Rahul Mishra, Tung Ngo, Yong-Xin Guo, Shunsuke Fukami, Hideo Sato, Hideo Ohno, and Hyunsoo Yang. Electrically connected spin-torque oscillators array for 2.4 GHz WiFi band transmission and energy harvesting. *Nature Communications*, 12:2924, May 2021. ISSN 2041-1723. doi: 10.1038/s41467-021-23181-1. URL https://doi.org/10.1038/s41467-021-23181-1.

[223] Sucheta Mondal, Md Ahsanul Abeed, Koustuv Dutta, Anulekha De, Sourav Sahoo, Anjan Barman, and Supriyo Bandyopadhyay. Hybrid Magnetodynamical Modes in a Single Magnetostrictive Nanomagnet on a Piezoelectric Substrate Arising from Magnetoelastic Modulation of Precessional Dynamics. *ACS Applied Materials & Interfaces*, 10(50):43970–43977, 2018. doi: 10.1021/acsami.8b19243. URL https://doi.org/10.1021/acsami.8b19243.

[224] Stuart S. P. Parkin, Masamitsu Hayashi, and Luc Thomas. Magnetic Domain-Wall Racetrack Memory. *Science*, 320(5873):190–194, 2008. doi: 10.1126/science.1145799. URL https://www.science.org/doi/abs/10.1126/science.1145799.

[225] Sourabh Manna, Rohit Medwal, Surbhi Gupta, John Rex Mohan, Yasuhiro Fukuma, and Rajdeep Singh Rawat. Anisotropy-assisted bias-free spin Hall nano-oscillator. *Applied Physics Letters*, 122(7):072401, 2023. doi: 10.1063/5.0130624. URL https://doi.org/10.1063/5.0130624.

[226] Lukas Körber, Christopher Heins, Tobias Hula, Joo-Von Kim, Sonia Thlang, Helmut Schultheiss, Jürgen Fassbender, and Katrin Schultheiss. Pattern recognition in reciprocal space with a magnon-scattering reservoir. *Nature Communications*, 14:3954, 07 2023. ISSN 2041-1723. doi: 10.1038/s41467-023-39452-y. URL https://doi.org/10.1038/s41467-023-39452-y.

[227] Yanan Zhong, Jianshi Tang, Xinyi Li, Bin Gao, He Qian, and Huaqiang Wu. Dynamic memristor-based reservoir computing for high-efficiency temporal signal processing. *Nature Communications*, 12:408, 01 2021. ISSN 2041-1723. doi: 10.1038/s41467-020-20692-1. URL https://doi.org/10.1038/s41467-020-20692-1.

[228] Matteo Cucchi, Christopher Gruener, Lautaro Petrauskas, Peter Steiner, Hsin Tseng, Axel Fischer, Bogdan Penkovsky, Christian Matthus, Peter Birkholz, Hans Kleemann, and Karl Leo. Reservoir computing with biocompatible organic electrochemical networks for brain-inspired biosignal classification. *Science Advances*, 7(34):eabh0693, 2021. doi: 10.1126/sciadv.abh0693. URL https://www.science.org/doi/abs/10.1126/sciadv.abh0693.

[229] K. Schultheiss, R. Verba, F. Wehrmann, K. Wagner, L. Körber, T. Hula, T. Hache, A. Kákay, A. A. Awad, V. Tiberkevich, A. N. Slavin, J. Fassbender, and H. Schultheiss. Excitation of Whispering Gallery Magnons in a Magnetic Vortex. *Phys. Rev. Lett.*, 122:097202, Mar 2019. doi: 10.1103/PhysRevLett.122.097202. URL https://link.aps.org/doi/10.1103/PhysRevLett.122.097202.

[230] Justin M. Shaw, William H. Rippard, Stephen E. Russek, Timothy Reith, and Charles M. Falco. Origins of switching field distributions in perpendicular magnetic nanodot arrays. *Journal of Applied Physics*, 101(2):023909, 2007. doi: 10.1063/1.2431399. URL https://doi.org/10.1063/1.2431399.

[231] Berk, Cassidy and Jaris, Mike and Yang, Weigang and Dhuey, Scott and Cabrini, Stefano and Schmidt, Holger. Strongly coupled magnon-phonon dynamics in a single nanomagnet. *Nature Communications*, 10:2652, 2019. ISSN 2041-1723. doi: 10.1038/s41467-019-10545-x. URL https://doi.org/10.1038/s41467-019-10545-x.

[232] Wei-Gang Yang and Holger Schmidt. Acoustic control of magnetism toward energy-efficient applications. *Applied Physics Reviews*, 8(2):021304, 2021. doi: 10.1063/5.0042138. URL https://doi.org/10.1063/5.0042138.

[233] Y. Yahagi, B. Harteneck, S. Cabrini, and H. Schmidt. Controlling nanomagnet magnetization dynamics via magnetoelastic coupling. *Phys. Rev. B*, 90:140405, Oct

2014. doi: 10.1103/PhysRevB.90.140405. URL https://link.aps.org/doi/10.1103/PhysRevB.90.140405.

[234] R. P. Cowburn, A. O. Adeyeye, and M. E. Welland. Configurational Anisotropy in Nanomagnets. *Phys. Rev. Lett.*, 81:5414–5417, Dec 1998. doi: 10.1103/PhysRevLett.81.5414. URL https://link.aps.org/doi/10.1103/PhysRevLett.81.5414.

[235] S. Goolaup, A. O. Adeyeye, N. Singh, and G. Gubbiotti. Magnetization switching in alternating width nanowire arrays. *Phys. Rev. B*, 75:144430, Apr 2007. doi: 10.1103/PhysRevB.75.144430. URL https://link.aps.org/doi/10.1103/PhysRevB.75.144430.

[236] G. C. Han, B. Y. Zong, P. Luo, and Y. H. Wu. Angular dependence of the coercivity and remanence of ferromagnetic nanowire arrays. *Journal of Applied Physics*, 93(11):9202–9207, 05 2003. ISSN 0021-8979. doi: 10.1063/1.1572197. URL https://doi.org/10.1063/1.1572197.

[237] S. Goolaup, N. Singh, A. O. Adeyeye, V. Ng, and M. B.A. Jalil. Transition from coherent rotation to curling mode reversal process in ferromagnetic nanowires. *The European Physical Journal B - Condensed Matter and Complex Systems*, 44, 03 2005. ISSN 1434-6036. doi: 10.1140/epjb/e2005-00122-7. URL https://doi.org/10.1140/epjb/e2005-00122-7.

[238] M Maicas, M Rodrguez, E López, M.C Sánchez, C Aroca, and P Sánchez. Magnetic switching fields in square monolayer and bilayer nanodots. *Computational Materials Science*, 25(4):525–530, 2002. ISSN 0927-0256. doi: https://doi.org/10.1016/S0927-0256(02)00330-0. URL https://www.sciencedirect.com/science/article/pii/S0927025602003300.

[239] Miguel Romera, Philippe Talatchian, Sumito Tsunegi, Flavio Abreu Araujo, Vincent Cros, Paolo Bortolotti, Juan Trastoy, Kay Yakushiji, Akio Fukushima, Hitoshi Kubota, Shinji Yuasa, Maxence Ernoult, Damir Vodenicarevic, Tifenn Hirtzlin, Nicolas Locatelli, Damien Querlioz, and Julie Grollier. Vowel recognition with four coupled spin-torque nano-oscillators. *Nature*, 563, 11 2018. ISSN 1476-4687. doi: 10.1038/s41586-018-0632-y. URL https://doi.org/10.1038/s41586-018-0632-y.